THE OPTICAL ENVIRONMENT FROM THE TIP VORTICES OF A HELICOPTER IN DIFFERENT FLIGHT REGIMES

A Dissertation

Submitted to the Graduate School

of the University of Notre Dame

in Partial Fulfillment of the Requirements

for the Degree of

Doctor of Philosophy

by

Christopher O. Porter

Mark Rennie, Co-Director

Eric Jumper, Co-Director

Graduate Program in Aerospace and Mechanical Engineering

Notre Dame, Indiana

October 2011

THE OPTICAL ENVIRONMENT FROM THE TIP VORTICES OF A HELICOPTER IN DIFFERENT FLIGHT REGIMES

Abstract

by

Christopher O. Porter

Aero-optical aberrations associated with turbulent compressible flow fields can seriously degrade the performance of an optical system; the effect of these aberrations increases as the wavelength of the transiting light becomes shorter, and so is particularly strong at visible and near-infrared wavelengths. These aero-optic aberrations originate from both spatial- and temporal-variations of the index-of-refraction, and are associated with the low-pressure cores and concomitant reduced density within the vortical structures in certain turbulent flow field such as free-shear layers and tip vortices. To date, aero-optics research has focused primarily on fixed-wing aircraft travelling at compressible-flow speeds, where compressible shear layers and turbulent boundary layers are the dominant source of aero-optic aberrations. Helicopter platforms, on the other hand, operate at much lower Mach numbers ($M<0.3$) and are actually best suited for hover. In this case, the optical aberrations produced from shear-layer or turbulent boundary-layer flows are greatly reduced or eliminated in the case of hover; instead, aero-optic aberrations result primarily from the wake of the rotor that can have tip speeds up to a Mach number of one. The tip vortices shed from the rotor blades, have an

aberrating effect similar to the vortices in a compressible shear-layer that forms behind a turret on a fixed-wing aircraft.

In this dissertation, experimental and numerical results are presented that both calibrate and validate a scaling relationship derived from Euler's equations and the Lamb-Oseen vortex model. Extended numerical simulations of basic helicopter flow-field features were performed for a medium-sized helicopter both in hover and in forward flight to determine estimates of the spatial- and temporal-degradation of a collimated beam traveling through the rotor-blade wake. The results indicate that the severity of the aberration is highly dependent on the vortex circulation strength and core radius. Even with the most conservative estimates, the farfield effects of light propagating through these tip vortices greatly reduces the irradiance delivered on target through both tip/tilt and higher order effects. Finally, the use of adaptive optics to correct for these aberrations is examined for the case of hover.

For my mother, Zenda K. Porter

and my father, William S. Porter (1950-2011)

CONTENTS

FIGURES

TABLES

ACKNOWLEDGMENTS

The Office of Naval Research under Award Number N00014-07-1-0291 sponsored these efforts. The author appreciates the guidance of both co-advisors, Dr. Eric Jumper and Dr. Mark Rennie. Dr. Rennie has spent countless hours discussing the data and reviewing this dissertation and other papers, and his help is greatly appreciated. Dr. Stanislav Gordeyev also deserves many thanks for his support and guidance throughout this project as well as others projects. Dave Cavalieri, Mike Zenk, Mike Swadener, and Joel Preston were all vital to the success of the experiments performed during my time here. My fellow friends and graduate students, Jacob Cress and Zach Ponder, also deserve my gratitude. Many hours have been spent with them discussing ideas and concepts. The Arthur J. Schmitt Foundation Fellowship for Engineering and Science has provided financial support to the author during this time, greatly easing the burden of graduate school. Finally, and most importantly, my Lord who has opened doors for me that I could have never imaged in my wildest dreams.

NOMENCLATURE

A	Lamb-Oseen momentum deficit; self-similarity proportionality constant
$A(P)$	wave amplitude
A_D	aperture diameter
AP	aperture ratio
Az	azimuth angle
a	speed of sound
a_1	apparent viscosity coefficient
b	span
$C_{D,0}$	drag coefficient at zero degree angle of attack
CDF	cumulative distribution function
C_l	lift coefficient
C_P	specific heat at constant pressure
C_T	thrust coefficient $= T/[0.5\pi\rho\Omega^2 R^4]$
$C_{T\text{-}P}$	temperature-pressure relationship constant
c	speed of light in a vacuum; blade chord
D	turret diameter
dl	small discretized vortex filament element
Ei	exponential integral
El	elevation angle
$G(AP)$	aperture gain function
G_{10}	aperture gain function normalized by an aperture ratio of 10
h	perpendicular distance from a point $\vec{r}$ to a vortex filament

I	irradiance
I_0	diffraction-limited irradiance
K_{GD}	Gladstone-Dale constant
k	wave number; circulation proportionality constant
k_n	nth cumulant
L	length; propagation distance
M	Mach number
M_V	vortex Mach number, V_θ/a
m	mean
N	Biot-Savart shape factor
N_b	number of blades
n	index of refraction
OPD	Optical Path Difference
$\mathrm{OPD}_{\mathrm{Norm}}$	normalized OPD
OPL	Optical Path Length
P	static pressure; position
P_0	laser power; total pressure
PDF	probability distribution function
R	rotor radius; gas constant
Re_V	vortex Reynolds number, $2\Gamma/\upsilon$
$\vec{r}$	radial position vector
r,θ,z	cylindrical coordinates
r_0	initial vortex core radius
r_c	vortex core radius
r_{tip}	radial position of tip-vortex filament
SR	Strehl ratio
s_1, s_2	arbitrary positions
T	static temperature
T_0	total temperature
T_{Ad}	adiabatic temperature

TPP	tip path plane
t	time
t_0	vortex core time offset
u,U	scalar function (electric field)
u,v,w	Cartesian velocity components
V_r	radial velocity
V_z	axial velocity
V_θ	tangential velocity
W	wavefront
$\vec{x}$	position vector
x, y, z	Cartesian coordinates
x', y'	nearfield coordinates
x_0,y_0	center of vortex
α	angle of attack; Lamb-Oseen constant (1.25643); viewing angle
β	modified elevation angle
Γ	circulation
γ	specific heat ratio
δ	apparent viscosity
ε	permittivity of free-space
ζ	relative beam angle to the helicopter rotor
θ_{tw}	linear blade twist
λ	wavelength
μ	advance ratio; permeability of free-space
μ_n	nth statistical moment
ν	frequency; speed of light in a medium; kinematic viscosity
ρ	density
σ	solidity ratio (blade area/disk area); standard deviation
ϕ	characteristic function
$\phi(P)$	wave phase
χ	scaling relationship (WCM)

ψ_b	blade azimuthal location
ψ_R	relative rotor phase angle
ψ_w	wake age
ω	angular frequency
Ω	rotor rotational frequency
$\vec{\mathcal{E}}$	electric field
$\vec{\mathcal{H}}$	magnetic field

Subscripts

0	initial or reference value
∞	farfield
RMS	root mean square
SL	sea level
loc	local
Ad	adiabatic

CHAPTER 1:

INTRODUCTION

1.1. Overview

This dissertation details the first investigation into the aero-optic effects of rotor wakes, and in particular their blade-tip vortices, with emphasis placed on the effect that these vortices have on optical systems mounted to medium-sized helicopters. At the start of this project, one fundamental question presented itself repeatedly: "What, if any, aero-optic effects exist that could adversely affect an optical system mounted to a helicopter?" Although plenty of theories that deal with aerodynamically related flow features and their impact on optical systems exist, there are currently no data in the literature to definitively answer this question. While other sources of aberrations may, and probably do exist, the remainder of this dissertation will show that at least one source, the blade-tip vortices, will significantly reduce the effectiveness of optical systems mounted on helicopters. The different methods of defining an optical system's effectiveness will be expanded upon throughout the dissertation.

This chapter will discuss the motivation for this investigation, as well as briefly look at the history of aero-optics and airborne lasers. In Chapter 2, optical properties and concepts needed and used throughout this dissertation are defined. Chapter 3 reviews

published literature concerning the kinematics of rotor-tip vortices. Chapter 4 discusses the merging of optical analysis and fluid dynamics to calculate aero-optic effects from a single tip vortex. The chapter concludes with the development of a numerically-calibrated scaling relationship for a single tip vortex, a grid resolution study, and an estimate of the severity of the rotor-induced aero-optic environment around a medium-sized helicopter. Chapter 5 details two experimental investigations along with computational fluid dynamic (CFD) simulations to verify the scaling relationship developed in Chapter 4. Chapter 6 expands upon the kinematics of a single tip vortex to the kinematics of the system of tip vortices that make up the wake of a helicopter, while Chapter 7 looks at the resulting aero-optics of a helicopter's wake. Finally, Chapter 8 provides conclusions and final thoughts on the use of optical systems on helicopters and potential future work.

1.2. Motivation

Lasers and other optical instrumentation are now routinely mounted on aircraft for a variety of reasons; however, new applications are arising, such as optical communications and directed energy. For these new applications, it is critically important to the successful operation of the system to maintain a tightly focused spot on a farfield target. For a given optical system, the ability to focus a beam of light on a farfield target is impaired by optical aberrations in the intervening air between the laser and the target. In particular, as light travels through an inhomogeneous index-of-refraction field, aberrations are imprinted onto the wavefront as regions of the beam

speed up or slow down, resulting in a non-planar wavefront. These aberrations degrade the ability to focus the beam on a target in the farfield. The relationship between the magnitude of optical aberrations and the quality of the focused farfield spot is discussed in detail in Chapter 2.

For air, the Gladstone-Dale relation links variations in the index-of-refraction field to density variations:

$$n = 1 + \rho K_{GD}. \tag{1.1}$$

One source of density variations occurs because of temperature fluctuations associated with atmospheric turbulence (Tatarskii and Zavorotnyi 1985). The associated atmospheric-optics problem is relatively well understood since it affects different applications ranging from astronomical observations to aerial imaging and tracking. On the other hand, density variations are also created by the turbulent, compressible flows surrounding an aircraft in flight (Jumper and Fitzgerald 2001; Siegenthaler 2008). These optical aberrations originate from aircraft-generated flows and are referred to as "aero-optic" aberrations. In general, aero-optics is a less-mature field compared to atmospheric-optics. Furthermore, aero-optic flows are typically more challenging than atmospheric-optics flows, due to the higher aberration magnitudes and the much higher frequency content (see Chapter 2).

1.3. History of Airborne Laser Systems

Prior to examining the use of laser systems on helicopters, it is informative to first review the development of airborne high-energy laser (HEL) systems in general. As will

be shown, the challenges uncovered by previous investigations into mounting HEL systems onto fixed-wing aircraft will clarify the motivations and details associated with using a helicopter as the mounting platform.

In the late 1970s and early 1980s, optical turrets were extensively studied as the use of lasers on aircraft started to become feasible. The first optical systems used a laser with a long wavelength, limiting the systems range and farfield irradiance delivered on target. However, in the 1980s, airborne optical systems switched to using a laser with a much shorter wavelength, thereby increasing the ideal irradiance that could be delivered on target:

$$I_0 \propto \frac{P_0 A_D^2}{L^2 \lambda^2}, \tag{1.2}$$

where P_0 is the laser power, A_D is the aperture diameter, L is the propagation distance, and λ is the laser wavelength.

As both laser technology and adaptive-optical systems improves, the use of directed-energy systems on aircraft becomes increasingly more feasible. These two advancements produce an increase in the range of the optical system and irradiance that can be delivered on a target (Duffner 2009). A consequence of reducing the laser's wavelength to increase the range and power of the system is that the effects of compressible flow fields near the aircraft itself are now made significantly more important. In particular, while the hemispherical turret provides an efficient means for directed energy to enter or exit the aircraft and enable the beam to track over a full range of elevation and azimuth angles, the flow field of the turret includes a shear-layer and a separated flow region aft of the turret that becomes optically active at compressible flow

speeds. At the shorter wavelengths that will likely be used in new laser systems, the optical effects created from the flow field around the aircraft, specifically the turret, can no longer be ignored. The optical aberrations produced by these aero-optic effects would limit the realistic field-of-regard of HEL systems to forward-looking angles. Even at forward-looking angles, vibrations induced by unsteady flow near the turret can result in optical jitter (Gordeyev and Jumper 2010).

As an example of the nature of the aero-optical environment surrounding an optical turret, Figure 1.1 shows the magnitude of optical aberration on an outgoing beam from a flat-windowed turret as a function of viewing-angle. The data were acquired in the University of Notre Dame's Airborne Aero-Optics Lab (AAOL), which provides in-flight measurements of the optical distortions due to compressible flows, see Figure 1.2 (Porter *et al.* 2011). The $\mathrm{OPD_{Norm}}$ ($OPD_{RMS}/(\rho/\rho_{SL})M^2D$) term shown in Figure 1.1 will be discussed in detail in following sections of this dissertation; however, it relates directly to the reduction in performance of an optical system. Note that the data in Figure 1.1 is proportional to the Mach number squared amongst other quantities.

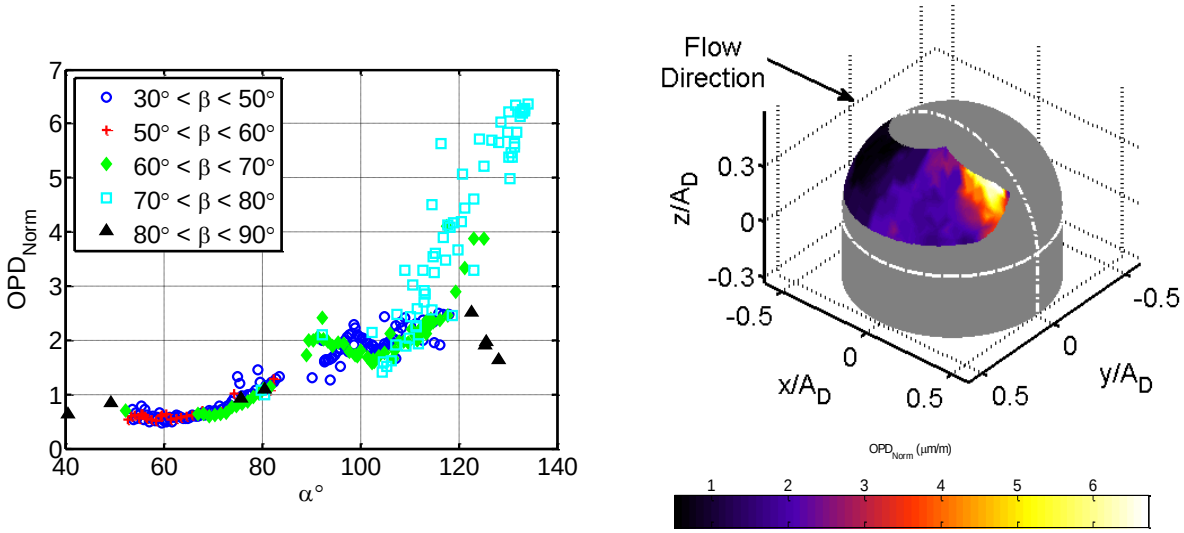

Figure 1.1: Average normalized OPD on a beam of light projected into the AAOL turret, acquired at various viewing angles illustrating the effect of compressible flow on optical system performance (Porter *et al*. 2011, see Figure 1.2).

Figure 1.2: Notre Dame's Airborne Aero-Optics Laboratory. Left) Two Citations flying in formation to measure the aero-optics effects of flow around a turret. Right) Picture of the laser on the turret taken during the first successful flight test (Porter *et al*. 2011).

1.4. Applied Aero-Optic Research

With the ability to measure optically-active flows, and an understanding of the mechanisms that cause optical aberrations, aero-optics research has progressed to the investigation of methods to mitigate or eliminate aero-optic effects. As shown above, prototype HEL systems have for the most part been flight tested on fixed-wing aircraft and in high speed flows, where the most important aero-optic flows include shear layers

(Fitzgerald and Jumper 2004; Rennie *et al.* 2008; Wittich 2009), turbulent boundary layers (Cress *et al.* 2008; Gordeyev *et al.* 2003), and even shocks.

In an effort to increase the field-of-regard for hemispherical turret designs, both flow-control and adaptive-optic techniques have been employed to either suppress or correct aero-optic aberrations. Flow control approaches typically perturb the flow on, or in the vicinity of the turret. By doing so, they either delay boundary-layer separation or influence the behavior of the downstream wake. Even with the complex and highly three-dimensional flow behind a turret, Figure 1.3 (Morgan *et al.* 2011), gains in the field-of-regard have been made using passive flow-control techniques (Ladd *et al.* 2009). For example, as reported in Gordeyev and Jumper (2009), the field-of-regard for a turret was extended while the vortex-induced jitter of the turret was reduced using either synthetic jets or passive pins. Another promising passive flow-control approach uses fences attached to the turret, possibly in conjunction with a downstream fairing to control the pressure distribution on the turret. This delays boundary-layer separation and prevents the formation of local supersonic flows (Rennie *et al.* 2010a).

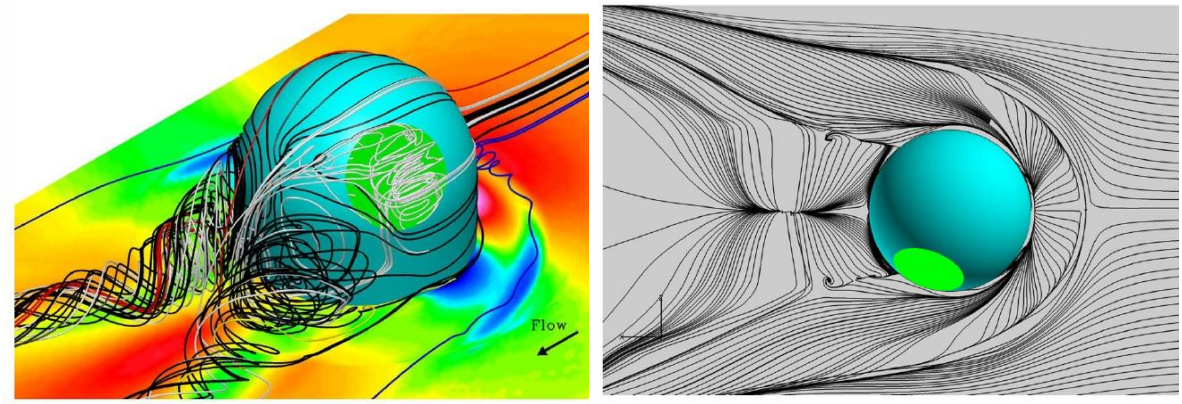

Figure 1.3: Computational time-mean surface pressure contours and streamlines around a flat-windowed turret (left) and mean flow surface topology (right) (Morgan *et al.* 2011).

Aero-optic aberrations can also be mitigated using adaptive-optic (AO) approaches (Tyson 1991). In this case, the outgoing laser beam is preconditioned with the conjugate of the aero-optic aberrations using a deformable mirror (DM). As the beam passes through the optically-active flow, the aero-optic aberrations correct the wavefront distortion placed on the beam by the DM. This results in a beam with a planar wavefront that emerges from the other side of the flow. The time scales at which these corrections must be made correspond to the time scales of the fluidic structures propagating through the beam. At the Mach 0.8 cruise speeds of typical fixed-wing aircraft, the important spectral content of the aero-optic aberrations associated with shear-layer flows is in the range of a few hundred Hertz up to a few kilohertz. For a closed-loop feedback AO system to operate stably, the rate at which information must be gathered and processed is approximately 50 to 100 times greater (depending on the system gain) than the frequency of the aberration that is being corrected (Nightingale *et al.* 2005). This means that in order to correct the aberrations of a typical shear-layer flow, the AO system would require a sampling rate on the order of 100 kHz; this kind of frequency response is beyond the capability of conventional AO systems.

One approach to improving the bandwidth of the AO system is to regularize the vortices in the shear-layer through flow control techniques so that their passage frequency and strength at a given location is coherent and predictable (Rennie *et al.* 2006). This combination of flow-regularization in conjunction with an AO approach is called "feed-forward adaptive optics" and can be performed using currently-available hardware (Duffin 2009; Nightingale *et al.* 2008; Rennie *et al.* 2009; Wallace *et al.* 2010).

1.5. Optical Systems on Helicopter

Given the difficulty in suppressing or correcting compressible, optically-active flows, it would seem to be advantageous to avoid them altogether. In this regard, helicopters might present an attractive platform for optical systems based on their comparatively-low operational flight speeds. Ideally, helicopters are designed and best suited for hover (Leishman 2000). Even at typical cruise speeds, a helicopter's airspeed is still too low to generate significant compressible-flow effects due to flow around the helicopter's airframe or an attached turret. Instead, in the case of helicopters, compressible-flow effects and the associated aero-optic aberrations are expected to originate primarily from the rotor-blade tip vortices.

The wake system, and particularly the tip vortices shed from the rotor blades, will include significant regions of weakly-compressible flow resulting from the curvature of the flow field. As shown in (Bagai and Leishman 1993; Vatistas 2005), the pressure and density within the cores of the tip vortices are significantly reduced, producing aero-optic aberrations similar to the kind of aberrations already observed within the vortical structures contained within shear-layer flows (Fitzgerald and Jumper 2004; Rennie *et al.* 2008). The fact that the optical aberrations originating from tip vortices can present a serious disturbance for a transiting beam is convincingly illustrated by Figure 1.4 (with permission of Mike Paschal), which shows that the tip vortices from a Boeing 737-400 are strong enough to produce optical aberrations that are clearly visible to the naked eye. For a hovering helicopter, the rotor-blade tip vortices propagate downward in a helical pattern and past the helicopter fuselage (Figure 1.5); as such, they pass through the line-of-sight of an optical system mounted in the helicopter or attached

to the belly of the helicopter (Figure 1.6). During forward flight, these vortices might also propagate into the path of the outgoing beam depending on factors such as the flight speed and the elevation/azimuth angle of the outgoing beam.

Figure 1.4: A 737 landing at San Antonio airport, in which the wingtip vortices are visible due to aero-optic effects. Picture taken and reproduced with permission from Mike Paschal.

Figure 1.5: Wingtip vortices rendered visible from condensation due to the low-pressure vortex cores (pictures taken from rcgroups.com and Gizmodo.com).

The question that this research addresses is, “what effect do tip vortices have on the wavefront of a beam of light?” In addition to the investigation of individual vortices, the research also investigates the aero-optic environment around a helicopter caused by the rotor tip-vortex system. The helicopter investigations are performed for both hover and forward flight, to illustrate how the aero-optic environment varies with the flight speed of the aircraft. The data presented throughout this dissertation is representative of a generic medium-sized helicopter.

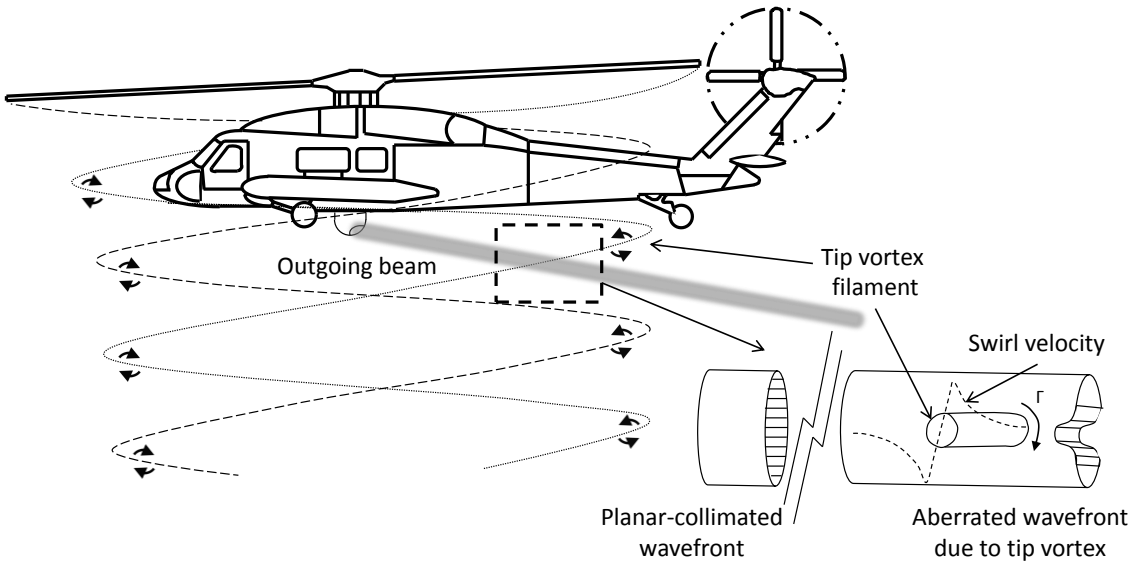

Figure 1.6: Optical turret mounted beneath a medium-sized helicopter in hover.

CHAPTER 2:

OPTICS

2.1. The Aero-Optics Problem

The density of a gas at a given location in space and time is dependent on the pressure and temperature. Therefore, fluctuations in either the pressure or temperature result in density fluctuations. These density fluctuations are directly related to fluctuations in the index-of-refraction by:

$$n(\vec{x},t) - 1 = K_{GD}\,\rho(\vec{x},t), \tag{2.1}$$

where n is the index-of-refraction, and K_{GD} is the Gladstone-Dale constant. For gases, the Gladstone-Dale constant is a weak function of wavelength, and is equal to 0.225 cm^3/kg at a wavelength of 1 μm (Stathopoulos *et al.* 2009).

The index-of-refraction is the ratio of the speed at which light propagates through a vacuum to the propagation speed in a given medium. The refractive index field for a given medium can vary in both space and time, in which case the speed at which light propagates through that medium is a function of both space and time. When a planar wavefront propagates through a spatially- and temporally-varying density (refractive index) field, the emerging wavefront is distorted. This distortion reduces the ability to focus the beam to a spot in the farfield (Figure 2.1).

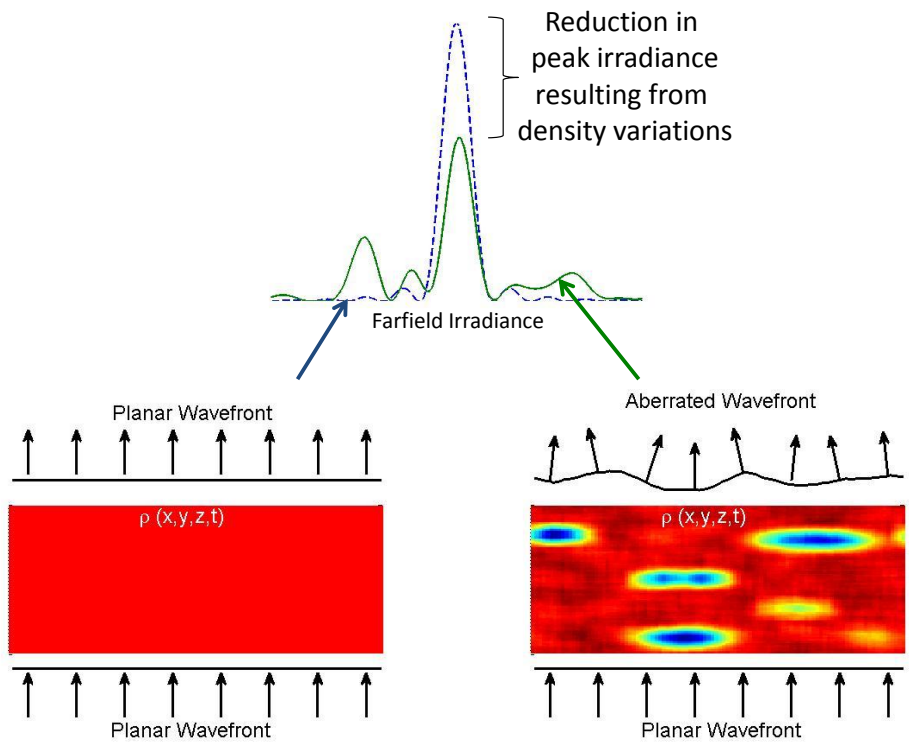

Figure 2.1: Effect on a planar wavefront as it passes through an inhomogeneous density field (right) compared to the ideal diffraction-limited case (left).

2.2. Optics

To analyze the effect of spatial or temporal variations in the refractive index on a beam of light, two common optical analysis techniques are used: (1) geometric optics and (2) Fourier optics (scalar wave theory). Geometric optics is the simpler approach, in which the propagation of light in an optical system is modeled using rays. In geometric optics, the direction of the light rays can change through either reflection or refraction; however, diffraction is not modeled.

The next level of complexity in optical analysis techniques is Fourier optics, also known as scalar wave theory, physical optics, or scalar diffraction theory. In Fourier

optics, diffraction is defined as "any deviation of light rays from rectilinear paths which cannot be interpreted as reflection or refraction (Goodman 2005)." In 1665, Grimaldi discovered diffraction when looking at the shadow created from a light source after passing through an aperture large enough that the penumbra effect was negligible. According to geometric optics theory, a sharp boundary would be expected to exist between the light and dark regions; however, in reality, the transition from the light to the shadow occurred gradually.

Huygens postulated a solution to this problem, which eventually helped lead to the understanding of the wave properties of light. Huygens suggested that every point on a wavefront, or locus of points in the beam that have the same phase, could be modeled as a new point source of light waves (Figure 2.2). These new sources, or "secondary" spherical disturbances, determine the wavefront at a later instant in time. Since light rays travel perpendicular to the wavefront, Huygens was able to relate geometric optics to Fourier optics.

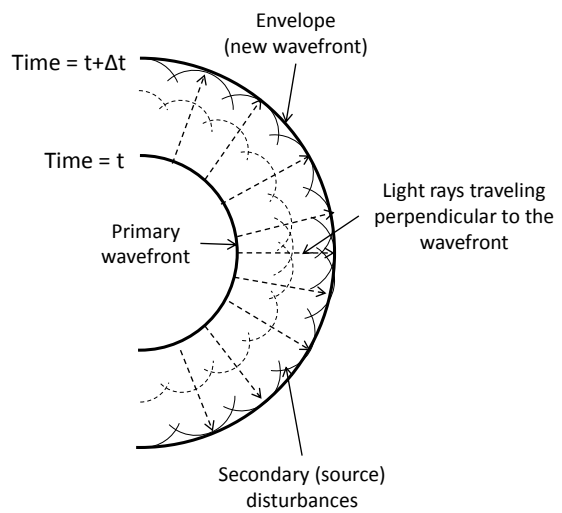

Figure 2.2: Huygens principle of secondary wavelet envelope.

Optics can also be separated into two categories, the *nearfield* or the *farfield*. Aero-optic laboratory measurements are typically made by examining light in the nearfield. On the other hand, it is also important to understand the effect of nearfield aberrations on the beam in the farfield, where diffraction effects must be accounted for. When dealing with the nearfield, geometric optics are typically used, while farfield calculations require the use of Fourier optics.

2.2.1. Nearfield (Geometric) Considerations

As mentioned above, the index-of-refraction, *n*, is the ratio of the speed of light, *c*, in a vacuum to the speed of light in a given medium, *v*. Therefore, given a variable index-of-refraction field, as a beam of light propagates through the field, the distance that each ray in the light beam travels during a given amount of time is different.

One method of quantifying the effect of an aberrating medium is by computing the optical path length (OPL):

$$OPL(\vec{x},t) = \int_{s1}^{s2} n(\vec{x},t)ds = \int_{t_{s1}}^{t_{s2}} \frac{c}{v(\vec{x},t)} v(\vec{x},t)dt = \int_{t_{s1}}^{t_{s2}} cdt\,, \qquad (2.2)$$

where *s* is the propagation path of the light ray. The OPL, therefore, is related to the time required for light to travel from one point to another. When the distance of propagation is small, the amount that a ray deviates from a straight path is also small. Therefore, Eq. (2.2) can be simplified, with negligible loss of accuracy, by integrating along just the nominal direction of the light path, *x*:

$$OPL(\vec{x},t) = \int_{s1}^{s2} n(\vec{x},t)dx. \qquad (2.3)$$

The difference at any point between the OPL and the mean OPL is the optical path difference (OPD):

$$OPD(\vec{x},t) = OPL(\vec{x},t) - \overline{OPL}(\vec{x},t) \tag{2.4}$$

where the over bar denotes the spatial mean of the OPL.

One way of thinking about OPL is it is the effective distance a light ray must travel in order to pass through the aberrating region, if the light ray were traveling at the speed of light in a vacuum, c. The OPD is then the difference from the mean OPL for a spatially-varying index-of-refraction field. As such, a positive OPD indicates portions of the wavefront that must effectively travel longer distances in order to traverse the aberrating region, and therefore emerge from the aberrating region lagging the mean wavefront. In other words, the wavefront is the conjugate of the OPD.

2.2.2. Nearfield (Diffraction) Effects

Geometric optics work very well at modeling the behavior of light in the immediate nearfield before diffraction effects begin to dominate. To account for diffraction effects, Maxwell's equations provide the fundamental basis for the propagation of light waves:

$$\begin{gathered} \nabla \times \vec{\mathcal{E}} = -\mu \frac{\partial \vec{\mathcal{H}}}{\partial t} \\ \nabla \times \vec{\mathcal{H}} = \epsilon \frac{\partial \vec{\mathcal{E}}}{\partial t} \\ \nabla \cdot \epsilon \vec{\mathcal{E}} = 0 \\ \nabla \cdot \mu \vec{\mathcal{H}} = 0 \end{gathered} \tag{2.5}$$

where $\vec{\mathcal{E}}$ is the electric field, $\vec{\mathcal{H}}$ is the magnetic field, μ is the permeability, and ϵ is the permittivity of the propagation medium. Assuming the medium is isotropic, homogeneous, non-dispersive, and non-magnetic, Eq. (2.5) reduces to:

$$\nabla^2\vec{\mathcal{E}} - \left(\frac{\mathrm{n}}{\mathrm{c}}\right)^2 \frac{\partial^2\vec{\mathcal{E}}}{\partial \mathrm{t}^2} = 0. \tag{2.6}$$

The same form of the equation appears when applied to the magnetic field, and therefore, the vector wave equation is reduced to the scalar wave equation. One solution to the scalar form of this equation is the Huygens-Fresnel equation (Goodman 2005):

$$U(x,y) = \frac{z}{i\lambda}\iint U(x',y')\frac{e^{ikr}}{r^2}dx'dy'$$
$$\text{where } r = \sqrt{z^2 + (x-x')^2 + (y-y')^2} \tag{2.7}$$

and (*x*,*y*) is the plane at a distance *z* from the diffracting aperture at (*x'*, *y'*). Equation (2.7) is difficult to solve. However, if a binomial expansion of *r* is used, and only quadratic terms kept, Eq. (2.7) reduces to the Fresnel approximation:

$$U(x,y) = \frac{e^{ikz}e^{\frac{ik}{2z}(x^2+y^2)}}{i\lambda z}\iint_{-\infty}^{\infty}\left\{U(x',y')e^{\frac{ik}{2z}(x'^2+y'^2)}\right\}e^{-i\frac{2\pi}{\lambda z}(xx'+yy')}dx'dy'. \tag{2.8}$$

In Eq. (2.8), even diffraction effects in the nearfield (which may or may not be negligible) are accounted for.

2.2.3. Farfield Considerations

The wavefront distortions illustrated in Figure 2.1 will degrade the ability to focus a beam on a target in the farfield. In this case, the term "farfield" refers to distances sufficiently far from the aberrating medium such that diffraction effects dominate the

beam. The farfield irradiance pattern of the beam is computed from its nearfield wavefront using Fourier Optics (Goodman 2005). Since farfield irradiance patterns are the ultimate goal, the Fraunhofer approximation is used, which requires that:

$$z > \frac{2{A_D}^2}{\lambda} \tag{2.9}$$

where z is the distance from the diffracting aperture, A_D is the diameter of the aperture, and λ is the wavelength of the light. When this holds true,

$$e^{\frac{ik}{2z}(x'^2+y'^2)} \cong 1 \tag{2.10}$$

such that the Fresnel approximation is further reduced to,

$$U(x,y) = \frac{e^{ikz}e^{\frac{ik}{2z}(x^2+y^2)}}{i\lambda z}\iint_{-\infty}^{\infty} U(x',y')e^{-i\frac{2\pi}{\lambda z}(xx'+yy')}dx'dy'. \tag{2.11}$$

The irradiance in the farfield, $I(x,y,t)$, is related to Eq. (2.11) by:

$$I(x,y,t) = \left|U(x,y)e^{-2\pi ivt}\right|^2. \tag{2.12}$$

In Eq. (2.11), the aperture distribution function is related to the nearfield wavefront,

$$U(x',y') = e^{-i\frac{2\pi}{\lambda}(-OPD)}, \tag{2.13}$$

such that the final irradiance distribution in the farfield is given by:

$$I(x,y) = \left(\frac{1}{\lambda z}\right)^2\left(\iint_{-\infty}^{\infty} e^{-i\frac{2\pi}{\lambda}(-OPD)}e^{-i\frac{2\pi}{\lambda z}(xx'+yy')}dx'dy'\right)^2. \tag{2.14}$$

Based on Eq. (2.9), a system using a wavelength of 1 μm, with an aperture of 30 cm, would require a distance of 180 km before the Fraunhofer approximation would become appropriate. This suggests that at distances less than 180 km, the Fresnel approximation must be used and not the Fraunhofer approximation (see Goodman 2005).

However, the use of a converging lens has the effect of exactly placing the Fraunhofer diffraction distribution of the irradiance field at the focal point of the lens. In other words, for the Fraunhofer approximation to be valid when using a converging lens, the distance of the observation plane (z) is reduced to lengths approximately equal to the focal length of the lens. As a result, aero-optics analyses typically use geometric optics to obtain the nearfield distortions and the Fraunhofer approximation to calculate the farfield irradiance pattern assuming the beam is collimated with a planar wavefront.

2.2.4. Effectiveness of an Optical System

For a beam with a flat wavefront and circular aperture, the farfield irradiance pattern of the focused beam is a diffraction-limited spot, or Airy's Disk. This pattern has a peak irradiance at the center of the spot, I_0, which is the maximum irradiance that can be achieved by the optical system under ideal conditions. If the beam wavefront is not flat, then the farfield irradiance pattern is typically more spread out than the diffraction-limited spot, and the peak irradiance at the center of the spot is generally less than I_0. The ratio of the on-target irradiance to the diffraction-limited on-target irradiance, I_0, is called the Strehl ratio (SR). The Strehl ratio is determined using Eq. (2.14) twice; once for an ideal beam (OPD = 0, denominator), and a second time for the aberrated beam (numerator):

$$SR = \frac{I}{I_0} = \frac{\left(\iint e^{i\frac{2\pi}{\lambda}OPD} dx'dy'\right)^2}{(\iint dx'dy')^2}. \tag{2.15}$$

Alternately, an approximate determination of the Strehl ratio for an optical system can be obtained using the Maréchal approximation,

$$\mathrm{SR}(\mathrm{OPD_{RMS}}) = 1 - \left(\frac{2\pi \mathrm{OPD_{RMS}}}{\lambda}\right)^2 + \cdots \tag{2.16}$$

A full derivation of the Maréchal approximation, starting from Eq. (2.15), is found in Ross (2009). Ross notes in his literature review that neither the original works by Maréchal (written only in French), or Born and Wolf (1997), which is the most complete derivation written in English, show the form that has become the most commonly used expression for the Strehl ratio (the large-aperture approximation, LAA):

$$\mathrm{SR}(\mathrm{OPD_{RMS}}) = \mathrm{e}^{-\left(\frac{2\pi}{\lambda}\mathrm{OPD_{RMS}}\right)^2}. \tag{2.17}$$

Equation (2.17) is a special case of the Maréchal approximation that applies to aberrations with Gaussian phase error distributions, in addition to the assumptions made by Maréchal: 1) uniform irradiance amplitude across a circular aperture, 2) small phase errors in the wavefront, and 3) an aperture diameter much larger than the wavelength of the aberrations. Despite these assumptions, the exponential approximation of the Strehl ratio appears to work well outside its assumption limitations. Appendix B provides a full description of the LAA, its assumptions, and the effect of using the LAA when these assumptions are not met. Appendix B also develops an extension to the LAA for non-Gaussian phase error distributions.

The *Strehl ratio* will serve as the figure of merit throughout this dissertation assuming a wavelength of 1.0 μm. However, there are instances in which the Strehl ratio can be misleading. For instance, a wavefront with only tip/tilt, which has the effect of bore-sight error, will result in a reduction of the Strehl ratio as the center of the spot is no longer at the center of the target. However, this does not necessarily indicate a reduction

in the irradiance delivered to the target. To account for this shortcoming, another metric for the farfield beam performance is often used, called "power in the bucket" (PIB).

Simply stated, the PIB is the integral of the irradiance on some predefined viewing area of the target divided by the integrated diffraction-limited irradiance over that same viewing area. By knowing the total irradiance an ideal beam will deliver, a ratio is obtained, indicating the reduction in total irradiance over the viewing aperture. As shown in Figure 2.3, it is entirely possible to have a very low Strehl ratio while having a very high PIB. The problem with PIB is that it requires additional knowledge of the target size and distance to the target. Furthermore, for any given aberration, different values for PIB are obtained by simply changing the target area as illustrated in Figure 2.3. In Figure 2.3, the Strehl ratio remains constant as does the aberration applied to the beam, but the PIB decreases as the target area decreases.

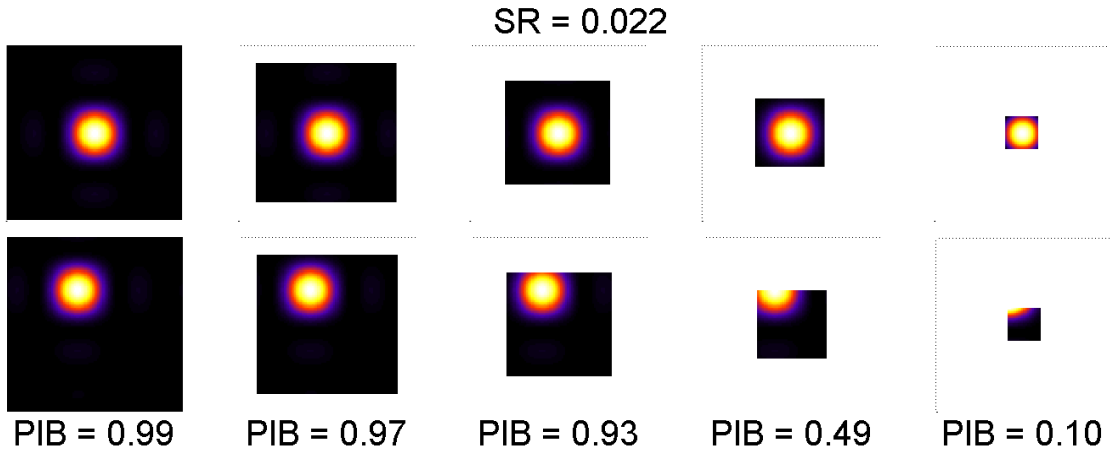

Figure 2.3: Differences in the Strehl ratio and PIB ("power in the bucket") metrics for the effectiveness of an optical system, illustrated using a tip/tilt aberration. The top row of each column is the diffraction-limited farfield irradiance, and the bottom row is the farfield irradiance resulting from the effect of an aberration that produces tip/tilt on the beam. Although the Strehl ratio for the tip/tilt-aberrated beam remains constant at 0.022, the PIB ratio decreases as the target size decreases.

2.3. System Design

Assuming Eq. (2.17) is valid, system designers have two options when attempting to improve the Strehl ratio: (1) reduce the OPD_{RMS} of the optical system and/or beam path or, (2) increase the wavelength. Figure 2.4A shows how the Strehl ratio changes for different OPD_{RMS} values as the wavelength varies. From Figure 2.4A it appears obvious that the effect of optical aberrations can be minimized by using long wavelengths. Figure 2.4B shows, however, how the irradiance at the center of the Airy's disc, I_0, changes with wavelength. The center irradiance in Figure 2.4B has been normalized by the center irradiance obtained for a wavelength of 1 μm. As shown in Figure 2.4B, the center irradiance increases dramatically as the wavelength of the beam is reduced.

As such, Figure 2.4 illustrates the problem faced by optical-system designers when choosing the system wavelength. Shorter-wavelength systems can achieve dramatically higher peak irradiances on target, but are more susceptible to the effects of optical aberrations. Current optical systems are trending towards using lasers with shorter wavelengths in order to increase the maximum-achievable target irradiance; this trend demonstrates the importance of aero-optics research to reduce the OPD_{RMS} of airborne systems. For directed-energy systems to work over a full range of azimuth and elevation angles, measuring, predicting, and correcting aero-optical effects is essential.

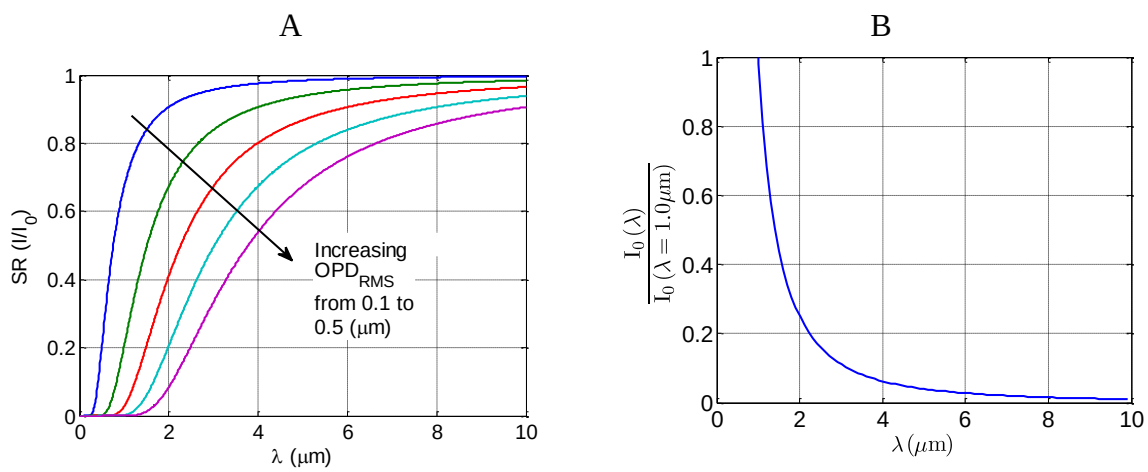

Figure 2.4: A) The change in Strehl ratio for various OPD_{RMS} values as a function of wavelength using the Large Aperture Approximation. B) Peak irradiance of a diffraction-limited spot normalized by the peak irradiance of a diffraction-limited spot at a wavelength of 1 μm.

2.4. Summary

This chapter serves as an introduction to optical analysis methods and concepts that will be used throughout this dissertation. In general, nearfield optical calculations performed in this dissertation will be done using geometric optics, while the Fraunhofer approximation will be used to estimate farfield irradiance patterns. From the farfield irradiance, Strehl ratios will be calculated and used as the figure of merit for the effectiveness of the optical system or approach under evaluation.

CHAPTER 3:

KINEMATICS OF TIP VORTICES

3.1. Introduction

The optical principles presented in Chapter 2 showed how a beam of light is aberrated by a medium with varying index of refraction. Furthermore, the chapter showed how index-of-refraction variations are directly related to the variations in air density that exist, for example, in a compressible flow field (Eq. (2.1)).

The aero-optical aberrations associated with a compressible flow field are therefore directly related to the thermodynamic properties of the flow, that is, pressure, temperature, density, and ultimately index of refraction. Furthermore, it has also been shown that thermodynamic properties for important aero-optic flows are in turn closely related to the underlying flow's velocity field; in particular, Fitzgerald and Jumper (2004) showed that pressure and density variations in free shear-layer flows are associated with vortical structures in the flow. As such, before an examination of the thermodynamic properties for tip-vortex flow fields can be undertaken, it is necessary to first review the fundamental kinematic properties of flow fields for both single tip vortices and helicopters. Methods of determining the thermodynamic properties from the velocity flow fields discussed in this chapter will then be presented in Chapter 4.

The first step towards understanding the aerodynamic environment of tip vortices is to understand the dynamics of a single vortex in free space. After the basic concepts of the dynamics of a single vortex are provided, the investigation can proceed to more complicated vortex methods that model a helicopter in hover and in forward flight (see Chapters 6 and 7). The remainder of this chapter will provide a detailed review of the current methods to model a tip vortex, and will conclude by defining the exact model that is used in this dissertation to investigate the optical properties of tip vortices.

3.2. Tip Vortex Velocity Field Models

The fluid mechanics of wing-tip vortices have been studied extensively since they dominate the wakes of lifting vehicles and have a direct impact on aircraft spacing near airports (Devenport *et al.* 1996; Green and Acosta 1991; Iungo *et al.* 2009; Rossow 1999; Zang *et al.* 2006). These studies show that the tip-vortex flow field consists of a rotational core surrounded by an irrotational outer region. The core region of the vortex may also contain jet-like or wake-like axial velocity components, depending on the particular origin and history of the vortex (Payne 1987; Stallings 1992; Visser 1991).

Although the global wake structure for a helicopter may be significantly different from that of a fixed-wing aircraft, the flow field for a single tip vortex is essentially the same and shows good agreement with the Lamb-Oseen mathematical vortex model. Lamb and Oseen (Rossow 2006) independently developed a mathematical model of a vortex, Eq. (3.1), by solving a simplified form of the Navier-Stokes equation. They assumed the flow field is axially symmetric and time dependent, eliminating higher-order

terms from the Navier-Stokes equations. The flow field is assumed to have a point potential swirl distribution at $t = 0$, and diffuses due to viscous effects. The resulting velocity components describing the Lamb-Oseen vortex in free space are:

$$V_\theta(r,\theta) = \frac{\Gamma}{2\pi r}\left(1 - e^{-\alpha\left(r/r_c\right)^2}\right)$$
$$V_r(r,\theta) = 0 \tag{3.1}$$

where r_c is the core radius of the vortex, Γ is the circulation, and α is a constant that has been determined to be 1.25643 (Leishman 2000). The vortex core radius, r_c, is defined as the distance from the center of the vortex to the point of maximum tangential velocity.

The original Lamb-Oseen model is two-dimensional and does not include an axial velocity component that could be used to model, for example, the momentum deficit generated by a lifting surface. Newman expanded upon the Lamb-Oseen model by deriving an exponential solution to the simplified Navier-Stokes equations, retaining the axial component and assuming Eq. (3.1) to be the actual swirl distribution:

$$V_z(z) = -\frac{A}{z}e^{-\alpha\left(r/r_c\right)^2}. \tag{3.2}$$

The magnitude of the momentum deficit is determined through the parameter A.

Other models have also been used to approximate a tip vortex, such as the Rankine vortex,

$$V_\theta(r) = \begin{cases} \frac{\Gamma r}{2\pi {r_c}^2} & 0 \le r \le r_c \\ \frac{\Gamma}{2\pi r} & r \ge r_c \end{cases}, \tag{3.3}$$

the $n = 1$ (Scully 1975) vortex,

$$V_\theta(r) = \frac{\Gamma r}{2\pi(r_c{}^2 + r^2)}, \tag{3.4}$$

or the $n = 2$ vortex (Vatista 2006),

$$V_\theta(r) = \frac{\Gamma r}{2\pi\sqrt{r_c{}^4 + r^4}}. \tag{3.5}$$

Figure 3.1 shows the normalized velocity profiles of the four models (Eq. (3.1), Eq. (3.3), Eq. (3.4), and Eq. (3.5)). Compared to the other models, the Rankine vortex model drastically overestimates the peak velocity for a given circulation; the general shape of the model, when transitioning from the inner to the outer region, is not consistent with measurements either. On the other hand, the $n = 2$ vortex (Leishman 2000; Vatista 2006)

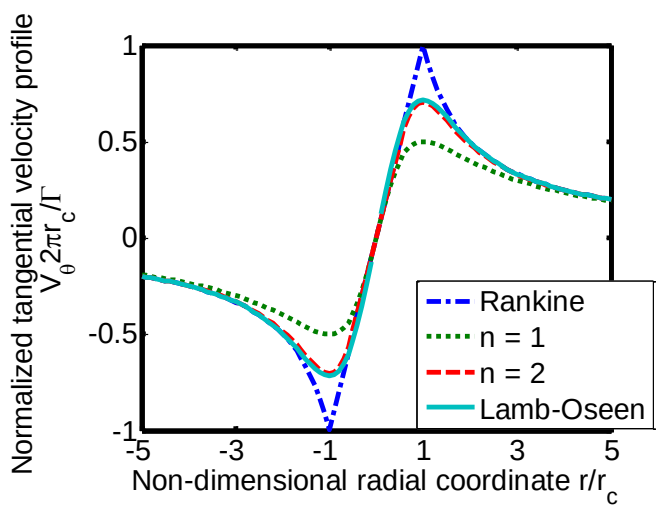

Figure 3.1: Comparison of the velocity profile for different vortex models (Bagai and Leishman 1993).

and Lamb-Oseen vortex models provide generally good agreement with experimental measurements for both fixed-wing and helicopter tip vortices. Figure 3.2 shows, for example, a comparison of the Lamb-Oseen vortex model to experimental hotwire measurements in the tip vortex generated by a rectangular wing (Babie 2008). Schlieren

investigations of actual tip vortices have been used as a basis for evaluating the performance of different vortex models (Bagia and Leishman 1993), and these studies have also demonstrated the accuracy of the Lamb-Oseen vortex model.

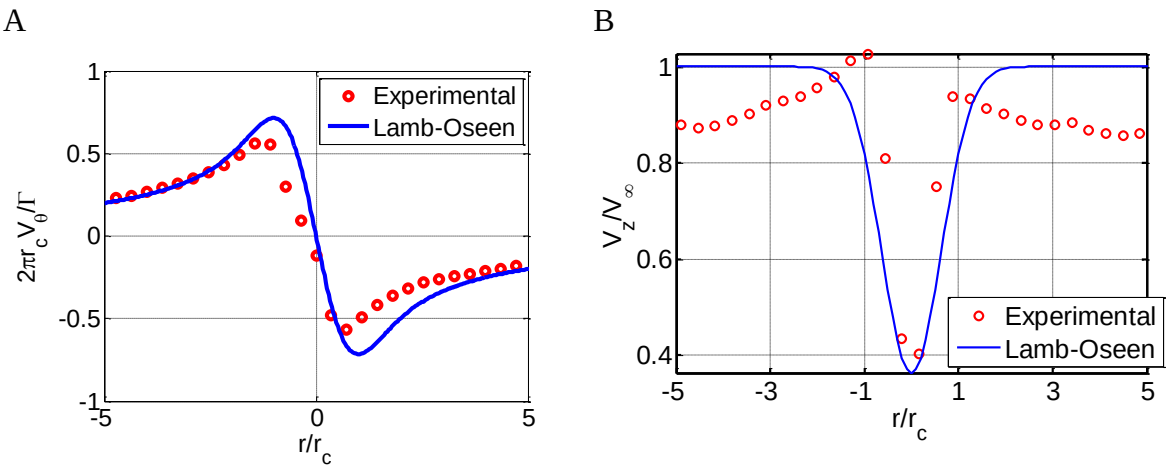

Figure 3.2: Comparison of the Lamb-Oseen vortex model to experimental hotwire measurements of a wing tip vortex: A) Azimuthal velocity component B) Axial velocity component (Babie 2008).

3.2.1. Estimation of Vortex Parameters - Circulation

For the vortex models presented in the preceding section, the two parameters required to uniquely define the vortex flow field are the vortex circulation, Γ, and the vortex core radius, r_c. Estimation of the vortex circulation for realistic helicopter flow fields is discussed in this section, while the following section presents a procedure for modeling the vortex core radius and growth downstream of the generating blade tip.

Helicopter maneuvers are for the most part dominated by hovering or near-steady flight conditions, in which case the lift generated by the rotor blades balances the weight of the helicopter. The corresponding bound circulation from each rotor blade is shed into a root vortex, a blade vortex sheet, and a tip vortex. From an aero-optic standpoint, however, the most important component of the shed circulation is the part shed from

approximately the outer third of the rotor blades, since only this part of the total circulation rolls up into a strong tip vortex (see Chapter 6). Furthermore, since the flow speeds at the rotor tip are the fastest, the strongest compressibility effects occur in the tip vortices. The combination of both of these conditions means that the tip vortex should produce the strongest aero-optic aberrations. The circulation associated with the tip vortex from a helicopter blade can be estimated using the following equation:

$$\Gamma = kc\Omega R\left(\frac{C_T}{\sigma}\right) \tag{3.6}$$

where the theoretical value of the proportionality constant k is *2*, although measurements have suggested values as high as $k = 3$ (Bagai and Leishman 1993; Beddoes 1985).

As an aside, it should be noted that there is usually considerable scatter in experimental measurements of helicopter tip-vortex circulation. As an example, experimentally-determined data for the circulation shed from the rotor blade on a UH-60A helicopter are shown in Figure 3.3 (Teager *et al*. 1996). Note Figure 3.3 does not show the circulation of the rotor tip vortex but rather, shows the total circulation shed from the outer 5m of a rotor blade. This outboard circulation was computed from the experimentally-measured velocity field using:

$$\Gamma = \oint V \cdot ds = \int_A \nabla \times V \cdot dA. \tag{3.7}$$

Each numbered value in Figure 3.3 refers to a different test day. As the figure shows, at a given forward flight speed, say 50 knots for example, the measured circulation varied from 90 m^2/s to 130 m^2/s on different days, or ± 18%.

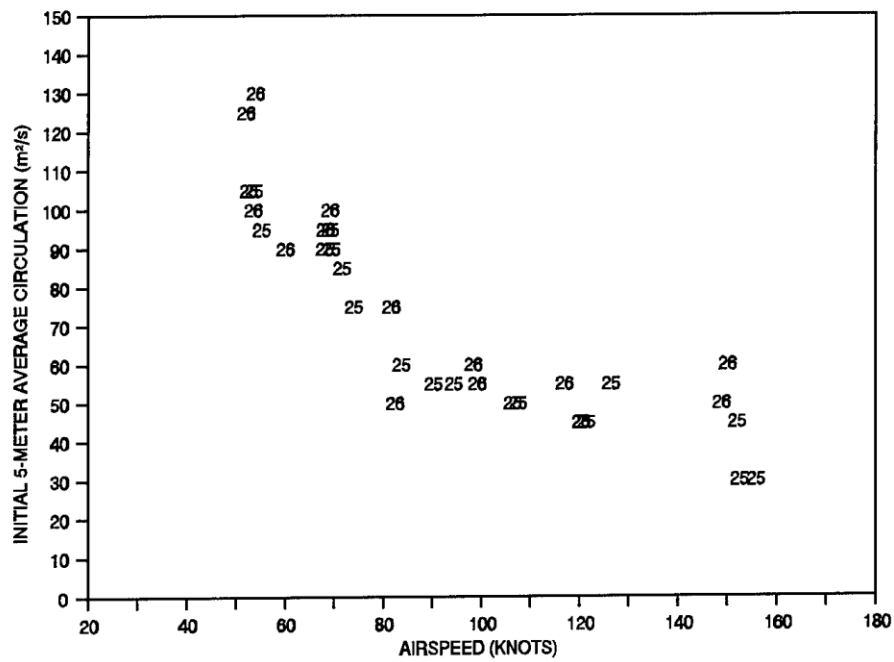

Figure 3.3: Average circulation vs. airspeed (knots) shed from the outer 5 meters of a rotor blade for a UH-60A. Taken from Teager *et al.* 1996.

3.2.2. Estimation of Vortex Parameters - Core Radius

As shown in Eq. (3.1) and Eq. (3.2), the vortex core radius is an important parameter in determining the velocity field of a vortex in free space. The core radius typically grows with time, or downstream distance from the vortex origin, by means of viscous and turbulent diffusion. Lamb estimated this growth rate for simple *laminar* flows as (Leishman 2000; Rossow 2006):

$$r_c = \sqrt{4\alpha\nu t}. \tag{3.8}$$

In Eq. (3.8), ν is the kinematic viscosity, t is the time since the creation of the vortex, and α is the same constant used in Eq. (3.1).

In most cases, however, flows associated with tip vortices are turbulent and therefore the core grows faster than predicted by Eq. (3.8). Equation (3.8) also models a

core radius of zero at $t = 0$, while tip vortices have a finite thickness which is approximately equal to the thickness of the blade at $t = 0$. An improved model for the core radius that accounts for turbulent growth and a nonzero initial core radius is:

$$r_c = \sqrt{4\alpha\delta\upsilon(t - t_0)}, \tag{3.9}$$

where δ is a coefficient to account for turbulent diffusion (apparent viscosity) and t_0 effectively shifts the values of the core radius backwards in time to produce a nonzero core radius at $t = 0$ (Garry and Kist 1993; Leishman 2000). Figure 3.4 shows how the addition of an initial core radius and turbulent growth factor, Eq. (3.9), compares to Eq. (3.8) and measured data (Leishman 2000). As shown in Figure 3.4, the growth of the core radius is related to the wake age, Ψ_w, where the wake age is defined as the angle the blade has rotated since the initial shedding of the tip vortex. Therefore, at a wake age of 360 degrees, the blade has made one complete revolution from the initial time the tip vortex was shed. In Figure 3.4, the dotted line labeled "Lamb's result" corresponds to Eq. (3.8). The dashed line in Figure 3.4 corresponds to Eq. (3.9) with the core growth rate increased (i.e. using an apparent viscosity, δ, greater than one) to account for turbulent diffusion but no time offset. Finally, the solid line in Figure 3.4 corresponds to Eq. (3.9), and accounts for both turbulent diffusion and an initial nonzero core radius; Figure 3.4 clearly shows that this model most closely matches experimental data. As such, Eq. (3.9) is used in this dissertation because of its capacity to most accurately model the widest range of experimental conditions.

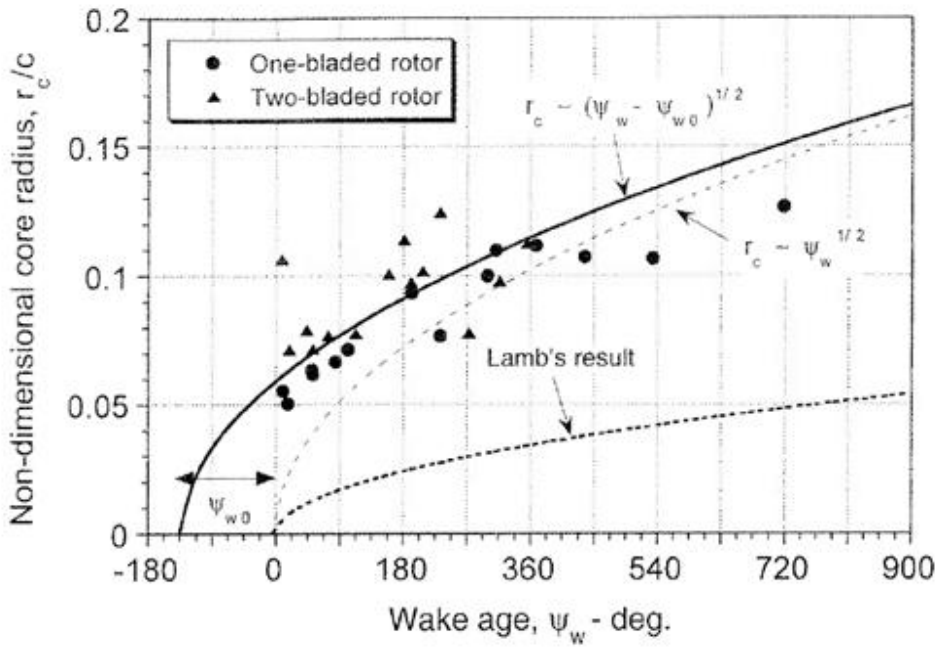

Figure 3.4: Measured vortex core radius and comparison to different growth rate models (Leishman 2000).

3.3. Reynolds Number Effects

Although other models for the vortex core radius exist (Garry and Kist 1993), in general, all of the models show the same general dependence of the core radius on the square root of time. The main difference between the different models is the way in which the apparent viscosity, δ, is modeled (Anathan and Leishman 2004; Ramasamy and Leishman 2004; Ramasamy and Leishman 2007). In particular, the tip-vortex Reynolds number is defined as:

$$Re_v = \frac{2\Omega Rc}{\nu}\left(\frac{C_T}{\sigma}\right) = \frac{2\Gamma}{\nu}. \tag{3.10}$$

Since the apparent viscosity is the ratio of turbulent to viscous dissipation, it makes sense that the apparent viscosity should be related to the tip-vortex Reynolds number.

To relate the apparent viscosity to the tip-vortex Reynolds number, the following was proposed (Anathan and Leishman 2004; Ramasamy and Leishman 2004; Ramasamy and Leishman 2007):

$$\delta = 1 + a_1 Re_v. \tag{3.11}$$

Figure 3.5 shows how this model for apparent viscosity compares to experimental data. Furthermore, Figure 3.5 shows that the coefficient a_1 in Eq. (3.11) can range from approximately $5\text{x}10^{-5}$ to $4\text{x}10^{-4}$, but that a good intermediate value that matches most of the experimental data is a_1 = 0.0002. Incorporating Eq. (3.11) into Eq. (3.9) for the vortex core radius gives:

$$r_c = \sqrt{r_0^2 + 4\alpha\nu\left[1 + a_1 \frac{2\Omega Rc}{\nu}\left(\frac{C_T}{\sigma}\right)\right]\left(\frac{\psi_w}{\Omega}\right)}. \tag{3.12}$$

Equation (3.12) is used throughout the remainder of this dissertation to define the size of the core radius. The initial core radius, r_0, is set to 5% of the blade's chord and a nominal value of a_1=0.0002 is used.

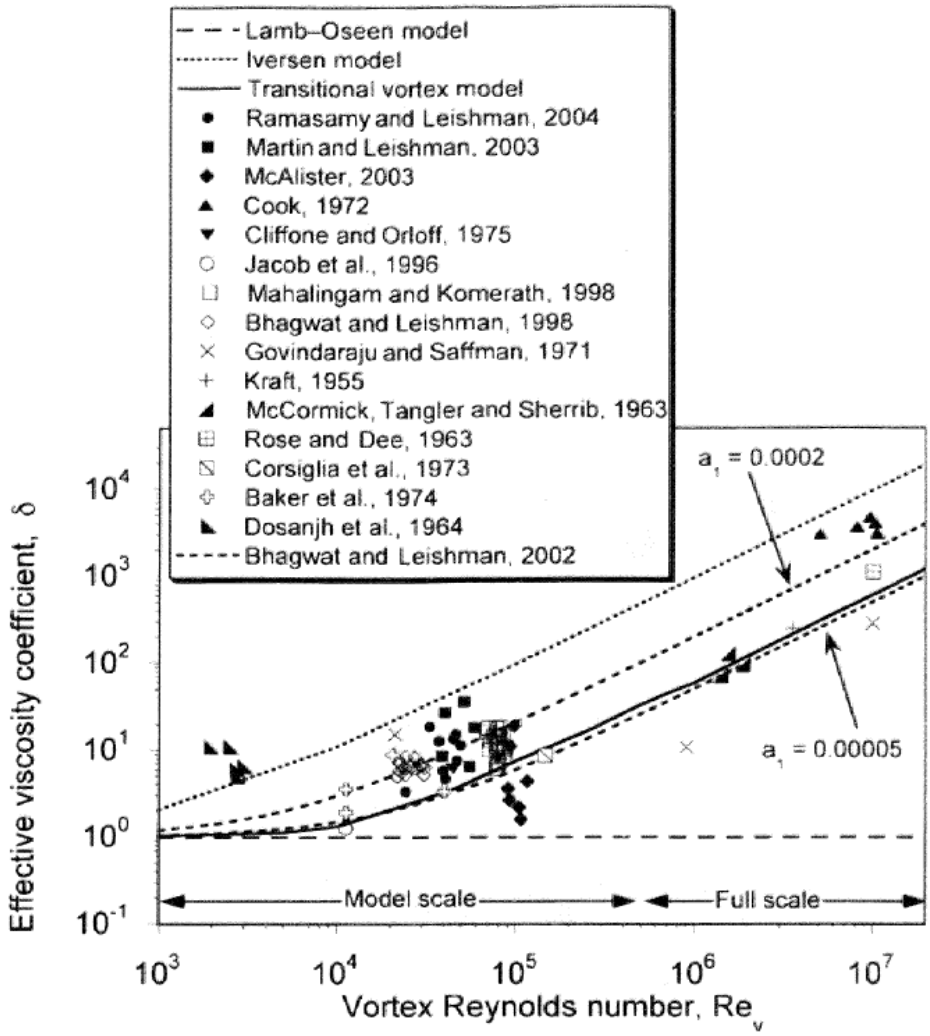

Figure 3.5: Variation of δ with vortex Reynolds number based on Eq. (3.11) from Ramasamy and Leishman (2007).

3.4. Summary

As shown in the preceding sections, there is some variation in the mathematical models for tip-vortex velocity fields proposed in the literature. Furthermore, other factors not mentioned above can have an effect on the vortex velocity field, such as strain in the flow field. In general, however, the Lamb-Oseen vortex model shown in Eq. (3.1), the vortex circulation formula in Eq. (3.6), and the vortex core growth model in Eq. (3.12)

have been shown to match experimental data with good accuracy; as such, these models will be used throughout this dissertation. It will be shown in Chapter 5 that these mathematical models for the vortex velocity field also match experimental data acquired as part of this dissertation research.

CHAPTER 4:

OPTICAL PROPERTIES OF TIP VORTICES

4.1. Introduction

As shown in Chapter 2, the optical aberrations produced by a compressible flow are ultimately related to the density variations within the flow. In this chapter, computational methods are described for computing thermodynamic properties, including the density, from a known velocity field for a tip-vortex flow. The first computational method assumes that the flow field is isentropic. The second method, the Weakly Compressible Model (WCM), is based on adiabatic heating and cooling and has been shown to predict the optical properties of a weakly-compressible free-shear layer with good accuracy. Optical data computed using both approaches are presented for vortex flow fields generated using the Lamb-Oseen vortex model.

The chapter will then show the development of relationships describing the scaling of tip-vortex optical data to different flight conditions. These scaling relationships are "calibrated" using the optical data generated using the isentropic and WCM computational methods to produce formulas for the estimation of tip-vortex optical properties in any flight regime. Finally, the formulas are used to generate a simple prediction of the optical effect of a tip vortex created by a medium-sized helicopter to

illustrate the usefulness of the derived scaling relationship as well as provide a first estimate of the severity of the aero-optic environment around a helicopter.

4.2. Previous Investigations into Optical Effects of Vortices

Before describing the computational methods used in this investigation, it is informative to first briefly review the work of other researchers into the optical effect of tip vortices; this work includes investigations by Aboelkassem and Vatistas (2007), Berry and Hajnal (1983), Sterling *et al.* (1987), Vatistas (2006), and Xiaoliang *et al.* (2007)[1]. These investigations were aimed primarily at advancing the understanding of compressible vortices through experimental optical methods. The first investigations used a geometric optics approach to analyze the experimentally-measured deformation of the free surface of vortices in water. More recently, the optical effects of vortices have been computed from fundamental fluid-mechanic analyses.

4.2.1. Previous Optical Measurements

The first attempt to explain the optical properties of vortices started with an explanation of the shadows seen in riverbeds below vortices in water (Berry and Hajnal 1983). Starting with the Navier-Stokes equations, Berry and Hajnal (1983) derived a model describing the deformation of the surface of the water, which they related to the shadows (optical aberration) beneath the vortex. Using asymptotics, an approximate

[1] Paper is written in Chinese with an English abstract and figure captions. Inferences are made from math and figures alone as the author cannot read Chinese.

solution to their model was derived and the caustic surfaces (boundaries separating accessible and inaccessible region to a family of light rays) resulting from the vortex were found. While the optical analysis of Berry and Hajnal dealt with the deformation of the water surface, Figure 4.1, the deformation of the water surface is analogous mathematically to the variation of density within a compressible vortex since both are governed by the same set of equations (Vatistas 2005); as such, the analysis also applies to compressible vortices in air. The experimental results of Berry and Hajnal, along with results from a refined mathematical model from Aboelkassem and Vatistas (2007) are shown in Figure 4.2. As shown in Figure 4.2, the propagation of light along the axis of rotation of the vortex results in two bright rings of light, clearly showing the effect that tip vortices can have on a transiting beam of light.

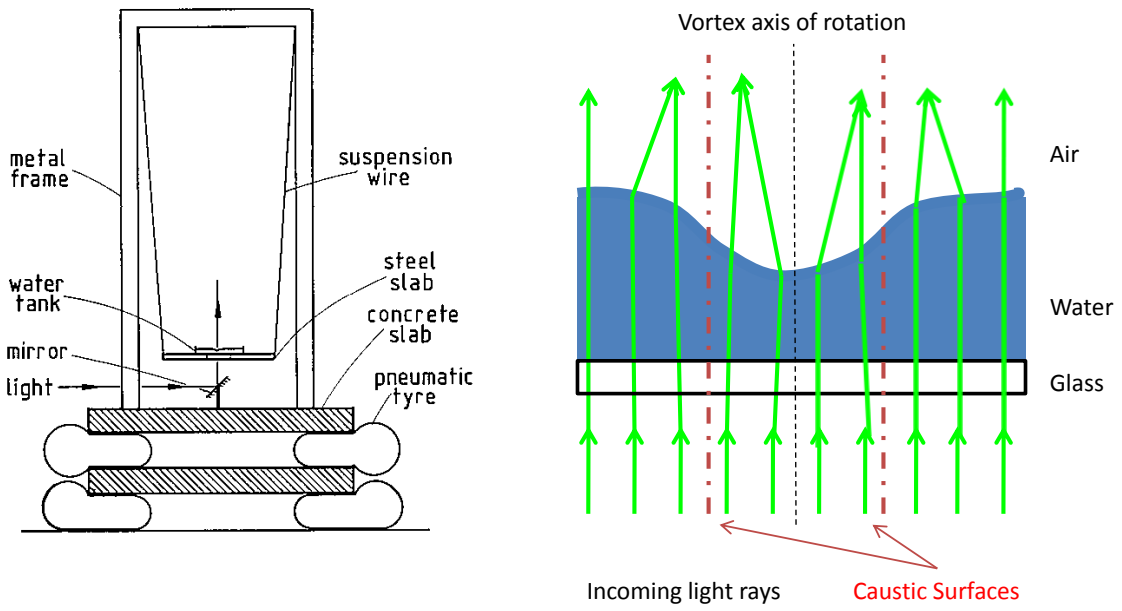

Figure 4.1: Experimental setup to measure the optical effects of a vortex in water (Berry and Hajnal 1983).

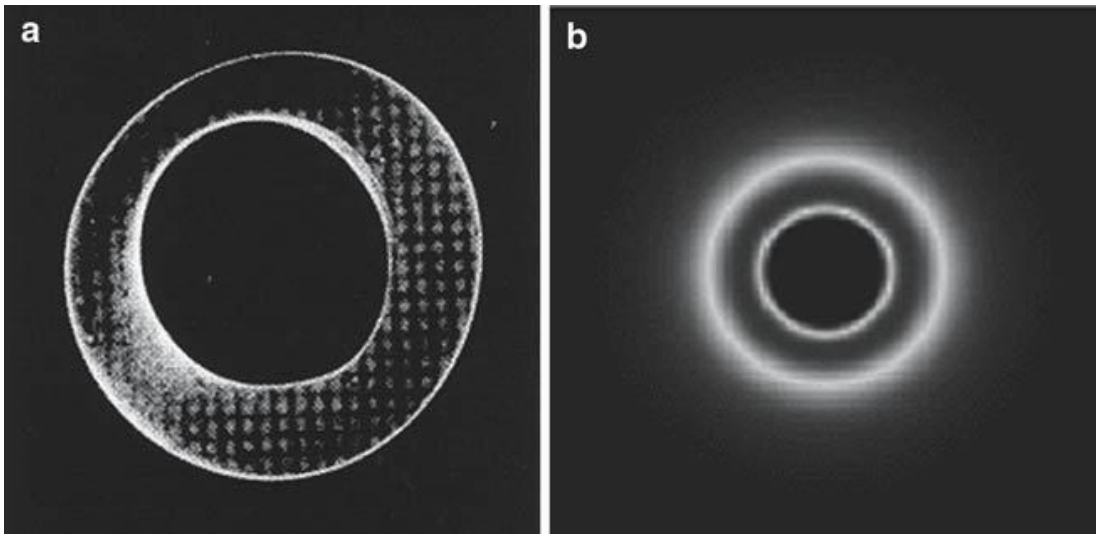

Figure 4.2: Caustic surfaces produced by *n=2 compressible* steady vortex. A) Experiments: Berry and Hajanal (1983); B) Vatistas theory. Taken from Aboelkassem and Vatistas (2007).

Since the light rings shown in Figure 4.2 are related to the density of the flow field, these optical models have been used to non-intrusively estimate tip-vortex flow-parameters. For example, early models assumed that the central ring in Figure 4.2 provided a direct measurement of the vortex core radius. This is the case when the isentropic-Rankine vortex model is used to simulate the velocity flow field. However, with the more advanced tip-vortex mathematical models, such as the Lamb-Oseen vortex or *n=2* vortex models, Bagai and Leishman (1993) showed that the radius of the inner light ring does not correspond to the radius of the vortex core. On the other hand, they showed that experimental Schlieren images agreed more closely with the optical analysis of an isentropic *n=2* vortex model when compared with the Rankine vortex prediction.

As such, while optical investigations into tip vortices are limited, they have indicated that the Lamb-Oseen vortex model or $n=2$ vortex model provide much better descriptions of the flow field then the Rankine or $n=1$ vortex models. The main advantage of optical measurements of tip vortices, however, is not their ability to provide insight into the flow physics of tip-vortices, but rather to map out the entire propagation path of a tip vortex non-intrusively. For example, using wide-angle Schlieren, Bagai and Leishman (1993) were able to map out the propagation path of the tip vortices on a model helicopter in hovering flight (see Chapter 6, specifically Figure 6.2). More recently, background-oriented Schlieren was used to measure tip vortices in flight (Kindler *et al*. 2007), again showing the usefulness of optical measurement techniques.

4.2.2. Previous Thermodynamic Computations

In addition to the optical measurements described in the preceding section, mathematical models have also been developed for the thermodynamic properties of compressible vortices. Essentially all of these theoretical investigations into the thermodynamic properties of vortices predict that the pressure within the core of an axisymetric vortex is lower than the ambient pressure. As a result, the density within the core is lower than the ambient density (Colonius *et al.* 1991; Ellenrieder and Cantwell 2000; Orangi *et al.* 1999; Rott 1959). Despite different assumptions made in these works, the temperature within the core was also always predicted to be lower than the ambient temperature (Figure 4.3). While the magnitude of the pressure drop varies slightly in each of the predictions, the primary discrepancy is the temperature drop within the cores.

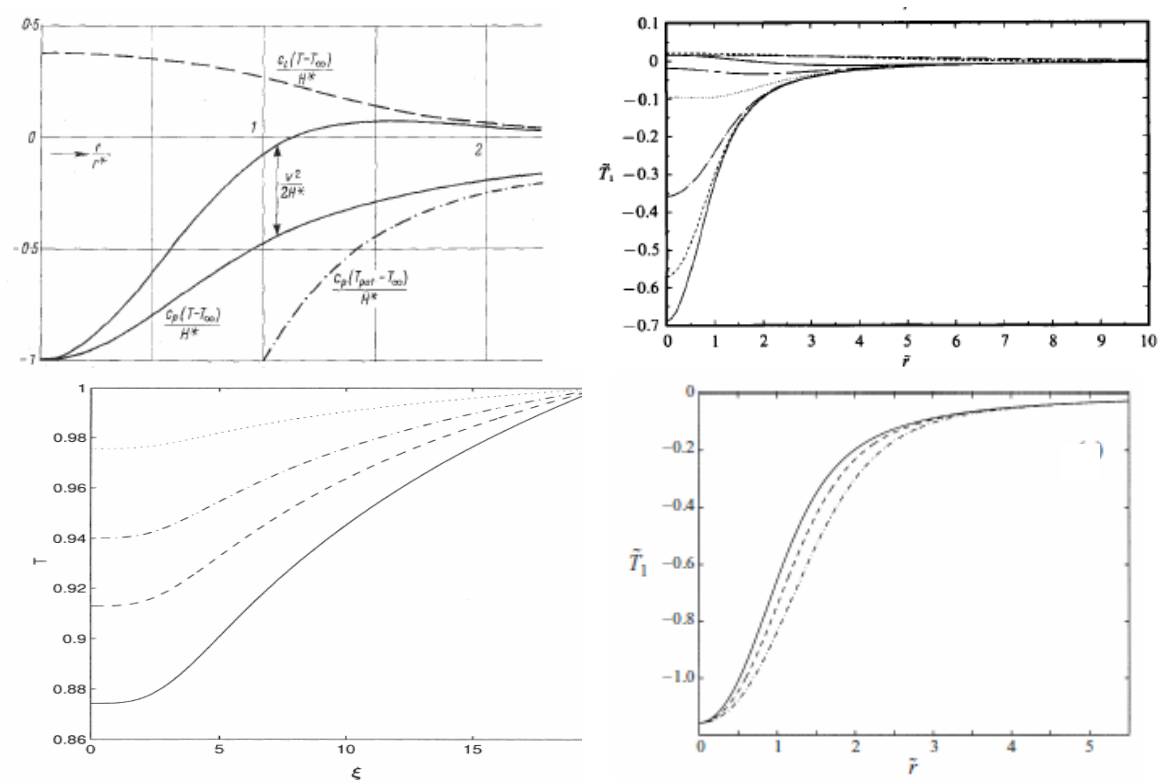

Figure 4.3: Calculated temperature distributions within the core of a vortex from Rott (1959 – Top Left), Colonius *et al.* (1991 – Top Right), Orangi *et al.* (1999 – Bottom Left), and Ellenrieder and Cantwell (2000 – Bottom Right). In virtually all cases the temperature in the core (left side of each plot) is shown to be lower than the freestream conditions.

While most researchers agree on a temperature drop in the vortex core, there is debate over the magnitude of the temperature reduction in and surrounding the core. For example, Aboelkassem and Vatistas' (2007b) revised vortex model predicts a reduction in temperature, pressure, and density. They point out that "the traditional homentropic flow hypothesis, often employed in vortex stability and optical studies, is shown to undervalue the density and greatly overestimate the temperature (see Figure 4.4)." Unfortunately, experimental data for the temperature distribution in a tip vortex with sufficient detail to resolve these questions do not exist, to the knowledge of the author.

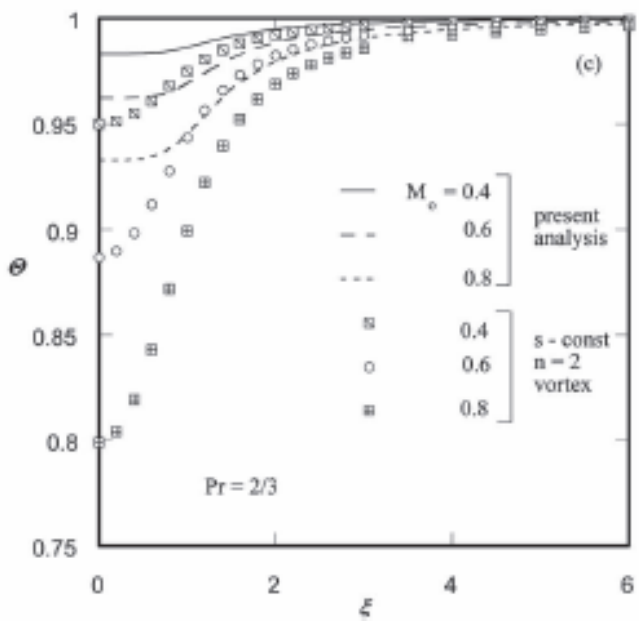

Figure 4.4: Temperature comparison between Aboelkassem and Vatistas (2007b) revised compressible vortex model and the standard homentropic model ($\Theta = T/T_\infty$, $\zeta = r/r_c$).

In summary, although there is general agreement over the pressure drop within the core, as shown above, there is considerable debate over the magnitude of the temperature drop within the core of a tip vortex. From an optical standpoint, this presents a serious problem since the magnitude of the density drop (and hence the magnitude of the optical aberration) within the vortex core depends upon the magnitude of the temperature drop. To account for this lack of a clear understanding of the temperature distribution in a tip vortex, the next section presents two different computational approaches to determining the thermodynamic properties of tip vortices. Each of these approaches contains different assumptions regarding the thermodynamic conditions within the vortex core. Optical data for each approach are then computed and compared in an attempt to evaluate how serious an effect the exact temperature model has on the predicted optical aberration. Furthermore, in Chapter 5, the computational methods

described in the next section are compared with experimental data in a further attempt to evaluate the effect of temperature modeling on the predicted aberration.

4.3. The Weakly Compressible Approach

As shown by Eqs. (2.2) and (2.3), prediction of the optical aberrations imposed by a region of optically-active fluid requires that the density variations in the region be known. In this research, two versions of the "weakly-compressible approach" was used to compute the thermodynamic properties, including density variations, of the flow. The weakly-compressible approach makes use of the fact that for many types of subsonic flows, the velocity field of the flow is not modified by compressibility effects until the freestream Mach number is in the high-subsonic regime or even close to one. Therefore, in the weakly-compressible regime, thermodynamic properties are decoupled from the velocity field of the flow, so that it is not necessary to compute thermodynamic and velocity data simultaneously; rather, it is possible with little loss of accuracy, to compute the velocity field of the flow of interest first, and then compute the thermodynamic properties of that flow from the pre-determined velocity field. This kind of "thermodynamic overlay" is a useful tool for aero-optic investigations since many experimental and computational methods exist to obtain the velocity field of a fluid, while instantaneous pressure, temperature and density data are difficult to acquire, especially at the time scales associated with high-speed aero-optic flows. The weakly-compressible approach is more fully described in (Fitzgerald and Jumper 2004).

The weakly compressible approach has been shown to accurately model compressible shear-layer flows with high-speed Mach numbers up to 0.8 (Nightingale *et. al*. 2005; Rennie *et al*. 2008); in this case, the applicability of the weakly-compressible assumption can be determined by the computation of a convective Mach number for the shear-layer flow (Papamoschou and Roshko 1988). For tip-vortex flows, a conditional check for the weakly-compressible assumption similar to the convective Mach number for shear-layer flows does not exist. However, an indication of the applicability of the weakly-compressible assumption for helicopter tip-vortex flows can be obtained by examining velocity fields computed using the mathematical models presented in Chapter 3 for realistic helicopter flight conditions. Using the parameters for a generic medium-sized helicopter summarized in Appendix D, the tip-vortex circulation computed using Eq. (3.6) for typical flight conditions is in the range 17.5 to 26.25 m^2/s. Figure 4.5 shows how the tangential Mach number (V_θ/a) of a tip vortex with a circulation in this range varies with wake age (i.e. downstream distance from the generating rotor tip). Two curves are shown corresponding to the above minimum and maximum circulations where for each curve, the initial core radius was set to 5% of the blade chord and the smallest apparent viscosity, based on Eq. (3.11), was used to model the growth of the vortex with increasing wake age. The figure shows that just downstream of the rotor blade (i.e. $\psi_W = 0$) the tangential Mach number in the tip vortex approaches 0.4 for $\Gamma = 26.5$ m^2/s, so that it is possible that compressibility effects might influence the velocity profile of the tip vortex in this case (Vatistas 2005). It is unlikely, however, that an optical system mounted on the helicopter would be aimed through the wake just downstream of the rotor blades; in fact, an outgoing beam passing through the wake in this region would also

most likely be obstructed by the blades themselves. Instead, the distance along tip vortex from the blade tip to the point at which the vortex begins to enter the line of sight of an optical system mounted on the helicopter would typically be fairly large, for example, $\psi_W \approx 360$ degrees for the case of an optical system aimed outward in a direction parallel to the rotors. Figure 4.5 shows that at a wake age of $\psi_W = 360$ degrees the tangential Mach number has decreased to well below 0.2, which is too low for compressibility effects to influence the tip-vortex velocity field; however, as will be shown below, these tangential Mach numbers are still large enough to generate significant optical aberrations. Furthermore, there is other evidence in the published literature supporting the weakly compressible approach; for example, in Bagai and Leishman (1993), an isentropic,

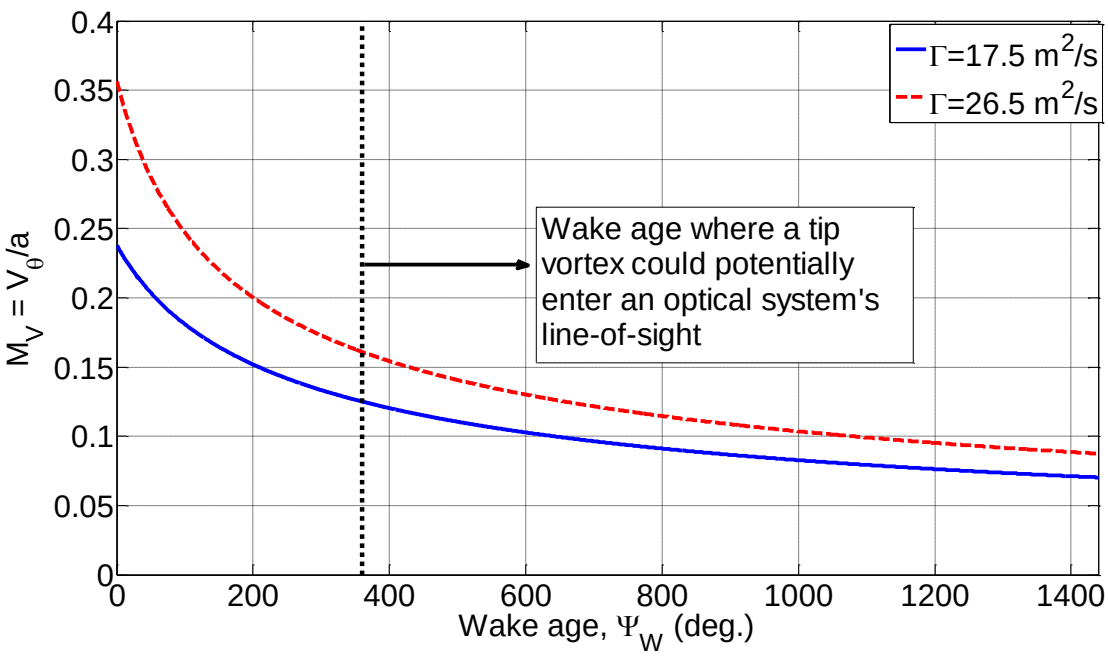

Figure 4.5: Vortex Mach number at various wake ages, illustrating that at the initial roll-up of the tip vortex, compressibility effects are significant, but by a wake age of 360 degrees the vortex Mach number is small and a weakly-compressible approach is warranted.

weakly-compressible approach was used to model the optical effects seen in Schlieren images of rotor tip vortices with good accuracy. In summary, the preceding arguments demonstrate that the optical effect of helicopter tip vortices can be modeled using the weakly compressible approach within acceptable accuracy.

In this dissertation, two versions of the weakly compressible approach are investigated: the first is an isentropic model, and the second is the weakly compressible model (WCM) described in Fitzgerald and Jumper (2004). Both the isentropic and WCM thermodynamic overlays are inviscid models. The objective of the thermodynamic overlays is to start with a known velocity field and calculate a solution of the five thermodynamic variables: ρ, T, P, T_0, and P_0. The algorithm used to calculate these thermodynamic variables is constructed from the fundamental fluid mechanic equations consisting of continuity, momentum, the 1st and 2nd Law of Thermodynamics, and the ideal gas law. Although some or all of the following may already appear in the literature, it is informative to review in detail the specific form of the fundamental fluid-mechanic equations for a tip-vortex flow, which is presented in the following subsections.

4.3.1. Continuity

For the case of a free-space vortex, it is convenient to formulate the fluid-mechanic equations in cylindrical coordinates since this coordinate system best matches the geometry of the flow field. The general form of the continuity equation in cylindrical coordinates is:

$$\frac{\partial \rho}{\partial t} + \frac{1}{r}\frac{\partial \rho r V_r}{\partial r} + \frac{1}{r}\frac{\partial \rho V_\theta}{\partial \theta} + \frac{\partial \rho V_z}{\partial z} = 0. \tag{4.1}$$

For the steady, two-dimensional (i.e. the axial flow component, V_z, is zero), axisymetric Lamb-Oseen vortex model (Eq. (3.1)), Eq. (4.1) reduces to

$$\frac{V_\theta}{r}\frac{\partial \rho}{\partial \theta} = 0. \tag{4.2}$$

As such, for the Lamb-Oseen vortex model, the continuity equation requires that the density field (and hence all thermodynamic properties) is also axisymetric. For a single, weakly-compressible tip vortex in free space, the condition of Eq. (4.2) is identically satisfied since there are no mechanisms to produce azimuthal variations of the flow properties. On the other hand, considering, for example, the case of a helicopter in hover, the helical vortex system underneath the helicopter induces large-scale variations in the flow properties such that the azimuthal variations of flow properties around a particular vortex filament in the helicopter wake system will be nonzero. However, as will be shown in Chapter 7, these azimuthal variations are still small for both hover and forward-flight conditions, so that Eq. (4.2) is still well satisfied even for helicopter vortex-wake systems.

If the axial-flow velocity component (Eq. (3.2)) is nonzero, then the continuity equation becomes:

$$-Ae^{-\alpha\left(r/r_c\right)^2}\left[\frac{1}{z}\frac{\partial \rho(r,z)}{\partial z} - \frac{\rho(r,z)}{z^2}\right] = 0. \tag{4.3}$$

Therefore, for conservation of mass to hold, the term within the brackets must be zero; the following two points can be made to demonstrate that this term is negligibly small for tip-vortex flows. First, as discussed above, the distance z over which the vortices must travel before they enter the line of sight of an optical system on the helicopter is very large. Furthermore, for tip-vortex flows, the variation of flow parameters including

density in the z direction is negligibly small compared to variations in the radial direction so that $d\rho/dz \sim 0$; the negligible variation of the vortex flow field in the flow direction is illustrated, for example, by the very small vortex-core growth rates that result from Eq. (3.12).

In summary, the Lamb-Oseen vortex model automatically satisfies the continuity equation. This is the case for both a single tip vortex, with or without an axial flow component, or for the vortices in a helicopter wake.

4.3.2. Energy

The flow field for a tip vortex is steady (Chapter 3); furthermore, viscous effects are small as shown by the small growth rate of the core (Eq. (3.12)), and the flow can be assumed adiabatic. Under these conditions, the energy equation reduces to $DT_0/Dt = 0$:

$$V_r \frac{\partial T_0}{\partial r} + \frac{V_\theta}{r}\frac{\partial T_0}{\partial \theta} + V_z \frac{\partial T_0}{\partial z} = 0. \tag{4.4}$$

Following similar arguments to those given in Section 4.3.1, for a steady, two-dimensional, axisymmetric vortex, this equation is automatically satisfied for both an isolated tip-vortex and for a full helicopter wake.

For a vortex flow field with a nonzero axial velocity component, the energy equation becomes:

$$\frac{Ae^{-\alpha\left(r/r_c\right)^2}}{z}\frac{\partial T_0}{\partial z} = 0. \tag{4.5}$$

This equation is also satisfied for an isolated vortex or full helicopter flow field, again following similar reasoning to that outlined in the preceding section dealing with conservation of mass.

4.3.3. Momentum, Equation of State, and Entropy Considerations

Besides the equation of energy and conservation of mass, the tip-vortex flow field must also satisfy the momentum equation and equation of state. For these equations, the Euler equation and the ideal-gas law are used:

$$\nabla P = -\rho \frac{D\vec{V}}{Dt} \tag{4.6}$$

$$\rho = \frac{P}{RT}. \tag{4.7}$$

The final equation used in the thermodynamic computations is different for the isentropic and WCM methods. For the isentropic computational method, the following relationship is used:

$$TP^{1-\gamma/\gamma} = T_0 P_0^{1-\gamma/\gamma}, \tag{4.8}$$

where

$$T_0 = T + \frac{\vec{V}^2}{2C_p}. \tag{4.9}$$

Equation (4.8) is an outcome of the Gibbs equation, which in turn is a combination of the energy equation and the *Tds* equations for an ideal gas assuming constant specific heats (Cengel and Boles 2002; Sonntag *et al.* 2003). It is derived under the condition of constant entropy (i.e. *ds* = 0).

In the development of the WCM, Fitzgerald and Jumper (2004) first used an isentropic thermodynamic overlay. However, when compared to the experimentally measured aberrations for a compressible shear-layer flow, they found that the isentropic overlay over-predicted the amplitude of the aberrations. As a result, they switched from using the total temperature to using the adiabatic temperature, which provided results in better agreement with optical measurements:

$$TP^{1-\gamma/\gamma} = T_{Ad}P_{\infty}{}^{1-\gamma/\gamma}, \tag{4.10}$$

where the adiabatic temperature is defined as:

$$T_{Ad} = T_{0,\infty} - \frac{\vec{V}^2}{2C_p}. \tag{4.11}$$

Fitzgerald and Jumper (2004) found that this approximation provided optical results that were consistent with those measured experimentally in a weakly-compressible free-shear layer. While Eq. (4.10) yielded better results than the isentropic overlay, no derivation of Eq. (4.10) was ever presented, although the basis of the equation stems from modeling the separation of temperature in a Ranque-Hilsh tube.

Until the implementation of the WCM, optical aberrations from a free-shear layer were thought to result from the difference in index-of-refraction caused by the temperature difference of the high- and low-speed flows. However, the WCM proved that the low-pressure cells associated with the curvature of the flow field (vortical structures) were the primary cause of optical aberrations. This was a major breakthrough in the field of aero-optics.

Since the WCM is based on phenomena observed in the Ranque-Hilsh tube, it is interesting to note that Rott (1959) discusses the similarity in the “refrigeration” effect of

a single tip vortex and a Ranque-Hilsh tube. Rott suggests that the refrigeration effects are due to different phenomena since the existence of a "hot" outer edge is not predicted for tip-vortices. Despite this comment, it is still worthwhile to investigate the WCM due to the good results obtained using the WCM to model shear-layer flows. Later in this Chapter, the output of the isentropic model and the WCM are compared using velocity fields generated using the Lamb-Oseen vortex model, while in Chapter 5, the two methods are compared to experimental data.

4.3.4. Computational Algorithm

The preceding analysis has shown that the equations of conservation of mass and energy are identically satisfied by the Lamb-Oseen vortex model for the kinds of helicopter tip-vortex flow fields under consideration. The remaining equations, Eqs. (4.6), (4.7), and either (4.8) or (4.10), form a closed system of five equations with five unknowns: P, T, ρ, P_0, and T_0. This system of equations was solved using the iterative approach shown in Figure 4.6.

During the iteration process, numerically solving for the static pressure is the most computationally expensive operation. In this investigation, this was accomplished by discretizing Eq. (4.6) using a finite-difference scheme. The discretization used a forwards/backwards difference scheme at the borders of the computational domain, and a central difference scheme elsewhere. This yields a first-order accurate solution. The pressure was found by inverting the resulting sparse matrix. For the single tip-vortex studies, this was performed through direct inversion; for the large complete flow fields of

the helicopter, this was done using an iterative least-square *qr* technique in order to reduce the computational memory requirements.

Finally, in order to start the weakly-compressible computations, an assumption regarding the relationship between the temperature and pressure fields is made. Specifically, for the isentropic method, it is assumed that the parameters on either side of Eq. (4.8) are constant throughout the flow, that is:

$$TP^{1-\gamma/\gamma} = T_0 P_0^{1-\gamma/\gamma} = C_{T-P}, \tag{4.12}$$

where the constant $C_{T\text{-}P}$ in Eq. (4.12) is determined at the start of the computations using

freestream total conditions:

$$C_{T-P} = T_{0,\infty} P_{0,\infty}^{1-\gamma/\gamma}. \tag{4.13}$$

In other words, as shown by Eqs. (4.12) and (4.13) above, the flow is assumed to be homentropic. For the WCM method, the parameter on the right-hand side of Eq. (4.10) is a spatially-varying function that is also computed only once at the start of the computations, using the freestream static pressure and adiabatic temperature (as already shown in Eqs. (4.10) and (4.11).

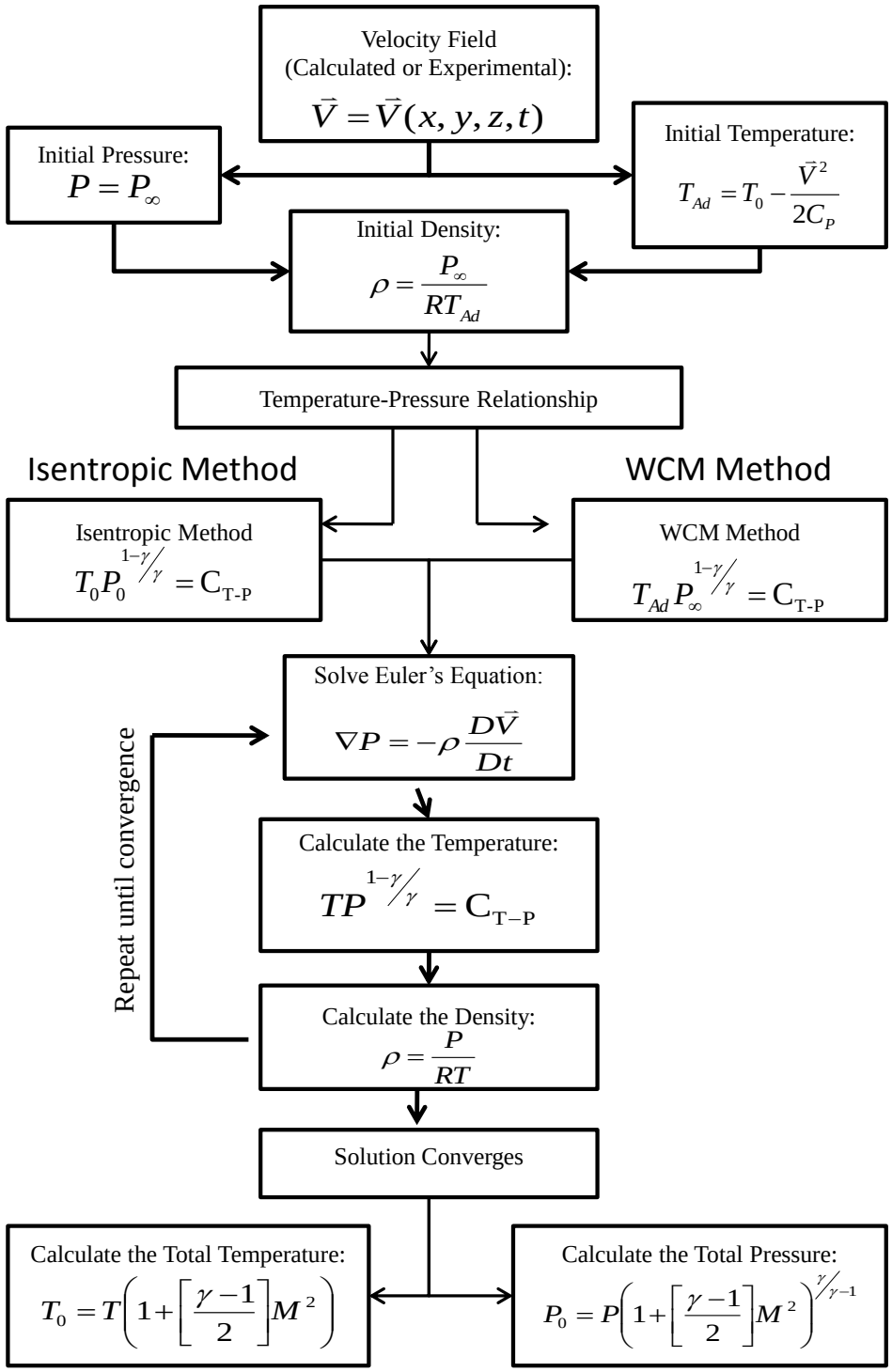

Figure 4.6: Calculation procedure for the isentropic and WCM methods.

4.4. Example of Tip-Vortex Optical Aberrations

In the following section, a comparison of the thermodynamic properties and optical aberration produced by a single tip vortex computed using the isentropic and the WCM methods is presented. For the comparison, a square computational domain with dimensions equal to 25 times the vortex-core diameter in the horizontal and vertical directions was used to ensure that the calculated thermodynamic properties had recovered to their freestream values by the edges of the computational domain. Furthermore, the velocity fields used in the comparison were computed for a vortex with a circulation strength of 21 m^2/s (Eq. (3.6)) and a core radius of 0.039 m (Eq. (3.12)). As shown in Appendix D, these vortex parameters correspond to typical values for a medium-sized helicopter.

Pressure, temperature, and density fields computed using the isentropic method are shown in Figure 4.7. A detailed comparison of the isentropic and WCM results is shown in Figure 4.8, which shows the computed pressure, temperature, and density plotted over slices through the center of the vortex. From Figure 4.8, it is evident that within the core of the vortex, the pressure, temperature, and density are all reduced.

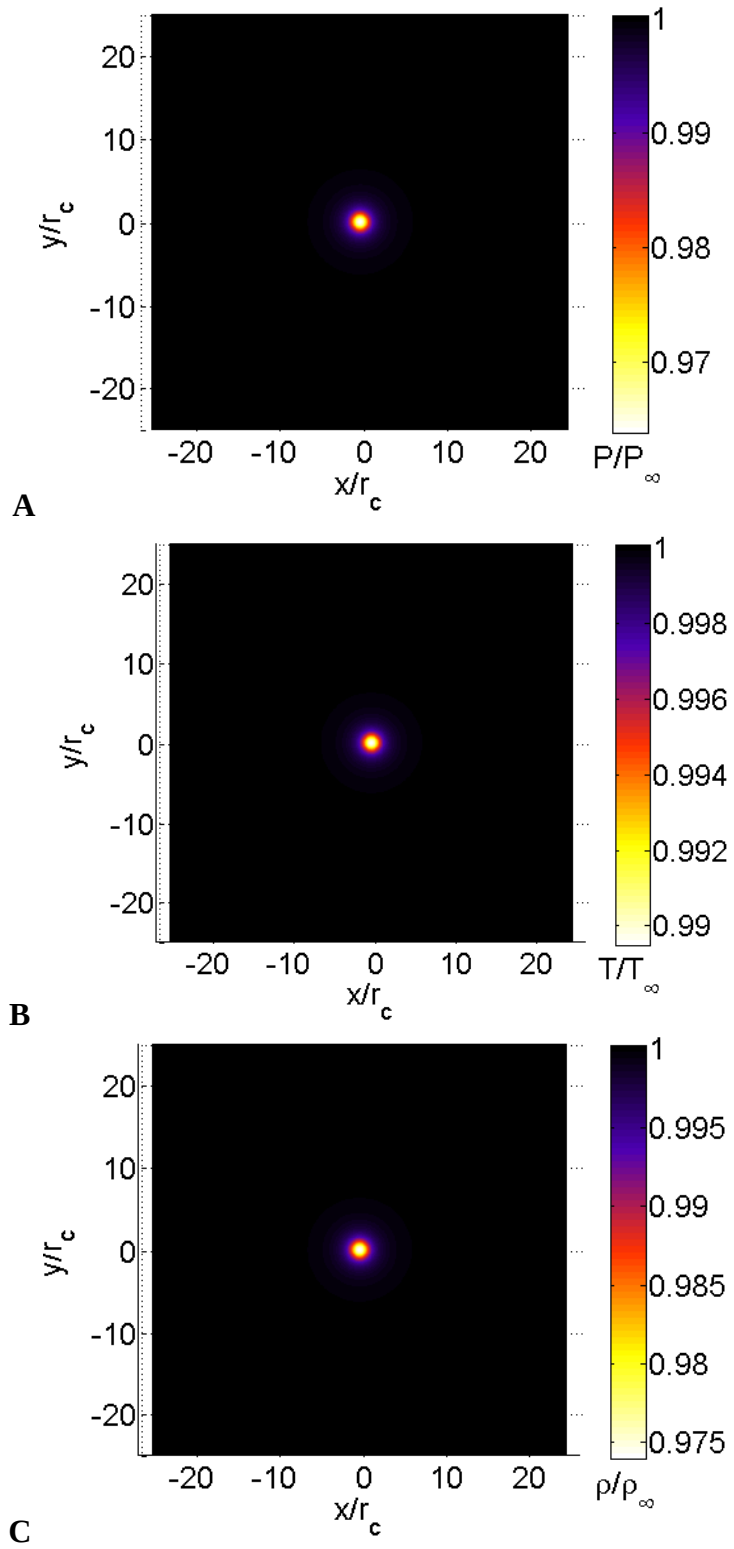

Figure 4.7: Pressure, temperature, and density fields computed using the isentropic thermodynamic method for a Lamb-Oseen vortex model: A) pressure, B) temperature, and C) density.

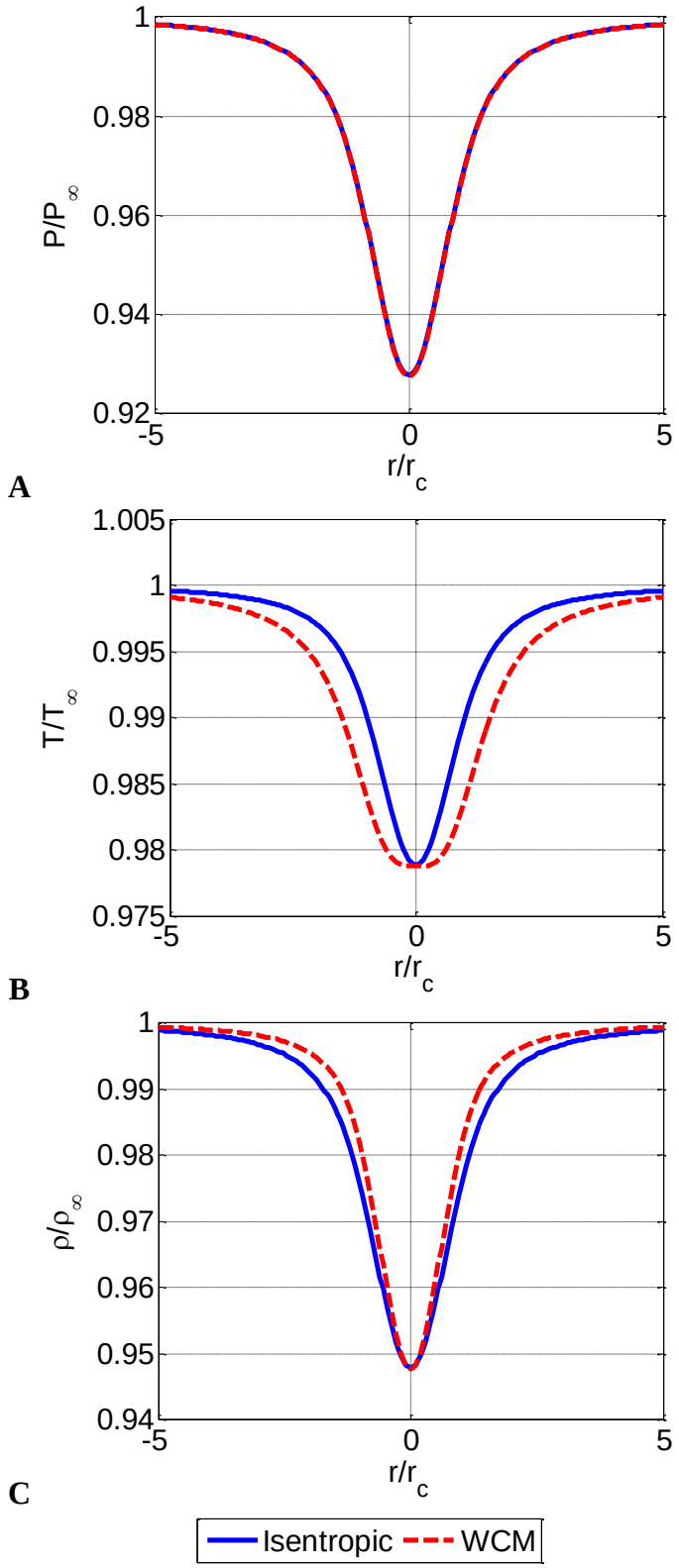

Figure 4.8: Comparison of the pressure (A), temperature (B), and density (C) using the isentropic method and the WCM method.

Comparing the isentropic solution to the WCM, the pressure fields calculated using both approaches are identical, with only a 0.03% difference between the two; it is noteworthy that in the free shear-layer calculations described in Rennie *et al*. (2008b), the pressure fields computed using the WCM and a full Navier-Stokes code were also nearly identical. On the other hand, the temperature distributions (Figure 4.8B) computed using the isentropic and WCM methods show much greater discrepancy; this outcome is consistent with the findings of Rennie *et al*. (2008b) as well as the investigations described previously in Section 4.2. In particular, although the WCM predicts the same magnitude of reduction in temperature as the isentropic model at $r/r_c = 0$, the WCM also predicts a greater reduction in flow temperature out to larger radial distances from the vortex center than the isentropic model (Figure 4.8B). These lower temperatures result from the adiabatic temperature model used in the WCM, Eq. (4.10). The effect is also clearly visible in the total temperature distribution shown in Figure 4.9. For both models, the total temperature distribution within the vortex is not constant, but rather reaches a minimum at the center of the vortex. Note that for a two-dimensional vortex, the velocity at the center of the vortex is zero, such that the total temperature used in the isentropic method and the adiabatic temperature used in the WCM are identical. Within the vortex, the tangential velocity causes a reduction in the adiabatic temperature used in the WCM, resulting in a reduced static temperature when compared to the isentropic solution. Finally, the velocity far from the core decays back to zero, so that the total temperature and adiabatic temperature used in the two methods are approximately equal, yielding identical freestream properties.

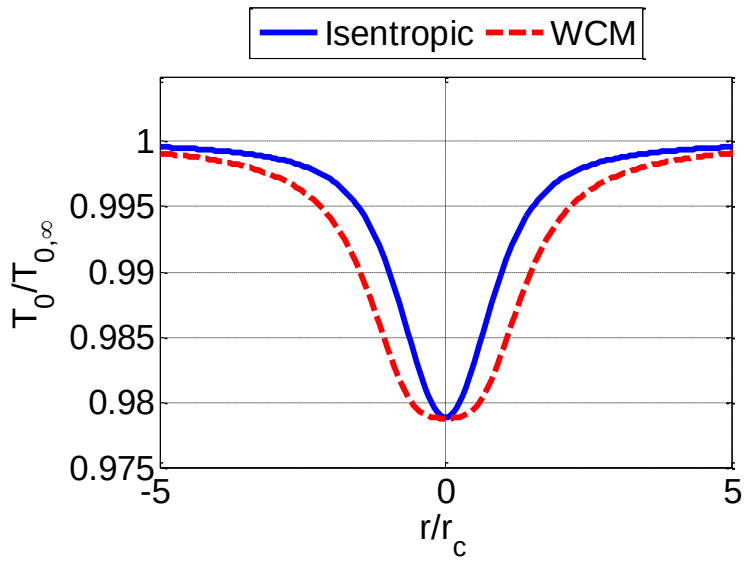

Figure 4.9: Comparison of the total temperature drop within a tip vortex calculated using the isentropic method and the WCM method.

The density fields computed using the isentropic and WCM methods are compared in Figure 4.8C. Due to the wider extent of reduced temperature (Figure 4.8B), the WCM actually produces a narrower region of reduced density than the isentropic method. Since the magnitude of the temperature drop at the center of the vortex (i.e. at $r/r_c = 0$) using each method is equivalent, the magnitude of the density drop at the center is also the same.

Finally, the optical aberrations associated with the density fields shown in Figure 4.8C are plotted in Figure 4.10. As shown, the isentropic method predicts a larger-magnitude OPD in the vicinity of the vortex core (i.e. near $r = 0$), and a concomitant larger reduction in Strehl ratio for a beam of light that passes through the vortex, than the WCM method. The greater reduction in OPD for the isentropic method is due to the fact that the isentropic method has a larger region of reduced density, which

can be seen in Figure 4.8C, such that the integrated effect of a beam of light passing through the density field is also greater for the isentropic method.

Despite the differences shown in Figure 4.10, the magnitudes of the optical aberrations predicted by both the isentropic and WCM methods are still reasonably close to one another. For example, the calculated OPD_{RMS} for the isentropic method is 0.3430 μm while the WCM method gives 0.2617 μm; the corresponding Strehl ratios are 0.4294 (isentropic method) and 0.5652 (WCM method). For most practical applications, these differences are relatively small, and it would be difficult to experimentally measure the kinds of differences between the isentropic and WCM predictions shown in Figure 4.10. Furthermore, it must be remembered that the objective of this dissertation research is to generate the first predictions for the optical environment surrounding a helicopter where, to the best of the author's knowledge, no such estimates currently exist. As such, perhaps the most noteworthy feature of Figure 4.10 is that the tip vortex for realistic helicopter flight conditions produces a large-magnitude optical aberration that would have a significant impact on the ability to focus an outgoing beam in the far field.

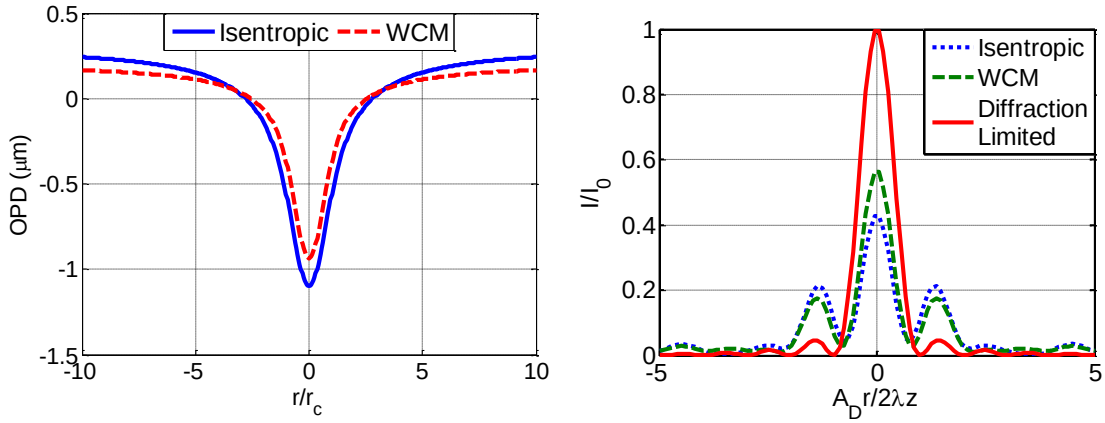

Figure 4.10: Comparison of the resulting optical properties using the isentropic method and the WCM method. Left) Calculated OPD, Right) Farfield irradiance pattern.

4.5. Analytical Solution for the Lamb-Oseen Vortex

An analytical solution for the optical effect of a Lamb-Oseen vortex can also be derived. This solution assumes isentropic flow, and also uses the weakly-compressible assumption, in that the density field and optical effect of the vortex are calculated from a pre-determined (i.e. the Lamb-Oseen) velocity field.

The solution procedure follows the approach outlined in Bagai and Leishman (1993). For an axisymmetric flow with no radial velocity component, the Euler equations are:

$$\frac{{V_\theta}^2}{r} = \frac{1}{\rho}\frac{\partial P}{\partial r}$$
$$V_z \frac{\partial V_z}{\partial z} = -\frac{1}{\rho}\frac{\partial P}{\partial z}. \tag{4.14}$$

Dimensional analysis of Eq. (4.14) for tip-vortex flows shows that the pressure gradient in the radial direction is an order of magnitude larger than the pressure gradient in the streamwise direction (Leishman 2000). Inserting the Lamb-Oseen velocity profile, Eq. (3.1), into Eq. (4.14) and neglecting the axial pressure gradient gives:

$$\frac{\Gamma^2}{4\pi^2 r^3}\left(1 - e^{-\alpha\left(\frac{r}{r_c}\right)^2}\right)^2 = \frac{1}{\rho}\frac{\partial P}{\partial r}. \tag{4.15}$$

For isentropic flow, the right hand side of Eq. (4.15) can be linearized, yielding:

$$\frac{1}{\rho}\frac{\partial P}{\partial r} = \frac{\gamma R T}{\rho}\frac{\partial \rho}{\partial r}. \tag{4.16}$$

Substituting Eq. (4.16) into Eq. (4.15) and integrating yields the density profile,

$$\rho = \frac{\rho_\infty \Gamma^2}{8\pi^2 a^2 r_c^2}\underbrace{\left[2\alpha Ei\left\{-\alpha\left(\frac{r}{r_c}\right)^2\right\} - 2\alpha Ei\left\{-2\alpha\left(\frac{r}{r_c}\right)^2\right\} - \frac{r_c^2 e^{-2\alpha\left(\frac{r}{r_c}\right)^2}\left(e^{\alpha\left(\frac{r}{r_c}\right)^2} - 1\right)^2}{r^2}\right]}_{f(r/r_c)} + \rho_\infty. \tag{4.17}$$

where Ei is the exponential integral, and ρ_∞ is the constant of integration.

In Eq. (4.17), the terms within the brackets can be represented by a function f that depends on r only (i.e. $f(r/r_c)$). As such, Eq. (4.17) shows that the analytical solutions to the density field associated with different tip-vortex flows are self-similar, and are a function of only the core radius and the circulation strength. Since the optical aberration (i.e. OPD) of the tip vortex is obtained from the density field, then the OPD is also a self-similar parameter (see below).

Figure 4.11 shows the comparison of the analytic solution (Eq. (4.17)) with the solution to the isentropic numerical method shown in Section 4.4 above. As shown, the two solutions are identical, thus validating the numerical iterative algorithm.

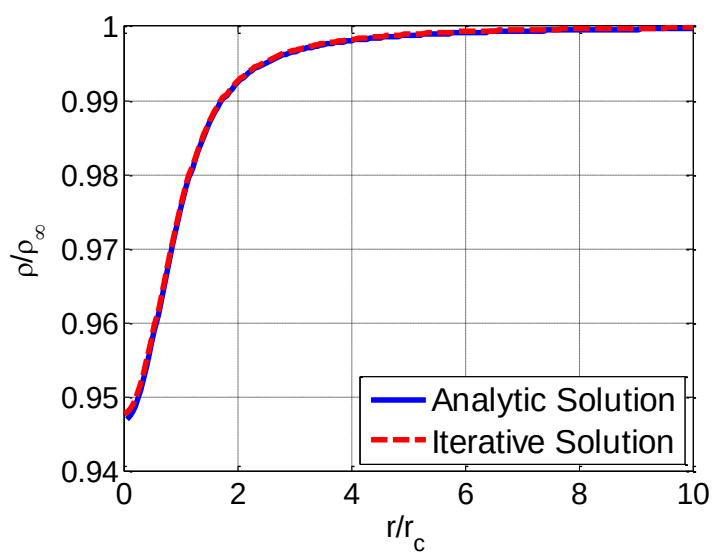

Figure 4.11: Comparison of numerical and analytical solutions to the tip-vortex flow shown in Figures 4.7 to 4.9.

The index-of-refraction is computed from the density field by inserting Eq. (4.17) into Eq. (2.1) and the OPL is found by integrating (Eq. (2.3)):

$$OPL(y) = \int_{-\infty}^{\infty} \left(1 + \frac{K_{GD}\rho_\infty \Gamma^2}{8\pi^2 a^2 r_c^2} f(r/r_c) + K_{GD}\rho_\infty\right) dx. \tag{4.18}$$

In Eq. (4.18), the function $f(r/r_c)$ represents the term in square brackets in Eq. (4.17), where $r = \sqrt{x^2 + y^2}$. The integral of the $f(r/r_c)$ term in Eq. (4.18) produces a constant that is dependant only on the y-coordinate which, for convenience, is represented by C(y) in Eq. (4.19) below:

$$\int_{-\infty}^{\infty} f(r/r_c)\, dx = r_c C(y). \tag{4.19}$$

As such, Eq. (4.18) can be rearranged as,

$$OPL(y) = x + C(y)\left(\frac{\rho_\infty}{\rho_{SL}}\right)\frac{\Gamma^2}{\mathrm{a}^2\mathrm{r_c}} + K_{GD}\rho_\infty x. \tag{4.20}$$

Using Eq. (2.4) to calculate the OPD gives:

$$OPD(y) = \frac{\rho_\infty}{\rho_{SL}}\frac{\Gamma^2}{\mathrm{a}^2\mathrm{r_c}}\left[C(y) - \frac{1}{A_D}\int_{-A_D/2}^{A_D/2} C(y)dy\right] = \frac{\rho_\infty}{\rho_{SL}}\frac{\Gamma^2}{\mathrm{a}^2\mathrm{r_c}} D(y) \tag{4.21}$$

where the function $D(y)$ is used to represent the term in brackets. Computing the root-mean-square (RMS) across the aperture gives:

$$\mathrm{OPD_{RMS}} = \left[\frac{1}{A_D}\int_{-A_D/2}^{A_D/2} \mathrm{OPD}(y)^2\, dy\right]^{1/2} = \frac{\rho_\infty}{\rho_{SL}}\frac{\Gamma^2}{\mathrm{a}^2\mathrm{r_c}}\left[\frac{1}{A_D}\int_{-A_D/2}^{A_D/2} \mathrm{D}(y)^2\, dy\right]^{1/2}. \tag{4.22}$$

The integral in Eq. (4.22) can be represented by an "aperture function," $G(A_D/2r_c)$, which shows how the calculated OPD_{RMS} depends on the ratio of the beam (or aperture) diameter to the vortex core diameter:

$$OPD_{RMS} = \left(\frac{\rho_\infty}{\rho_{SL}}\right)\frac{\Gamma^2}{a^2 r_c} G\left(\frac{A_D}{2r_c}\right). \tag{4.23}$$

The aperture function is discussed in further detail below. Equations (4.22) and (4.23) constitute the analytic, weakly-compressible, isentropic solution of the optical aberration from a beam of light propagating through a Lamb-Oseen vortex centered within the beam. As a final note, the OPD can be nondimensionalized by the OPD_{RMS}, which gives a relationship that depends only on the measurement aperture:

$$\frac{OPD}{OPD_{RMS}} = \frac{D(y)}{G\left(\frac{A_D}{2r_c}\right)}. \tag{4.24}$$

4.6. Optical Scaling Relationship for a Two-Dimensional Tip-Vortex

In Section 4.4 it was shown that the optical aberrations produced by a tip-vortex with parameters corresponding to a medium-sized helicopter will seriously degrade the far field performance of a beam of light that passes through the vortex. The data shown in Section 4.4 were calculated, however, for a single set of vortex parameters and flight conditions, and it is important to note that the aberrating effect of a tip vortex will be considerably different for other flight conditions. For example, Figure 4.12 shows how the spatial OPD_{RMS} of a tip-vortex aberration changes as a function of the vortex circulation strength and vortex core radius. The data in Figure 4.12 were calculated using the procedures described in Section 4.3; that is, by computing Lamb-Oseen velocity

fields for different vortex parameters, and then computing the optical effect using the isentropic method. Note that for the results shown in Figure 4.12, the ratio of the beam diameter to the vortex core diameter was held constant at $A_D/2r_c = 10$ as in Figure 4.10. This is an important consideration because of the highly spatially-localized character of the tip-vortex aberration, so that the computed OPD_{RMS} can vary significantly based on the size of the measurement aperture (aperture effects are discussed in greater detail in Section 4.6.2). Figure 4.12 shows that the optical effect of a tip vortex changes significantly with both the circulation strength and core radius.

The OPD_{RMS} of the aberration due to a tip vortex can also depend on other parameters not illustrated in Figure 4.12, such as the freestream pressure (i.e. altitude) and temperature. As such, considerable utility would be gained if a relationship were developed that could be used to quickly determine the aberrating effect of tip vortices for different flight conditions by scaling from existing computational or experimental data. Scaling relationships such as this have been found to exist for other types of aero-optic flows (Cress *et al.* 2008; Gordeyev *et al.* 2003; Gordeyev and Jumper 2009).

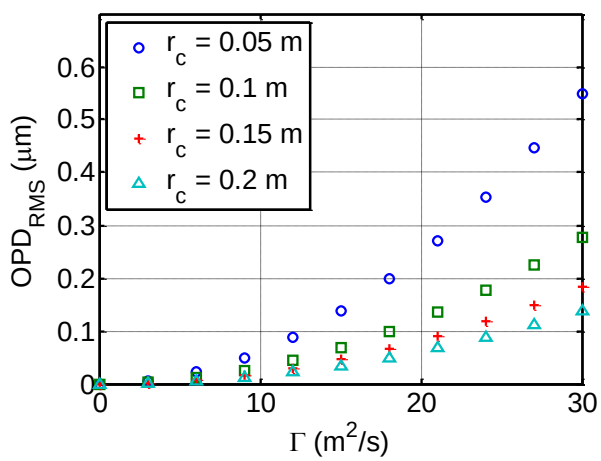

Figure 4.12: Optical aberrations computed for various tip-vortex parameters using the Lamb-Oseen vortex model and the isentropic method. For all data shown, $A_D/2r_c = 10$.

This kind of scaling relationship can be formed from the analytical solution derived in Section 4.5 above. While Eq. (4.21) shows how the OPD for a tip vortex depends on the specific flight conditions, it is more useful to look at the OPD_{RMS} since this provides a single parameter that can be used to rapidly compare the severity of the optical aberration associated with different flight conditions. Equation (4.23) can thus be considered to be a "scaling relation" for the severity of the optical aberration due to a two-dimensional vortex.

Assuming the circulation of the vortex is proportional to the circulation associated with the wing or rotor-blade lift, the scaling relation (Eq. (4.23)) can also be expressed as

$$OPD_{RMS} = \left(\frac{\rho}{\rho_{SL}}\right)\frac{C_l^2 M^2 c^2}{r_C} G\left(\frac{A_D}{2r_c}\right). \tag{4.25}$$

Equation (4.25) shows that the spatial OPD_{RMS} is a function of the lift coefficient, Mach number, chord length, and vortex core radius. In particular, this equation shows that if the rotor blade lift decreases, so will the OPD_{RMS}, eventually going to zero as the lift goes to zero. Furthermore, Eq. (4.25) exhibits the same Mach-number-squared dependency found in boundary-layer experiments (Cress *et al.* 2008; Gordeyev *et al.* 2003) and turret experiments (Gordeyev and Jumper 2009; Porter *et al*. 2011); as such, as the local Mach number goes to zero so does the OPD_{RMS}. An increase in the core radius also results in a reduction in OPD_{RMS}; this can happen if, for example, the vortex diffuses due to viscous effects, or if vortex breakdown occurs.

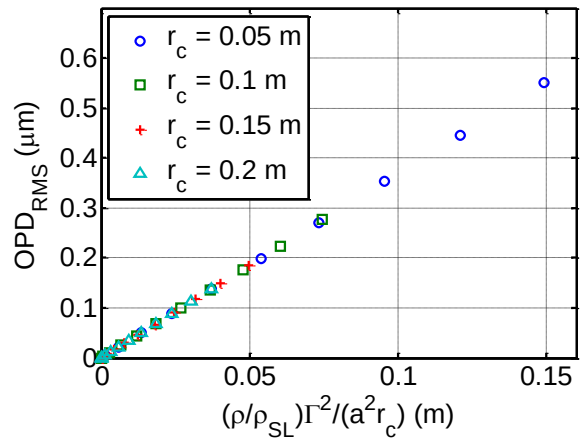

Figure 4.13: Numerically-computed tip-vortex data scaled according to Eq. (4.23).

To demonstrate that Eqs. (4.23) and (4.25) can be used to scale tip-vortex optical aberrations, the optical data shown in Figure 4.12 were re-plotted using the scaling parameter shown in Eq. (4.23). Figure 4.13 shows that this scaling parameter successfully collapses the data onto a single curve. The slope of the line shown in Figure 4.13 was computed using a least-squares approach, giving a value of 3.695:

$$OPD_{RMS} = 3.695\left(\frac{\rho}{\rho_{SL}}\right)\frac{\Gamma^2}{a^2 r_C}. \tag{4.26}$$

Again, since all of the data in Figure 4.12 had an aperture ratio $A_D/2r_c$ = 10, the coefficient 3.695 is therefore the value of the aperture function G for $A_D/2r_c$ = 10, that is, $G(10)$ = 3.695. Equation (4.26) is essentially a "numerically-calibrated analytical solution" for tip-vortex optical aberrations, in the sense that it was developed from basic fluid-mechanic equations with the final constant of proportionality determined by a curve fit to numerical data.

The calibrated numerical constant in Eq. (4.26) was calculated using the isentropic thermodynamic method. However, as shown in Figure 4.10, the isentropic and WCM computational methods generate slightly different results for OPD and OPD_{RMS}.

To compare the differences between the two methods, OPD and OPD_{RMS} data were recalculated with the WCM using the same database of Lamb-Oseen tip-vortex velocity fields; these results gave a coefficient of 2.805, compared to 3.695 for the isentropic method (see Figure 4.14). In effect, due to the slightly different flow physics assumed by the WCM, the WCM has a different aperture function than the isentropic method, and the value of the aperture function for the WCM at an aperture ratio $A_D/2r_c$ = 10 is $G(10)$ = 2.805.

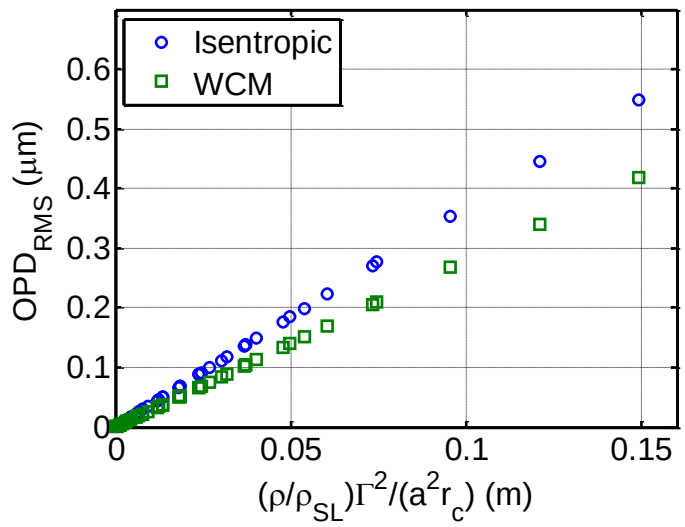

Figure 4.14: Comparison of OPD_{RMS} computed using the isentropic and WCM methods for Lamb-Oseen tip-vortex velocity fields scaled according to Eq. (4.23).

4.6.1. Effect of Axial Velocity Component

For the data shown in Figure 4.13 and Figure 4.14, the vortex velocity fields were two-dimensional in the sense that the axial velocity components were zero. In reality, tip-vortex velocity fields typically include a wake-like or jet-like axial velocity component. An axial velocity component in the tip-vortex flow from a fixed wing or

rotating helicopter blade can arise, for example, from the momentum deficit of the wing or rotor blade (Bhagwat and Leishman 2002):

$$A = \frac{V_\infty^2 c \left(\frac{b}{2}\right) C_{D,0}}{8\pi(\delta\nu)}, \tag{4.27}$$

where $C_{D,0}$ is the drag coefficient at zero angle of attack. Since the circulation strength of the tip vortex is proportional to the freestream velocity, the momentum-deficit constant A can be rewritten as:

$$A = \frac{\Gamma^2 C_{D,0}}{64\pi(\delta\nu)}. \tag{4.28}$$

Optical aberrations computed using the isentropic and WCM methods for tip-vortex flow fields that include an axial-flow component are shown in Figure 4.15 (isentropic method) and Figure 4.16 (WCM method). Realistic values for the axial-flow components used to generate the tip-vortex flow fields were determined using Eq. (4.28), in which different values of the diffusion coefficient, δ, that spanned the range given by Eq. (3.11) were used. Figures 4.17 to 4.19 also compare the temperature, density, and axial flow predicted by the two methods. Figure 4.15 shows that the OPD computed using the isentropic method is essentially insensitive to the axial-flow component. This is because, for the isentropic method, the temperature is not modified by the existence of the axial flow, and the optical aberration is produced only by the pressure and density well associated with the vortex tangential velocity.

On the other hand, Figure 4.16 shows that the axial-flow component has a small effect on the OPD computed using the WCM method. In particular, the magnitude of the dip in the OPD at the core of the vortex increases as the magnitude of the axial-flow component increases (which corresponds to <u>decreasing</u> δ in Figure 4.16). This behavior

is the outcome of the adiabatic temperature model that is incorporated into the WCM method, Eq. (4.10), which predicts a smaller reduction in temperature in the core of the vortex as a result of the axial-flow component, that further lowers the density and OPD in the vortex core. This temperature-based reduction in OPD is in addition to the reduction in OPD that originates from the pressure well associated with the vortex tangential velocity, which is the only source of density and OPD variation in the isentropic method. In Chapter 5, it will be shown that the isentropic and WCM methods also produce noticeably different results for experimental tip-vortex flows that include an axial-flow component.

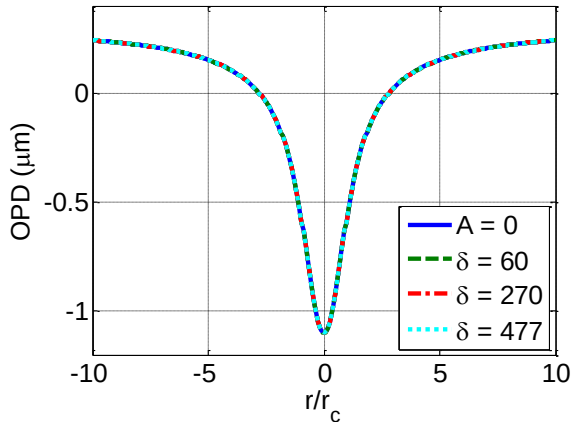

Figure 4.15: Comparison of OPD profiles computed using the isentropic method for Lamb-Oseen velocity fields with different momentum-deficit coefficients.

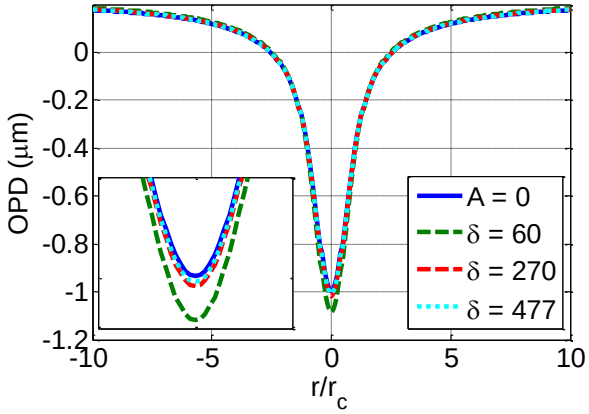

Figure 4.16: Comparison of OPD profiles computed using the WCM method for Lamb-Oseen velocity fields different momentum-deficit coefficients.

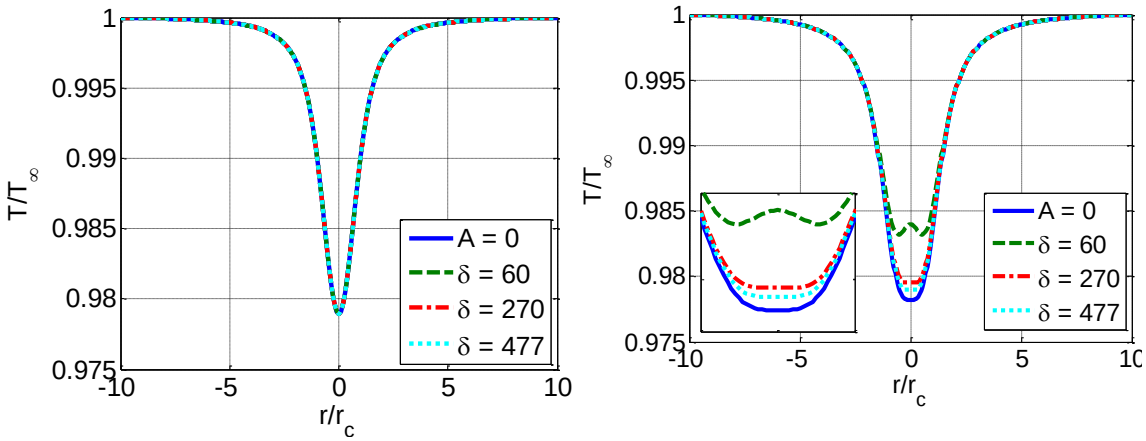

Figure 4.17: Comparison of the temperature profiles computed using the isentropic method (left) and WCM method (right) for Lamb-Oseen velocity fields with different momentum-deficit coefficients.

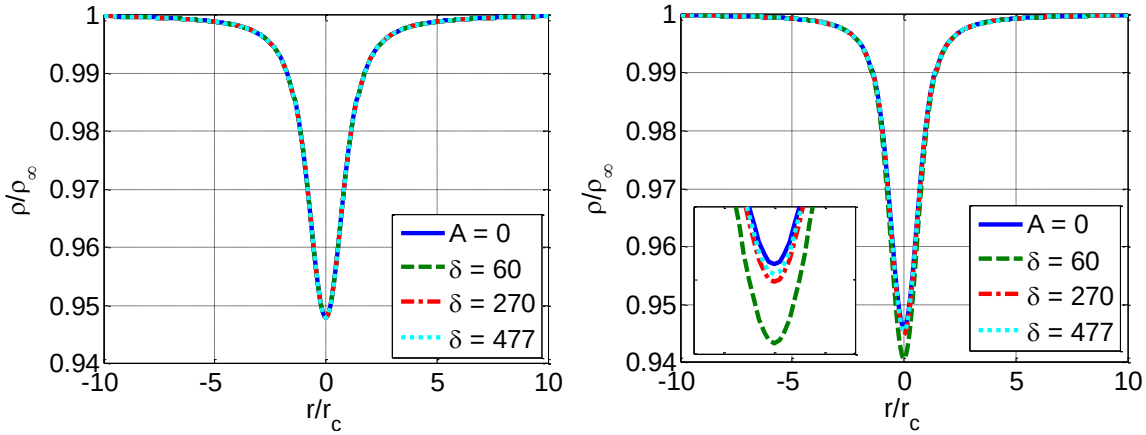

Figure 4.18: Comparison of the density profiles computed using the isentropic method (left) and WCM method (right) for Lamb-Oseen velocity fields with different momentum-deficit coefficients.

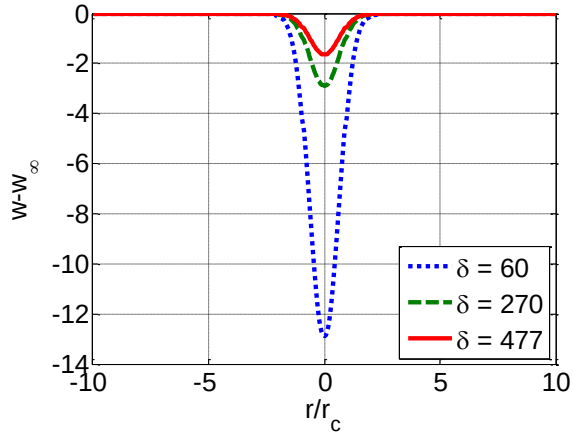

Figure 4.19: Momentum deficit within the Lamb-Oseen vortex for different apparent viscosities based on Eq. (4.28).

The development of a scaling relationship that accounts for both tangential and axial velocity components could be developed by solving Euler's equation for the case of a general tip-vortex flow involving both flow components. However, since the optical aberration imposed on a beam is dominated by the tangential flow effect, a simple estimation of the additional effect of the axial-flow component may be obtained by linearly combining the axial flow effect with the tangential-flow effect shown in Eq. (4.23). The effect of the axial velocity component on the WCM was determined by re-solving the Euler equations (Eq. (4.14)), this time neglecting the radial pressure gradient and including only the axial velocity component, Eq. (3.2). Using an analysis similar to that shown in Section 4.5.3, the following proportionality relationship was obtained:

$$OPD_{RMS} \propto \left(\frac{\rho}{\rho_{SL}}\right)\frac{\mathrm{A}^2\mathrm{r_C}}{\mathrm{a}^2\mathrm{z}^2}. \tag{4.29}$$

Equation (4.29) shows how the $\mathrm{OPD_{RMS}}$ varies as a function of just the axial velocity component of the vortex velocity field. Linearly combining Eq. (4.23) with Eq. (4.29) gives:

$$OPD_{RMS} = \underbrace{C_1\left(\frac{\rho}{\rho_{SL}}\right)\left(\frac{r_C}{a^2}\right)\left(\left[\frac{\Gamma}{r_C}\right]^2 + C_2\left[\frac{\mathrm{A}}{\mathrm{z}}\right]^2\right)}_{\chi} \tag{4.30}$$

where C_1 and C_2 are constants that must be fit to experimental or numerical data.

Figure 4.20 shows the $\mathrm{OPD_{RMS}}$ computed using the WCM method for tip-vortex flows that include axial-flow components, plotted against the two-dimensional scaling relationship, Eq. (4.23). On the other hand, Figure 4.21 shows the same data plotted against Eq. (4.30). Figure 4.21 shows that the scaling relationship of Eq. (4.30)

successfully collapses the data onto a single line. The constants of the fit shown in Figure 4.21 are C_1 = 3.002 and C_2 = 45.9, which were determined by minimizing the error of the fit in a least squares sense.

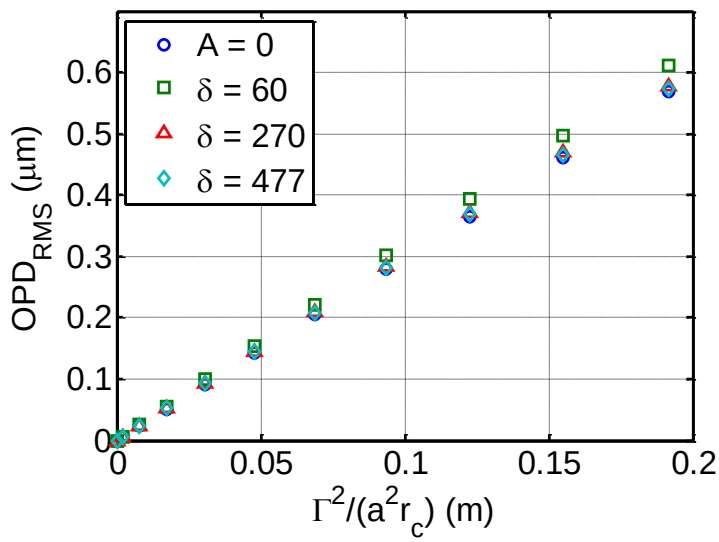

Figure 4.20: Effect of axial velocity component on optical aberrations calculated using the WCM method.

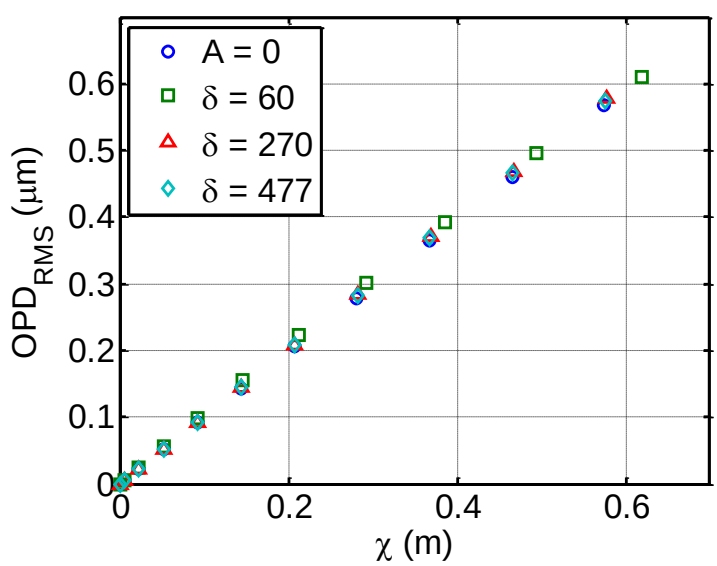

Figure 4.21: WCM-computed optical aberrations for tip vortices with both tangential and axial velocity components plotted using the scaling relationship of Eq. (4.30).

4.6.2. Aperture Effects

In Section 4.5 it was shown that, due to the spatially-localized nature of the tip-vortex aberration, the OPD_{RMS} on a beam of light that passes through a tip vortex strongly depends on the aperture size, since the aperture limits how much of the aberration is "seen" by the beam. This is shown graphically in Figure 4.10, which shows how the aberration produced by a tip vortex is greatest at the center of the vortex and drops off with lateral distance away from the core. As such, the calculated OPD_{RMS} of the aberration changes as the beam aperture changes because, first, the tip/tilt of the part of the aberration contained within the aperture can change depending on the size and location of the aperture. Secondly, as shown in Figure 4.10, the aberration has a finite size so that the OPD_{RMS} due to the aberration becomes smaller as the aperture becomes much larger than the vortex. In summary, the beam aperture acts as a spatial gain, *G(AP)*, either increasing or decreasing the calculated spatial OPD_{RMS}.

Siegenthaler (2008) previously investigated the way in which the beam aperture size alters the effect of an optical aberration. An important difference exists, however, between the work of Siegenthaler and the tip-vortex aberrations studied here. Specifically, for the continuous, sinusoidal-like aberrations investigated by Siegenthaler, the OPD_{RMS} tended towards a maximum value as the aperture increased while, for the tip vortices studied here, the OPD_{RMS} tends towards zero.

The nature of the effect that aperture size has on the aberration caused by a tip vortex is illustrated in Figure 4.22A. The data in the figure were generated by first computing different Lamb-Oseen velocity profiles for different vortex parameters and then computing the corresponding OPDs and spatial OPD_{RMS} as a function of aperture

size. As shown in Figure 4.22A, the OPD_{RMS} varies significantly with the size of the aperture. However, non-dimensionalization of the aperture diameter by the vortex core diameter collapses the data onto a single curve as shown in Figure 4.22B, where the OPD_{RMS} has been normalized by the OPD_{RMS} at an aperture ratio of 10. The curve shown in Figure 4.22B can be considered to be the "normalized aperture function," $G_{Norm}(AP)$, for a tip vortex, and shows how the computed OPD_{RMS} depends on the aperture ratio, $AP = A_D/2r_c$. Normalization of the aperture function by the value at $AP = 10$ was chosen for the simple reason that the tip-vortex aberration more or less "fills" the aperture at this aperture ratio. Furthermore, values of the aperture function were computed in Section 4.6 for both the isentropic and WCM methods for an aperture ratio of 10, so that the full aperture function can be obtained by multiplying the curve in Figure 4.22B by the coefficients determined in Section 4.6, that is:

$$G(AP) = CG_{Norm}(AP) \tag{4.31}$$

where, from Section 4.6, $C = 3.695$ for the isentropic method and 2.805 for the WCM method (or $C_1 = 3.002$ and $C_2 = 45.9$ for the WCM method with an axial-flow component, see Section 4.6.1). As such, the overall scaling relationship that includes aperture effects is shown in Eq. (4.32):

$$OPD_{RMS} = 3.695\left(\frac{\rho}{\rho_{SL}}\right)\frac{\Gamma^2}{a^2 r_C}G_{Norm}(AP). \tag{4.32}$$

The aperture function can be used to scale tip-vortex OPD_{RMS} data to different measurement apertures. For example, Figure 4.23 shows tip-vortex aberrations computed for different circulation strengths and beam apertures. Figure 4.23A shows the data

without any adjustment for the aperture ratio, *AP*, while Figure 4.23B shows the same data adjusted to the same aperture ratio *(AP = 10)* using the gain function, *G(AP)*, shown in Figure 4.22B. As shown by Figure 4.23B, scaling the data to the same aperture ratio collapses the data onto a single line.

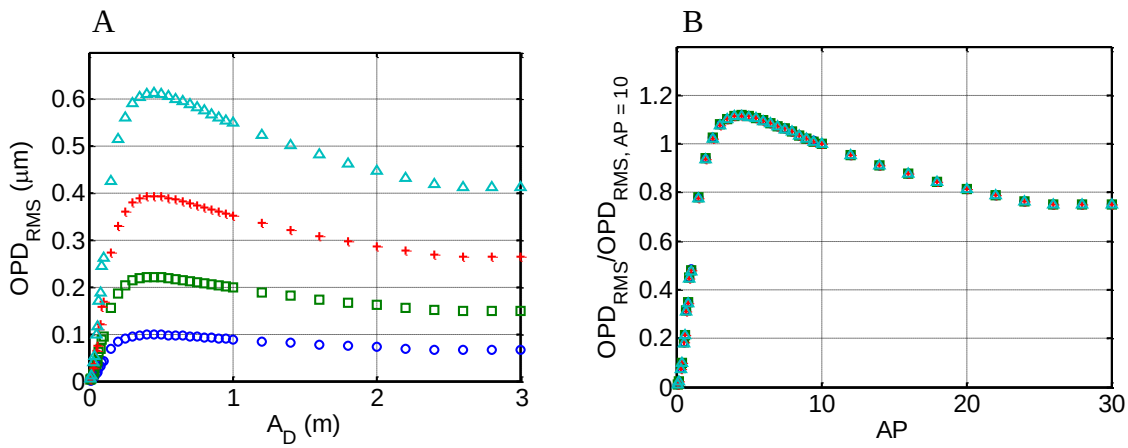

Figure 4.22. Effect of aperture diameter on the computed OPD_{RMS}; (A) the calculated OPD_{RMS} for different aperture diameters and (B) the same data non-dimensionalized by the OPD_{RMS} at an aperture ratio of 10, plotted against the aperture ratio, $AP = A_D/2r_c$.

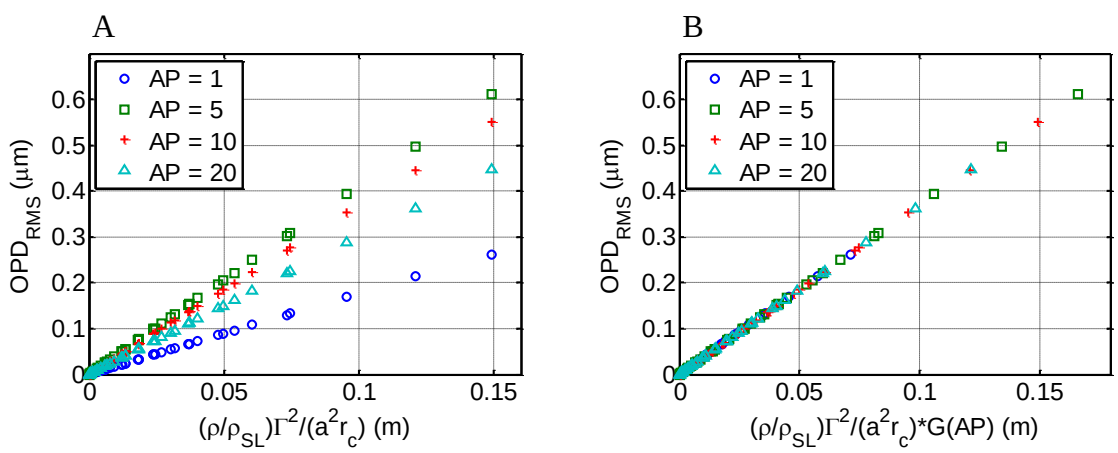

Figure 4.23. Correction for aperture-to-core ratio: A) Uncorrected scaling B) Corrected scaling.

Finally, it should be noted that the aperture function shown in Figure 4.22B was derived for the specific case of the isentropic method based on the Lamb-Oseen velocity profile, and that the aperture function will appear differently for other experimental or

numerical data that are governed by different physical effects. As an example, Figure 4.24 compares the aperture functions (normalized by the value at *AP* = 10) for the isentropic and WCM methods. The figure shows that the two aperture functions have a similar shape, with only minor differences between the two.

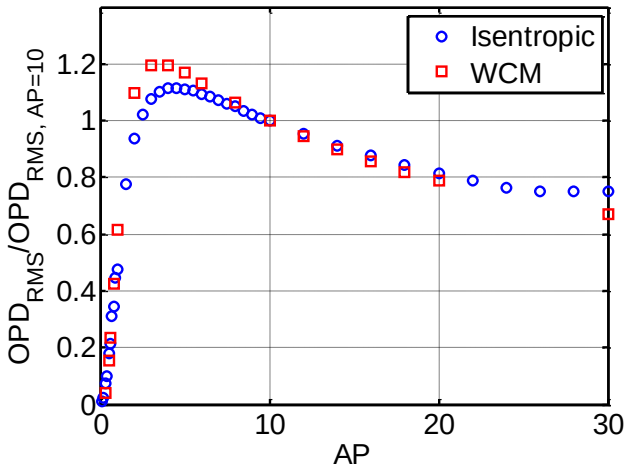

Figure 4.24: Comparison of the normalized aperture functions for the isentropic and WCM methods.

4.7. Effect of Grid Resolution

Since the pressure for the isentropic method or WCM is calculated from a finite-difference scheme, the accuracy can depend on the resolution of the grid; as such, to ensure grid-independent solutions, a grid-resolution study was performed. The study was performed for a single, Lamb-Oseen tip-vortex in free space, using a computational domain that was 20 times larger than the vortex core diameter. Several different grids used in the study are illustrated in Figure 4.25. The top plot in Figure 4.25 shows the full computational domain used for the study, with a nominal grid spacing that gave 11 grid points across the span of the vortex core. Two zoomed-in views of the computational

grid are also shown in Figure 4.25 with the bottom left containing 11 grid points in the vortex core while the bottom right figure shows 51 grid points in the vortex core.

Figure 4.26 shows: (A) the minimum pressure, (B) the minimum density, (C) the OPD_{RMS}, and (4) the SR as a function of the grid resolution, up to the maximum tested resolution of grid points used to define the profile of the vortex core. The figure shows that the pressure and density are largely unaffected by further refinement of the grid once ~20 grid points are within the core. On the other hand, Figure 4.26 shows that the computed OPD_{RMS} and Strehl ratio can become sensitive to the grid resolution if small aperture ratios are used; this was avoided by using *AP=10* for these computations. Based on the results shown in Figure 4.26, all of the single tip-vortex calculations were performed using a grid with at least 20 points in the vortex core.

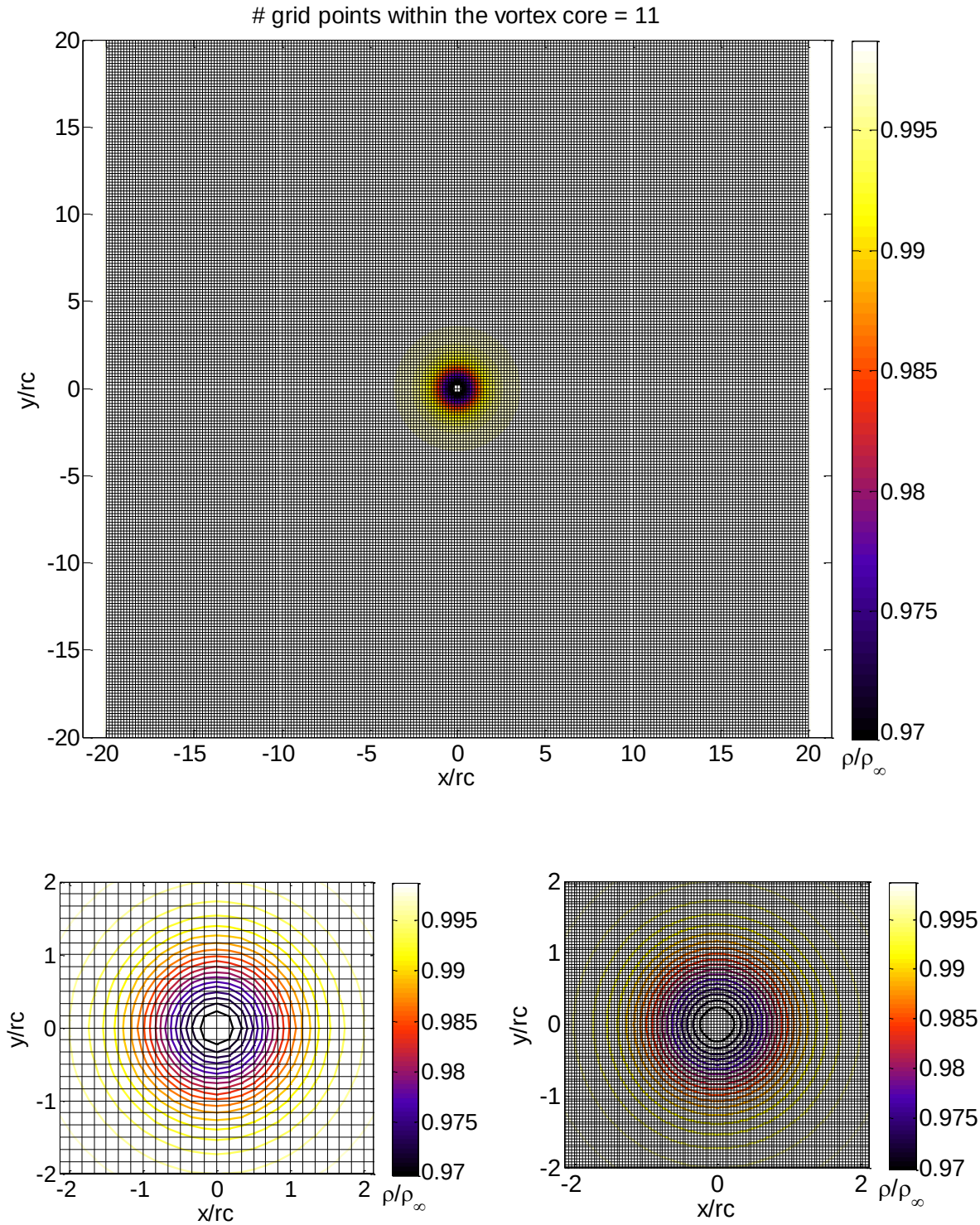

Figure 4.25: Computational grid and calculated density contours. Top) Full computational domain with 11 grid points within the core along $y/r_c = 0$. Bottom Left) Zoomed in view of the computational grid with 11 grid points along the $y/r_c = 0$. Bottom Right) Zoomed in view of computational grid with 51 grid points along the $y/r_c = 0$.

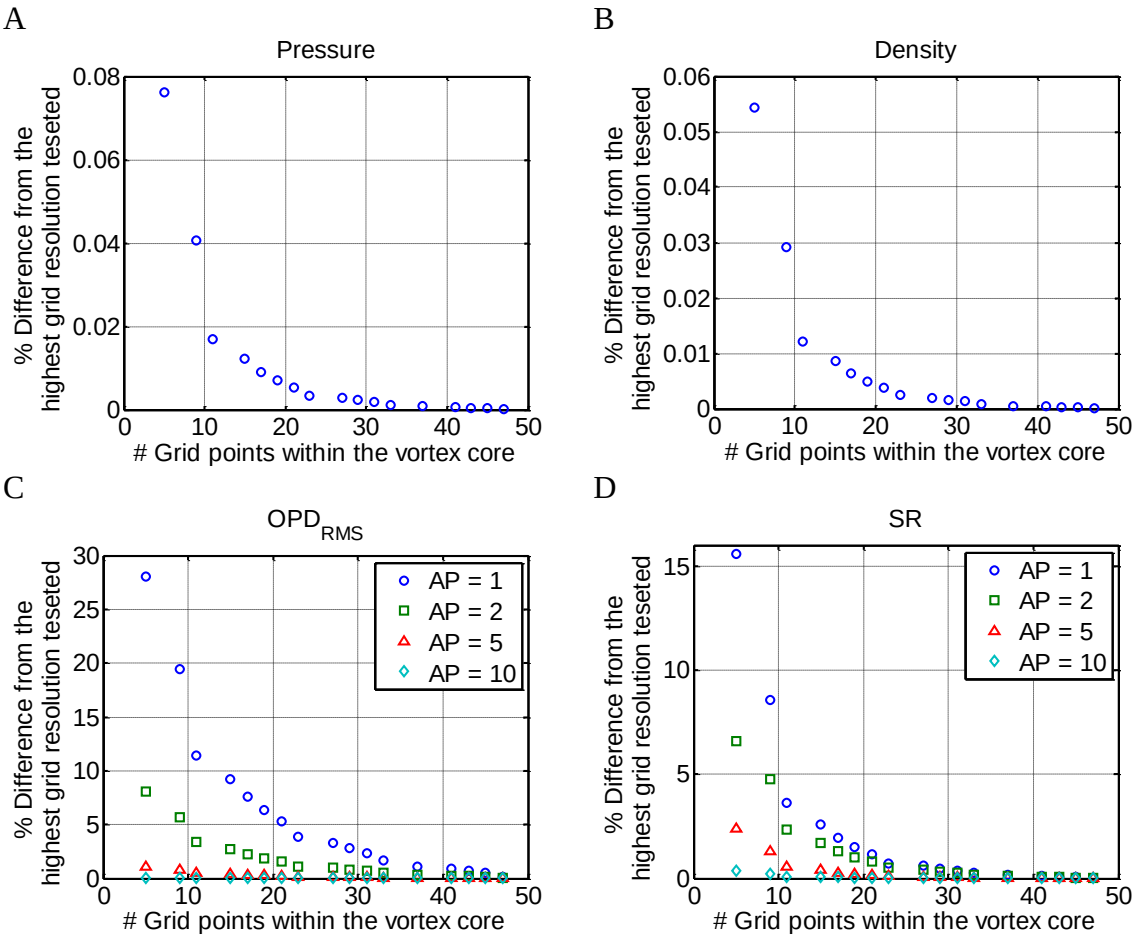

Figure 4.26: Dependence of computational solution on the number of grid points within the vortex core: A) minimum pressure, B) minimum density, C) OPD_{RMS} and D) SR.

For the full helicopter flow-field calculations presented in Chapter 7, the total available memory (in this case, 32 GB without memory swapping) set limits on the grid spacing and number of data points. As such, in this case a full grid refinement study was impractical; instead, the full helicopter flow field was compared to the results for a single vortex for different grid resolutions, in order to evaluate the error in the computations. Grid-resolution considerations for the full helicopter computations are more fully discussed in Chapter 7.

4.8. Simple Estimation of the Optical Effect of a Helicopter Tip Vortex

Using Eq. (4.32), it is possible to make a simple estimation of the severity of the aberrations that can be expected from the vortex wake of a helicopter under typical operating conditions. Note that the estimation presented here is for the case of the vortex centered within the outgoing beam, which is the orientation modeled by Eq. (4.32); calculations of the optical effect of a full helicopter wake for both hover and forward flight conditions with the vortex at any position within the optical aperture are presented in Chapter 7. The estimation was made for the case of a helicopter in hover using a tip-vortex circulation strength of 21 m^2/s (Appendix D), which is a representative value for a medium-sized helicopter (Bagia and Leishman 1993; Leishman 2000; Ramasamy and Leishman 2007). The aberrating effect of the blade vortex system was evaluated for a fuselage-mounted optical system that is pointed outwards in a direction parallel with the rotor disk, as depicted in Figure 1.6.

Besides the vortex circulation strength, the remaining parameter needed to fully define the vortex and hence enable the use of Eq. (4.32) is the vortex core radius r_c. As discussed in Chapter 3, the vortex core radius grows with time t (or distance) away from the blade tip where the vortex originated. The growth distance of the vortex was determined by computing the helical paths taken by the tip-vortex filaments (also depicted in Figure 1.6) using Landgrebe's prescribed-wake model (Leishman 2000). To account for the variability in the growth rate of the tip vortices, estimates were computed for two values of the turbulent diffusion parameter, δ = 60.5 and δ = 477, which are moderately-low and moderately-high values for a medium-sized helicopter.

Using the parameter values defined above, Figure 4.27 shows the OPD_{RMS} computed using Eq. (4.32) on a beam that passes through the tip vortex as a function of wake age. Based on Landgrebe's model, the tip vortex has a wake age of approximately 360 to 720 degrees before it moves into the line of sight of an optical system mounted on (or under) the helicopter fuselage. In other words, the blade creating a given tip vortex makes one to two full revolutions from the instant the tip vortex was created to the point at which it propagates into the line of sight of the fuselage-mounted optical system. As shown in Figure 4.27, the OPD_{RMS} at a wake age of 360 degrees ranges from ~0.14 μm to ~0.4 μm depending on the value of δ.

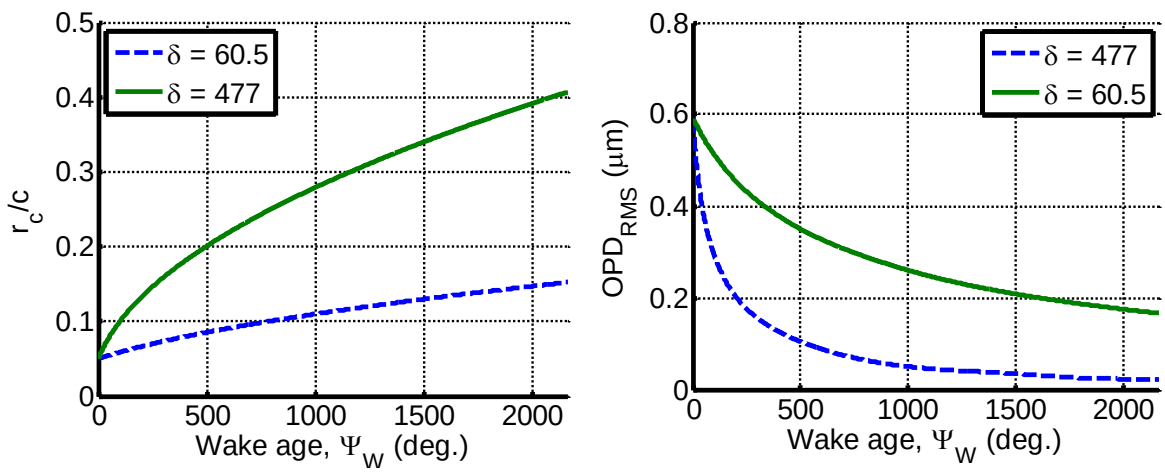

Figure 4.27: Predicted core radius and OPD_{RMS} for a medium-sized helicopter in hover, with an aperture of 0.3 m.

The computed OPD_{RMS} for the two cases shown in Figure 4.27 and the calculated Strehl ratio (for a nominal 1 μm wavelength) for each are listed in Table 4.1. The data in Table 4.1 show that the effect of the blade vortex on the outgoing beam strongly depends on the value of the empirical core-growth parameter δ; however, Table 4.1 also shows that even the best-case value for δ still produces a 50% reduction in Strehl ratio. In

summary, this simplified example has demonstrated that a helicopter tip vortex can have a significant aberrating effect on an optical system mounted on the helicopter. The magnitude and character of the aberrations for a helicopter in hover and forward flight are investigated in further detail in Chapter 7 of this dissertation.

TABLE 4.1:

AERO-OPTIC ENVIRONMENT BENEATH A MEDIUM-SIZED HELICOPTER

Γ (m^2/s)	r_c/c	δ	AP	OPD_{RMS} (μm)	SR
21	0.1712	477	1.753	0.1372	0.5083
21	0.0768	60.5	3.906	0.3914	0.2514

CHAPTER 5:

EXPERIMENTAL MEASUREMENTS OF TIP-VORTEX ABERRATIONS

The preceding chapters have presented methods for computing the flow field and optical aberration associated with a tip vortex. In this chapter, the results of experimental measurements of the aberrating effect of wingtip vortices are presented. These results are compared to the predictions of the weakly-compressible methods and the scaling relationship presented in Chapter 4. The chapter concludes with the presentation of a computational fluid dynamic (CFD) investigation that gives further insight into the thermodynamic properties of a realistic tip-vortex flow.

5.1. 60 Degree Half Span Delta Wing Experiment

The first experiment was performed in the 10 cm x 10 cm test section of one of the indraft tunnels at Hessert Laboratories. The tunnel has a contraction ratio at the inlet of 150:1 and is capable of flow velocities ranging from Mach 0.2 to Mach 0.8. The test section was identical to that used by Cress *et al.* (2010) for aero-optical boundary layer measurements. A tip vortex was generated in the test section using a 60 degree, half-span delta wing with a five-centimeter half chord placed on the floor 20 cm upstream of the center of the optical access point. An additional 100 cm length of straight duct was

added behind the optical section to minimize the effect of downstream disturbances on the vortex in the optical section (see Figure 5.1).

Measurements were performed with the delta wing set to three different angles of attack: 5, 10, and 15 degrees; furthermore, for each angle of attack, three different freestream Mach numbers, 0.4, 0.5, and 0.6, were investigated. The test-section Mach number was set based on static and total pressure measurements made upstream of the delta wing. The test-section blockage, based on the frontal area of the wing, ranged from 7% to 23%, depending on the angle of attack of the wing.

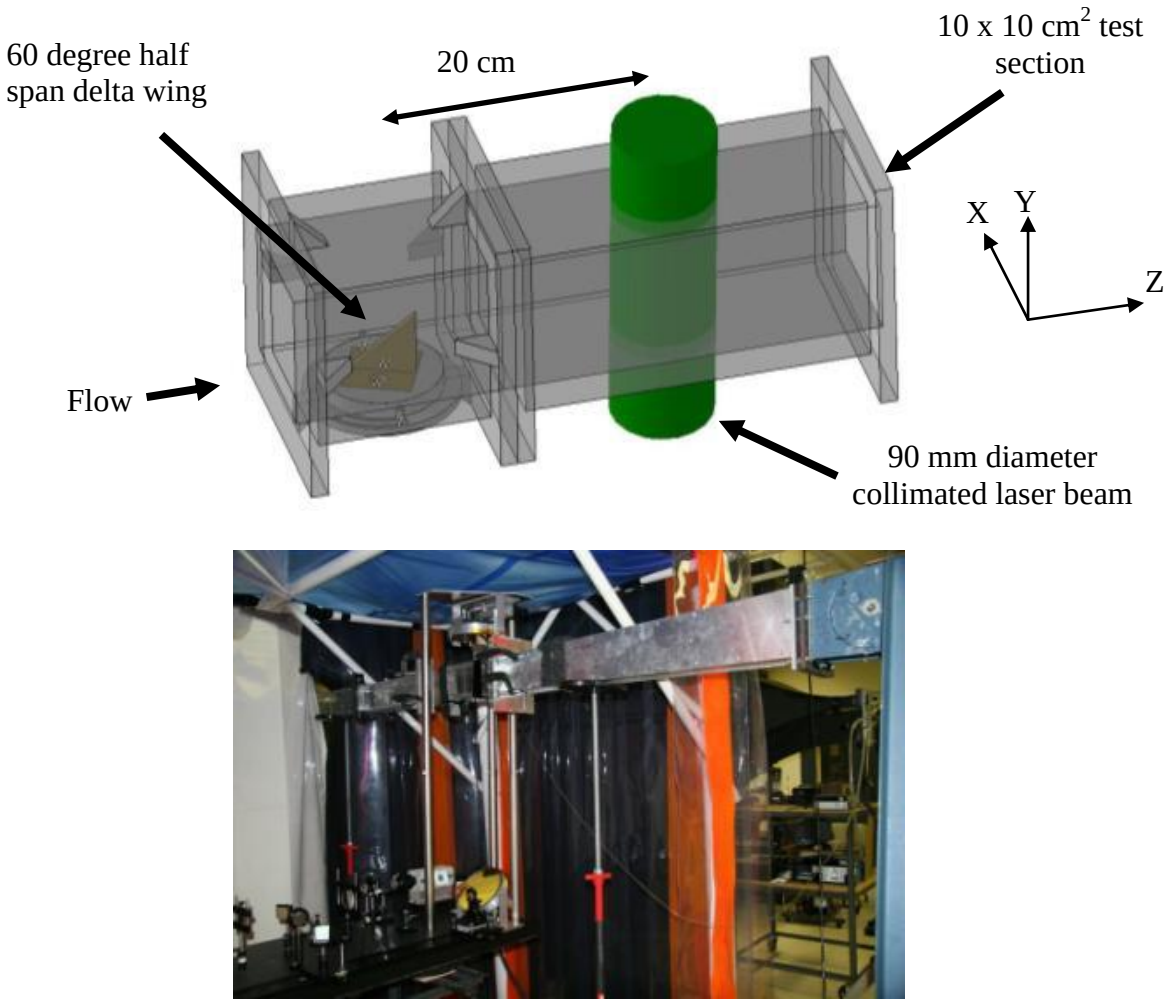

Figure 5.1: Experimental setup in the 10 x 10 cm^2 indraft tunnel for optical and flow field measurements of a 60 degree half-span delta wing model.

Initial tests began with flow visualization to establish the location and verify the generation of a vortex. On hot humid days, the vortex could be visualized from condensation within the low-pressure core of the vortex. Figure 5.2 shows two pictures of the vortex in the tunnel rendered visible from condensation. Note that the vortex is shifted slightly to the right of center in Figure 5.2; in the next section, this offset will also be seen in the wavefront data.

View From the Side View From the Bottom

Figure 5.2: Vortex behind a 60 degree half-span delta wing, rendered visible from condensation.

5.1.1. Shack-Hartmann Wavefront Measurements

A Shack-Hartmann sensor was used to measure the wavefront distortion on a 90 mm diameter collimated beam that was passed through the vortex downstream of the delta wing (see Figure 5.1). The beam was created using a pulsed laser with a 5x parabolic-mirror beam expander. During each test, 200 independent “snapshots” of the beam wavefront were acquired at a nominal sampling frequency of 10 Hz.

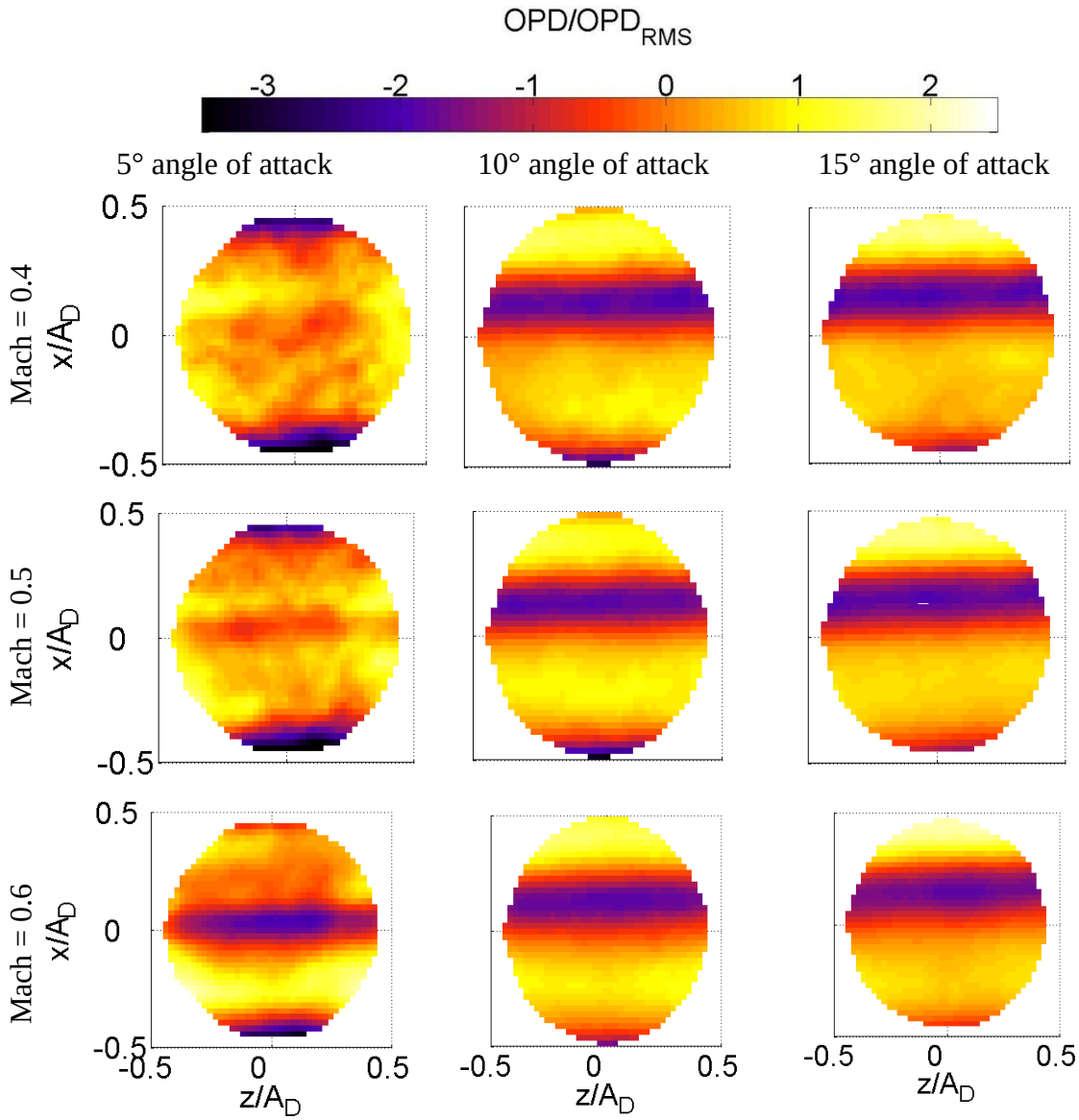

Figure 5.3: Mean experimental wavefront data of the vortex behind a 60-degree half-span delta wing.

To increase the signal-to-noise ratio of the measurements, the beam was double passed through the test section. Furthermore, to eliminate the effect of spurious index-of-refraction variations in the beam train that would also appear as noise, a set of relay optics was used to reimage the aberrated wavefront at the beam-expander parabolic mirror onto the wavefront sensor. Finally, Chauvenet's criterion (Coleman and Steele

1999), a statistical rejection method based on a normal distribution, was applied to each lenslet of the wavefront sensor to determine and eliminate any outliers from the wavefront data sets.

Figure 5.3 shows the time-average OPD from each data set with tip/tilt removed, normalized by the time-averaged spatial OPD_{RMS}. The trough at the center of each image is the wingtip vortex, where flow is from left to right. Additional insight into the character of the data can also be obtained from Figure 5.4 which shows instantaneous wavefronts acquired at Mach 0.6. On the left of Figure 5.4 is the mean wavefront shown in Figure 5.3, while the center plot in Figure 5.4 shows the frame (out of the 200 frames used to compute the average) with the smallest OPD_{RMS}; the plot on the right shows the frame with the largest OPD_{RMS}. As shown in Figure 5.3, when normalized by the OPD_{RMS}, the average wavefront spans a range from approximately a minimum OPD/OPD_{RMS} of -3 at the center of the vortex to a maximum OPD/OPD_{RMS} of +3 outside the vortex. As such, the experimental OPD data shown in Figure 5.3 conform to the similarity condition of Eqs. (4.23) and (4.24).

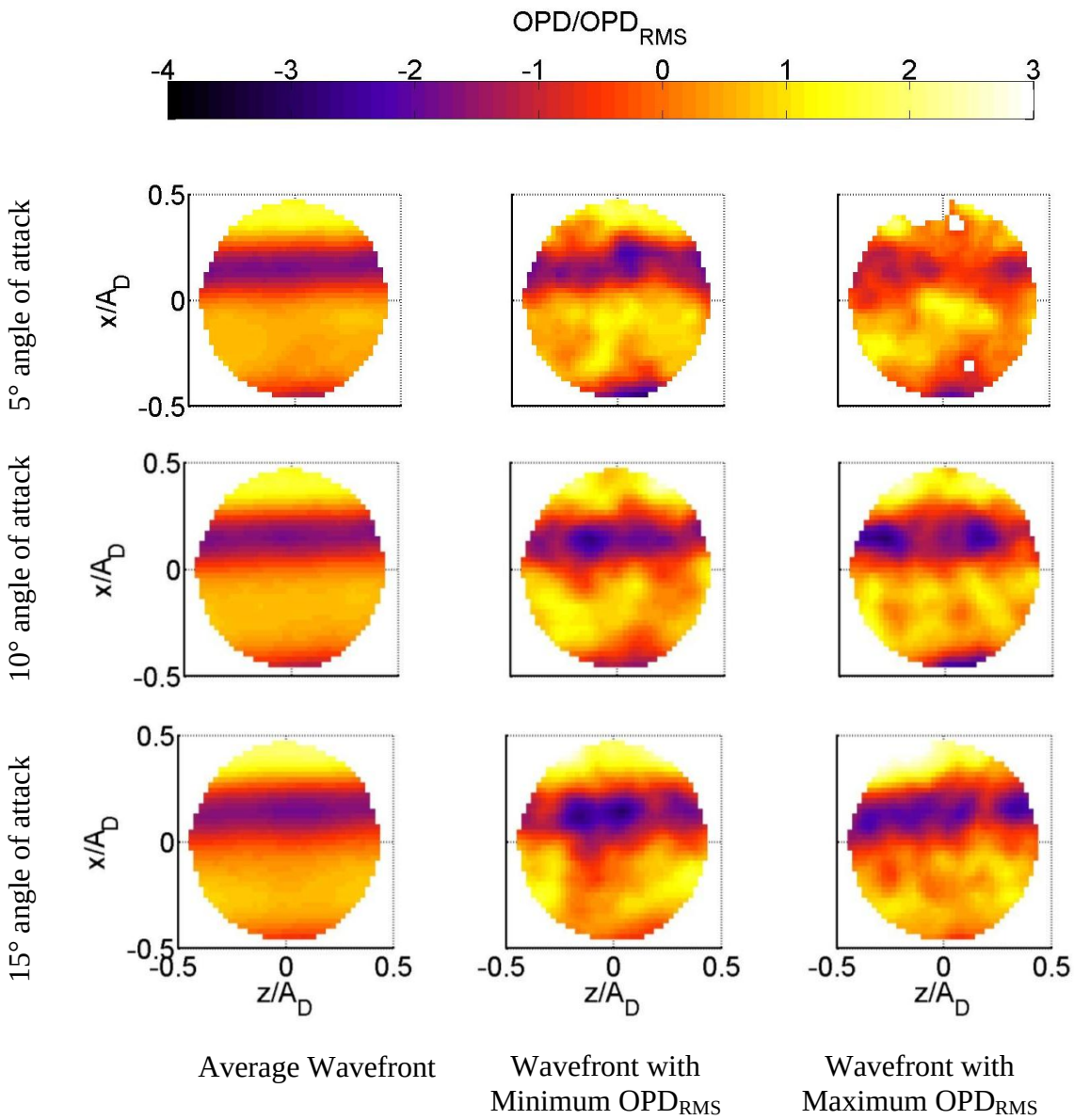

Figure 5.4: Mach 0.6 mean and instantaneous wavefronts behind a 60 delta wing.

5.1.2. Cross-wire Measurements

The velocity field at the location of the wavefront measurements was also measured using a cross-wire. To obtain all three velocity components behind the delta wing, the flow was surveyed twice with the cross-wire rotated by 90 degrees between

surveys; these data were then combined to obtain the three-dimensional velocity field using the method described in Huu Nho and Béguier (1995) for the mean components. All the hotwire data were taken at a freestream Mach number of 0.4 for wing angles of attack of 5, 10, and 15 degrees. The results of the cross-wire survey are plotted in Figure 5.5. The contours represent the w (i.e. streamwise) component, while the vectors represent the u and v components, normalized by $2\pi r_c/\Gamma$. The 15 degree case had a maximum normalized tangential velocity ratio, $2\pi r_c V_\theta/\Gamma$, of 0.7124, although for the 10 degree test case it was only 0.6325. For reference, the Lamb-Oseen vortex has a maximum normalized tangential velocity ratio of 0.7153.

The vortex core radius was calculated by determining the radial location of local maximum velocities in the measured velocity field, and computing the core radius as half that distance. Since hotwire data were only acquired at Mach 0.4, the core radius at Mach 0.5 and 0.6 was estimated by scaling from the radius measured at Mach 0.4 according to the square root of the time (see Section 3.3) for the flow to travel from the delta wing to the measurement location. The circulation strength was also calculated for each hotwire data set using both forms of Eq. (3.7) which showed good agreement. To estimate the circulation strength at Mach 0.5 and 0.6, the velocity-field data acquired at Mach 0.4 were scaled using:

$$V_{scaled} = \frac{V_{M=0.4}}{V_{\infty,M=0.4}} V_{\infty,newMach}, \tag{5.1}$$

and the circulation strength was then recalculated.

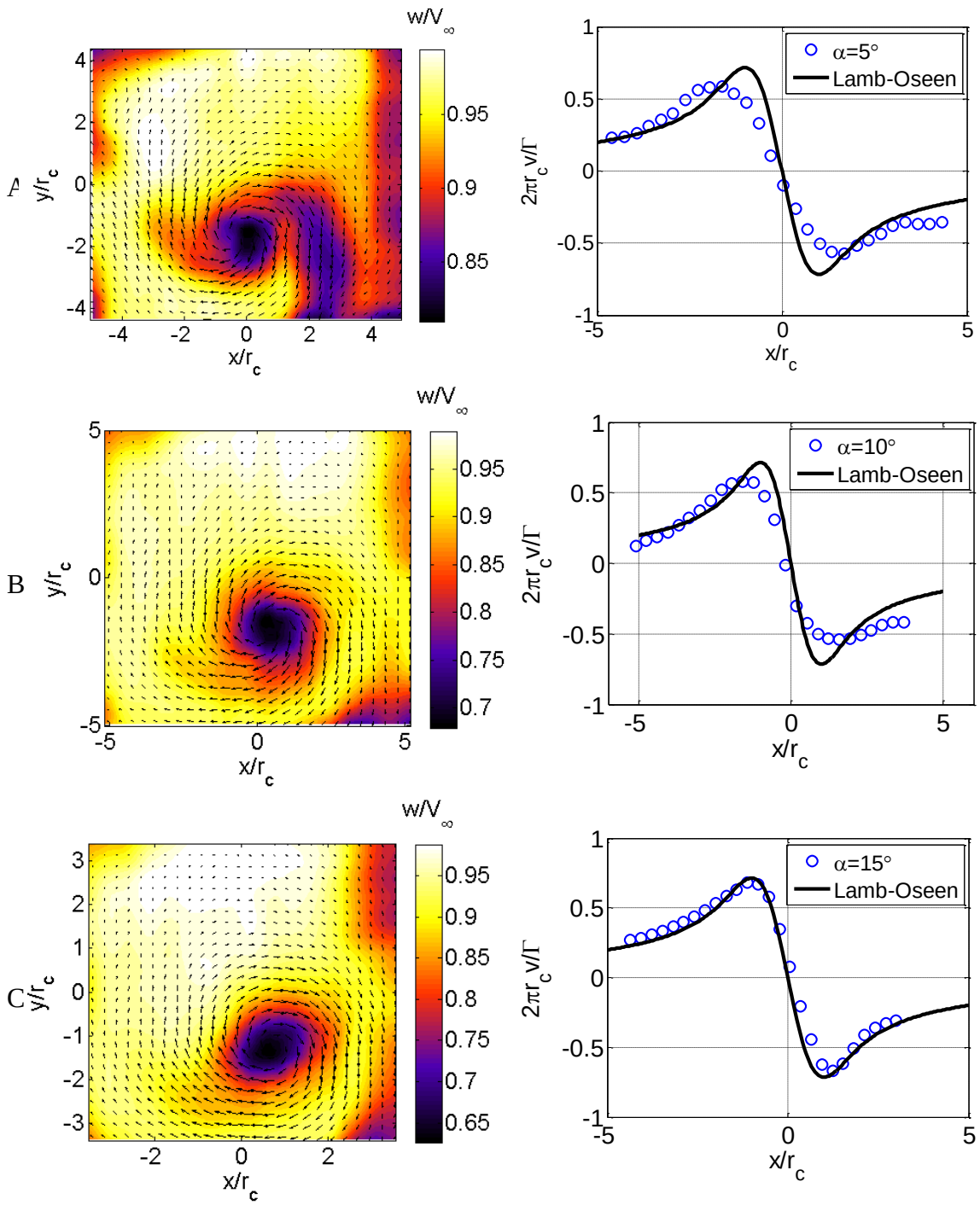

Figure 5.5: Normalized measured velocity field behind a half-span 60 degree delta wing at Mach 0.4. A) 5 degree angle of attack B) 10 degree angle of attack C) 15 degree angle of attack.

5.1.3. Comparison of Measured Wavefronts to the Weakly-Compressible Approach

The mean velocity field measured using the cross-wire was used to compute optical aberrations using the isentropic and WCM methods; these numerically-computed aberrations are compared to the experimentally-measured aberration in Figure 5.6. Figure 5.6 shows that both the isentropic and WCM methods produce a dip in OPD at the center of the test section where the vortex core was located (i.e. near $x \approx 0$), similar to the experimental result. For the isentropic method, the peak-to-valley magnitude of the OPD dip in the vortex core is slightly less than the experimental result, but matches the experiment fairly closely. On the other hand, the peak-to-valley magnitude of the OPD dip for the WCM method is larger than, but still within experimental error of the experimental result. The fact that the WCM method gives a much larger prediction for the OPD dip in the vortex core is the result of the significant axial-flow velocity component in the measured tip-vortex flow field, which is clearly visible in Figure 5.5. In particular, it was shown in Section 4.5.1 that the WCM computes a noticeably lower density and OPD in the vortex core when the tip-vortex flow field includes an axial-flow component; on the other hand, the isentropic method is insensitive to the axial-flow component.

Figure 5.6 also shows that the experimentally-measured OPD drops off at the edges of the test section; this drop-off in OPD at the edges of the test section is reproduced by the WCM method but not by the isentropic method. The drop-off in OPD at the edges of the test section is actually caused by the boundary layers on the test-section walls, which are clearly shown in Figure 5.5 by the reduced streamwise velocities at the edges of the measurement domain. As shown in, for example (Schlichting 2000),

the effect of the reduction in flow velocity within the boundary layer causes the temperature of the fluid in the boundary layer to be higher than the nominal flow temperature in the test section due to recovery effects. The drop-off in OPD near the test-section walls is therefore caused by the higher temperature and concomitant reduced density in the boundary layer, and is therefore produced by a different kind of mechanism (i.e. temperature variations) than the dip in OPD at the vortex core, which is primarily produced by a reduction in pressure and density (Ponder *et al*. 2010). As such, it is not surprising that the isentropic method does not reproduce the drop-off in OPD caused by the wall boundary layer, since the isentropic method was not designed to model either the non-isentropic character of the boundary layer or the increase in temperature in the boundary layer due to recovery effects. As for the WCM method, the fact that it appears to reproduce the experimentally-measured reduction in OPD in the boundary layer must also be considered fortuitous, since the WCM method was also not designed to accurately model boundary-layer flow. In particular, the WCM produces an increase in temperature in the boundary layer due to Eq. (4.10); however, Eq. (4.10) was incorporated into the WCM method to model the kinds of temperature variations that occur within vortices as described by the Hilsch effect, not to model recovery temperature effects in boundary layers.

In summary, Figures 5.5 and 5.6 show that both the isentropic and WCM methods predict the measured aberration within experimental error. The WCM method slightly over-predicts the magnitude of the dip in OPD in the vortex core, and this over-prediction is caused by the adiabatic temperature approximation used in the WCM, Eq. (4.10), and how it acts on the measured axial-flow velocity component of the delta-wing tip vortex.

Furthermore, the fact that the WCM reproduces the measured trend of decreased OPD in the test-section boundary layer must be considered a fortuitous outcome since the WCM was not formulated to model the temperature recovery effect in compressible boundary layers. Further comparisons of the isentropic and WCM methods to experimental data are also shown in the following section.

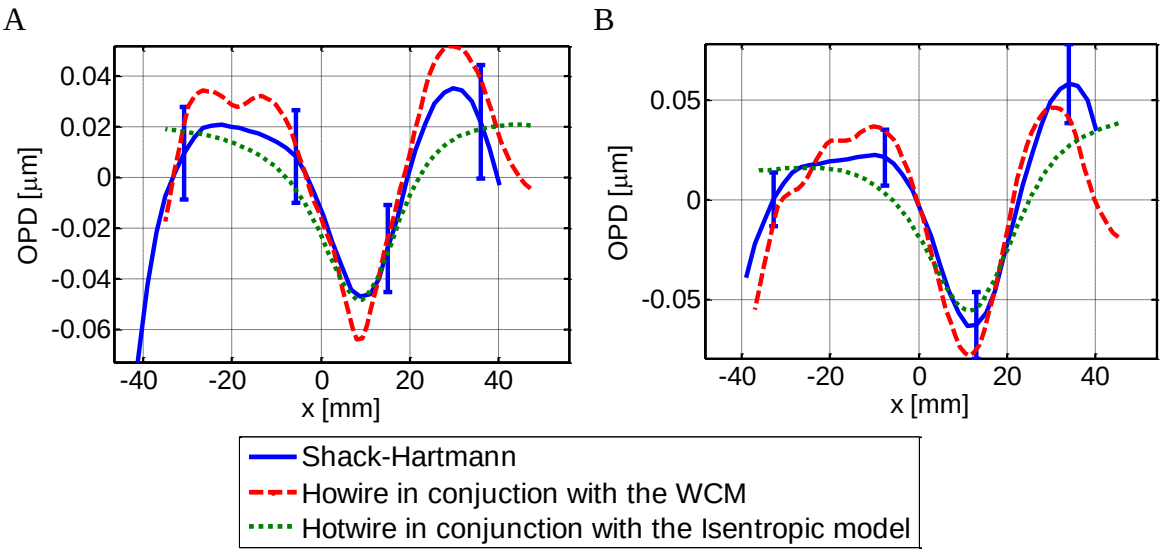

Figure 5.6: Comparison of measured wavefront data and wavefronts computed from cross-wire measurements behind the delta wing using the weakly compressible methods. A) 10 degree angle of attack B) 15 degree angle of attack. The errorbars are shown at four distinct points, but are representative of the error at all 31 points on the wavefront profile shown.

5.2. White Field, Dual NACA 0012 Experiment

For the 60-degree half span delta wing experiments described in Section 5.1, a large delta wing model was used in order to generate a vortex with sufficient strength for accurate optical measurements; because of this requirement, and the small area of the wind tunnel used, the model blockage reached 23 percent at the highest angle of attack tests. Furthermore, the data (both optical and hotwire) showed reduced streamwise

velocities near the test-section walls that were probably caused by the wall boundary layers. A second experiment was therefore performed in the much larger White Field wind tunnel to reduce the blockage and wall effects. The White Field subsonic wind tunnel is a closed-loop, temperature-controlled wind tunnel capable of freestream velocities of Mach 0.67 with an empty test section. The test section measures 91 cm x 91 cm and is 274.3 cm long. The reported freestream turbulence intensity is less than 0.05% (Cress 2010).

The vortex generator used in the White Field tests consisted of two identical NACA 0012 wings with chord lengths of 8.89 cm and spans of 44.45 cm that were joined at the quarter-chord locations and set at opposite angles of attack (see Figure 5.7). A steel rod running through the quarter chord location connected the wings, with a small gap between the ends of the two wings. The steel rod provided structural support to the wings, preventing bending, and reducing the lateral displacement of the wingtips due to wind loads (estimated up to 360 lb_f, Figure 5.8). Beyond the structural advantages of using two wings as configured above, this configuration also increased the circulation strength of the vortex and reduced vortex meander (Cheung 1993). The blockage based on frontal area of this two-wing vortex generator never exceeded 2.4 percent.

Figure 5.7: Photographs of the vortex generator for the White Field tests, consisting of two NACA 0012 wings at opposite angles of attack.

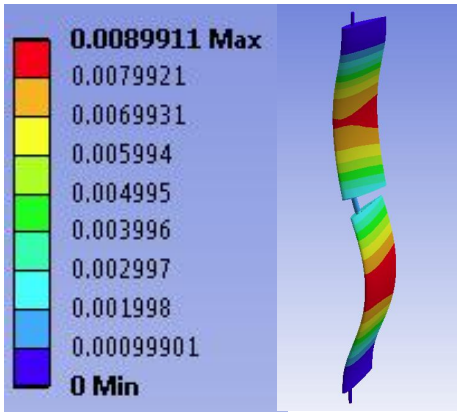

Figure 5.8: Displacement (inches) of the White Field vortex generator under maximum wind load of 360 lb_f of lift from each wing.

The data acquisition procedure was identical to the process used in the delta wing experiments described above. However, two notable changes were made in the equipment used in this experiment. The first was that the wavefront data were acquired using a high-speed Shack-Hartmann sensor built around a Photron FastCam high-speed CCD camera. This high-speed wavefront sensor not only had a significantly higher frame rate than the sensor used in the delta-wing experiments (5 kHz vs. 30 Hz), but it also had a higher spatial resolution (61 x 71 lenslets vs. 33 x 44 lenslets). The higher frame rate of the Photron FastCam helped to reduce "smearing" effects in the calculated mean wavefront images.

The second main difference in the test equipment used was that the cross-wire was replaced with a seven hole probe (SHP) to measure all three velocity components simultaneously (Gallington 1980). Aeroprobe Corporation built and calibrated the custom L-shaped probe specifically for this application. Calibrations were performed at Mach numbers of 0.3, 0.4, 0.5, and 0.6. At each Mach number, 2,295 data points were acquired spanning flow angles up to 65 degrees. Based on the calibrations, the reported

error in the velocity measurements was less than 2% of the nominal velocity. The probe pressures were measured using a ±5psid range Scanivalve ZOC33 module with a reported accuracy of 0.08% of full scale.

5.2.1. High-Speed Wavefront Measurements

The wavefront measurements were made approximately 172 cm (~20 chords lengths) downstream of the trailing edge of the vortex generator, using a 12.7 cm diameter beam that was double passed through the tip vortex. Reference wavefronts were taken with the tunnel off to remove any aberration in the beam not associated with density variations in the air from the running of the tunnel. Photographs of the optical setup are shown in Figure 5.9.

Figure 5.9: Optical setup for the White Field experiments.

Wavefronts were acquired with the vortex-generator wings set at an angle of attack of 6, 8, 10, 12, and 14 degrees. For each angle of attack, the freestream Mach number was initially set to approximately 0.1. The Mach number was then increased in ~0.05 increments until the wings began to shake. Using this approach, at 6 degrees, a maximum freestream Mach number of 0.6053 was achieved, while at 14 degrees, a maximum freestream Mach number of only 0.38 was achieved. Therefore, the Reynolds

number based on the vortex-generator chord ranged from 500,000 to 1,100,000 depending on the freestream velocity tested.

Figure 5.10 shows the average wavefronts at Mach 0.38 for all the tested angles of attack of the vortex generator. As with the delta-wing results shown in Figure 5.3, the dip in the mean OPD in Figure 5.10 is due to the tip vortex. On the other hand, due to the much larger test section in the White Field tunnel, the wavefronts in Figure 5.10 do not show any reduction in OPD near the edges due to the boundary layers on the test section walls, as can be seen in Figure 5.3. Furthermore, when normalized by the OPD_{RMS}, all of the mean wavefronts shown in Figure 5.10 span the approximate range in OPD/OPD_{RMS} of -3 to +3, further demonstrating the self-similar nature of the tip-vortex optical aberration (Eq. (4.23) and (4.24)).

The high-speed wavefront data shown in Figure 5.10 were acquired at a sampling frequency of 5 kHz over a sampling time of 0.2 seconds; this sampling time was not long enough to fully capture the low-frequency behavior of the tip vortex, such as the low-frequency "meandering" that tip-vortices usually exhibit. As such, in order to evaluate the effect of any low-frequency behavior of the tip vortex on the measured aberration, additional wavefront measurements were made using the same "slow" CLAS2D wavefront sensor used in the delta-wing tests. For these CLAS2D measurements, 200 "snapshots" of the wavefront were made at a nominal sampling frequency of 10 Hz, giving an overall sampling period of approximately 20 to 30 seconds. This sampling period is much longer than any expected time scale for low-frequency meander of the tip vortex so that the low-speed CLAS2D wavefront data accurately captures the behavior of the tip vortex at the larger time scales.

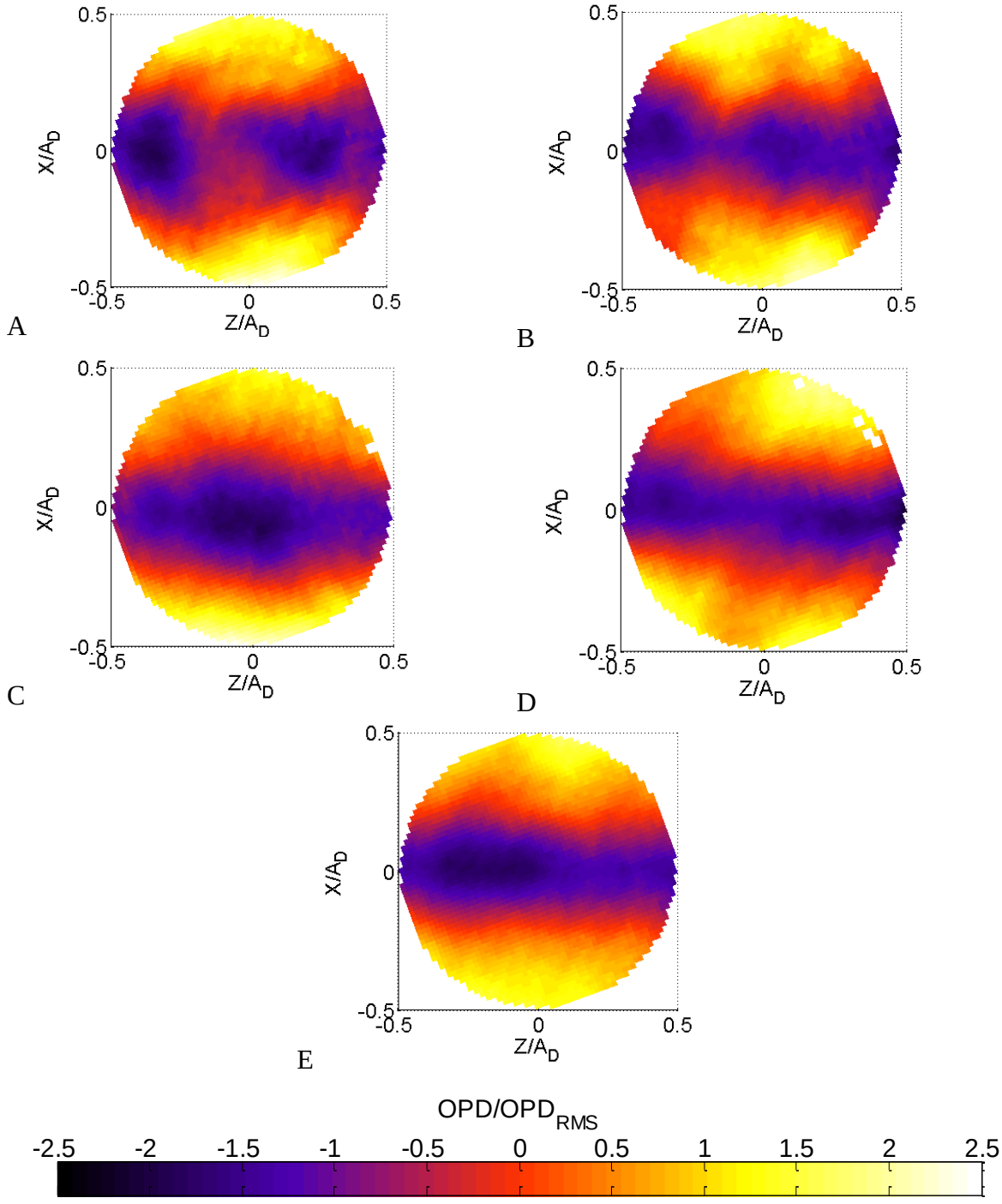

Figure 5.10: Average normalized OPD from the White Field experiment at a freestream Mach number of 0.38. The data is arranged by increasing angle of attack: A) 6°, B) 8°, C) 10°, D) 12°, and E) 14°.

A comparison of the mean, nondimensional wavefronts measured using the high- and low-speed wavefront sensors for similar test conditions is shown in Figure 5.11. The CLAS2D measurements were made at a freestream Mach number of 0.3344, which is slightly faster than the measurement made using the FastCam at a Mach number of 0.3201. The figure shows that the aberration measured using the low-speed CLAS2D wavefront sensor is slightly smaller in magnitude but wider in extent than the aberration measured using the high-speed sensor. These differences are most likely a consequence of the low-frequency meander of the vortex which was captured by the longer-period CLAS2D measurements; that is, shifting of the vortex position within the CLAS2D wavefront images would be expected to produce a lower peak OPD and a wider extent of optical aberration in the averaged result.

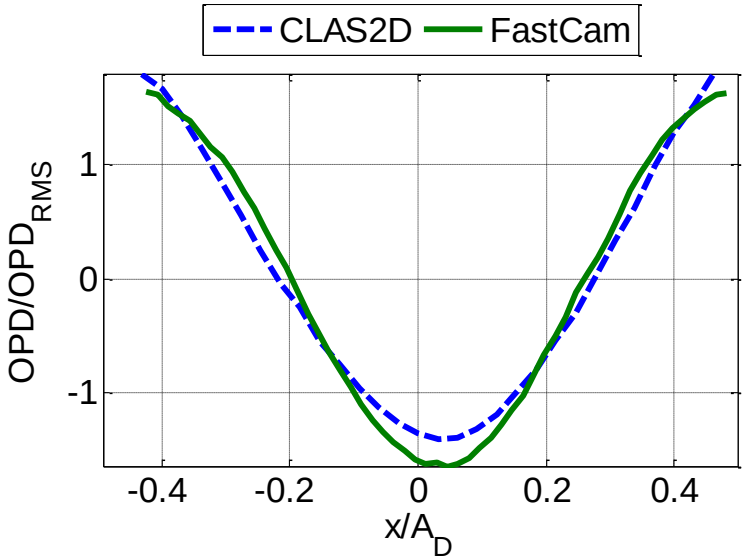

Figure 5.11: Comparison of mean, nondimensional wavefront profiles measured using the CLAS2D wavefront sensor and the high-speed wavefront sensor.

5.2.2. Seven Hole Probe (SHP) Velocity Measurements - White Field

In a separate tunnel entry, the velocity field of the tip vortex was measured at the same downstream location as the wavefront measurements using a seven hole probe (SHP) for freestream Mach numbers of 0.27 and 0.38. The probe was traversed over a 12.7 cm x 12.7 cm area using uniform steps of 0.42 cm in both directions, resulting in a 30 x 30 grid of data points. For each data point, the probe was positioned at the new location and, after waiting several seconds for the probe pressures to settle, the pressure of each port was recorded simultaneously along with the total and static pressures from an upstream pitot-static probe. The whole process of moving the probe and acquiring the data took ~21 seconds per data point, resulting in approximately 5.5 hours per flow-field mapping. Due to the long run time, especially at the higher Mach numbers, the tunnel was run for a short period of time before starting the actual data collection in order to stabilize the tunnel at a temperature where the tunnel cooling system could maintain a constant test-section temperature for extended periods. It should be noted that, due to the filtering effect that the long pressure tubes attached to the SHP had on the pressure measurements, no attempt was made to resolve the frequency content of the SHP data; rather, the velocity data acquired by the SHP were averaged over the 20 second sampling time used to acquire the data. This means that the time-averaged velocity data acquired with the SHP may have been affected by low-frequency meander of the vortex that could have occurred during the sampling period.

Figures 5.12 and 5.13 show the measured velocity and vorticity fields for different angles of attack of the vortex generator at freestream Mach numbers of 0.27 and 0.38 respectively. The circulation of the vortex in each case was found by integrating over the

vorticity fields (Eq. (3.7)) shown in Figures 5.12 and 5.13. The core radius was found by calculating the distance between the maximum and minimum u- and v-components. As discussed by Devenport *et al.* (1996), the circulation strength calculated from the time-averaged SHP data *is not* affected by low-frequency vortex wander, although the core radius and peak velocities will be over- and under-estimated respectively.

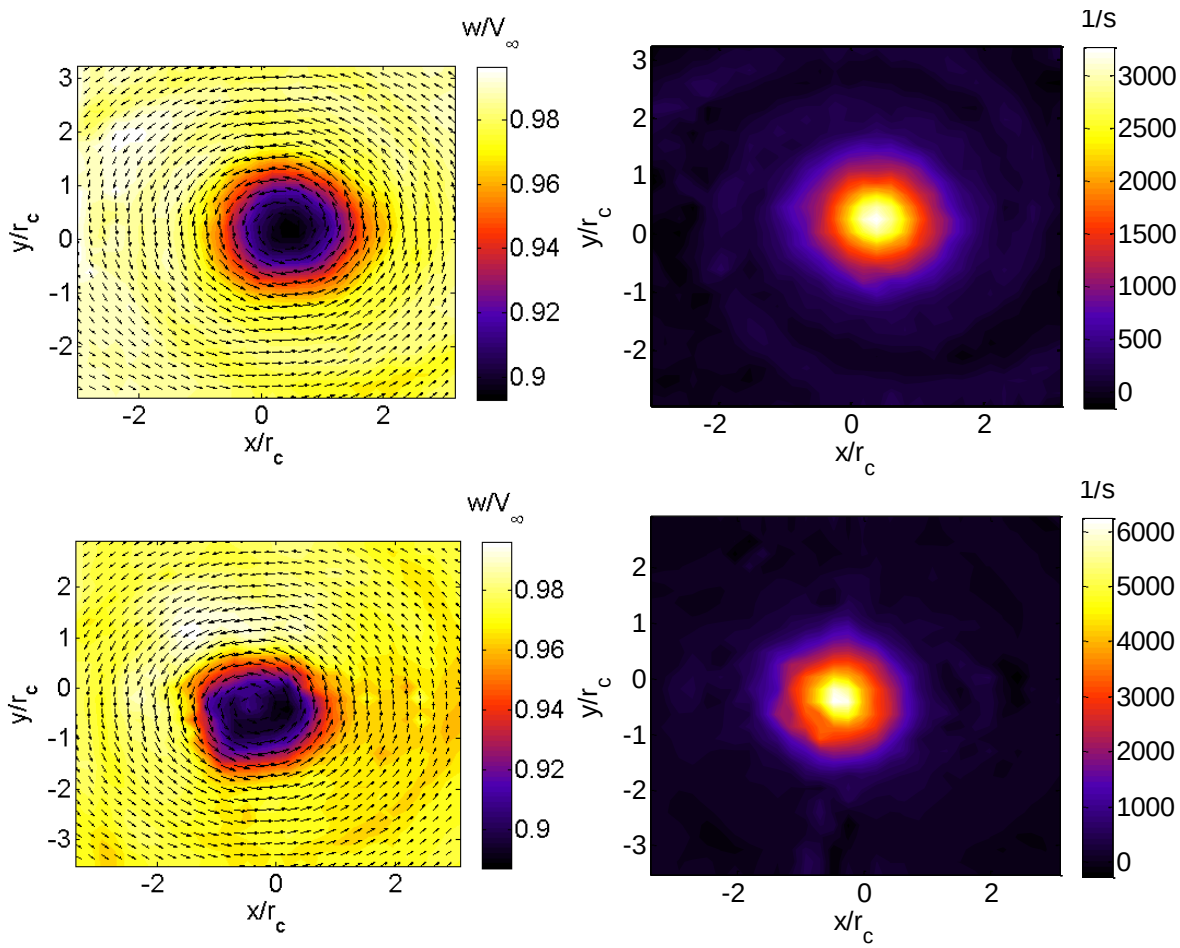

Figure 5.12: Velocity fields (left column) and corresponding vorticity fields (right column) downstream of the dual-wing vortex generator measured using a seven hole probe. The run conditions from top to bottom are: Mach 0.27 at α=8° and Mach 0.27 at α=14°.

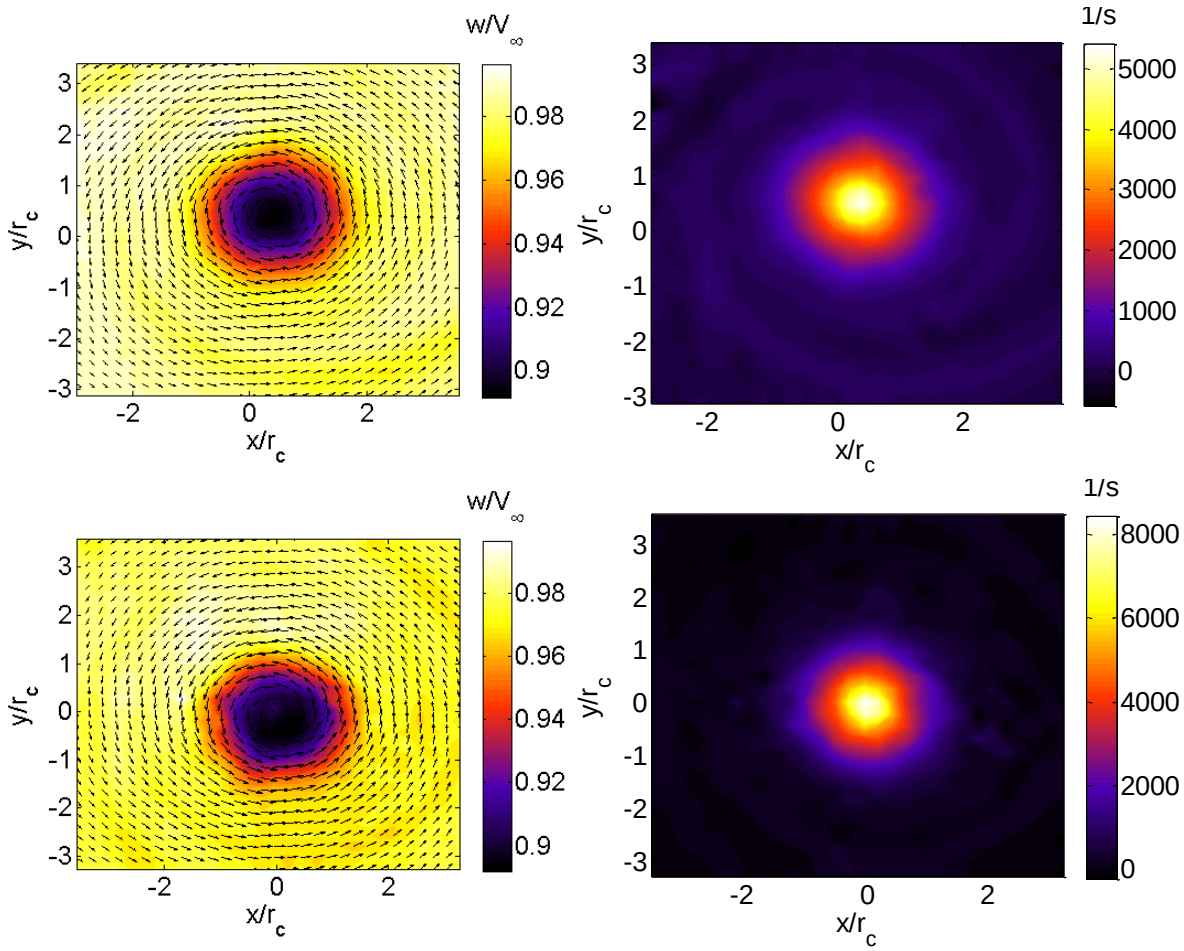

Figure 5.13: Velocity fields (left column) and corresponding vorticity fields (right column) downstream of the dual-wing vortex generator measured using a seven hole probe. The run conditions from top to bottom are: Mach 0.38 at α=8° and Mach 0.38 at α=12°.

The velocity profiles through the center of the vortex for each test point are shown in Figure 5.14 with the corresponding normalized velocities shown in Figure 5.15. The collapse of the data from Figure 5.14 onto a single curve in Figure 5.15 after normalization illustrates the self-similar nature of the vortex velocity profile. Figure 5.15 also shows a normalized Lamb-Oseen profile for comparison. The fact that the normalized peak velocities for the experimental data in Figure 5.15 are smaller than those

predicted by the Lamb-Oseen vortex model suggests that the experimental SHP data were affected by low-frequency vortex meander.

To investigate the supposition that the time-averaged SHP velocity profiles were affected by vortex meander, simulations of the effect of vortex meandering based on a bi-variant probability distribution function (Devenport *et al.* 1996; Iungo *et al.* 2009) were performed. In these simulations, the probability of the vortex wandering in any direction was assumed to be equal (eccentricity = 0.5), and the wandering amplitudes in the x- and y-direction were set to match the measured SHP data in the sense that the normalized peak tangential velocity of the simulation matched the average normalized peak velocity of the experimental data. The probability distribution function of the location of the center of the vortex is shown in Figure 5.16 and a comparison of the average and instantaneous velocity profiles is shown in Figure 5.17. It can be seen that the peak tangential velocity for the average profile in Figure 5.17 is noticeably reduced compared to the peak tangential velocity for the instantaneous profile, and that the magnitude of this reduction is similar to the magnitude of the reduction in the (time-averaged) experimental data compared to the instantaneous Lamb-Oseen profile in Figure 5.15.

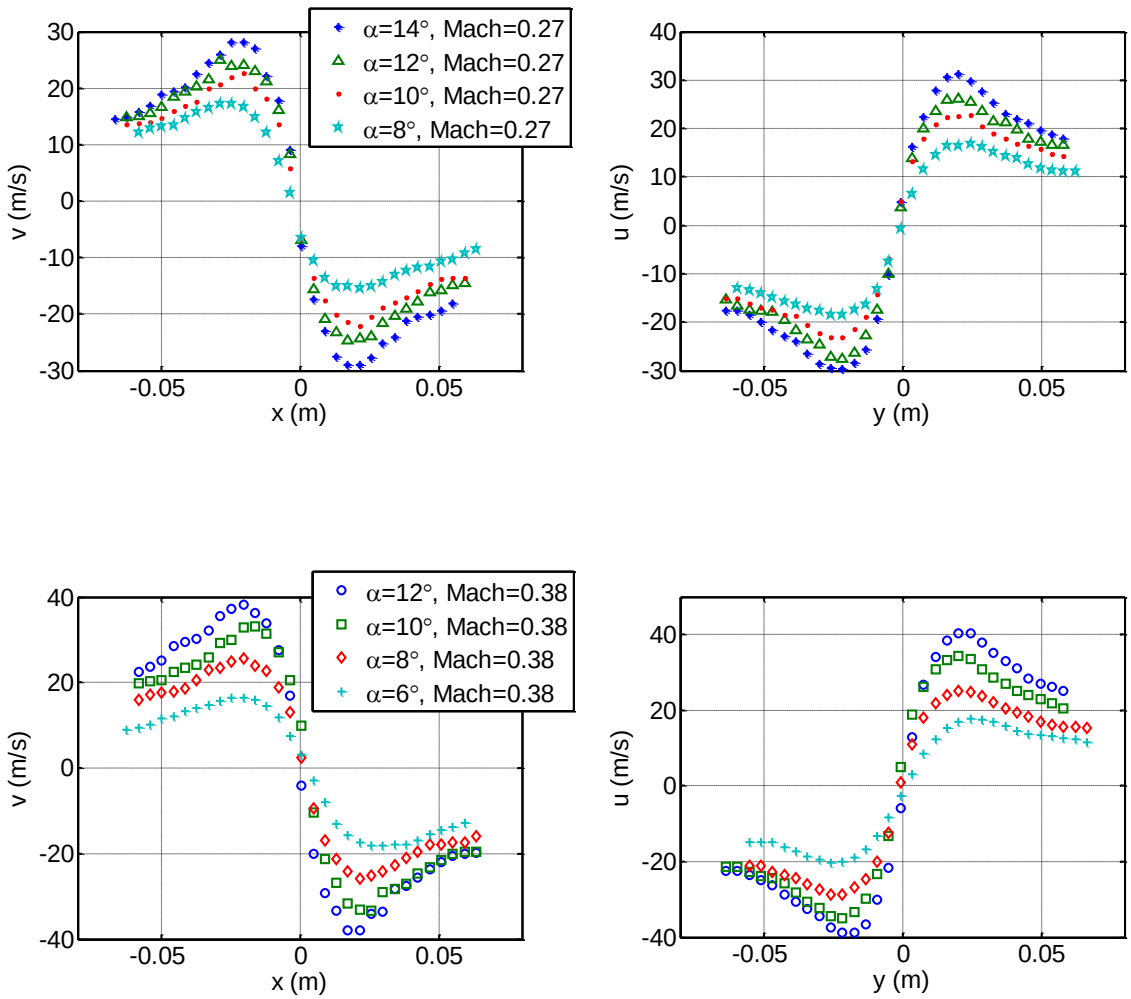

Figure 5.14: Measure SHP velocity profiles of the tip vortex from the dual-wing vortex generator.

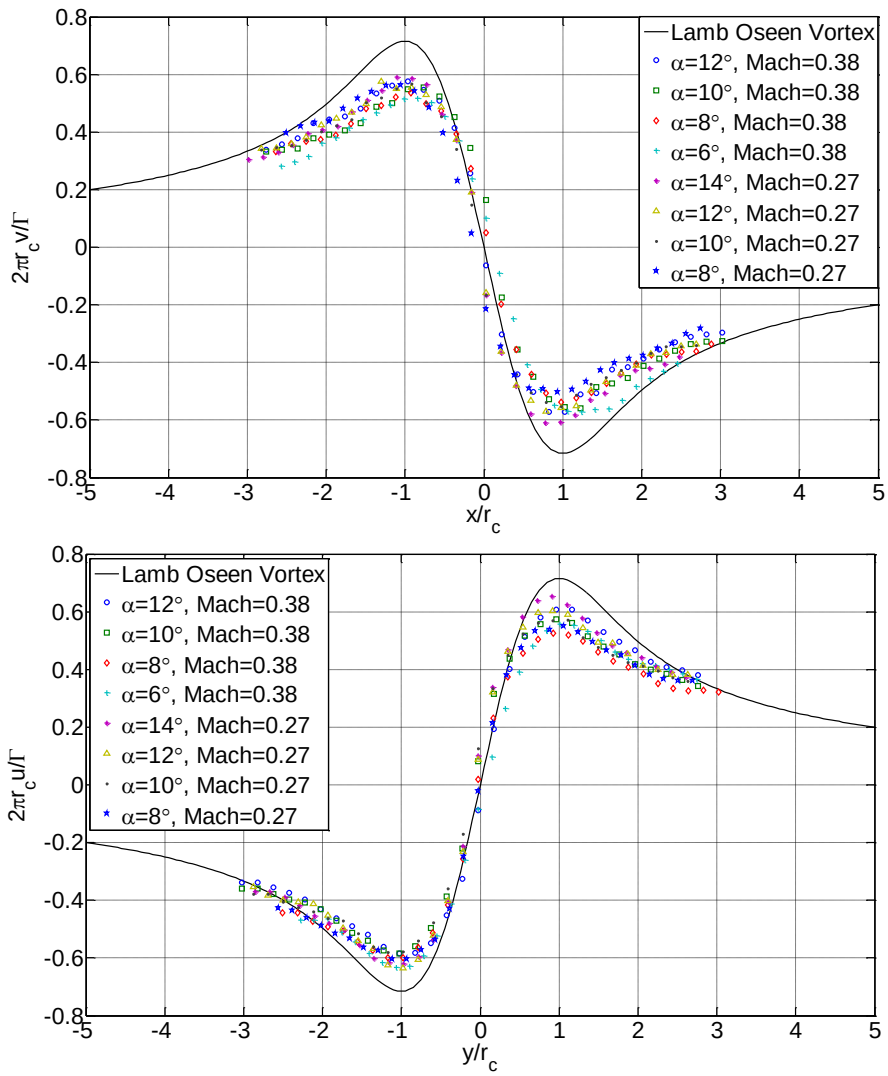

Figure 5.15: Normalized SHP velocity profiles compared to the Lamb-Oseen vortex.

As such, the comparison shown in Figure 5.17, which is based on a probabilistic model for vortex meander, further suggests that the time-averaged velocities measured by the SHP were artificially reduced below the instantaneous values by vortex meander. On the other hand, the wavefront data acquired using the high-speed wavefront sensor (Figure 5.10) were most likely not as strongly affected by vortex meander since the sampling period used to acquire the high-speed wavefront data was very short and no

probe interference is present. This means that, in order to compare the measured high-speed wavefronts with the wavefront predictions computed using the weakly-compressible approach, it is necessary to first correct the average velocity data to remove the effect of vortex meander. This was done by increasing the measured average velocity data shown in Figure 5.12 by the ratio of the instantaneous to the average velocities shown in Figure 5.17, or by approximately 18%.

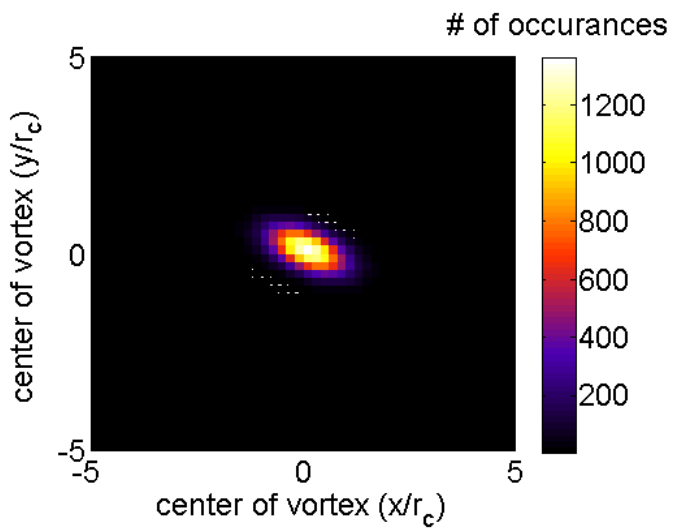

Figure 5.16: Bi-variant probability distribution function locating the center of the modeled Lamb-Oseen vortex in space.

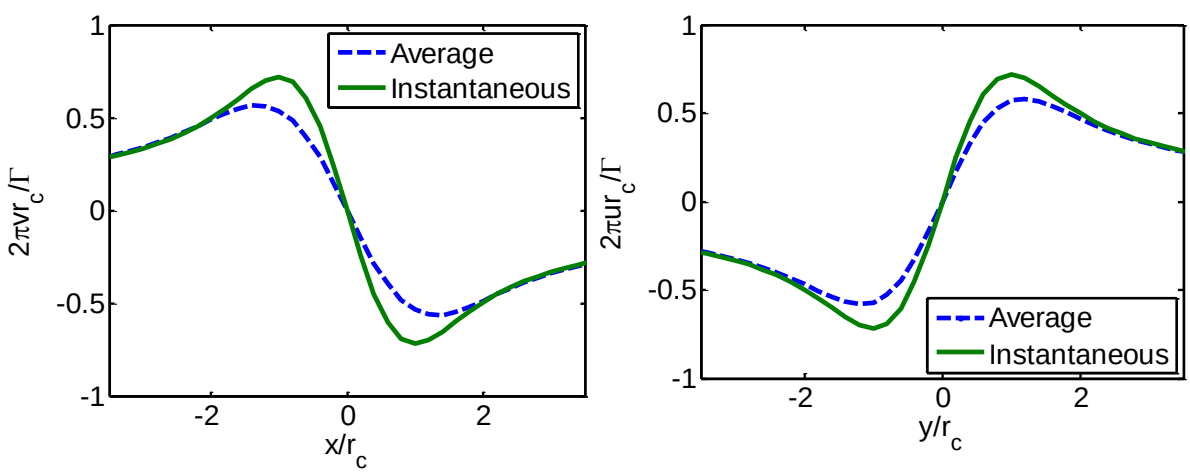

Figure 5.17: Comparison of average and instantaneous velocity profiles resulting from a simulation of the meander of a Lamb-Oseen vortex using the bi-variant probability distribution shown in Figure 5.16.

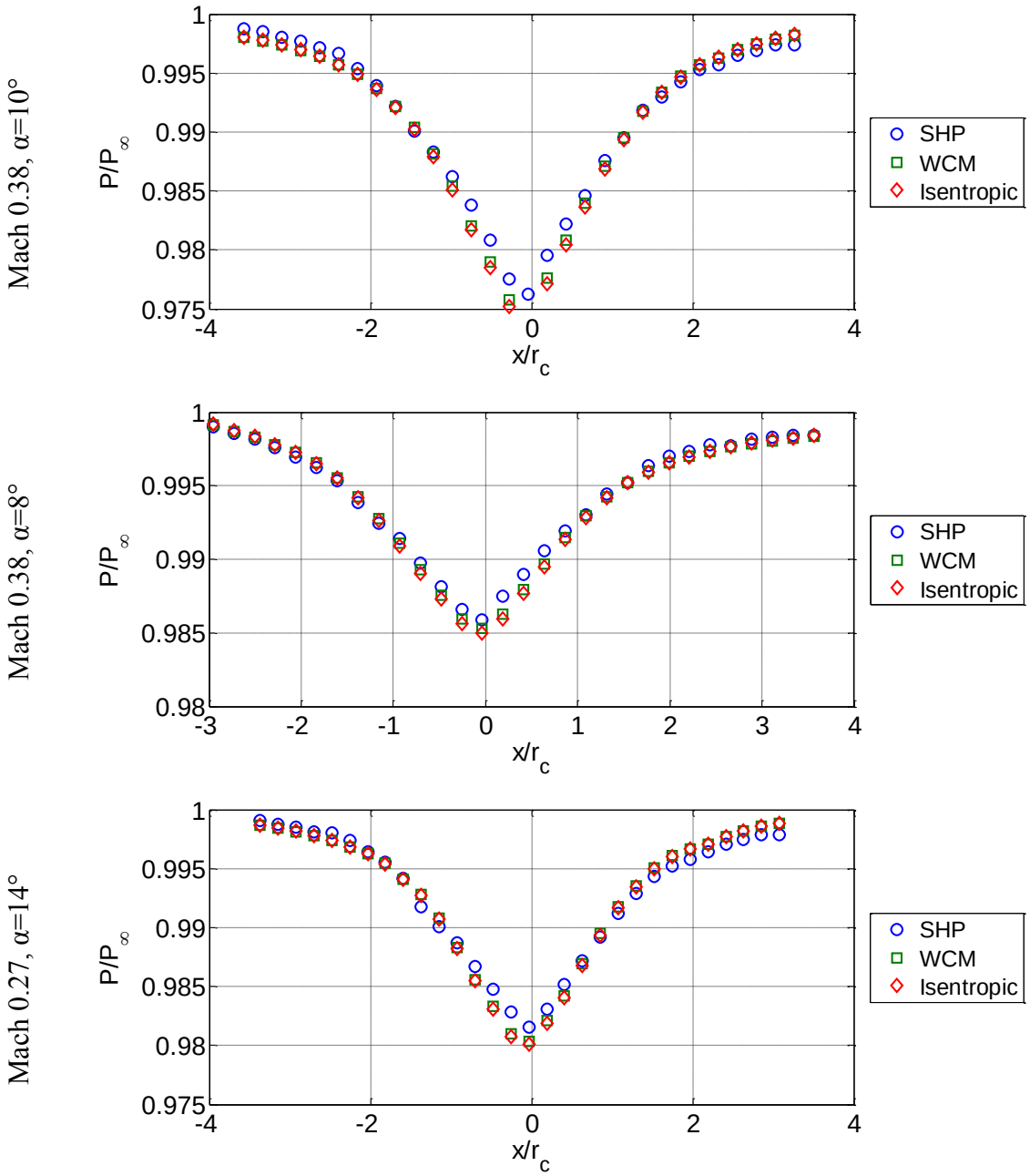

Figure 5.18: Comparison of the measured static pressure from the SHP to the WCM and isentropic thermodynamic overlays.

5.2.3. Comparison of Measured Wavefronts to the Weakly-Compressible Approach

Following the same procedure described in Section 5.1.3, the velocity data from the SHP was used with the WCM and the isentropic methods to compute optical aberrations which were then compared to the measured results. Figure 5.18 shows a comparison of the static pressure field measured using the SHP to the static pressures computed using the WCM and isentropic methods. Note that the time-averaged velocity data measured using the SHP were *not* corrected for vortex-meander effects prior to computing the isentropic and WCM results shown in Figure 5.18; this is because the SHP static pressure data shown in Figure 5.18 were also averaged over the sampling time of the SHP measurements, and so were also affected by vortex meander in the same way as the velocity data. As shown in Figure 5.18, both the isentropic and WCM models accurately capture the low pressure core of the vortex to within less than 2.7% of the measured value.

The density fields from the isentropic and WCM methods were then used to calculate the optical aberration on a beam of light propagating through the vortex, in this case, after first correcting the velocity field to account for vortex-wandering effects. Figure 5.19 shows a comparison of three of the test cases, Mach 0.38 with the vortex generator set at 10 degrees angle of attack, Mach 0.38 at 8 degrees, and Mach 0.27 at 14 degrees. The figure shows that, like the delta-wing results shown previously, both the isentropic and WCM methods match the measured data within experimental error. Furthermore, in all the cases shown in Figure 5.19, the WCM predicts a larger drop in OPD than the isentropic method; this is due to the axial velocity component of the measured velocity field, plotted in Figure 5.20, which was shown in Section 4.6.1 to

produce larger aberrations with the WCM method. The effect of the axial-flow component is better shown in Figure 5.21, which shows the result of a re-calculation of the WCM method with the axial-flow velocity component neglected; in this case, the WCM predicts a dip in OPD at the vortex core that is only slightly less than that predicted by the isentropic method.

In summary, like the delta-wing experiments shown in Section 5.1, the results of the White-Field tests further demonstrate that the optical aberration due to a tip vortex can be accurately modeled using the weakly-compressible approach. As such, the delta-wing and White-Field experiments demonstrate that the tip-vortex aberration originates primarily from the pressure and density well caused by the tip-vortex tangential flow field (and the SHP data of Figure 5.18 show direct experimental evidence for this pressure well). Both the delta-wing and White-Field experiments showed that the WCM method generally predicted an aberration magnitude that was larger than the experimentally-measured aberration, and that this was due to the interaction of the axial-flow component of the vortex flow field with the adiabatic temperature model incorporated into the WCM method, Eq. (4.10). Finally, in general, the experiments suggested that the predictions of the isentropic method slightly better match the measured OPD; however, both the isentropic and WCM predictions were within experimental error of the measured result.

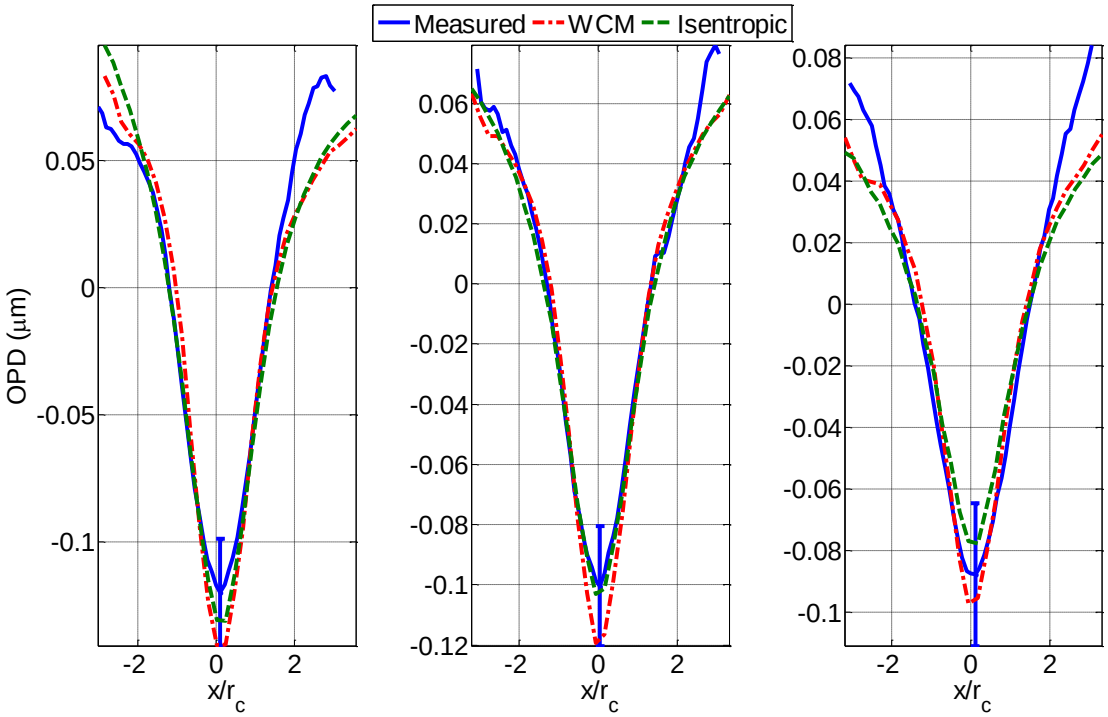

Figure 5.19: Comparison of the measured optical aberration from the Photron Fastcam Wavefront Sensor, the WCM, and isentropic thermodynamic overlays with wandering corrected velocity fields. The data correspond to Mach 0.38 at 10 degrees (left), Mach 0.38 at 8 degrees (center), and Mach 0.27 at 14 degrees (right).

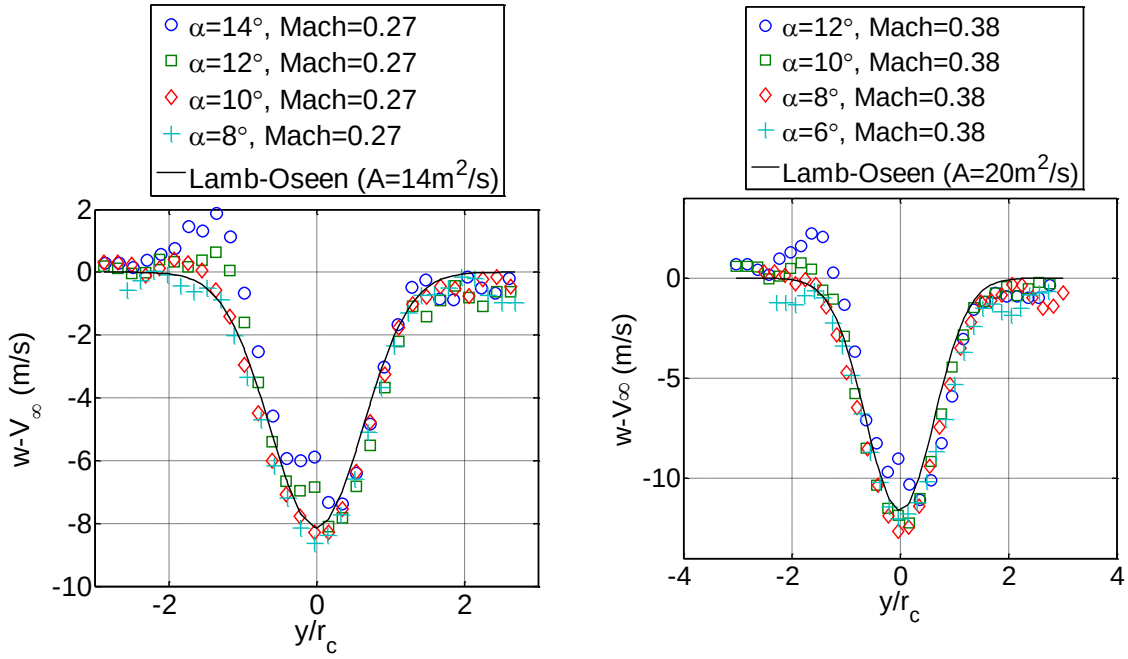

Figure 5.20: Axial velocity component from the SHP measurements.

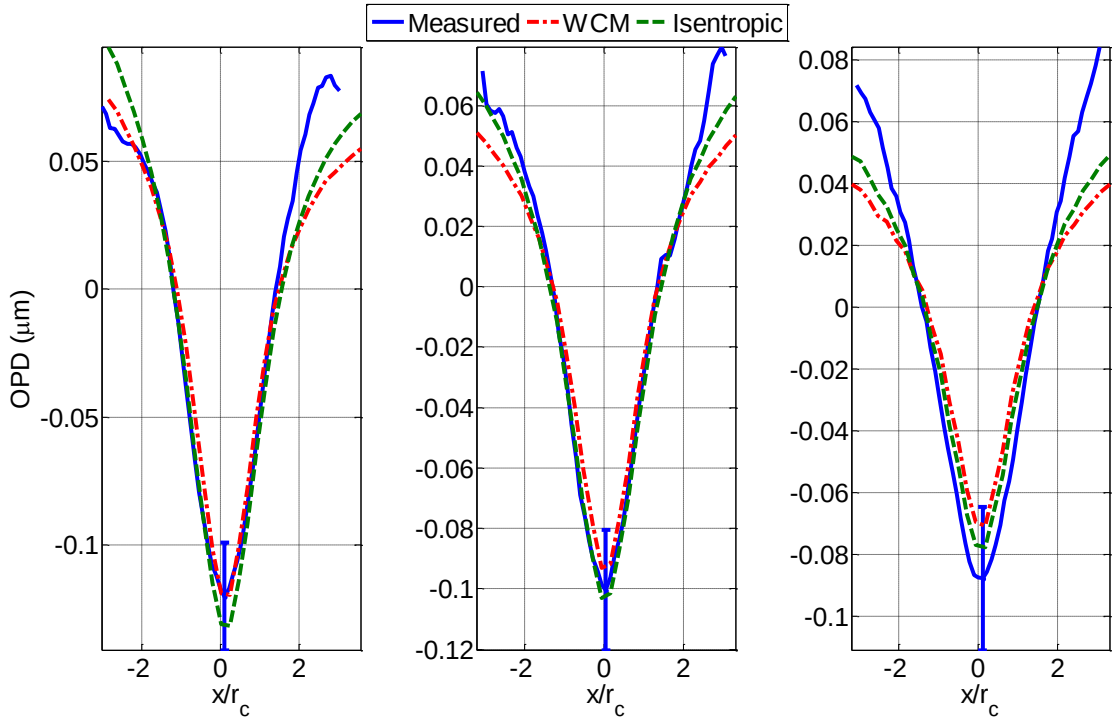

Figure 5.21: Comparison of the measured optical aberration from the Photron Fastcam Wavefront Sensor, the WCM, and isentropic thermodynamic overlays neglecting the axial velocity. The data correspond to Mach 0.38 at 10 degrees (left), Mach 0.38 at 8 degrees (center), and Mach 0.27 at 14 degrees (right).

5.3. Comparison of Experimental Results with the Scaling Relationship for OPD_{RMS}

The experimental data were also compared to the scaling relationship for OPD_{RMS} that was developed in Section 4.5. The experimental data were scaled by Eq. (4.23), which models only the vortex tangential-flow effect on the OPD_{RMS}. Figure 5.22 shows the data from the delta-wing experiments, data from the dual-wing tests acquired using the CLAS2D wavefront-sensor, and data from the dual-wing tests acquired using the high-speed wavefront sensor. Figure 5.22 also shows the results for the isentropic (dotted line) and WCM (dashed line) methods determined in Section 4.6 using the Lamb-Oseen velocity fields. The figure shows that all of the different experimental data sets collapse

onto a very narrow range when plotted against the scaling relationship of Eq. (4.23). The larger scatter in the data acquired using the high-speed wavefront sensor is most likely due to the short sampling period used for these data. The fact that Eq. (4.23), which models only the vortex tangential-flow effect, successfully collapses the data despite the axial-flow components that existed in both the delta-wing and dual-wing experiments, suggests that the optical aberration of a tip-vortex flow is insensitive to axial flow.

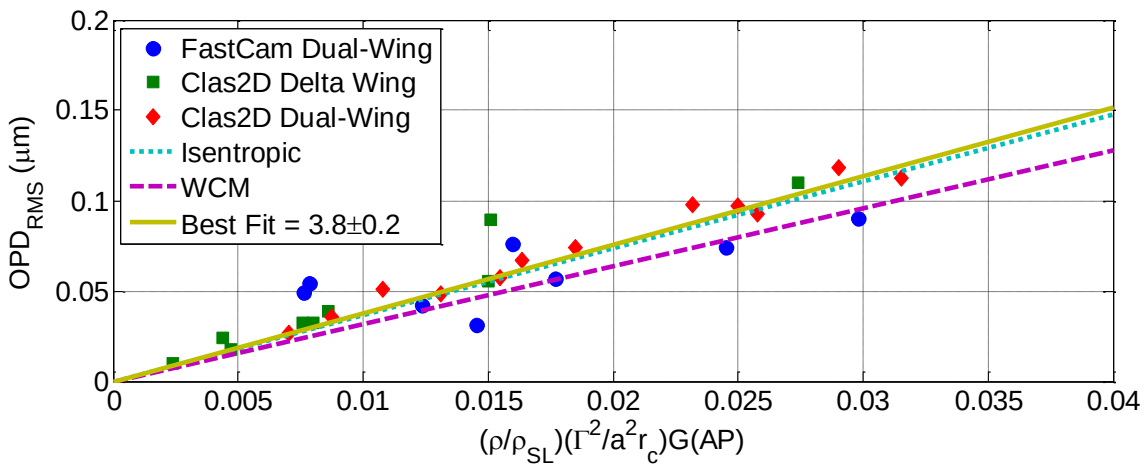

Figure 5.22: Comparison of the predicted scaling relationships (Eq. (4.23)) and the experimentally measured values with an estimated correction for vortex meander.

5.4. Detached Eddy Simulation - NACA0012 Flow Simulations

As a final investigation into the optical properties of a single wingtip vortex, Detached Eddy Simulations (DES) of a fixed wing were performed using Cobalt, a fully-compressible Navier-Stokes solver. For these calculations, the vortex was created using a three-dimensional rectangular wing. Boundary-layer calculations on the wing were performed using the Spalart and Allmaras (SARC) one-equation turbulence model, which makes corrections for rotation and streamline curvature effects (Kozlov *et al.* 2003). Figure 5.23 shows several different views of the computational grid that was used.

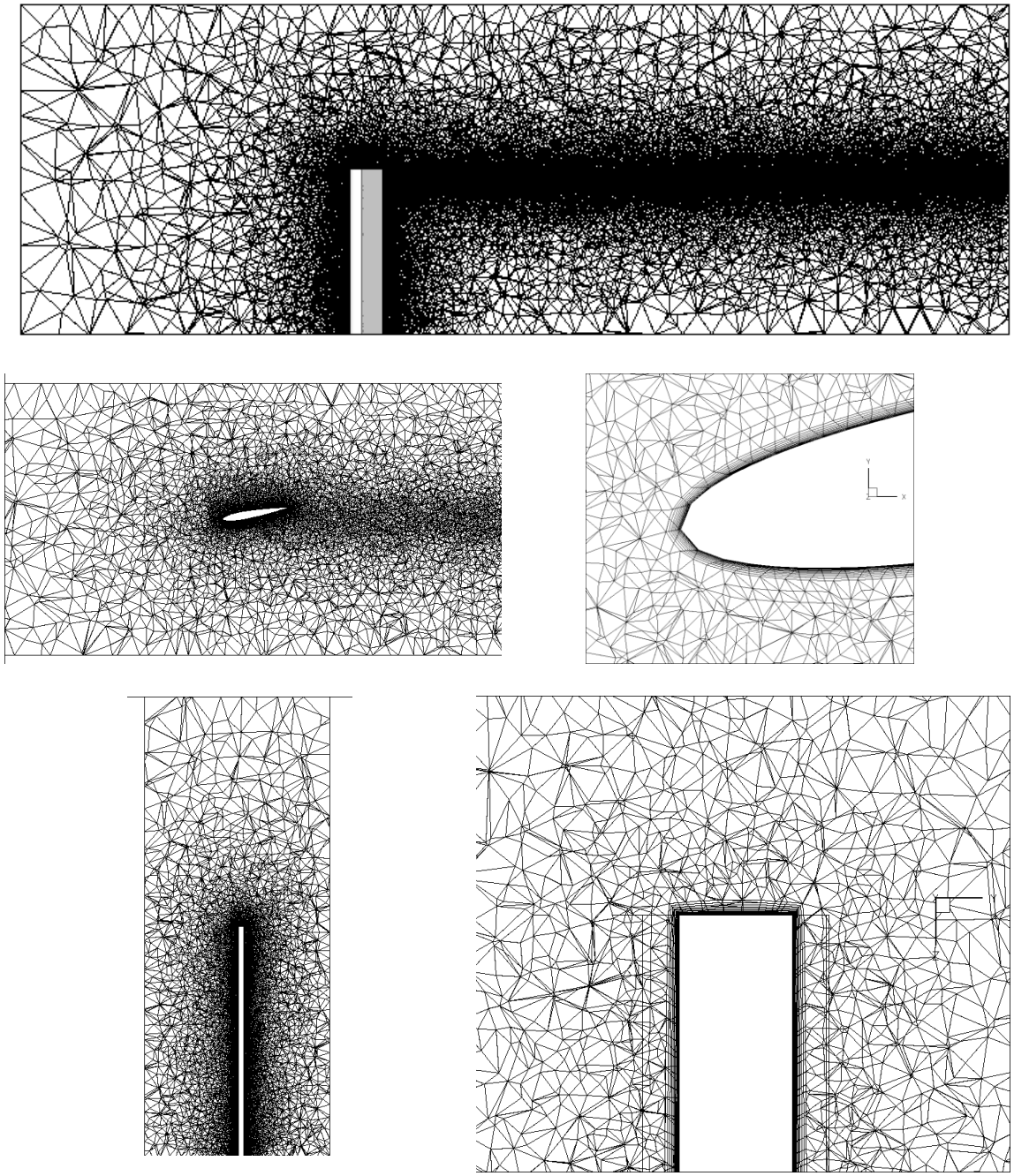

Figure 5.23: Grid around NACA 0012 resulting in 4.47 million grid points.

The wing had a NACA 0012 profile shape, chord of 0.5 m, span of 2.5 m, square tip, and was set at an angle of attack of 10 degrees. The wing was placed inside a simulated wind tunnel with dimensions of 15 m x 2 m x 5 m. The computational grid extended 10 chord lengths upstream of the wing and 20 chord lengths downstream of the wing. In order to simplify the computations, the boundary layer on the simulated wind-tunnel walls was not calculated in detail; rather, the walls of the wind tunnel were modeled using a slip boundary condition that prevented flow from crossing the walls, but still allowed a tangential velocity at the walls. The wing itself was modeled using an adiabatic no-slip wall condition, and the boundary layer on the wing was tripped to aid in keeping the flow attached.

A freestream Mach number of 0.4 was used in the calculation. Density contours of the flow field and an isosurface of the tip vortex are shown in Figure 5.24. Large density variations around the wing and the tip vortex are evident with the tip vortex being the primary density variation downstream of the wing, extending to the end of the computational domain. A slice of the computational domain normal to the flow at $x/c = 18$ was extracted and interpolated onto a uniform grid to calculate the circulation strength and core radius of the resulting tip vortex. The calculated circulation strength and core radius were then used to compute a Lamb-Oseen velocity profile, which is compared to the CFD-computed velocity profile in Figure 5.25. As shown, the Lamb-Oseen and CFD velocity profiles through the core match very well. The main differences between the CFD and Lamb-Oseen data occur outside the vortex core, likely caused by Reynolds-number effects (an increased tangential velocity outside the vortex core) and the effects of the edges of the CFD computational domain.

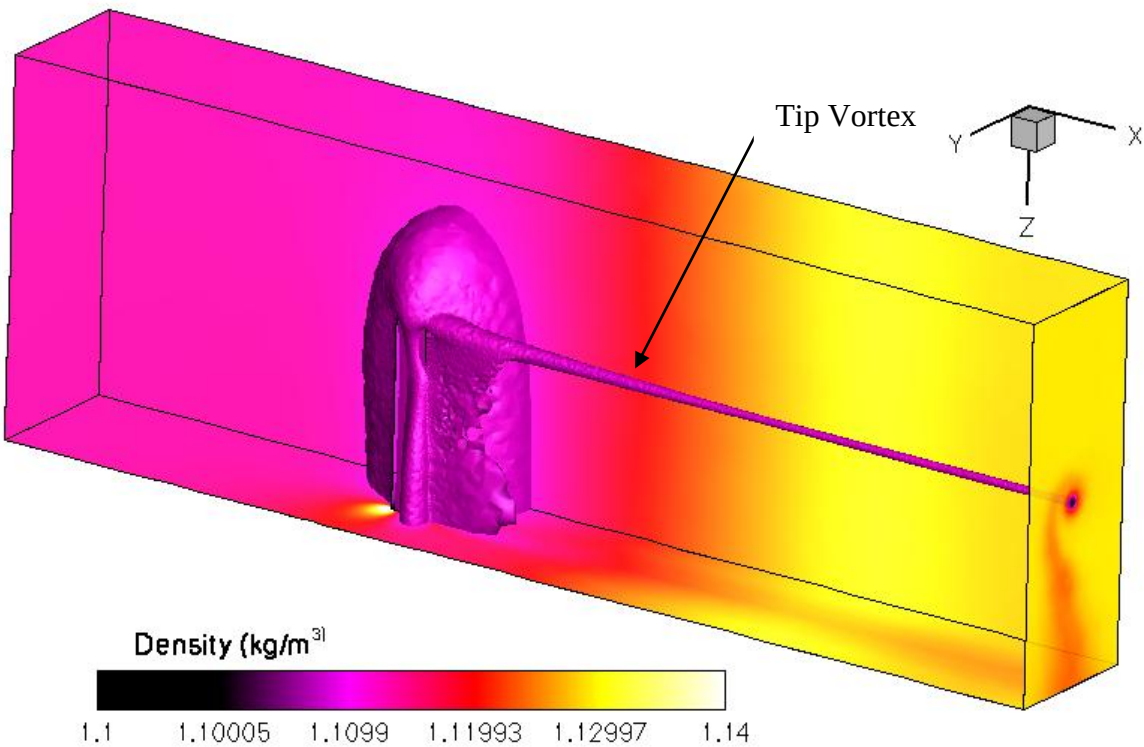

Figure 5.24: Density contour of the tip vortex from a NACA0012 at Mach 0.4 from DES calculations.

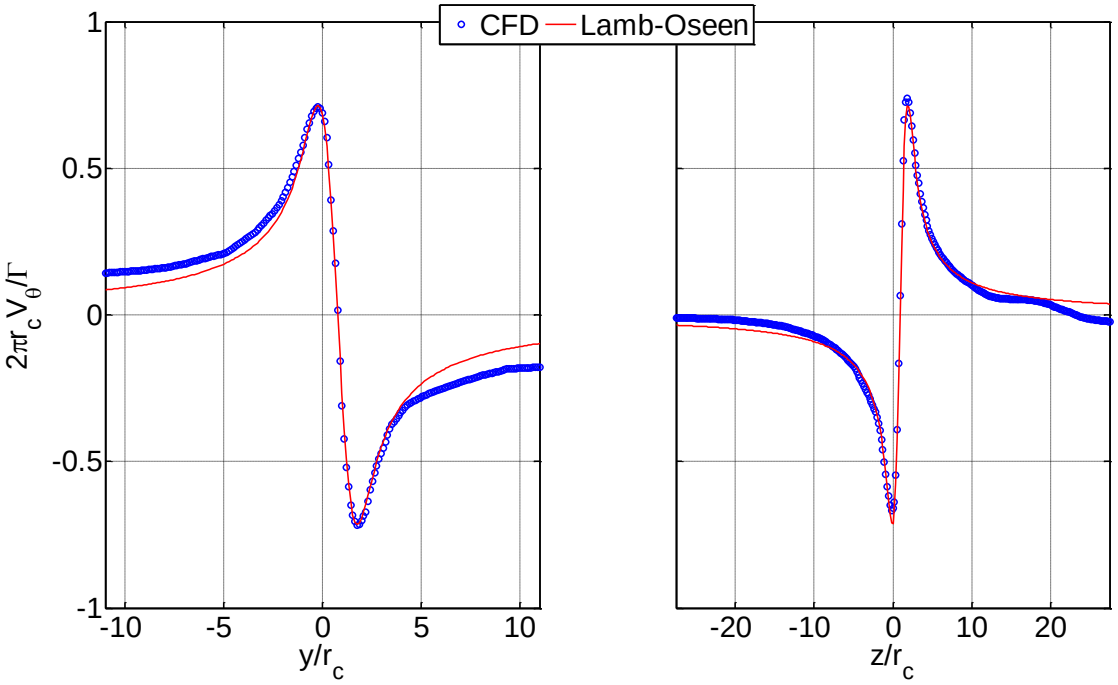

Figure 5.25: Comparison of the CFD results with the Lamb-Oseen vortex model at *x/c* = 18.

Figure 5.26 shows contour plots of the three velocity components at a location 18 chord lengths downstream of the wing. All of the velocity components in Figure 5.26 show the effect of the vortex; however, the streamwise component, *u*, clearly also shows the effect of the wake from the wing propagating into the sampling plane. This is evident from the axial deficit within the wake region. Due to wake blockage, the flow on the left and right side of the wake must accelerate to a velocity slightly greater than the freestream velocity to maintain continuity.

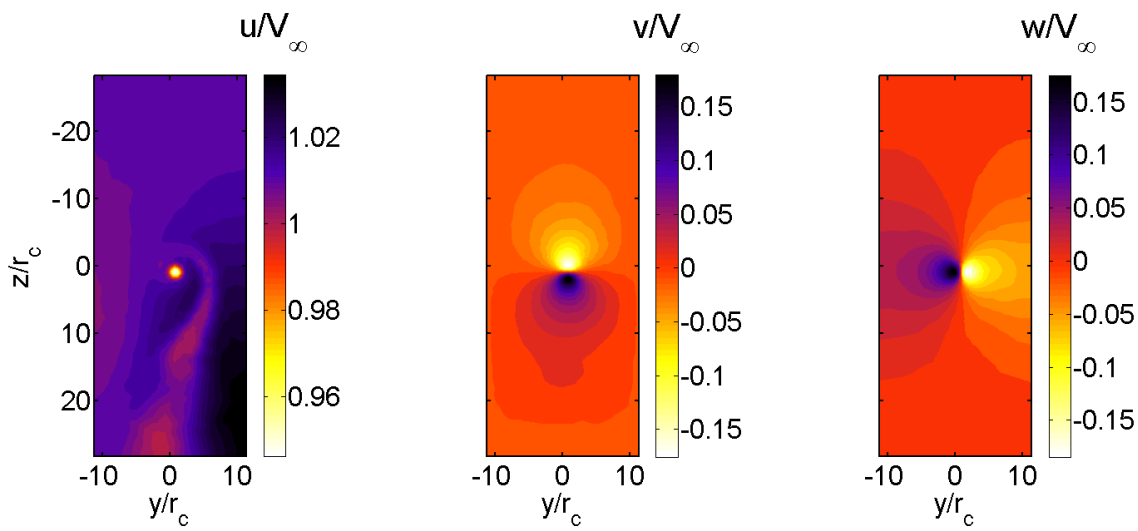

Figure 5.26: Contour plots of the three velocity components 18 chord lengths downstream of the leading edge of the wing.

Figure 5.27 shows the static thermodynamic properties at the same downstream location, while Figure 5.28 shows total properties. The figures show that, besides being influenced by the effect of the vortex, all of the static and total thermodynamic properties are also affected by the wake of the upstream wing. This wake region is the result of viscous effects on the upstream wing, such as the wing boundary layer or even partially separated flow regions, so that the total pressure and temperature within the wake are different from total properties in the surrounding flow or upstream of the wing. As such,

the value of the parameter $C_{T\text{-}P}$ is also different in the wake of the wing than in the surrounding flow, as shown in Figure 5.29.

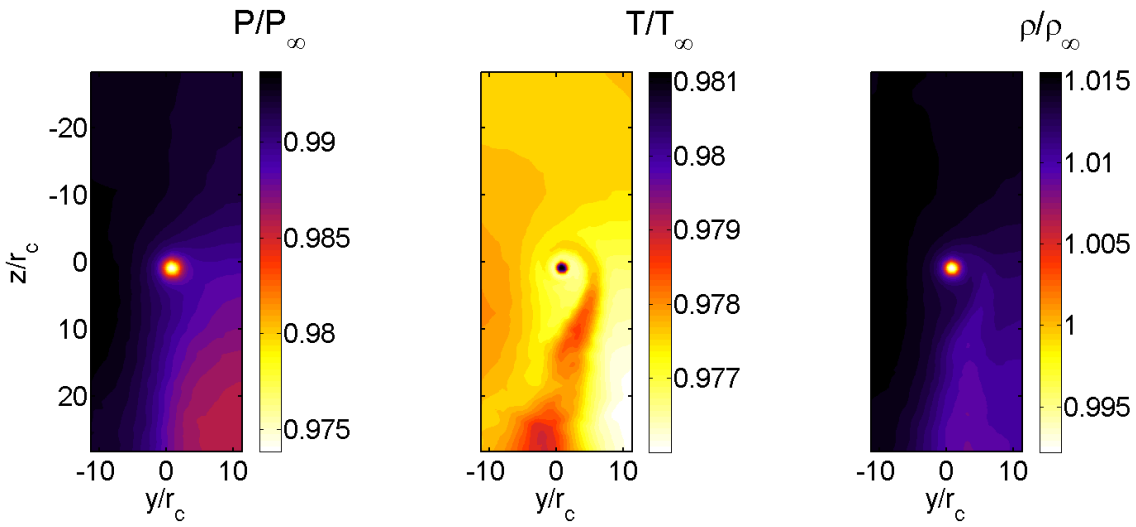

Figure 5.27: Contour plots of the static pressure, static temperature, and density 18 chord lengths downstream of the leading edge of the wing.

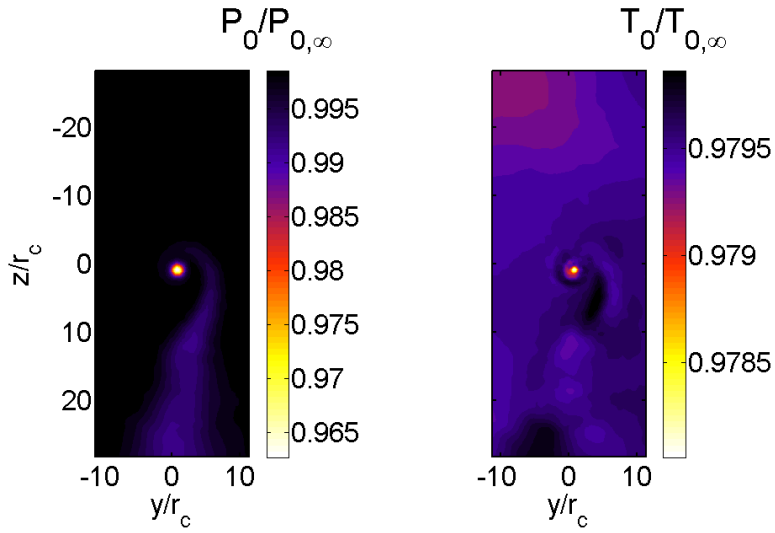

Figure 5.28: Contour plots of the total pressure and total temperature 18 chord lengths downstream of the leading edge of the wing.

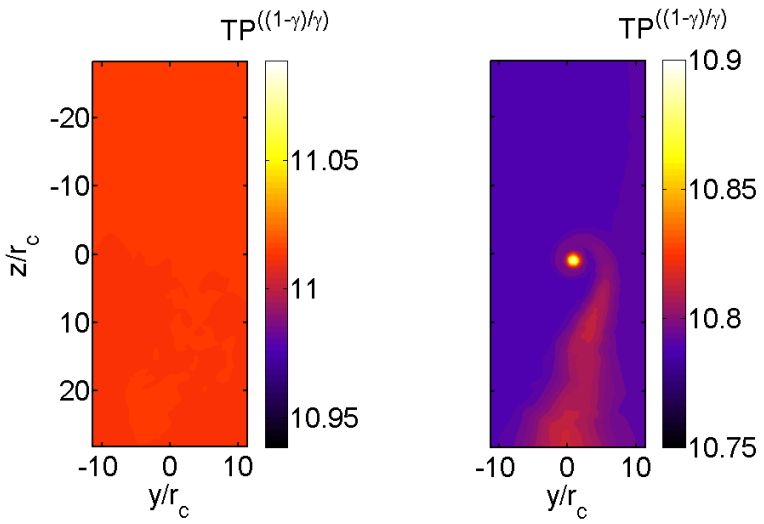

Figure 5.29: Contour plots of Eq. (4.12). The left plot is the calculated constant two chord lengths upstream of the wing, while the right plot is the calculated constant 18 chord lengths downstream of the leading edge of the wing.

The fact that the parameter $C_{T\text{-}P}$ is highly varying in the flow downstream of the wing violates assumptions used in the isentropic and WCM methods, that is, that the flow is either homentropic (isentropic method) or satisfies an adiabatic temperature model (WCM), and means that the weakly-compressible method will not be able to accurately predict the CFD results. This statement is confirmed by Figure 5.30, which shows that both the isentropic and WCM methods under predict the magnitude of the aberration compared to the CFD result. It is important to note that this situation is not produced by a failure in the physics contained in the weakly-compressible approach; in fact, if the pressure-temperature (i.e. $C_{T\text{-}P}$) variation shown in Figure 5.29 is used as an input into the weakly-compressible algorithm instead of the homentropic assumption, then the weakly-compressible algorithm actually produces an output that compares very closely to the CFD results (see Figure 5.31). The essential point is that the weakly-compressible

approaches outlined in Section 4.3 require a known velocity field as well as some kind of pressure-temperature model to permit the use of Eq. (4.8). In particular, the isentropic method assumes homentropic flow such that either side of Eq. (4.8) is assumed constant throughout the flow and can be determined from freestream conditions (Eq. (4.13)), while the WCM uses an adiabatic temperature model; however, more complex models that, for example, include the effects of an upstream wake would have to be generated by CFD or experimental studies.

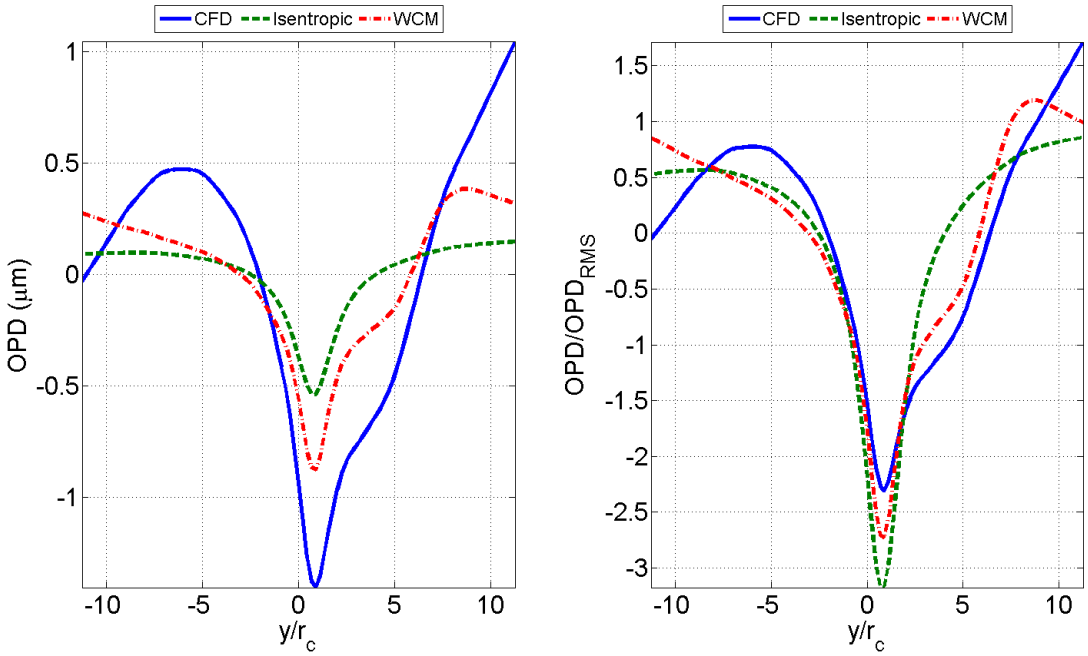

Figure 5.30: Comparison of the raw OPD (left) and normalized OPD (right) from the CFD, isentropic model, and WCM model.

The question therefore arises as to whether the homentropic or adiabatic-temperature models used in the isentropic and WCM methods are sufficient for the estimation of thermodynamic properties and optical effects in a helicopter vortex wake, or whether accurate optical predictions can only be achieved using CFD or experimental studies. There are several reasons that suggest that it should be possible to obtain

accurate results using the isentropic and WCM methods described in Section 4.3. First, for typical helicopter flight conditions, flow separation on the rotor blades is negligible and even boundary-layer thicknesses are small, suggesting that the CFD results shown in this section include a much stronger wake than would typically exist behind a helicopter rotor blade. Second, as already pointed out several times in this dissertation (e.g. Figure 4.5), the distance along the vortex from the tip of the generating rotor blade to the point where the vortex might enter the line of sight of a helicopter-mounted optical system is very large, and is several times larger than the 18 chord-length distance used in the CFD study. This longer distance would give more time for the effect of the rotor wake to diffuse thereby creating a more homentropic flow field. Finally, and most importantly, as shown in the preceding sections the weakly-compressible methods compared very well to experimental measurements of the optical effect of tip vortices. Furthermore, none of the White Field experimental data shows evidence of a wake from the upstream dual-wing vortex generator, despite the fact that the White Field data were acquired at almost exactly the same number of chord lengths downstream of the vortex generator as the CFD and were performed at a Reynolds number generally lower than that associated with helicopter flight; this observation also suggests that the CFD results shown in this section over-emphasize the effect of the wake. In summary, the CFD results shown in this section are useful in the sense that they serve as a reminder that the weakly-compressible methods described in Section 4.3 do not contain models to predict viscous wake regions; however, for typical helicopter flow fields, this is not a significant limitation since the effect of the viscous wake of the rotor blades on the flow field of the rotor vortex system is expected to be small.

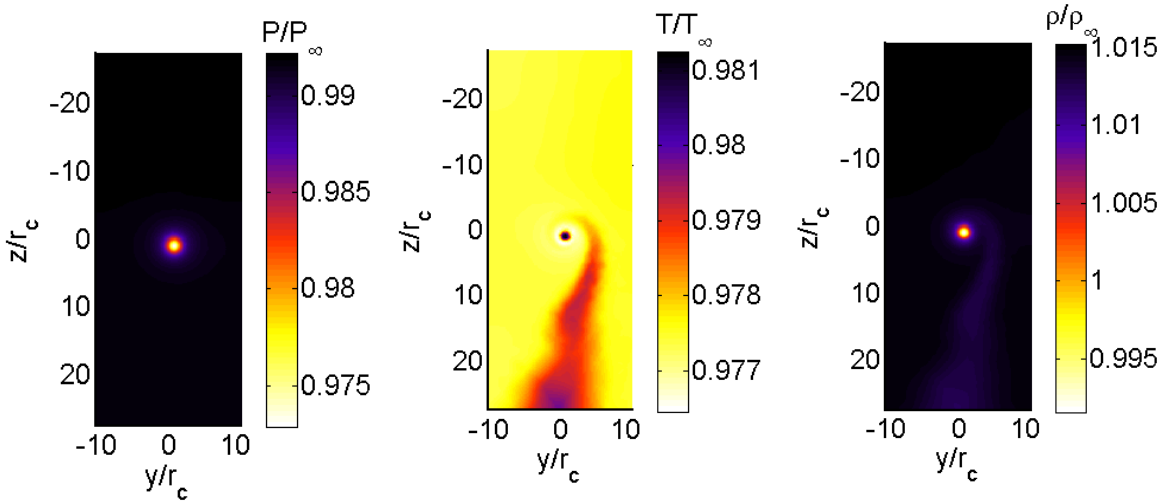

Figure 5.31: Weakly-compressible numerical method based on an iterated $C_{T\text{-}P}$ from the CFD.

5.5. Summary

The experimental data presented in this Chapter have confirmed the model for the optical effect of a tip vortex presented in the preceding two chapters. In particular, the experimental data have confirmed the existence of both a pressure well and a dip in OPD in the center of the tip vortex. Wavefront measurements of the optical effect of the tip vortex from both a delta-wing and dual-rectangular-wing vortex generator showed good agreement with computational methods developed in Chapter 4 that were based on the weakly-compressible assumption; these wavefront measurements also showed that the "isentropic" weakly-compressible method provided slightly better agreement with the experimental results although both the isentropic and WCM methods were within experimental uncertainty of the measured optical aberrations. In the remaining two chapters of this dissertation, computational methods and results are presented for the optical effect of the complete blade vortex system of a helicopter in hover and forward flight.

CHAPTER 6:

KINEMATICS OF HELICOPTER WAKES

In the preceding chapters, the aero-optical effect of a single tip vortex was investigated. As part of this investigation, a "weakly compressible" analysis approach was developed in which the flow field of the vortex was first computed and then subsequently used to compute the thermodynamic properties of the vortex. With the density field determined in this way, optical analysis methods described in Chapter 2 were used to estimate optical system performance. This approach was validated by experimental data.

In the following chapters, the same approach used to investigate the aero-optic effect of a single tip vortex is used to compute the aero-optic environment surrounding a full helicopter in flight. In this chapter, techniques are presented for computing the full velocity field around a helicopter. Chapter 7 presents the aero-optic results obtained by applying the weakly-compressible methods described in Chapter 4 to these velocity fields.

6.1. Vortex Model of the Rotor Wake

While the Lamb-Oseen vortex model is only valid for a single vortex in free space, it is a good approximation for wing-tip vortices. Helicopter flow fields, on the other hand, consist of many vortices shed from the rotor blades that form a helical pattern of vortex filaments below the rotor disc. While current computational power and numerical schemes are starting to make it possible to calculate the wake around a helicopter using full Navier-Stokes solvers, a much more common approach is to couple CFD with vortex methods. In this case, CFD is used to calculate the flow around the blade tip and the information is used by vortex methods to propagate the wake over a larger area.

6.1.1. Free-Vortex Methods

For free-vortex methods, the location of each vortex filament is calculated at discrete time steps. At every time step, each point on each vortex filament is displaced a distance equal to the induced velocity at that point multiplied by the time step. The induced velocity includes both self-induced effects as well as mutually-induced effects from other vortex filaments. Furthermore, vortex merging, ground effect, maneuverability, and even wind gusts can be accounted for. As explained in Leishman (Leishman 2000), these methods produce time-accurate solutions to the vorticity transport equation. In a slightly simplified form, the vorticity transport equation yields a partial, hyperbolic, first-order, quasi-linear differential equation:

$$\frac{\partial \vec{r}}{\partial \psi_w} + \frac{\partial \vec{r}}{\partial \Psi_\mathrm{b}} = \frac{1}{\Omega} \vec{V}_{loc}(\vec{r}, t). \tag{6.1}$$

In Eq. (6.1), ψ_b is the blade azimuthal location, ψ_w is the wake age, Ω is the rotor rotational frequency, and V_{loc} is the velocity at location r and instant t.

6.1.2. Prescribed Wake Methods

While free-vortex methods show good agreement with measured data, they are still computationally expensive. On the other hand, prescribed-wake methods avoid the difficulties of solving the vorticity transport equation directly by parametrically defining the location of the filaments. Typically, the models are developed from a mix of experimental and analytical methods. They are normally empirical in nature, providing a simple yet accurate model to real flow fields, and are significantly less computationally expensive than free-vortex methods.

Although using prescribed wake models results in a small loss in accuracy, they allow for rapid solutions with reduced computational expense, thereby facilitating parametric investigations of the helicopter flow field. For these reasons, a modified prescribed-wake analysis was used in this investigation to compute the location of the tip vortices in the wake as the first step towards estimating the aero-optical environment around a helicopter.

6.1.3. Landgrebe's Hovering Model

Leishman (Leishman 2000) provides a broad overview of different prescribed wake models. Each has its own strengths, weaknesses, and underlying assumptions. Throughout this dissertation, the helicopter vortex system for hover will be modeled using Landgrebe's model.

Landgrebe's model is an empirical model based on many different rotor configurations in hover. The model includes formulas to compute the locations of the tip vortices from both the inner and outer tips of the rotors, as well as vortices shed from any point along the span of the rotor. As pointed out in Leishman (2000), inclusion of both the tip and root vortices as well as the rotor spanwise vortex sheets is essential for rotor performance and induced-inflow calculations (Figure 6.1). On the other hand,

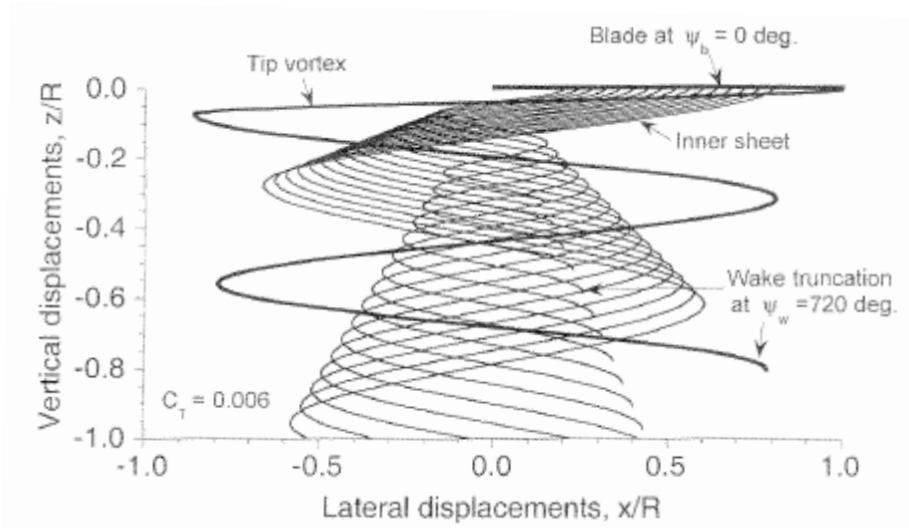

Figure 6.1: Schematic of Landgrebe's wake model showing the tip vortex filaments and inner vortex sheet (Leishman 2000).

shadowgraph and Schlieren images of helicopter wakes repeatedly indicate that only the tip vortices that roll up from the rotor's outer tip region show large density gradients and measureable optical effects (Figure 6.2). The reason why optical effects are confined to the rotor-tip vortices can be explained by the way the vortex wake rolls up underneath the helicopter rotor blades, shown schematically in Figure 6.3. In particular, Figure 6.3 shows that only the vorticity shed from approximately the outer 1/3rd of the blade rolls up

into strong vortex filaments (i.e. the “rotor-tip vortices”) and that this roll up occurs within a few chord lengths downstream of the rotor blade. On the other hand, Figure 6.3 shows that the vorticity shed from the inboard part of the rotor tends to propagate below the helicopter without coalescing into a strong vortex. As such, only the rolled-up vortices from the tip regions of the rotor blade have sufficient vorticity to create a strong optical aberration.

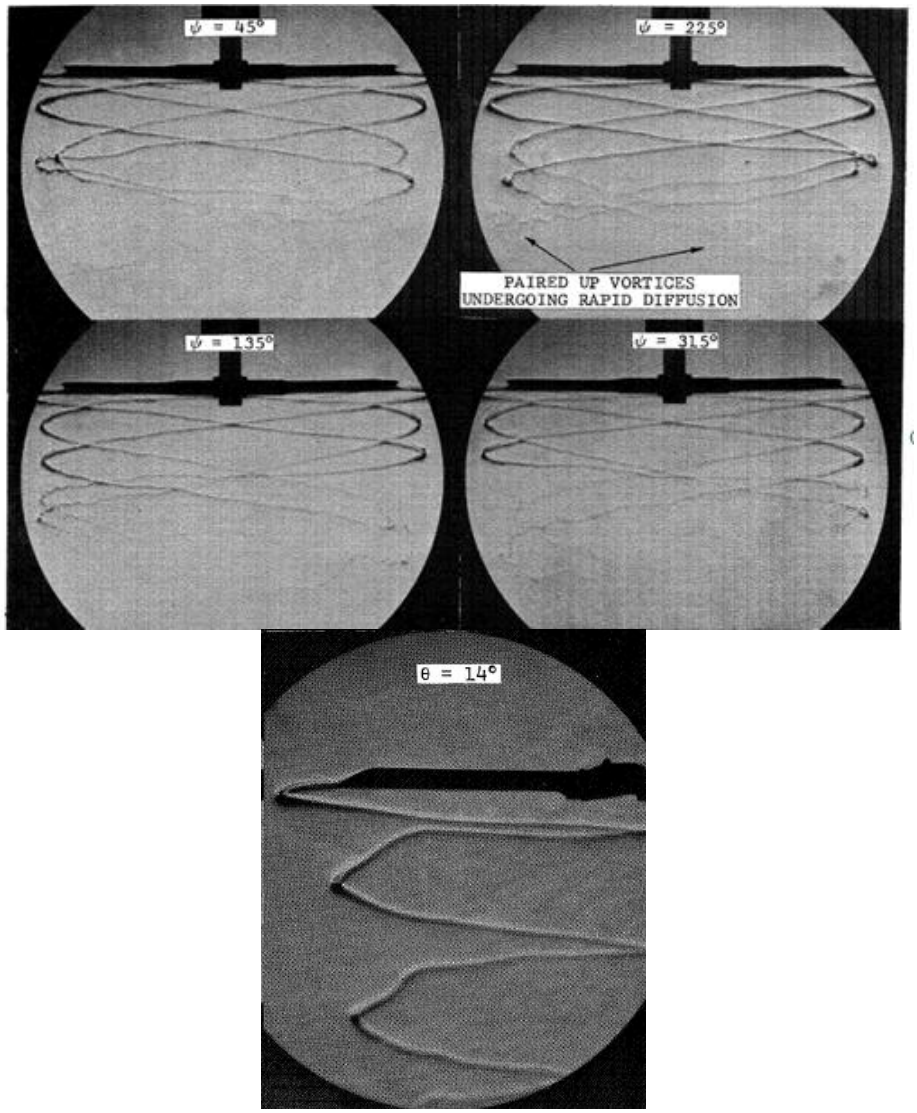

Figure 6.2: Schlieren images of a helicopter rotor wake, illustrating how only the tip-vortices shed from the outer tip of the rotor produce measurable optical aberrations (Tangler *et al.* 1973).

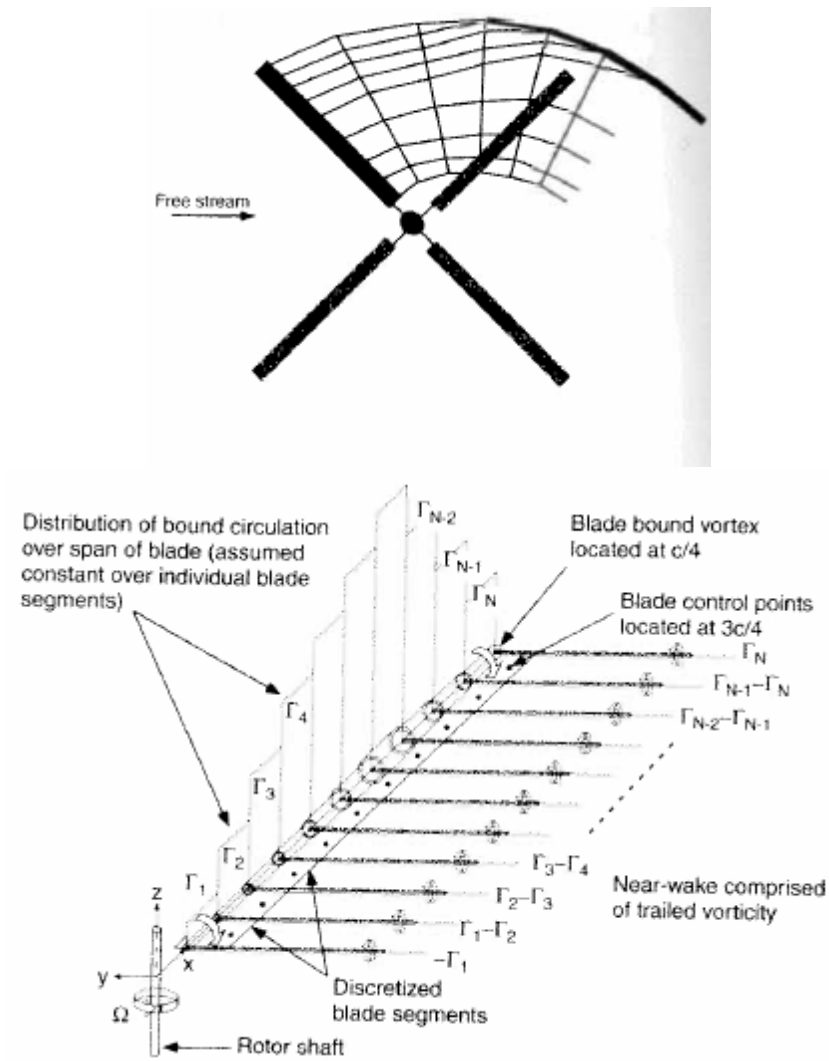

Figure 6.3: Schematic of the roll-up of the tip-vortices and circulation distribution around a rotor-blade (Leishman 2000).

From the arguments above, it should be possible to accurately compute the optical effect of the helicopter vortex wake by modeling only the rolled-up vortices from the helicopter rotor tips. Furthermore, even the induced flow from the remainder of the helicopter vortex wake should have very little effect on the optical aberration produced by the vortices shed from the rotor tips. In particular, as shown in Chapters 4 and 5, the optical effect of a tip vortex arises primarily from the pressure well (and concomitant

density well) associated with the tangential velocity component of the tip vortex. For the helicopter vortex system, the tangential velocity around the rotor-tip vortices is essentially produced entirely by the rotor-tip vortices themselves, with negligible additional tangential velocity induced by the rest of the wake vortices, which are too far away to have a strong effect. In other words, the bound vorticity shed into the inner part of the rotor wake not only produces no optical aberration itself, but it also has a negligible effect on the optical aberration produced by the outer, rotor-tip vortices. This statement will be fully tested in Appendix E, where it will be shown that the vortices shed from the inboard part of the helicopter rotors do indeed have a negligible effect on the optical aberration produced by a helicopter in hover.

Based on the preceding discussion, only equations for the outer, rotor-tip vortices will be presented. For the outer vortex filaments, Landgrebe's model gives the vertical displacement as:

$$\frac{z_{tip}}{R} = \begin{cases} -0.25\left(\frac{C_T}{\sigma} + 0.001\theta_{tw}\right)\psi_w & 0 \le \psi_w \le {}^{2\pi}/_{N_b} \\ \left(\frac{z_{tip}}{R}\right)_{\psi_w = {}^{2\pi}/_{N_b}} + k_2\left(\psi_w - \frac{2\pi}{N_b}\right) & \psi_w \ge {}^{2\pi}/_{N_b} \end{cases} \tag{6.2}$$

$$\text{where } k_2 = -(1.41 + 0.0141\theta_{tw})\sqrt{{}^{C_T}/_{2}}.$$

In Eq. (6.2), C_T is the thrust coefficient, σ is the solidity, N_b is the number of blades, θ_{tw} is the linear blade twist. The radial location of the tip vortex filament is determined by the following:

$$r_{tip} = 0.78 + 0.22e^{-(0.145+27C_T)\psi_w}. \tag{6.3}$$

Finally, the strength of the rotor-tip vortex filament is determined using Eq. (3.6).

Figure 6.4 shows an example of a tip-vortex system computed using these two equations. The calculations were performed using typical flight parameters for a medium-sized helicopter (see Appendix D). The helical barrier formed between the inside and outside of the wake is known as the slipstream. As shown, the slipstream contracts below the blades. The rate of contraction calculated from a one-dimensional momentum analysis gives a contraction ratio of 0.707; however, in Eq. (6.3) a value of 0.78 has been used instead which corresponds better to experimental measurements (Leishman 2000).

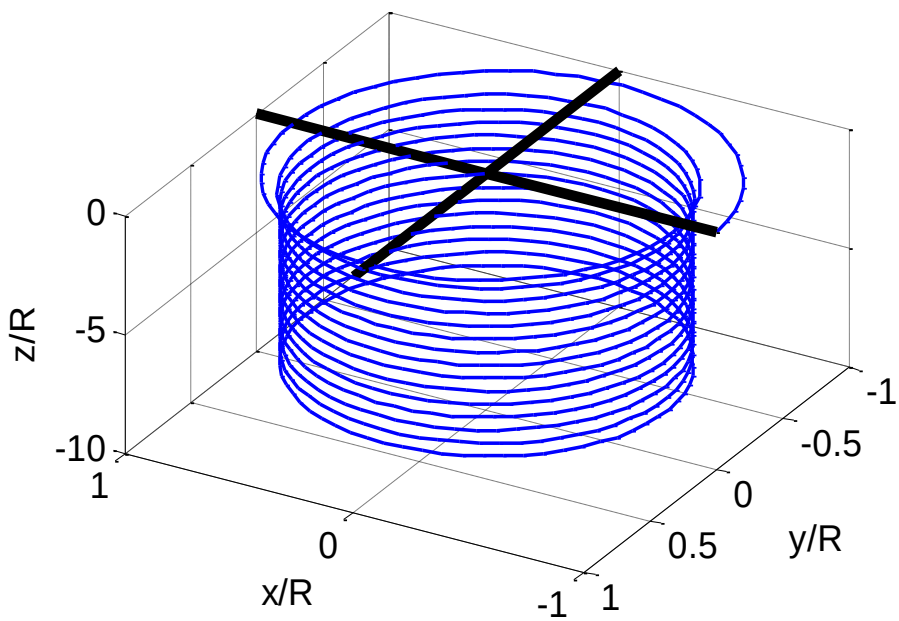

Figure 6.4: Landgrebe's model for the prescribed vortex geometry of a helicopter in hover. Only a single blade tip vortex filament is shown for clarity. The data has been normalized to the radius of the blade. The vertical axis is not to scale with the other two axes.

6.1.4. Beddoes' Forward Flight Model

For the case of forward flight, simple rigid models have been developed that model the wake geometry by assuming a uniform inflow such that the helical filament pattern is skewed backwards in the direction opposite from the direction of flight. However, during forward flight a uniform inflow does not exist, and vortex interactions become prevalent immediately. As such, in this work, a more-accurate, prescribed-wake model is used to compute the forward-flight wake geometry.

Beddoes's Generalized Wake Model is a modified, prescribed-wake model that closely matches both experimental data and free-vortex models by accounting for the non-uniform inflow. Beddoes' model parametrically prescribes the location of the forward-flight vortex system, and has been shown to agree very well with free-vortex calculations (Leishman 2000). This method was developed to provide an accurate model of the downwash of a helicopter in forward flight while avoiding the computational expense related to free-vortex methods. As stated in Beddoes (1985), free-vortex methods for modeling are unacceptable (due to computational expense) except as a basis for the evaluation of approximate methods.

The model calculates the distortion of the wake using a time-averaged downwash. Considering planes parallel to the tip path plane (TPP), the *x* and *y* locations of the vortex (Figure 6.5) are determined by:

$$\begin{aligned} x_v &= r_v \cos(\psi_v) + \mu_x \Delta\psi_v \\ y_v &= r_v \sin(\psi_v). \end{aligned} \tag{6.4}$$

In Eq. (6.4), ψ_v is the azimuthal angle of the blade at the instant the vortex was formed, and $\Delta\psi_v$ is the difference in azimuthal angle between the current blade location and ψ_v.

The z coordinate of the tip vortices is dependent on the rotor axial velocity as well as the local induced velocity. During forward flight, the wake is skewed because there is a relative upwash at the front portion of the disc and an increased downwash at the rear portion of the disk. A strong lateral variation of the downwash also exists in addition to the front to back variation. Therefore, the vertical displacement of the vortex filament at any point in space depends upon the blade location at the instant the filament was shed. The following three definitions are used to define the vertical displacement:

$$z_v = -\mu_z \Delta\psi_v + \begin{cases} -\lambda_i \left(1 + E\left[\cos\psi_v + \frac{\mu_x \Delta\psi_v}{2r} - \left|y'^3\right|\right]\right)\Delta\psi_v & \text{if } x_v < -r_v \cos\psi_v \\ -2\lambda_i\left(1 - E\left|y'^3\right|\right)\Delta\psi_v & \text{if } \cos\psi_v > 0 \\ \frac{-2\lambda_i x_v\left(1 - E\left|y'^3\right|\right)}{\mu_x} & \text{otherwise} \end{cases} . \tag{6.5}$$

The factor E in Eq. (6.5) is an empirical parameter that is fit to experimental data. As suggested by Leishman (2000),

$$E = \left|\frac{\chi}{2}\right| = \tan^{-1}\left(\frac{\mu_x}{-(\mu_z - \lambda_i)}\right) \Big/ 2, \tag{6.6}$$

where λ_i is the induced inflow, which can be found iteratively using the Newton-Raphson method. Figure 6.5 shows an example of a tip-vortex system computed using Eq. (6.4) and Eq. (6.5); the calculations were performed for a forward flight speed of 20 m/s and using typical medium-sized helicopter parameters summarized in Appendix D.

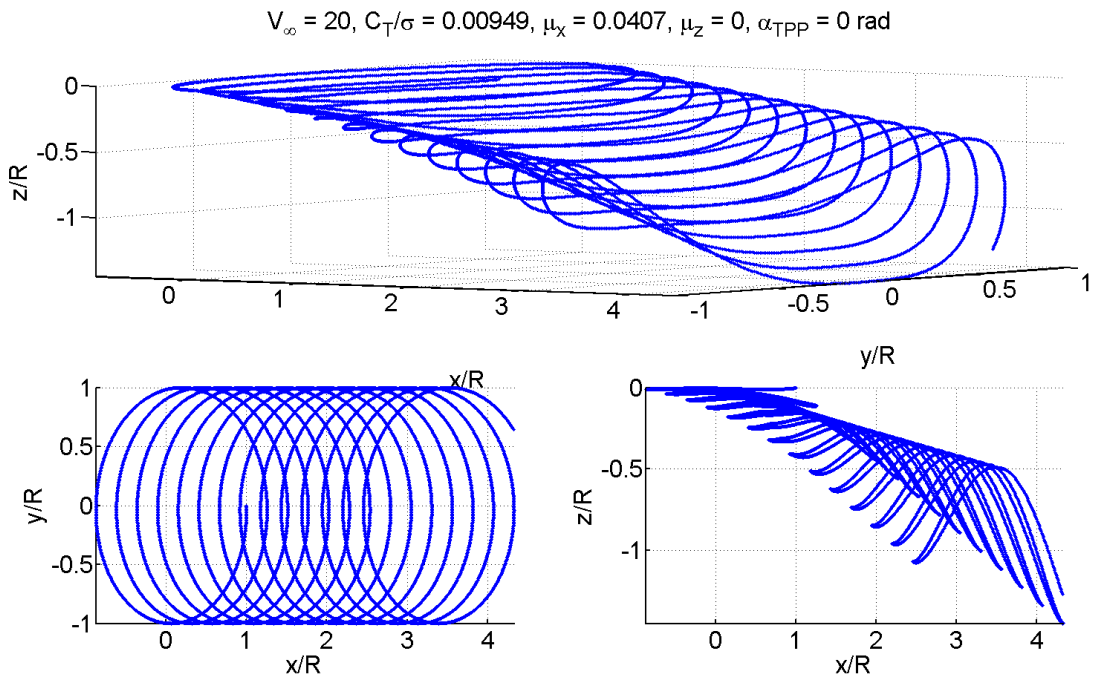

Figure 6.5: Beddoes' model of the tip-vortex geometry for a medium-sized helicopter in forward flight. The tip-vortex filament from only a single blade is shown for clarity. The data has been normalized to the radius of the blade.

6.2. Biot-Savart Law

Once the geometry of the rotor-blade tip-vortex system is known, the induced velocity at any position in space can be calculated using the Biot-Savart law. The general form of the Biot-Savart law is:

$$d\vec{v} = \frac{\Gamma}{4\pi}\frac{d\vec{l} \times \vec{r}}{|r|^3}. \tag{6.7}$$

It should be noted that the Biot-Savart law is derived under the assumption of incompressible flow so that the Biot-Savart law does not model possible compressible-flow effects on the induced velocity of the tip vortex. In this regard, the Biot-Savart law also follows the "weakly compressible" approach employed by this investigation, and

arguments showing that the weakly-compressible approach is valid for typical helicopter wake flow fields can be found in Section 4.3. When the Biot-Savart law is applied to the vortex system of a helicopter, the filaments are discretized into small segments, *dl*, to approximate the helical pattern of the tip vortices. Since the Biot-Savart law converges slowly, these computations must be made for vortex filaments extending far from the point of interest to ensure convergence.

When calculating the induced velocity for a vortex in free space, a revised version of the Biot-Savart law is needed. In particular, measured vortices have the following general characteristics: (1) the velocity at the center of the vortex is zero, (2) the tangential velocity reaches a maximum at the core radius, and (3) the tangential velocity decays to zero as the distance from the vortex core approaches infinity. Equation (6.7) does not yield these general characteristics; for example, as *r* becomes small the induced velocity modeled by Eq. (6.7) rapidly increases and becomes infinite when *r* is zero. A revised version of the Biot-Savart law that more-accurately models experimental vortex behavior is, (Leishman *et al.* 2002):

$$V_{ind} = \frac{\Gamma}{4\pi}\left[\frac{h^2}{(r_c^{2N} + h^{2N})^{\frac{1}{N}}}\right]\int \frac{d\vec{l} \times \vec{r}}{|r|^3}. \tag{6.8}$$

In Eq. (6.8), *h* is the perpendicular distance from the field point to the vortex filament segment and *N* determines the shape of the vortex velocity profile. For the calculations presented in Chapter 7, *N = 2* is used. This is the algebraic approximation of the Lamb-Oseen vortex and *not* the *n = 2* vortex model developed by Vatistas (2006) and shown in Eq. (3.5), although the two vortex models are very similar.

6.3. Pseudo-Free Vortex Check

As an illustration of the accuracy of the prescribed-wake approach, a computation was performed to determine how well Landgrebe's model matches the expected behavior of a free-vortex model. Specifically, if Landgrebe's model accurately approximates a free-vortex method, then the change in position of the vortex system predicted by Landgrebe's model after a time interval, *dt*, should match the change in position of each point on the vortex in the same time interval as a result of the velocity induced at that point by the vortex system. The check was performed by first computing a vortex geometry using Landgrebe's model, Figure 6.4. Next, the induced velocities at four randomly-selected points on the vortex were computed by integrating Eq. (6.8) along the length of the vortex; the displacements of these four points after a small time *dt* was then computed and compared to the location of the vortex predicted by Landgrebe's model for the same time interval. Note that the effect of spanwise vorticity and vorticity shed into the inner tip vortices was included in these calculations, since this part of the wake system is required to accurately determine the velocity at the test points even though it is not needed to compute the optical effect of the vortex wake (as discussed in Section 6.1.3). Figure 6.6 shows the two vortex filaments calculated using Landgrebe's model separated by a time *dt*, and also shows the location of the four randomly-selected points on the original vortex filament, and the induced velocity at those points. As shown in the figure, the direction and magnitude of the induced velocity at the four test points was very close to the correct amount required to move those points so they matched up with the new location of the vortex at the end of the time interval *dt*.

Other demonstrations of the accuracy of the prescribed-wake methods used in this research are shown in Figures 6.7 (Leishman 2000) and 6.8 (Leishman 2006). Figure 6.7a and b show the axial and radial displacement of an individual tip vortex as a function of its wake age, and shows that Landgrebe's model compares well with experimentally-measured values as well as free-vortex computations (including the root vortex and vortex sheet). For a helicopter in forward flight, Figure 6.8 shows the axial displacement of an individual tip vortex at two different blade azimuth angles, and shows that Beddoes' model compares well with a free-vortex method.

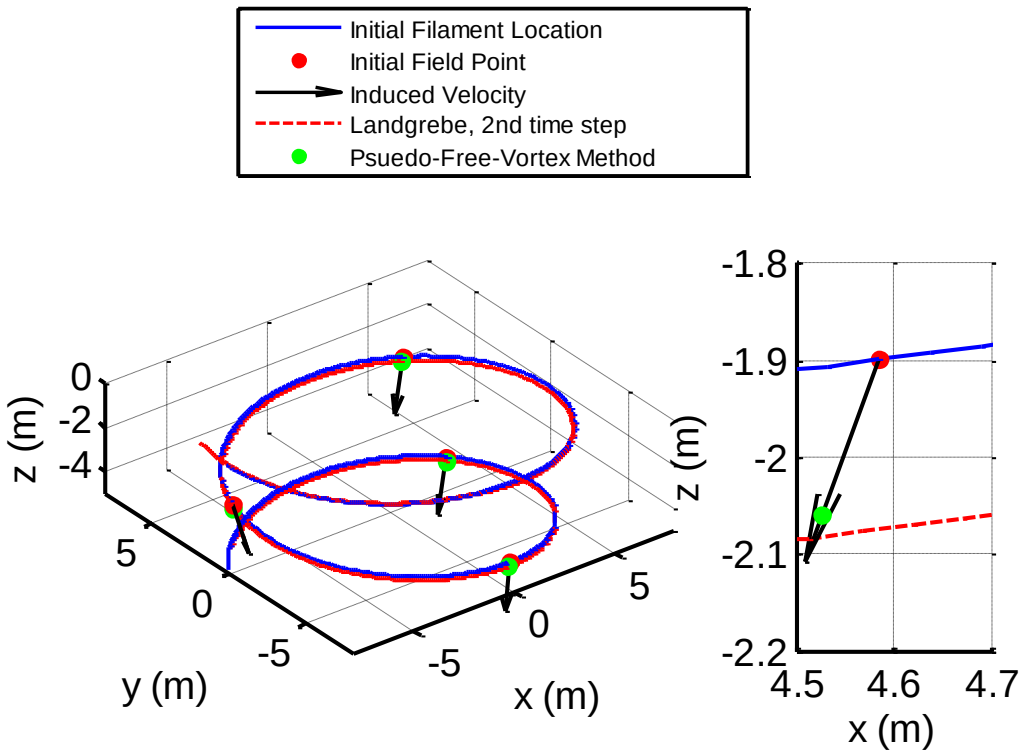

Figure 6.6: Comparison of Landgrebe's model and a pseudo free-vortex method based on Landgrebe's model with all the included circulation required for lift in the tip vortex.

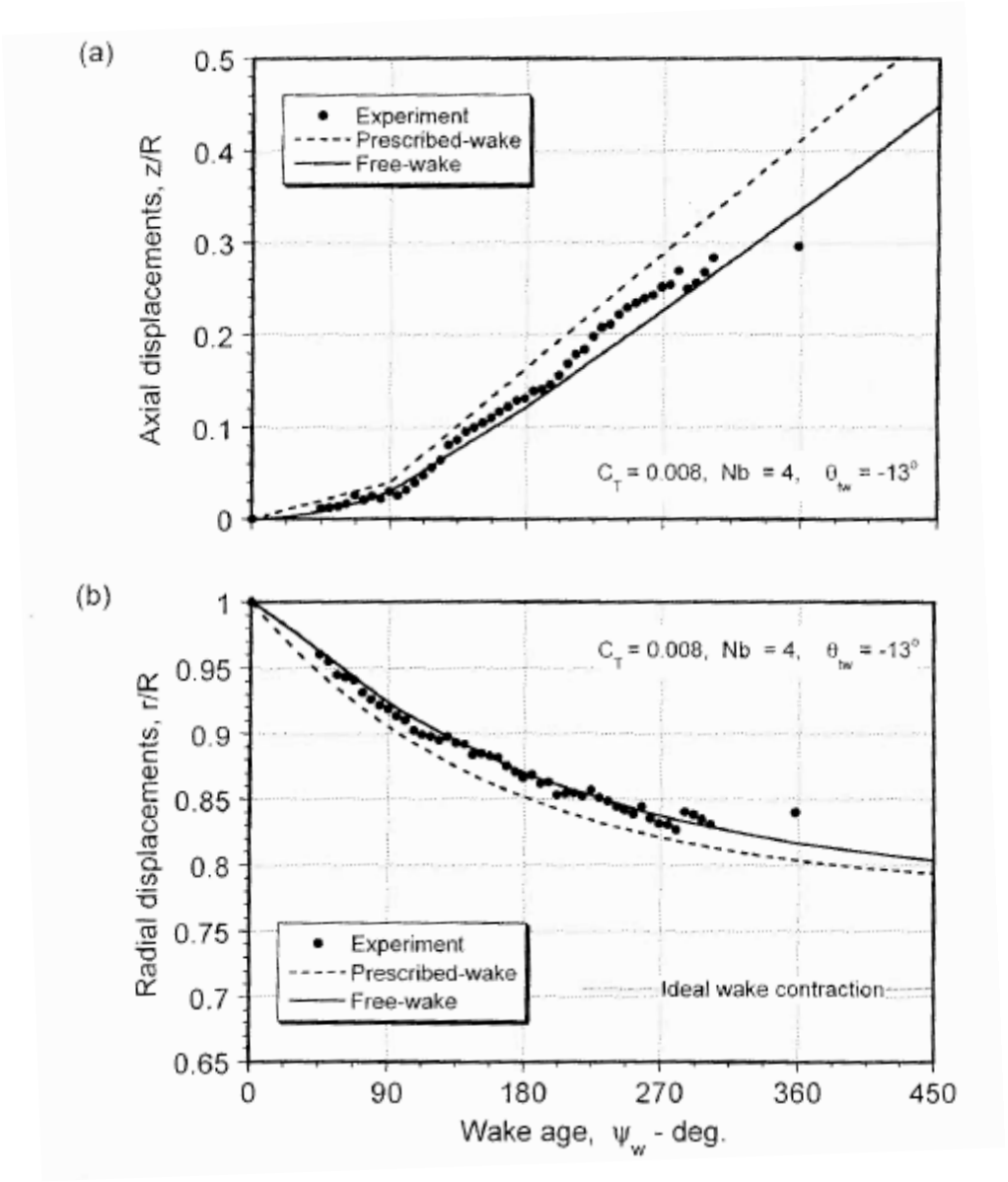

Figure 6.7: Comparison of prescribed wake methods, free vortex methods, and experimental measurements of the location of a tip vortex in hover (Leishman 2000).

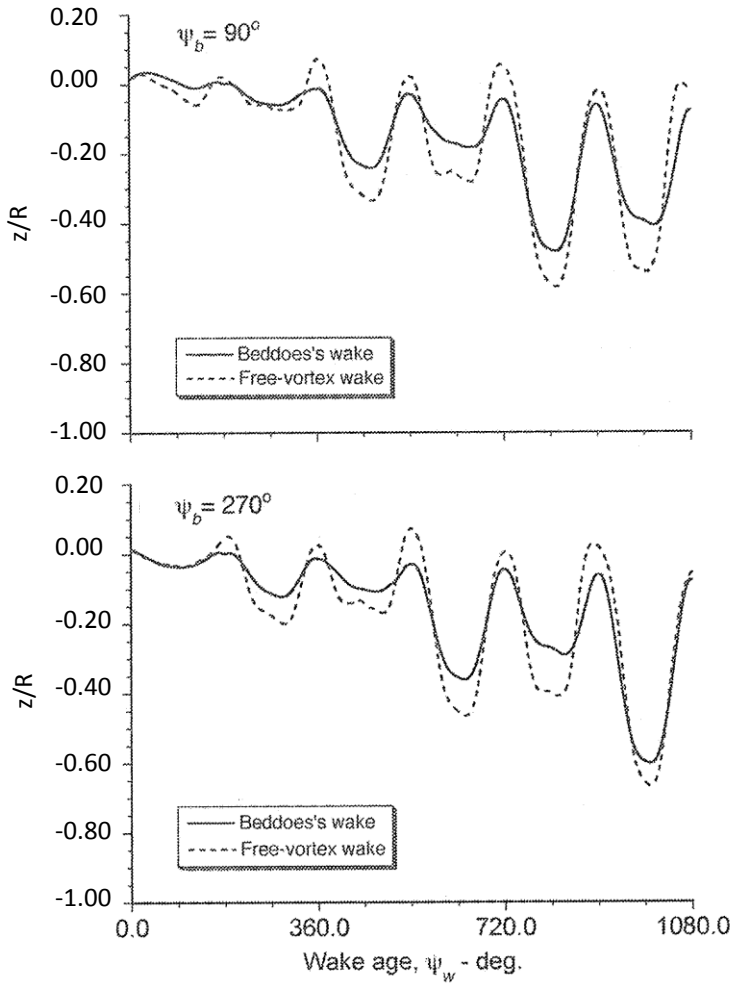

Figure 6.8: The axial displacement of a tip vortex as a function of the wake age using Beddoes's model and a free vortex model (Leishman 2006).

6.4. Cautionary Remarks

It should be noted that, due to limited measurements of the blade-tip vortex wake in the farfield of a medium-sized helicopter in either hover or forward flight, the models developed in this chapter are assumed to be valid up to larger wake ages than have actually been measured. For example, as shown in Figure 6.7, experimental

measurements of the wake geometry were only made out to a wake age of 360 degrees, which roughly corresponds to the wake age at which the tip vortices would just begin to propagate into the line-of-sight of a fuselage-mounted optical system. Similarly, in Figure 6.8, the comparison of Beddoes' model to the free-vortex wake model only extends to a wake age of 1080 degrees. Finally, a similar extrapolation is made concerning the trend of the growth of the vortex core, where as shown in Figure 3.4, measurements have only been made up to a wake age of 720 degrees.

The models of the blade-tip vortex wake presented in this chapter and used in the next chapter also do not account for the interaction of the tip vortices with the fuselage, or with each other, or with any other external obstructions/interactions to the tip vortex path; therefore the wake is always assumed to be symmetric and well-behaved. Finally, for the forward-flight speeds investigated in the next chapter, the circulation strength of the blade-tip vortex from the advancing rotor blade and the retreating rotor blade are assumed to be equal; at these flight speeds, the difference in velocity of the blade-tips is considered negligible.

CHAPTER 7:

THE AERO-OPTIC ENVIRONMENT AROUND A HELICOPTER IN HOVERING AND FORWARD FLIGHT

This chapter presents spatially- and temporally-resolved calculated data for the pressure, temperature, and density fields surrounding a helicopter in hover and in forward flight. The data were calculated using the "weakly compressible" approach described in Chapter 4. The density data, and associated index-of-refraction field, are used to determine the aero-optic effect on a beam of light projected from the helicopter as a function of aiming direction. Temporally-resolved aero-optic effects on the beam of light are shown for hover and as a function of forward flight speed.

7.1. Hovering-Flight Model - Numerical Setup

The aero-optic aberrations caused by the vortex-wake system of a four-blade, medium-sized, utility helicopter in hover were computed using the "weakly compressible" approach outlined in Chapter 4. The tip-vortex geometry was first computed using the Landgrebe model described in Chapter 6 and using the helicopter parameters tabulated in Appendix D, after which the velocity field was computed using the revised Biot-Savart law in Eq. (6.8), where the core radius and circulation strength of

the vortices were determined using Eq. (3.12) and Eq. (3.6) respectively. Once the velocity field was determined, thermodynamic properties including the pressure, temperature, density, and index of refraction were computed using the numerical methods described in Chapter 4. For the most part, these thermodynamic calculations were performed using the WCM method, although several check calculations were also performed using the isentropic method, which produced density fields that agreed closely (within 0.3%) with the WCM (see Section 7.6).

Figure 7.1 shows the tip-vortex geometry determined using Landgrebe's model, and the field points at which the velocity and the thermodynamic properties were calculated. For clarity, only one of the four vortex filaments is shown, and only one out of every 100 field points is plotted. As shown in Figure 7.1, the field points were located using a cylindrical coordinate system to take advantage of the axial symmetry of the vortex wake, and were concentrated around the tip vortex filaments to capture the large property gradients in this region. The typical field-point spacing used near the vortex filaments was $dr = dz = 0.001R$, yielding ~8-10 field points within the core radius of a vortex in both the radial and vertical directions. Based on the aperture ratio and grid resolution study of a single vortex (see Section 4.7) this resulted in an estimated error in the OPD_{RMS} of less than 2%. Forty revolutions of the tip-vortex filament were modeled to ensure convergence of the velocity calculations at all field points. The field points were placed so that the optical aberrations on an outgoing beam could be computed for a reasonable range of elevation angles of a turret mounted underneath the helicopter fuselage.

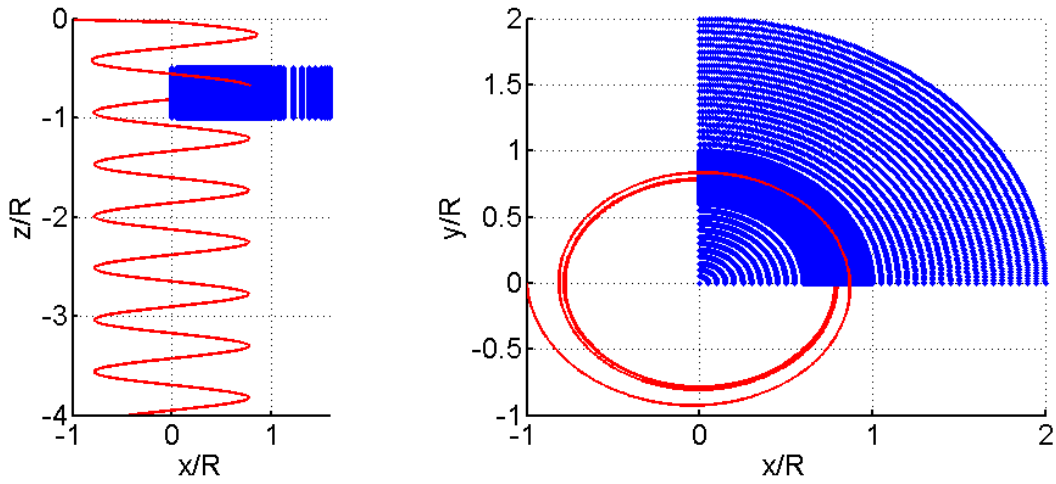

Figure 7.1: Wake geometry and field points used to compute the aero-optical environment of a helicopter in hover. Only one tip-vortex filament, and every 100th field point is shown.

Convergence tests were run in which 20, 40, 60, and 80 revolutions of the vortex wake were modeled. Using 80 revolutions as the basis for the correct answer, the error in truncating the wake was calculated. With only 20 revolutions, about a one percent difference in the velocity components was obtained. By 40 revolutions, the difference was reduced to less than 0.2%, which was considered a good balance between accuracy and computational expense. For all cases, the vortex filaments were discretized into straight line segments with a length corresponding to 0.01 radians of revolution, resulting in 25,133 discrete elements for a 40-revolution wake.

7.2. Hovering-Flight Model - Approximate Solution

As a qualitative example of the results of the numerical approach, a coarse field-point spacing was used to calculate the entire flow field from the tip path plane (TPP) to one blade radius below the TPP. The resulting pressure, temperature, and density are presented in Figure 7.2. These results conform to basic expectations for the helicopter wake. For example, as shown in Figure 7.2, the pressure within the slipstream directly underneath the blades is higher than atmospheric pressure; this result agrees with the predictions of simple one-dimensional momentum analyses assuming a uniform inflow. Figure 7.2 also shows that the static temperature within the slipstream is lower than the atmospheric temperature. The combination of the reduced temperature and increased pressure results in a higher density within the slipstream.

7.3. Hovering-Flight Model - Detailed Solution

To estimate the detailed optical aberration on a beam of light originating from beneath the helicopter (Figure 1.6), the finer field-point spacing described in Section 7.1 was used (Figure 7.1). Furthermore, the rotor-tip vortex circulation strength was set to 21 m^2/s, and vortex-core diffusion parameters of δ = 256 and a_1 = 0.0002 were used, which are typical values for a medium-sized utility helicopter (see Appendix D). It should be noted, however, that the values of these parameters can vary significantly with flight conditions; the effect of different parameters on the optical effect of the helicopter wake is examined in Section 7.4.1.

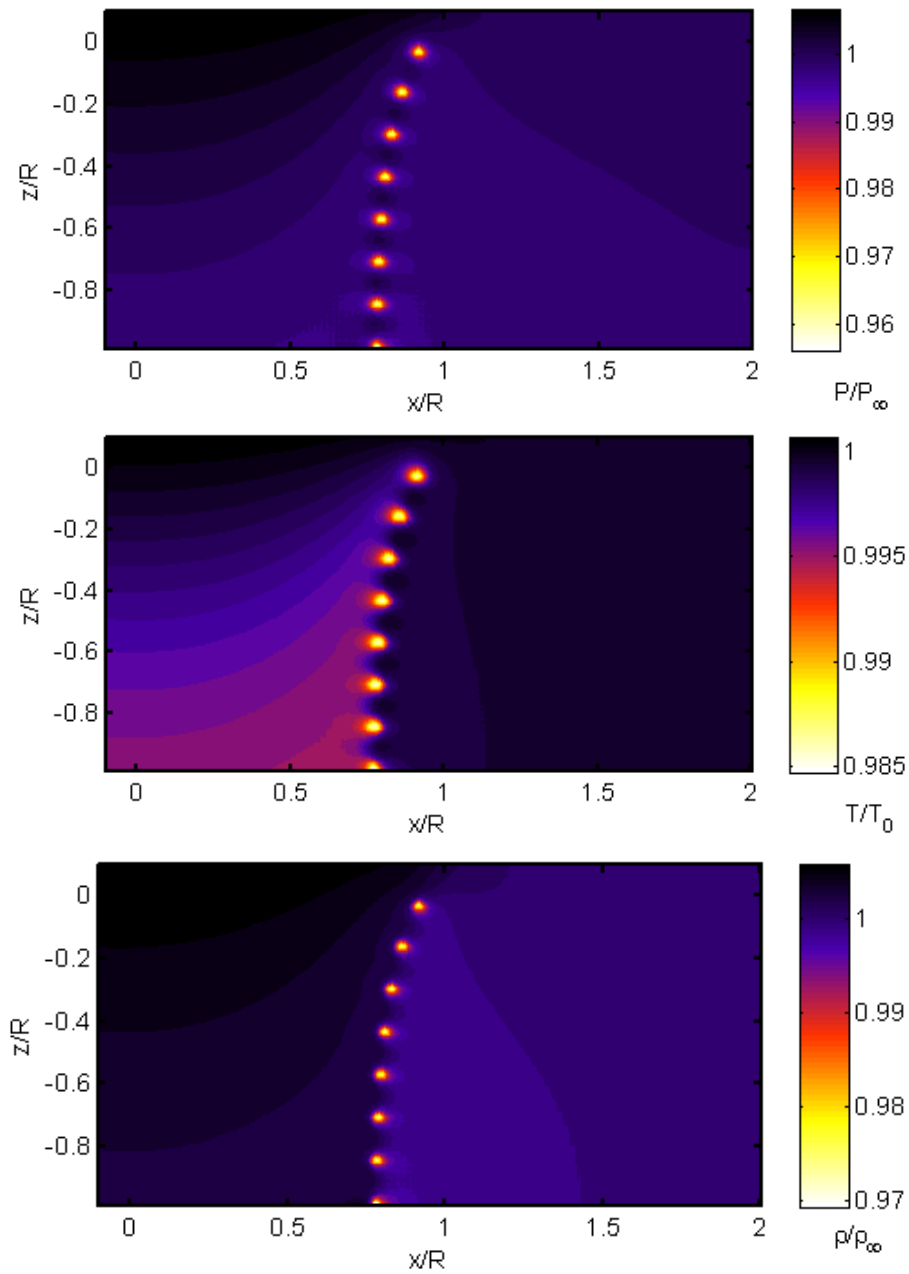

Figure 7.2: Vertical slice of the pressure, temperature, and density fields computed using a coarse solution grid, from the TPP to one blade radius below the TPP.

An isosurface of the computed density is shown in Figure 7.3. Like Figure 7.2, this figure also shows that most of the flow-field density variations occur very close to the vortex filament itself. Furthermore, the density drop in the vicinity of the vortex core decreases with increasing wake age, Ψ_w, due to the increase of the vortex core radius from turbulent diffusion.

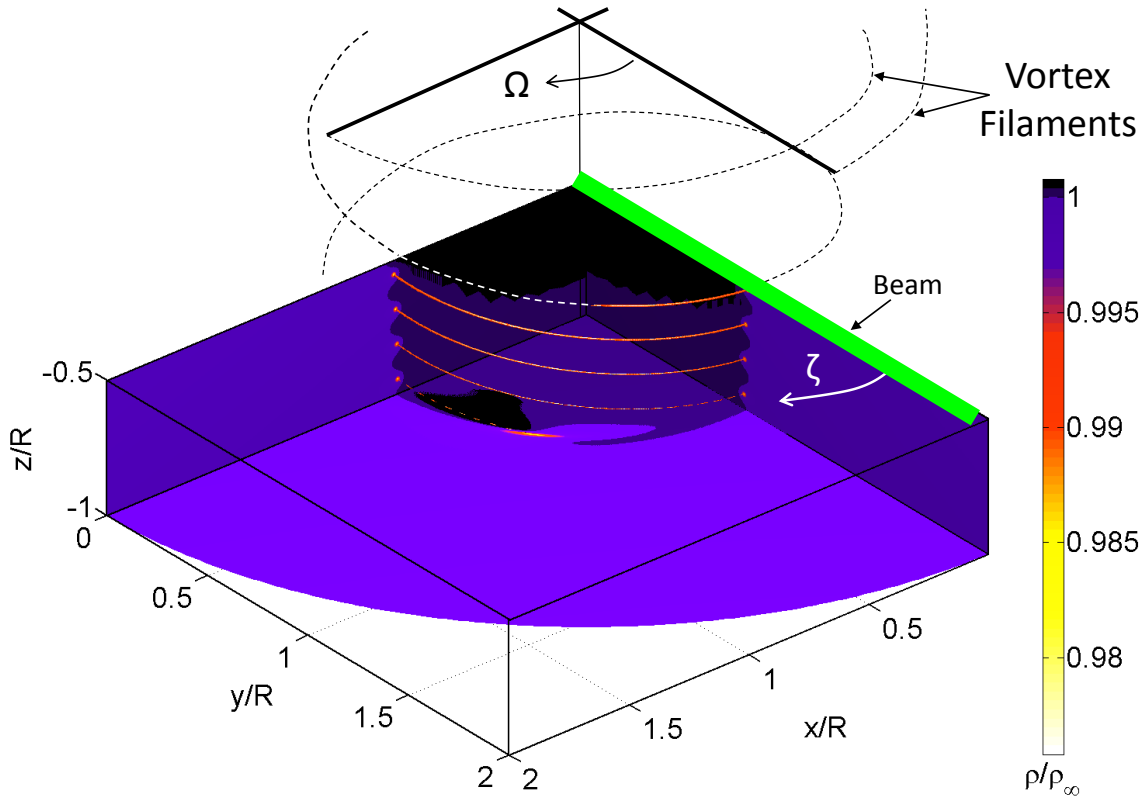

Figure 7.3: Density field below a medium-sized utility helicopter resulting from the blade-tip vortices.

Figure 7.4 shows the optical aberration on an outgoing beam originating from underneath the helicopter at four different relative-beam angles, $\zeta = Az - \psi_R$ (note that due to its axisymetric geometry, the optical effect of the wake in the case of hover depends on the difference between the beam aiming angle, Az, and the rotor phase ψ_R . The

aberrations were computed for a beam path with 0° elevation (i.e. parallel to the rotor plane). Furthermore, the aberrations were computed assuming a beam diameter of $A_D = 0.254$ m (10 inches) which was estimated to be a reasonable aperture size for a turret mounted on a medium-sized helicopter; however, the effect of different beam diameters is discussed below. The graphs in Figure 7.4 correspond to azimuth angles in which:

A) no vortex is in the line of sight (ζ=20°),

B) the center of the vortex is just entering the line of sight (ζ=57°),

C) the vortex center is partially in the line of sight (ζ=60°), and

D) the center of the vortex is centered in the line of sight (ζ=68°).

Figure 7.4 shows that the aberrations on the beam are relatively small unless the beam passes directly through a blade tip vortex (Figure 7.4D).

The OPD_{RMS} of the optical aberrations as a function of beam azimuthal angle are summarized in Figure 7.5 for elevation angles of 0, 10, and 20 degrees (where an elevation angle of 90 degrees is pointing straight down). It should be noted that the flow field produced using Landgrebe's model for the case of hover is axisymetric. This is a good approximation of experimentally-measured helicopter flow fields, at least for the first few wake revolutions (Kini and Conlisk 2002) before vortex merging begins. Given the axial symmetry of the flow, the phase variation of the aberrations shown in Figure 7.5 is equivalent to the time history of the optical aberration on a single outgoing beam aimed in a fixed direction as the helical wake rotates around the helicopter. In this case, for a four-bladed helicopter, the OPD_{RMS} from $\zeta = 0^o$ to 90° shown in Figure 7.5 would be repeated at a frequency equal to four times the revolution frequency of the rotor shaft.

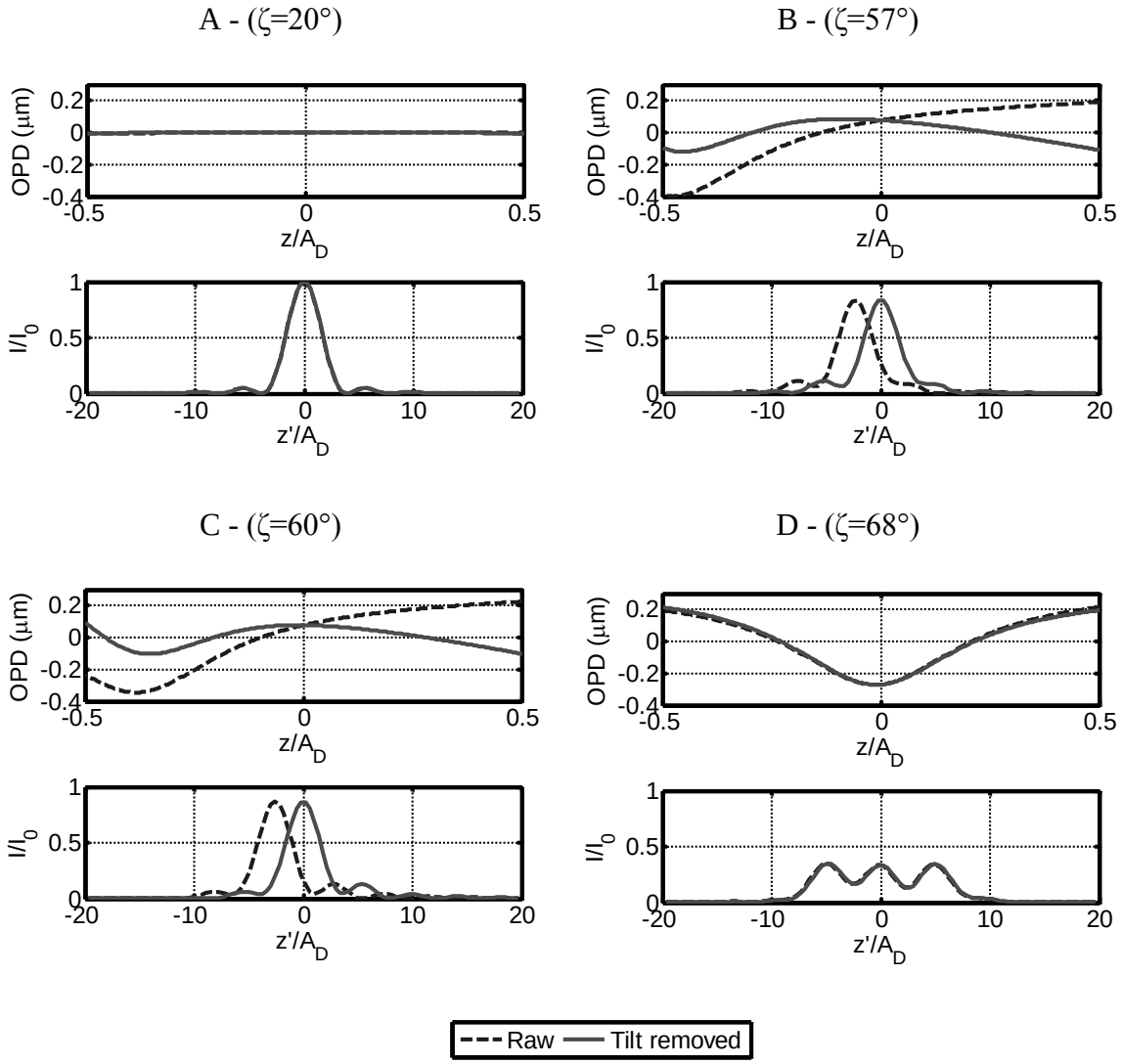

Figure 7.4: Instantaneous OPD and normalized farfield irradiance patterns for an outgoing beam at a 0° elevation and four different azimuth angles.

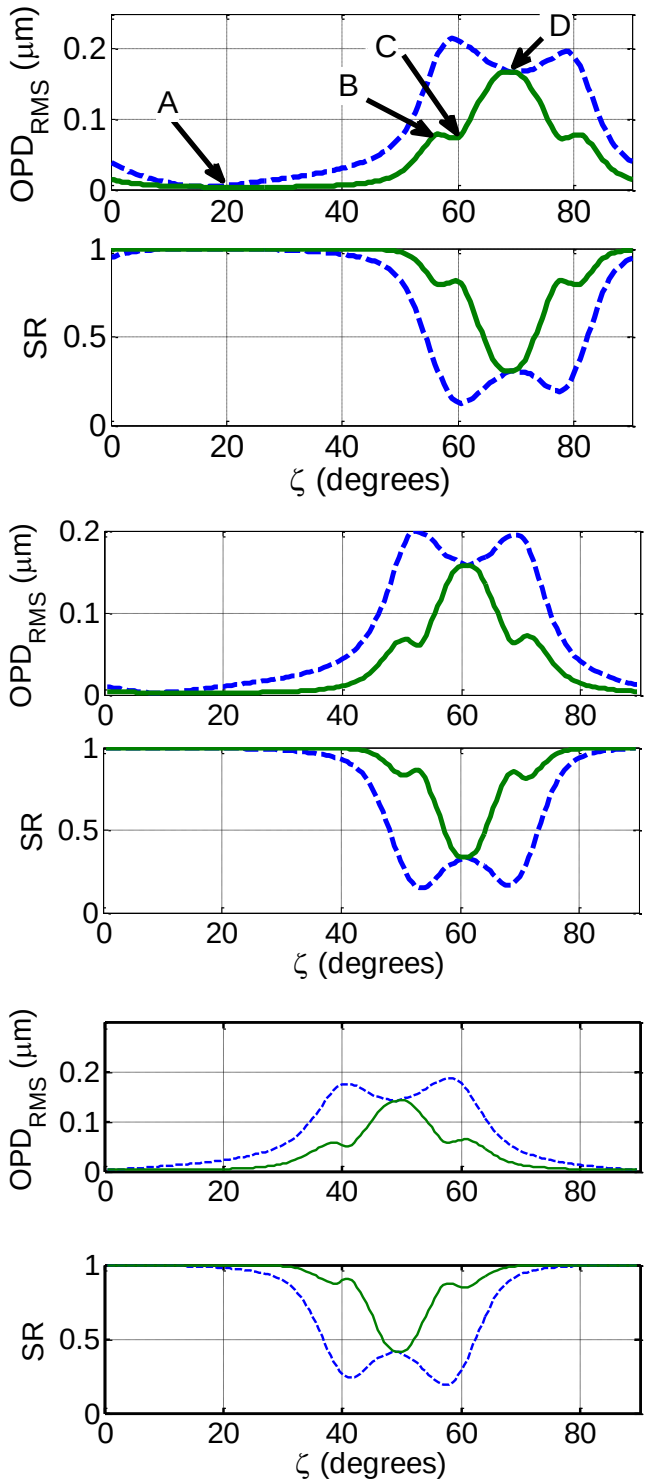

Figure 7.5: OPD_{RMS} and Strehl ratio versus relative-beam angle, ζ, for elevation angles of 0 degrees (top), 10 degrees (center), and 20 degrees (bottom). A, B, C, and D correspond to the instantaneous wavefronts and farfield patterns shown in Figure 7.4.

In Figure 7.5, two curves ("raw" and "tilt removed") are shown for each elevation angle, where "raw" corresponds to the uncorrected aberration and "tilt removed" corresponds to an infinite bandwidth fast-steering mirror removing the best-fit plane to the optical wavefront. In the "raw" signal, two local maxima can be seen in the spatial OPD_{RMS} as a function of beam azimuth angle. The first maximum corresponds to the point at which the center of the vortex core first enters the line of sight (Figure 7.4B) and the second to the instant at which the center of the vortex core is leaving the line of sight. The effect of this entering/exiting of the vortex core is to impart a large optical tilt on the beam that pulls the beam's central lobe off center in the farfield. As shown in Figure 7.5, applying a tilt correction greatly reduces the spatial OPD_{RMS} at these instances, and also greatly increases the Strehl ratio. The local minimum between these two peaks in the spatial OPD_{RMS} "raw" signal corresponds to the instant at which the vortex is in the center of the aperture (Figure 7.4D). At this instant, the OPD across the aperture is symmetric, such that no tilt is present in the raw signal and hence no increase in Strehl ratio is gained from the use of a fast steering mirror. Finally, the part of the cycle in which SR≈1 corresponds to the absence of a tip vortex within the path of the outgoing beam (Figure 7.4A), so that the diffraction-limited case is obtained in the farfield.

TABLE 7.1.

SUMMARY OF AERO-OPTIC ABERRATIONS FOR A HOVERING, MEDIUM-SIZED HELICOPTER

	Raw	Tilt removed
Time-averaged OPD_{RMS} (μm)	0.0714	0.0350
Minimum OPD_{RMS} (μm)	0.0026	0.0023
Maximum OPD_{RMS} (μm)	0.1994	0.1579
Time-averaged SR	0.7497	0.9004
Minimum SR	0.1502	0.3336
Maximum SR	0.9997	0.9998
% cycle, SR < 0.25	12.29	0
% cycle, SR < 0.50	27.93	7.82
% cycle, SR < 0.75	34.08	13.41

Statistical metrics for the OPD_{RMS} and Strehl ratio for the 0° elevation case are summarized in Table 7.1. These data can be used to evaluate the requirements and potential of adaptive optic (AO) control schemes. For example, when used for communications, the instantaneous Strehl ratio is important since a low Strehl ratio at any instant could result in a loss of the signal. On the other hand, only the mean Strehl ratio might be of interest in applications that require maximizing the power on target.

7.4. Hovering-Flight Model - Comparison to Scaling Relationship

In Chapter 4, a relationship for the optical aberration due to a single tip vortex in free-space was derived based on the Lamb-Oseen vortex model:

$$OPD_{RMS} = C_1 \left(\frac{\rho}{\rho_{SL}}\right) \frac{\Gamma^2}{\mathrm{a}^2 \mathrm{r_C}} G_{Norm}(AP), \tag{4.32}$$

where C_1 is 3.695 for the isentropic method and 2.805 for the WCM method and G_{Norm} is plotted in Figure 4.24. Recall that the assumptions used in the derivation of Eq. (4.32) were that the vortex was centered in the beam, and that the beam path was normal to the vortex path. These assumptions correspond to the conditions at the point $\zeta \cong 68°$ in Figure 7.5 (top graph) or $\zeta \cong 60°$ in Figure 7.5 (center graph); this also corresponds to the aberration shown in Figure 7.4D, where the vortex is centered in the outgoing beam. At an elevation angle of 0 degrees ($\zeta \cong 68°$), the core radius is 0.0771 m corresponding to a wake age of 495.6°, and the aperture ratio at this location is 1.7004. Using these values, Eq. (4.32) predicts an OPD_{RMS} of 0.1492 μm or 0.1351 μm for the isentropic and WCM methods respectively; the predicted value using the complete blade-tip vortex system is 0.1579 μm. The fact that the single tip-vortex relationship shown in Eq. (4.32) under predicts the OPD_{RMS} determined using the full vortex-wake model by only 5.5% and 14.4% for the isentropic and WCM predictions respectively demonstrates the usefulness of the scaling relationship. This also supports the claim made in Chapter 6 that the magnitude of the optical aberration for the full helicopter is dictated primarily by the section of tip-vortex filament that is nearest to where the outgoing beam crosses the helicopter wake, with the rest of the wake system making only a minor additional contribution to the overall aberration.

7.4.1. Different Wake Parameters

The results shown in Figure 7.4 and Figure 7.5 were computed using a vortex circulation strength of 21 m^2/s and a vortex core radius determined using (δ=256 , a_1=0.0002); these values were used because they are representative of a medium-sized utility helicopter and are in the approximate middle of the range of possible values (Appendix D). However, both the circulation strength and core radius are dependent on many variables such as the blade-tip shape, blade twist, atmospheric conditions, etc (see Section 6.4). For example, for the chosen helicopter weight and number of blades, results published in Bagai and Leishman (1993), and Beddoes (1985) indicate that the circulation strength could be as high as 30 m^2/s, corresponding to k=3 in Eq. (3.6). Similarly, based on the range of a_1 in Eqs. (3.11) and (3.12), the apparent viscosity, δ, could range from 64 (a_1=5×10^{-5}) to 511 (a_1=4×10^{-4}) for a circulation strength of 21 m^2/s. As shown in Eq. (3.12), the apparent viscosity has a significant effect on the growth of the vortex core radius, which in turn has a significant effect on the peak swirl velocity and therefore pressure drop, density drop, and hence optical aberration associated with the vortex core.

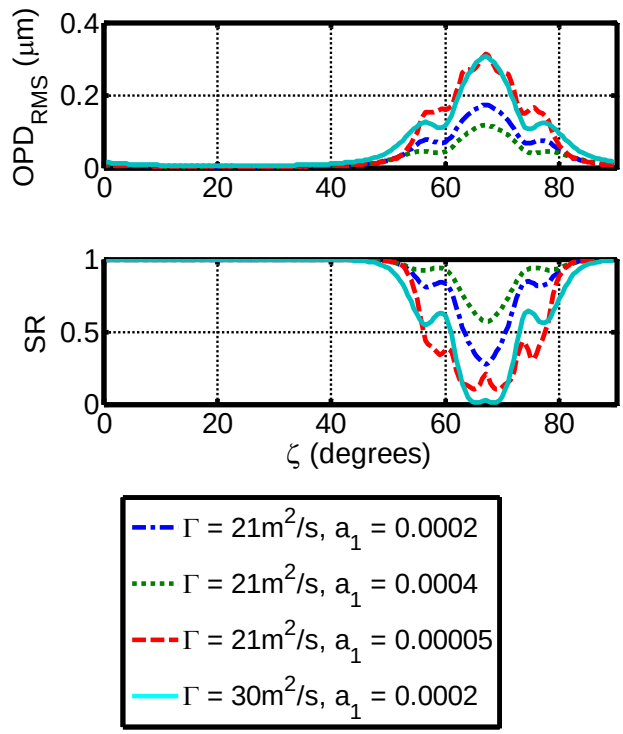

Figure 7.6: Sensitivity of optical aberration (λ = 1μm) to circulation strength and vortex growth rate for a helicopter in hover.

To illustrate how much the amplitude of the optical aberration is affected by just the vortex-core growth rate, Figure 7.6 shows two additional computations of the optical aberration using the maximum and minimum values of a_1 while maintaining all other parameters at the same values used in Section 7.3. For the final case shown in Figure 7.6 (solid line), the circulation strength was increased to 30 m^2/s while holding the core radius growth at δ=256 , a_1=0.0002. Figure 7.6 demonstrates that the optical aberration imposed by the vortex wake could be significantly more, or less, depending on the specific flight conditions, although even the worst cases present a large range of beam-aiming angles (or % of rotor period) in which the vortex imprints no aberration on the beam of light.

7.4.2. Effect of Beam Diameter

In Chapter 4, it was found that the optical effect of a single tip vortex on a beam of light depended upon the nondimensional ratio $A_D/2r_c$. For the tip-vortex wake of a full helicopter, the optical effect of the helicopter will also depend on the diameter of the outgoing beam. Due to the variation (i.e. growth) of the core radius of the helicopter tip-vortices with distance along the helical path of the wake, the value of the nondimensional parameter $A_D/2r_c$ will also depend on the exact point where the beam crosses the wake, as well as on the particular flight conditions. For the results shown in Figure 7.4 and Figure 7.5, the diameter of the beam was 0.254 m, which was assumed to be a realistic beam size for an optical system mounted on a medium-sized helicopter. Furthermore, at zero degrees elevation angle, the core radius at the point where the outgoing beam crossed the vortex wake was approximately 0.077 m, giving a value of the parameter $A_D/2r_c = 1.6$.

The effect of different outgoing beam diameters is shown in Figure 7.7. The data shown in Figure 7.7 were computed using the same helicopter parameters used in Section 7.3. The figure shows that as the beam diameter increases (and r_c stays the same), the optical effect of the helicopter wake on the beam changes in two ways. First, Figure 7.7 shows that the range of ζ over which the beam is strongly aberrated increases as A_D increases; this is due to the fact that a larger-diameter beam intersects a vortex in the helical wake of the helicopter over a larger range of relative beam angles ζ. If the beam diameter were increased to the point that it was larger than the vertical separation between vortices in the helical wake, then the beam would always pass through a vortex. Secondly, Figure 7.7 also shows that the magnitude of the aberration also changes as the

beam diameter increases. Careful inspection of Figure 7.7 shows that this variation of the aberration magnitude approximately follows the trend indicated by the aperture function plotted in Figure 4.22B. In other words, as the beam diameter increases, more of the tip-vortex aberration is captured within the beam, so that the OPD_{RMS} first increases until the beam diameter is large enough to capture the full aberration, after which the OPD_{RMS} drops off as the beam diameter continues to increase.

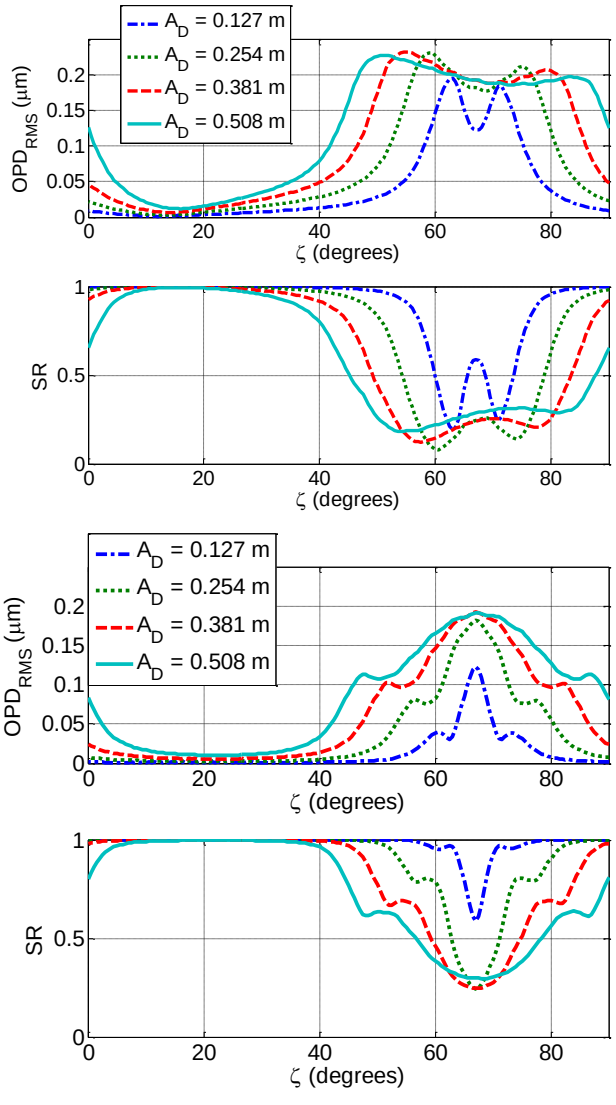

Figure 7.7: Effect of beam diameter on the OPD_{RMS} and Strehl ratio for a medium-sized helicopter hovering: A) raw data, B) tilt removed optical data.

7.5. Hovering-Flight Model - Optical Correction

As shown in Figure 7.5, and tabulated in Table 7.1, the difference in Strehl ratio between the raw signal and the tilt-removed signal illustrates the improvement that can be obtained by even a rudimentary AO correction of just optical tip/tilt. Figure 7.8A shows the slope of the best-fit line of the aberrated wavefront (i.e. the optical tilt) as a function of rotor phase angle for the hovering case examined in Section 7.3. Figure 7.8B is the corresponding power spectrum of the data in Figure 7.8A. Since the helicopter has a 4-blade rotor, the fundamental component of the power spectrum occurs at a nondimensional frequency of $\omega\Omega^{-1} = 4$. Figure 7.8B shows that the tilt of the aberration also contains significant high-frequency harmonic content due to the non-sinusoidal shape of the tilt slope in Figure 7.8A.

It should be noted however that the prescribed-wake model employed in this investigation does not account for aperiodic effects, such as vortex meander or vortex merging, which tend to alter the character of the aberration from cycle to cycle (see Section 6.4). If these aperiodic effects were small, then an open-loop controller based on the relative-beam angle, ζ, as well as the elevation angle and azimuthal angle of the outgoing beam might be sufficient to remove the majority of the signal tilt, and possibly even higher-order aberrations using a deformable mirror.

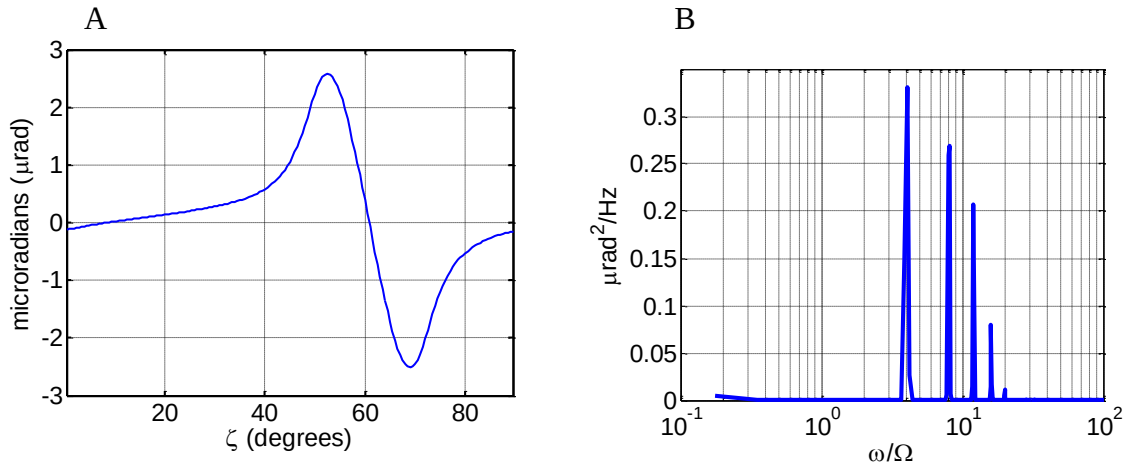

Figure 7.8: A) Optical tip/tilt of the helicopter wake aberration. B) Spectral decomposition of optical tip/tilt shown in A.

For this kind of open-loop control, any aperiodicity of the aberration would degrade the effectiveness of the correction. As a first approximation, the main effect of vortex meander or merging would be to slightly shift the location of the vortex filament up or down (i.e. in the z-direction in Figure 7.1) from the location predicted by Landgrebe's model. This means that the main outcome of these aperiodic effects would be to shift the effective relative-beam angle at which the outgoing beam crosses the tip vortex; as such, an idea of how aperiodic effects might influence an open-loop control approach can be obtained by examining the effect of a phase error in the open-loop controller. This was modeled by shifting the signal in Figure 7.8A to create a simulated phase error between the actual and expected vortex location, to produce an error in the actual tilt and the applied tilt correction. Figure 7.9 shows that the time-averaged Strehl ratio for the open-loop correction remains larger than the uncorrected Strehl ratio up to a $\pm 10°$ phase error in the applied correction. However, for phase errors greater than 10 degrees, an open-loop correction approach would actually make the outgoing beam

worse. Figure 7.9 also shows that if it is desired to maintain a minimum Strehl ratio larger than the minimum uncorrected Strehl ratio throughout the cycle, then the maximum permissible phase error is reduced to $\pm 4°$.

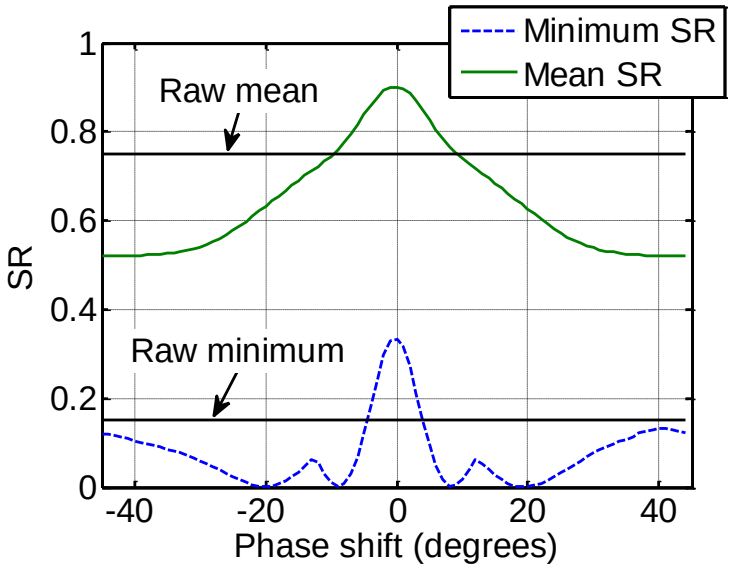

Figure 7.9: Effect on time-averaged Strehl ratio of a phase error between the expected and actual vortex location for a simple open-loop AO tilt-correction scheme.

The results shown in Figure 7.9 illustrate that an open-loop AO system could be beneficial; however, if effects such as vortex meander or merging significantly distort the geometry of the vortex system, then an open-loop AO system could result in a reduction in optical performance. In this case, a closed-loop AO system would have to be used where the optical tilt is measured and then sent to a fast-steering mirror to apply the appropriate correction. To assess this kind of closed-loop control approach, a closed-loop AO system simulation code (Cole and Washburn 2010) was adapted to analyze the tip/tilt coefficient and performance gains of closed-loop control. The code used the tip/tilt coefficient from the wavefront data in Section 7.2 to determine the effectiveness of a closed-loop AO correction for different sampling/update rates of the fast steering mirror.

The results for various controller bandwidths using a Type I (first-order) controller are shown in Figure 7.10. As shown, a controller with a bandwidth of 500 Hz or greater is capable of removing almost all residual tilt yielding results equivalent to an infinite bandwidth controller (ideal).

7.6. Comparison of Isentropic and WCM Models

As a final examination of the hovering-flight case, it is worth comparing the density-field solution obtained using the isentropic and WCM methods for the same hovering-flight velocity field. As was shown in Chapter 4, for the isolated tip vortex there is a slight difference in the thermodynamic properties computed using the isentropic and WCM methods, especially in the temperature and therefore density fields. Furthermore, the experimental data presented in Chapter 5 suggested that the isentropic method better matched the measured optical effect of the isolated tip-vortex flow.

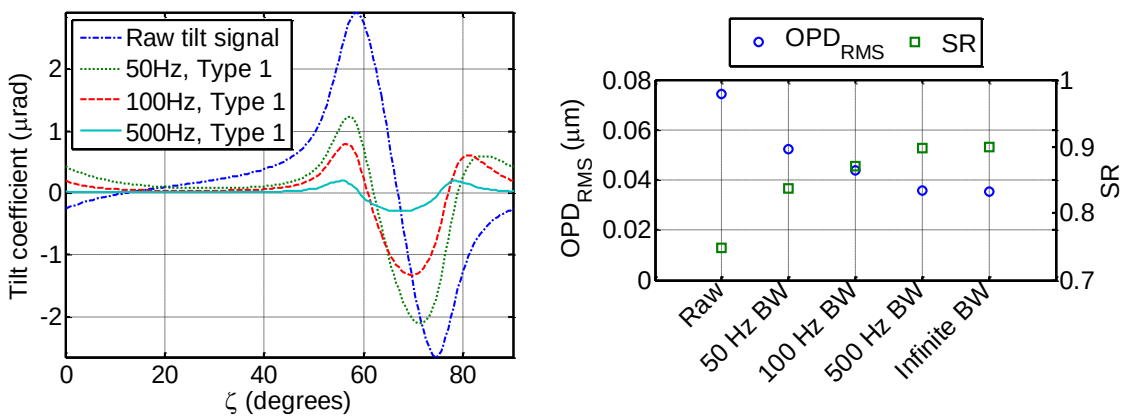

Figure 7.10: Optical system performance using a closed-loop Type 1 controller over a range of controller bandwidths. A) Residual tilt after correction and B) average OPD_{RMS} and SR over a single cycle.

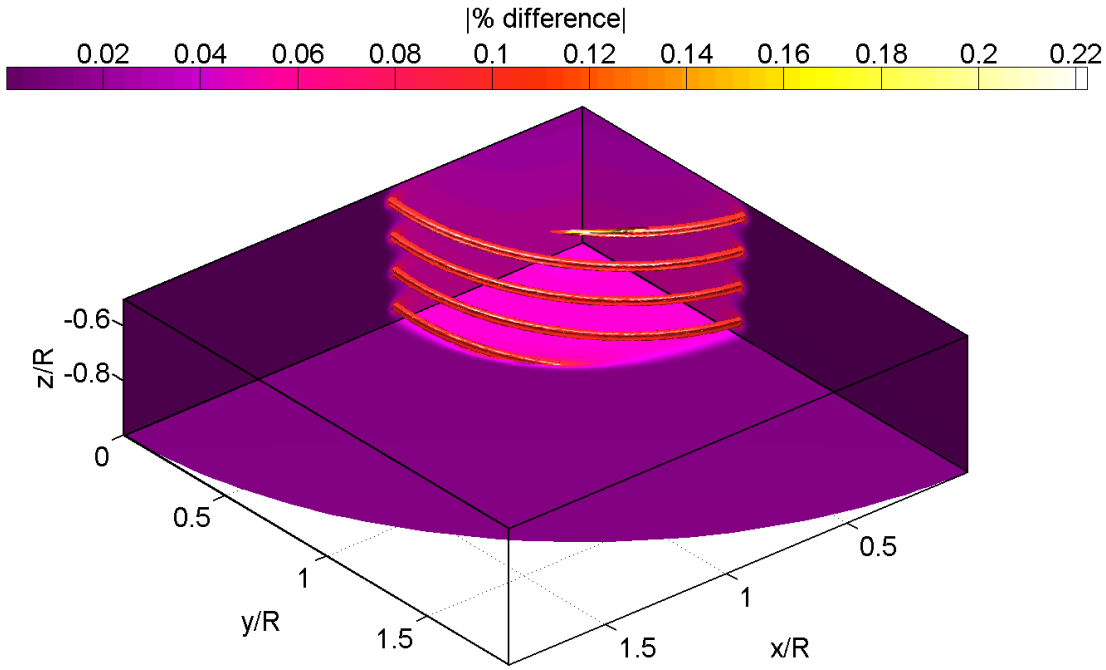

Figure 7.11: Comparison of the percent difference in the density from the isentropic and WCM methods for the full flow field hovering calculations.

Figure 7.11 shows the percent difference in the computed density fields for the hovering flow field investigated in Section 7.3; as illustrated in Figure 7.11, the two methods yield nearly identical density fields (within 0.3%). The OPD_{RMS} for both numerical methods was also calculated and is shown in Figure 7.12. As shown in the figure, the isentropic method predicts a slightly larger OPD_{RMS} value then the WCM method; this outcome conforms to the results of Chapter 4. Therefore, the WCM method produces slightly more optimistic predictions than the isentropic method for the optical effect of the helicopter vortex system.

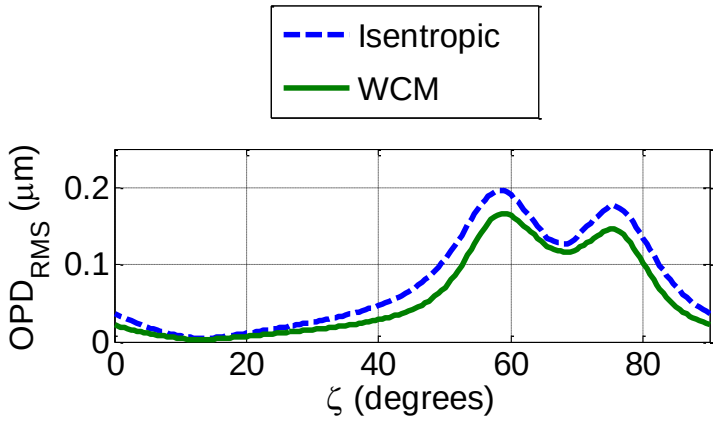

Figure 7.12: Comparison of the OPD_{RMS} predicted by the isentropic and WCM methods for the full flow field hovering calculations for a circulation strength of 21 m^2/s a vortex growth rate using a_1 = 0.0004.

7.7. Forward Flight - Helicopter Wake Characteristics

For a helicopter in hover, the blade wake system is predominantly axisymmetric (Leishman 2000; Leishman 2006), at least for the first two revolutions before it may become aperiodic due to vortex meander and merging (see Section 6.4). The flow field is dominated by the vortex sheet and tip vortices spiraling downward in a helical pattern. On the other hand, during forward flight, the wake is no longer axisymmetric since the forward-flight speed of the helicopter causes the wake to be swept backwards. From flow visualization studies, the tip vortices initially form a series of interlocking epicycloids. As shown in Figure 7.13, the interaction of the tip vortices results in the rolling up of two "super vortices" on the lateral edges of the vortex system, as described in (Leishman 2000; Wie *et al.* 2009).

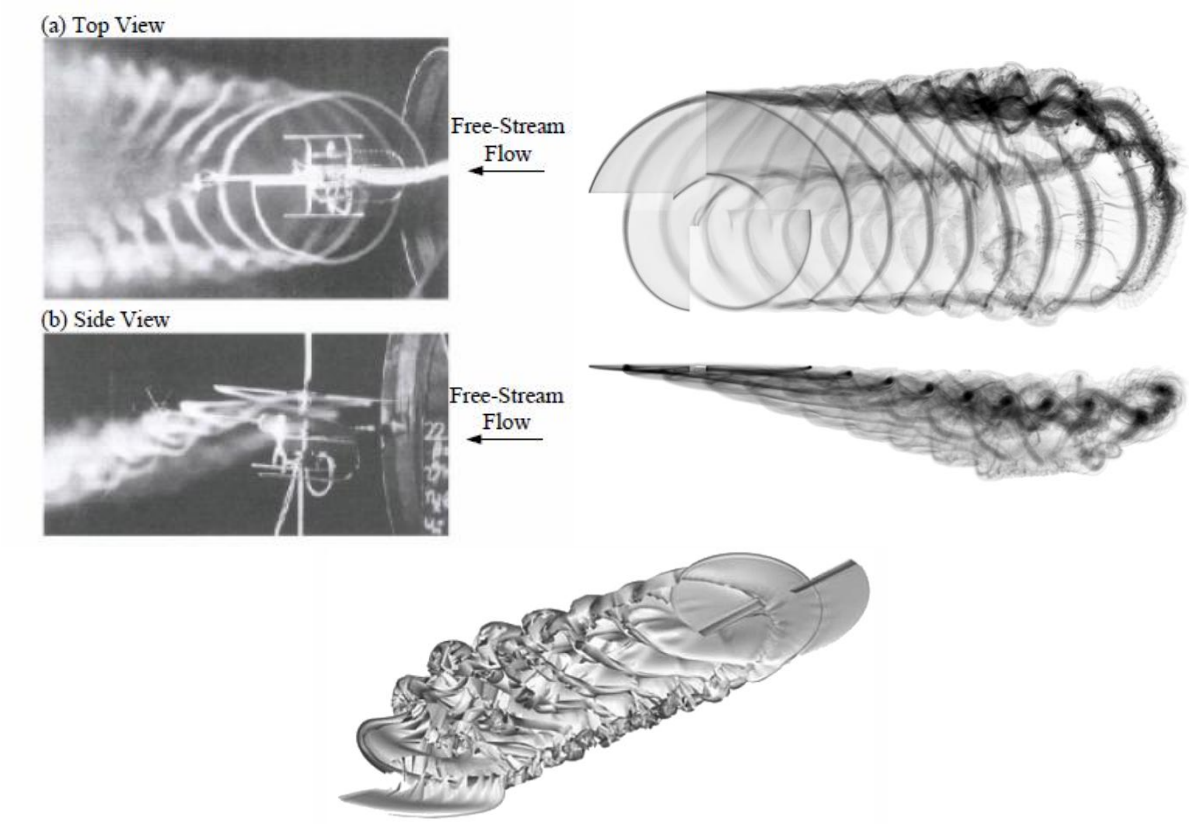

Figure 7.13: Visualization of the wake of a helicopter in forward flight. Top left) Smoke flow visualization from Rinehart (Leishman 2000), Top right) Computed particle vorticity field in the rotor wake (Stock *et al*. 2010), Bottom) Computed vorticity field in the rotor wake (Wie *et al.* 2009).

To investigate the aero-optic environment around a helicopter in forward flight the same weakly-compressible approach used in the hovering calculations presented above was employed. As discussed in Chapter 6, the modified prescribed wake model of Beddoes (Beddoes 1985; Leishman 2000) was used to determine the geometry of the forward-flight vortex system. The Biot-Savart law was then used to calculate the induced velocity throughout the area of interest around the helicopter, after which the weakly-compressible approach was used to compute the thermodynamic properties of the flow. Note that the data presented in this section were obtained using the WCM method,

although nearly identical results in the thermodynamic properties were obtained using the isentropic method (Section 7.9). With the density known, the corresponding Optical Path Difference (OPD) for a beam of light traversing the flow was computed and the Strehl ratio (λ = 1μm) was computed using the Fraunhofer approximation to determine the farfield effect of the tip-vortex system.

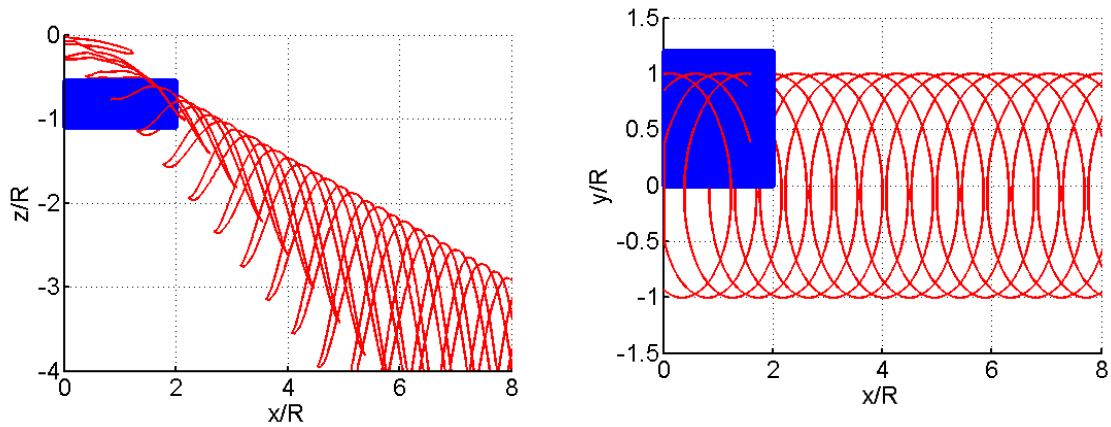

Figure 7.14: Tip-vortex geometry for a medium-sized helicopter (Appendix D) computed using Beddoes prescribed-wake method for a forward-flight speed of 20 m/s. Only one of the four blade-tip vortex filaments is shown for clarity. The region of field points at which the velocity and thermodynamic data were computed is shown in blue.

The calculations were performed for a medium-sized helicopter, with detailed parameters summarized in Appendix D. The tip-vortex geometry for a typical data set is shown in Figure 7.14. Figure 7.14 also shows the field points (blue) at which the velocity and thermodynamic data were calculated. The field points were spaced evenly in the *x*, *y*, and *z* directions at 0.0245 m intervals (or 0.003*R* where *R* is the radius of the blade). At this grid spacing, approximately 8-10 field points were contained within the vortex core; based on the aperture ratio and grid resolution study of a single vortex (see section 4.6) this spacing results in an estimated error in the OPD_{RMS} of less than 6%. The tip-vortex

system was modeled over forty revolutions of the rotor blade, which is the same number of revolutions used in the hovering calculations presented above.

Since the Beddoes' prescribed-wake model produces a wake with a symmetry plane along the line of flight of the helicopter, only half of the wake was modeled; this allowed the use of a higher spatial grid resolution for the same computational effort. In the results presented below, the data was mirrored about the symmetry plane to aid in the interpretation of the results. At a forward flight speed of 10 m/s, a series of calculations were performed with the rotor angle stepped in five degree increments until a full 90 degrees of rotation was achieved. At 15 m/s, the same calculations were performed but the blade was rotated in 10-degree increments. At the higher flight speeds investigated, the wake is swept farther back, requiring a much larger computational domain to capture the wake; therefore, only single rotor angles were computed at the higher flight speeds to serve as a basis for approximate methods presented at the end of the chapter.

7.8. Forward Flight - Numerical Results

To illustrated the shape of the forward-flight wake system, Figure 7.15 shows an isosurface of the calculated density at a forward flight speed of 10 m/s with a schematic of a medium-sized helicopter superposed to show the orientation of the wake. To further aid in the visualization of the wake of the helicopter, Figure 7.16 shows points in the computational domain where the magnitude of vorticity was 18 1/s (this value was chosen arbitrarily to best show the wake geometry) plotted for forward flight speeds of 10, 20, and 30 m/s.

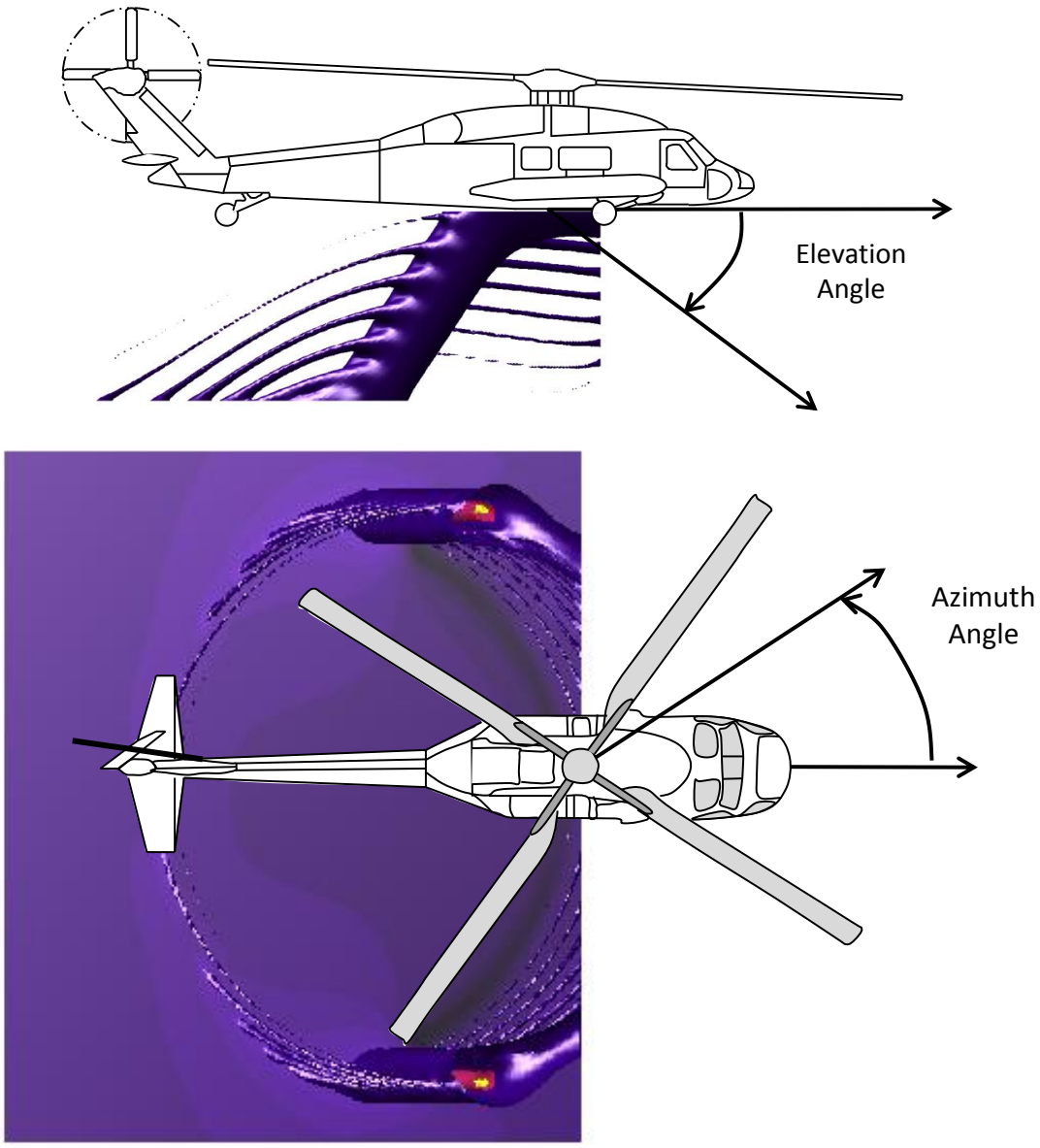

Figure 7.15: Reference figure of the wake with relationship to the helicopter at a forward flight speed of 10 m/s. Isosurfaces of the density field are shown.

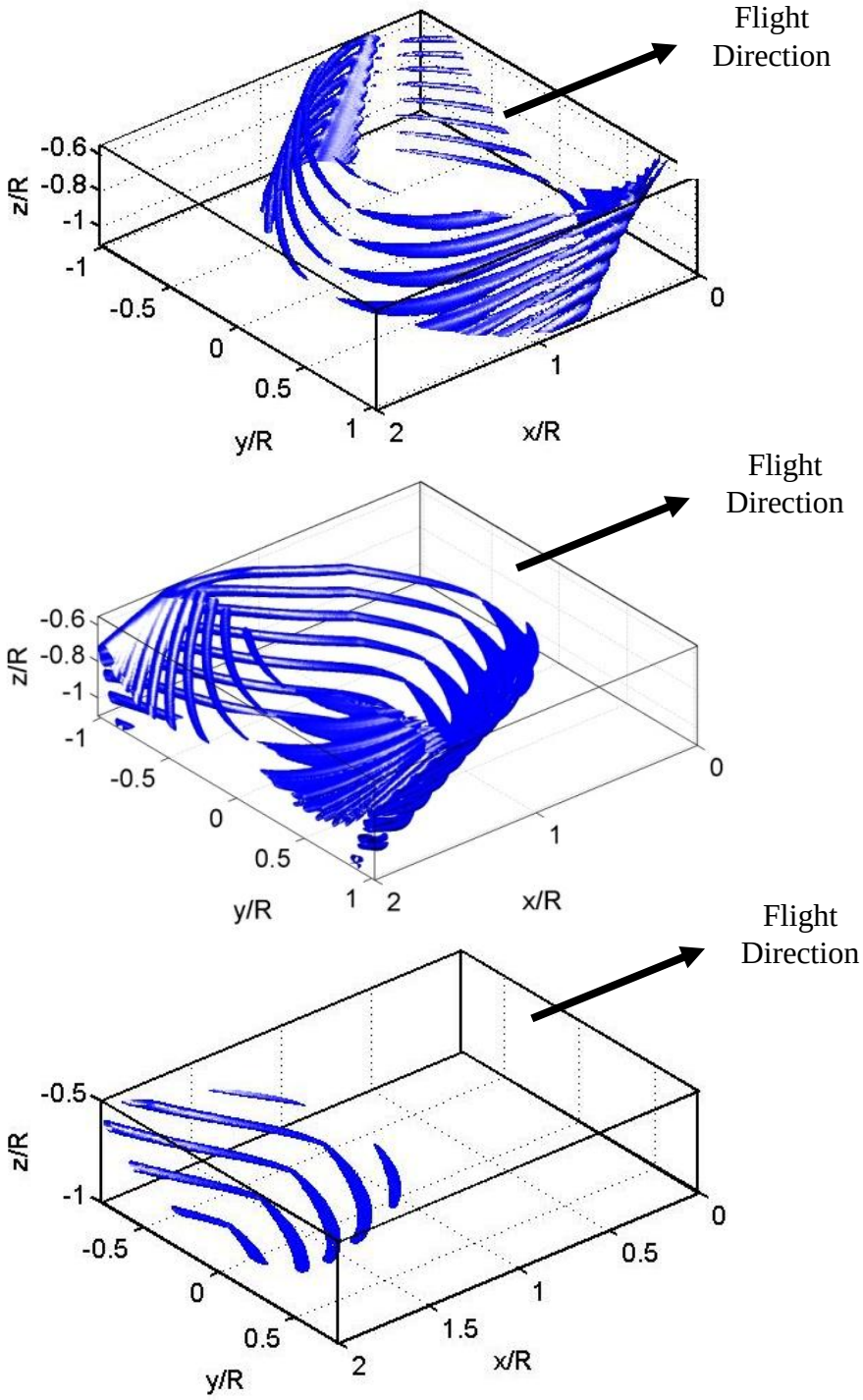

Figure 7.16: Contours of a constant angular velocity of 18 1/s. Top) V_∞=10m/s, Middle) V_∞=20m/s, and Bottom) V_∞=30m/s.

In the top two graphs (10 and 20 m/s flight speeds), the merging of the vortices into a much stronger "super vortex" along the sides of the wake is evident. Furthermore, as the forward flight speed of the helicopter increases, the wake from the blade tip vortices is swept more and more backwards, so that by 30 m/s only a small portion of the wake is still contained in the computational domain. At sufficiently-high forward flight speeds, the tip-vortices shed when the blades are passing in front of the helicopter are actually swept back above the plane of the rotor. While the sweeping back of the wake can create problems such as blade-vortex interactions (BVI), in terms of aero-optics the wake sweep-back is a desirable feature since it removes the wake vortices from the field-of-regard of an optical system mounted on the helicopter.

The computed wakes in Figure 7.16 show several similarities with the flow-visualization shown in Figure 7.13. First, the rollup of the tip vortices along the lateral edge of the wake into a "super vortex" is clearly visible. Furthermore, the presence of tip vortices in the middle of the wake that have been carried back behind the helicopter by the freestream are also clearly visible in Figure 7.16.

7.8.1. Optical Effect at a Single Rotor Phase Angle

The optical effect of the forward-flight helicopter wake will first be shown for a single phase angle of the rotor. Figure 7.17 shows the calculated density field at a forward velocity of 10 m/s and a rotor phase angle of ψ_R = 0 degrees. Using the density field shown in Figure 7.17, the index-of-refraction was calculated using the Gladstone-Dale relationship and then interpolated onto four simulated beam paths corresponding to azimuth angles of 90°, 109.5°, 135°, and 180°, all at an elevation angle of 0°. The

diameter of the simulated beam was set to 0.3 m, which was judged to be a reasonable beam diameter for an optical system carried by a medium-sized helicopter. For reference, an azimuth angle of zero degrees is defined as the beam pointing straight forward, while an elevation angle of zero degrees is defined as the beam travelling parallel to the TPP, with the beam propagating away from the belly of the helicopter as the elevation angle increases (see Figure 7.15). Figure 7.17 also shows the corresponding farfield irradiance patterns of the four beams which were calculated using the Fraunhofer approximation with a wavelength of 1.0 μm. For reference, a crosshair is placed at the central aiming point of the beam. For the irradiance patterns shown, no optical correction, such as the removal of tip/tilt has been made.

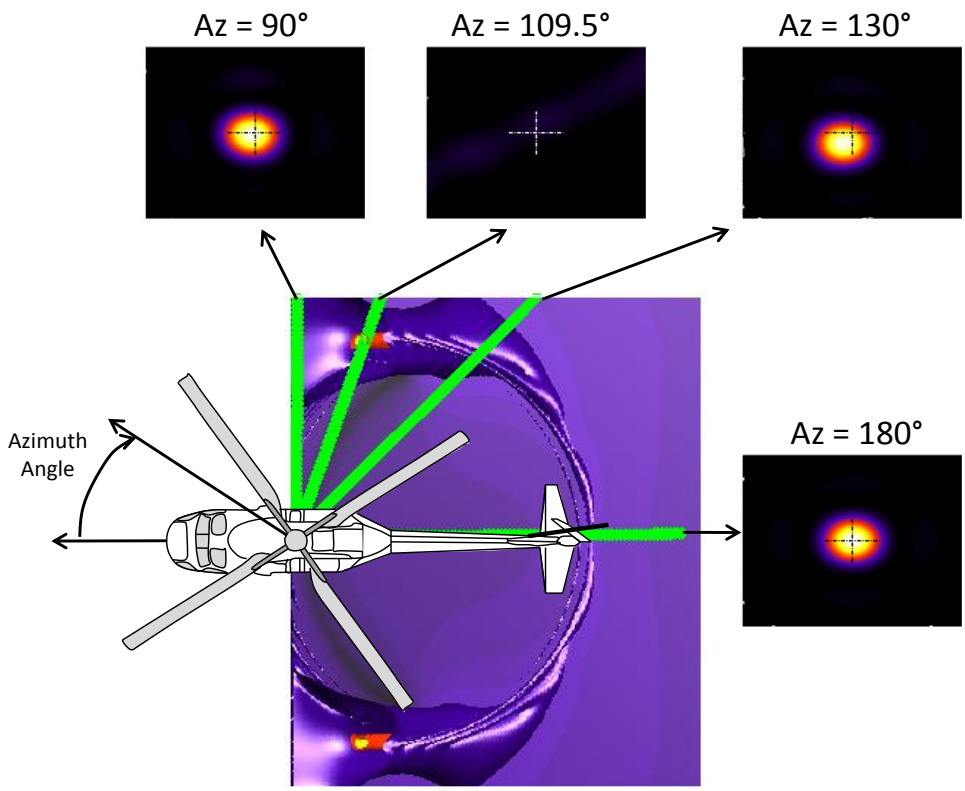

Figure 7.17: Calculated density field at a forward flight speed of 10 m/s and the corresponding farfield irradiance (λ=1.0 μm) pattern on an outgoing beam at four different azimuth angles.

At azimuth angles of 90° and 135°, the farfield irradiance pattern is very similar to the diffraction-limited irradiance pattern, although there is a small amount of bore-sight error present due to tip/tilt imposed upon the beam. For this particular rotor phase angle and flight speed, at 180° the beam misses the tip vortex structures in the wake and therefore is not affected by the wake. However, at 109.5°, the beam propagates through the center of the "super vortex" along the lateral edge of the wake; as a result, the main lobe of the beam is displaced off target by tip/tilt and also strongly diffused by the higher-order components of the aberration. The resulting Strehl ratio at this angle was reduced to below 0.1 illustrating the serious effect that the wake can have on an optical system in certain orientations.

Figure 7.18 summarizes the calculated OPD_{RMS} and Strehl ratio at an elevation angle of zero degrees for various azimuth angles of the outgoing beam ranging from 90° to 180° in 0.5° increments. The calculations were performed for forward flight speeds of 10 m/s (top) and 20 m/s (bottom). Considering the case of forward flight at 10 m/s, Figure 7.18 shows that the OPD_{RMS} increases sharply as the azimuth angle increases from 90° to approximately 109.5^o; however, a large portion of the increase is due to tip/tilt since the size of the "super vortex" is on the order of the beam diameter. As the "super vortex" becomes centered within the beam at 109.5^o, the tip/tilt effect of the super vortex becomes small, leaving mainly higher order aberrations. As the azimuth angle continues to increase, the density gradient of the super vortex once again produces a tip/tilt aberration on the beam. This decreases as the azimuth angle continues to increase and the beam no longer propagates through the vortex. The wake has a similar effect on the outgoing beam at 20 m/s.

For all the OPD data, the effect of removing tip/tilt was also investigated, and these results are also shown in Figure 7.18. By removing tip/tilt, the bore sight error at 90° and 135° is corrected. Correction of tip/tilt also increased the Strehl ratio at 109.5°; however, the beam is still strongly affected by the higher-order components of the aberration as it propagates through the center of the "super vortex." The Strehl ratio at this point remains below 0.2.

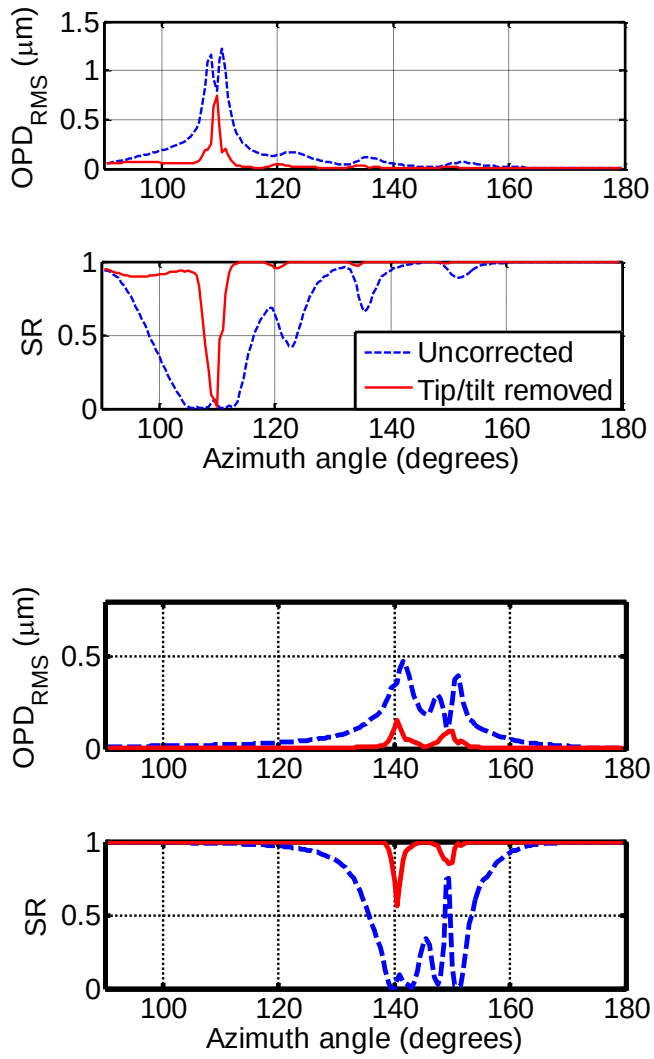

Figure 7.18: Calculated spatial OPD_{RMS} and Strehl ratio at an elevation angle of zero degrees at a forward flight speed of 10 m/s (top) and 20 m/s (bottom).

Figure 7.18 shows the effect of the helicopter wake on a beam projected outwards at an elevation angle of 0°. The same calculations were performed at other elevation angles. Figure 7.19 shows the computed OPD_{RMS} over a range of azimuthal and elevation angles for a simulated beam propagating through the computational domain; as such, Figure 7.19 gives a good representation of the effective field of regard of an optical system mounted on the helicopter. Again it can be noted that in Figure 7.19, positive elevation angles refer to the beam directed at targets below the helicopter. The location of the "super vortex" is clearly evident in Figure 7.19, as the region of high OPD_{RMS} and low Strehl ratio. The instantaneous location of the individual tip vortices can also be seen in Figure 7.19. Note that for the 10 m/s case, the large aberration associated with the super vortex appears to stop at an elevation angle of approximately 25°. This is merely an artifact of the finite extent of the computational domain. If the computational domain were larger, then the beam would still propagate through the super vortex at that elevation angle.

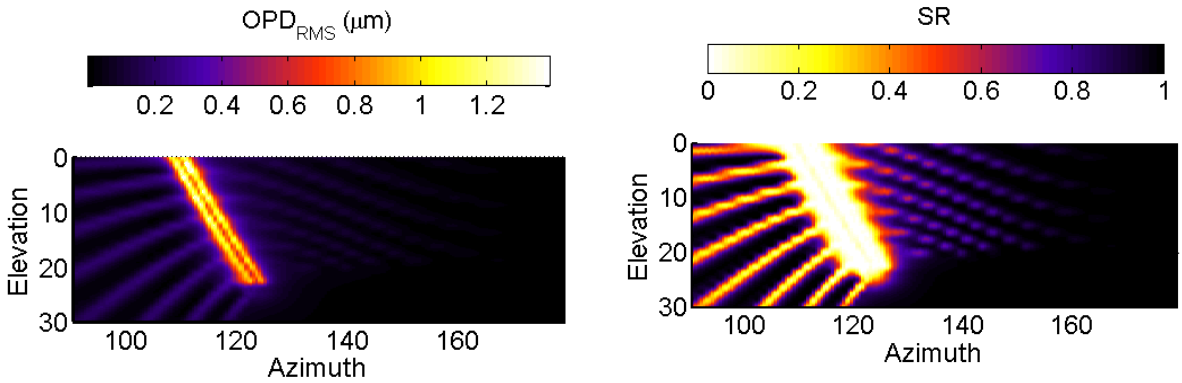

Figure 7.19: The calculated field-of-regard for a forward flight speed of 10 m/s: OPD_{RMS} (left) and Strehl ratio (right).

7.8.2. Optical Effect over a Full Rotor Cycle

Figure 7.19 shows the effective field of regard of a helicopter-mounted optical system at a single phase angle of the helicopter rotor. To illustrate how the field of regard changes as the rotor blades rotate through a full cycle, the optical aberrations at a forward flight speed of 10 m/s were calculated for different rotor angles, ψ_R, from 0 to 90 degrees in five degree increments. Figure 7.20 ($0<\psi_R<40$) and Figure 7.21 ($50<\psi_R<80$) show the calculated OPD_{RMS} and Strehl ratio (uncorrected for optical tip/tilt) in ten-degree increments. The figure shows how the small "ribbons" of low Strehl ratio associated with individual tip vortices move downward in the field of regard as the rotor angle changes, while the large low-Strehl-ratio "blind spot" in the field of regard caused by the super vortex remains essentially stationary. Figure 7.22 shows the OPD_{RMS} and Strehl ratio averaged over the blade rotation cycle.

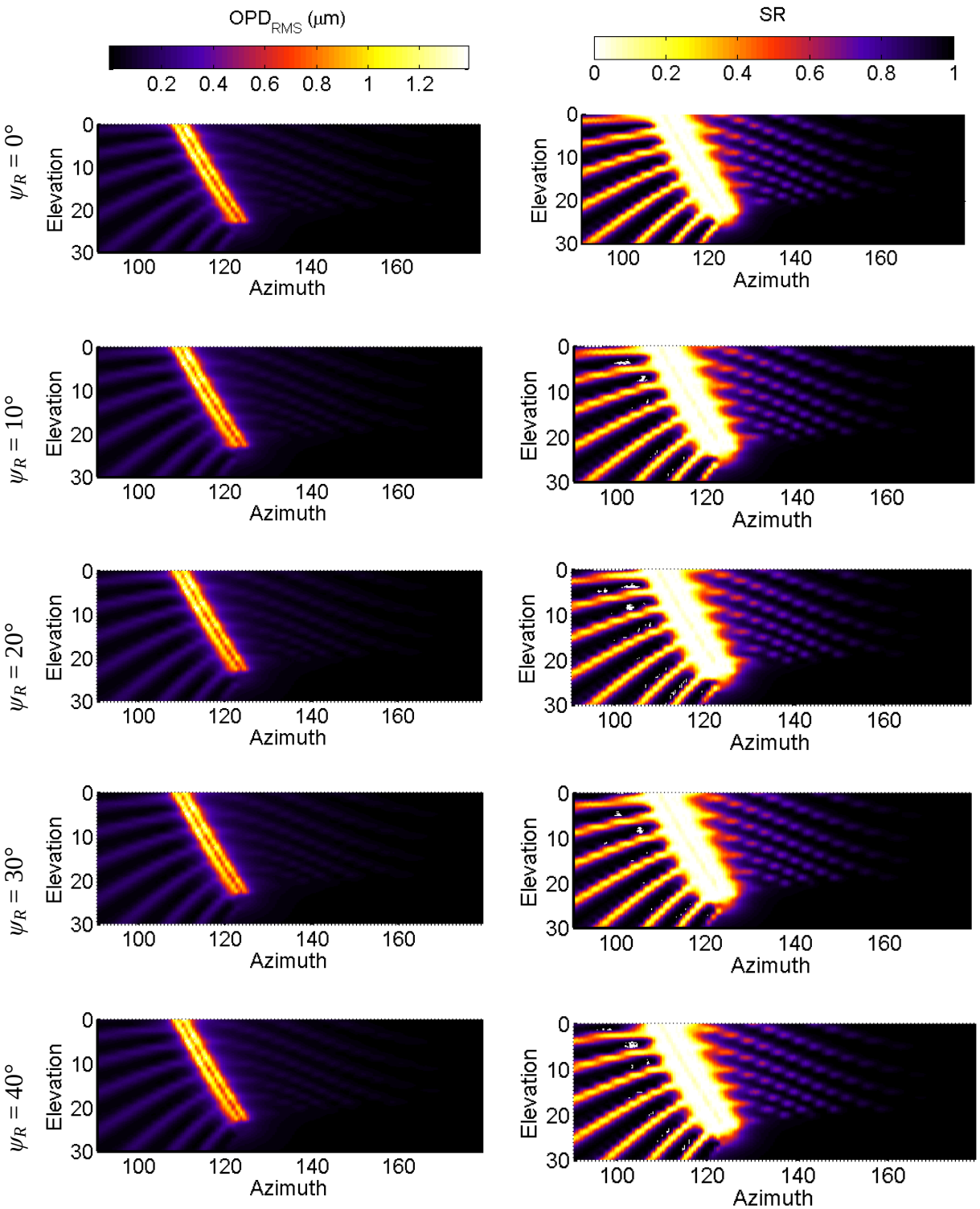

Figure 7.20: The calculated field-of-regard for a forward flight speed of 10 m/s rotating the blade in 10 degree increments from the top to the bottom: OPD_{RMS} (left) and Strehl ratio (right).

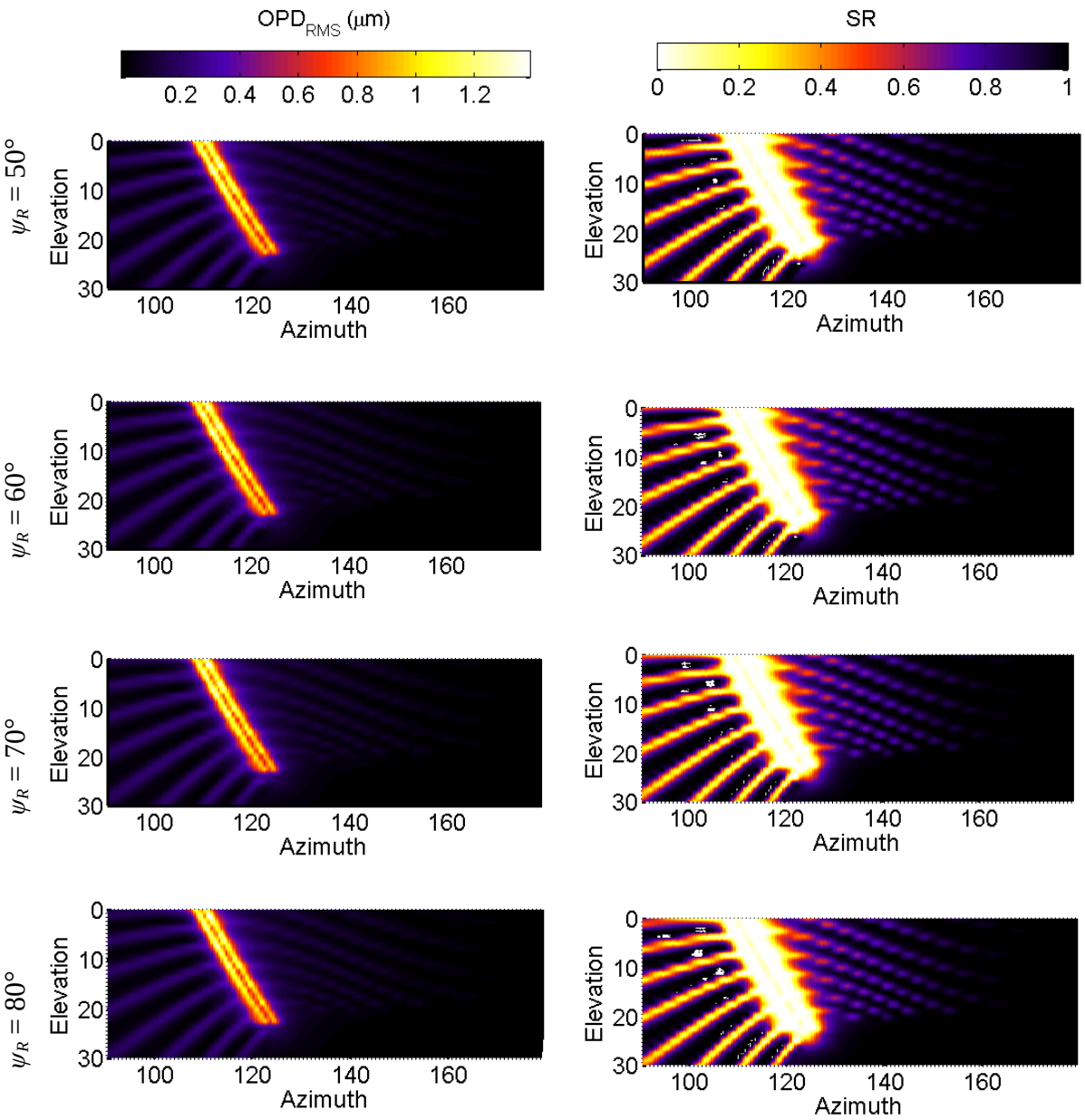

Figure 7.21: The calculated field-of-regard for a forward flight speed of 10 m/s rotating the blade in 10 degree increments from the top to the bottom: OPD_{RMS} (left) and Strehl ratio (right).

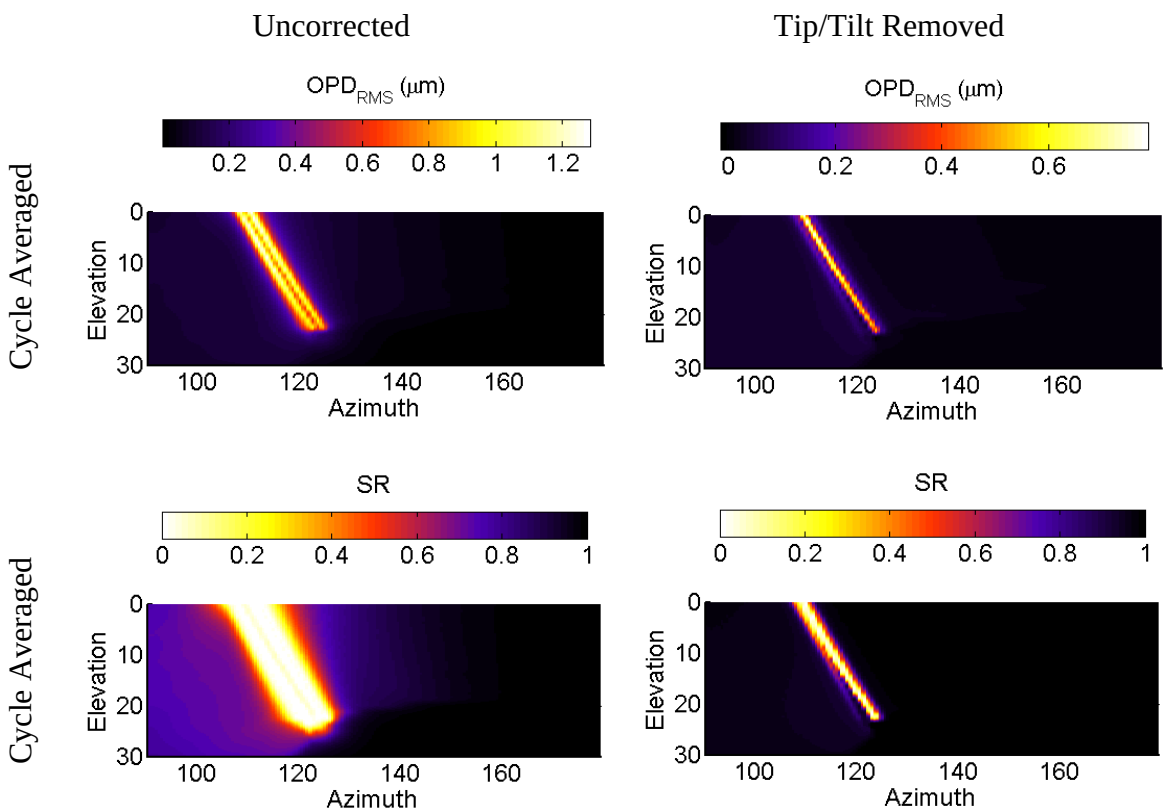

Figure 7.22: Time-averaged field-of-regard for a forward flight speed of 10 m/s rotating the blade in 5-degree increments: OPD_{RMS} (top) and Strehl ratio (bottom).

Up to a forward flight speed of 10 m/s, the vortex wake from the helicopter propagates mainly downwards, such that over the range of beam directions available within the computational domain, the beam never passes through more than a single tip vortex at a time (except for the super vortices on the edges of the wake). By a forward flight speed of 15 m/s however, the wake is swept back sufficiently that when looking backwards, the beam will propagate through multiple tip vortices. Figure 7.23 shows the calculated density field at a forward-flight speed of 15 m/s and a rotor phase angle of zero degrees, along with the corresponding instantaneous OPD_{RMS} and Strehl ratio for the range of azimuth and elevation angles available in the computational domain. In this

case, the super vortex on the lateral edge of the wake is still the dominant aberrating flow feature, but new regions of large OPD_{RMS} and corresponding low Strehl ratios are also evident corresponding to angles where the beam propagates through multiple tip vortices.

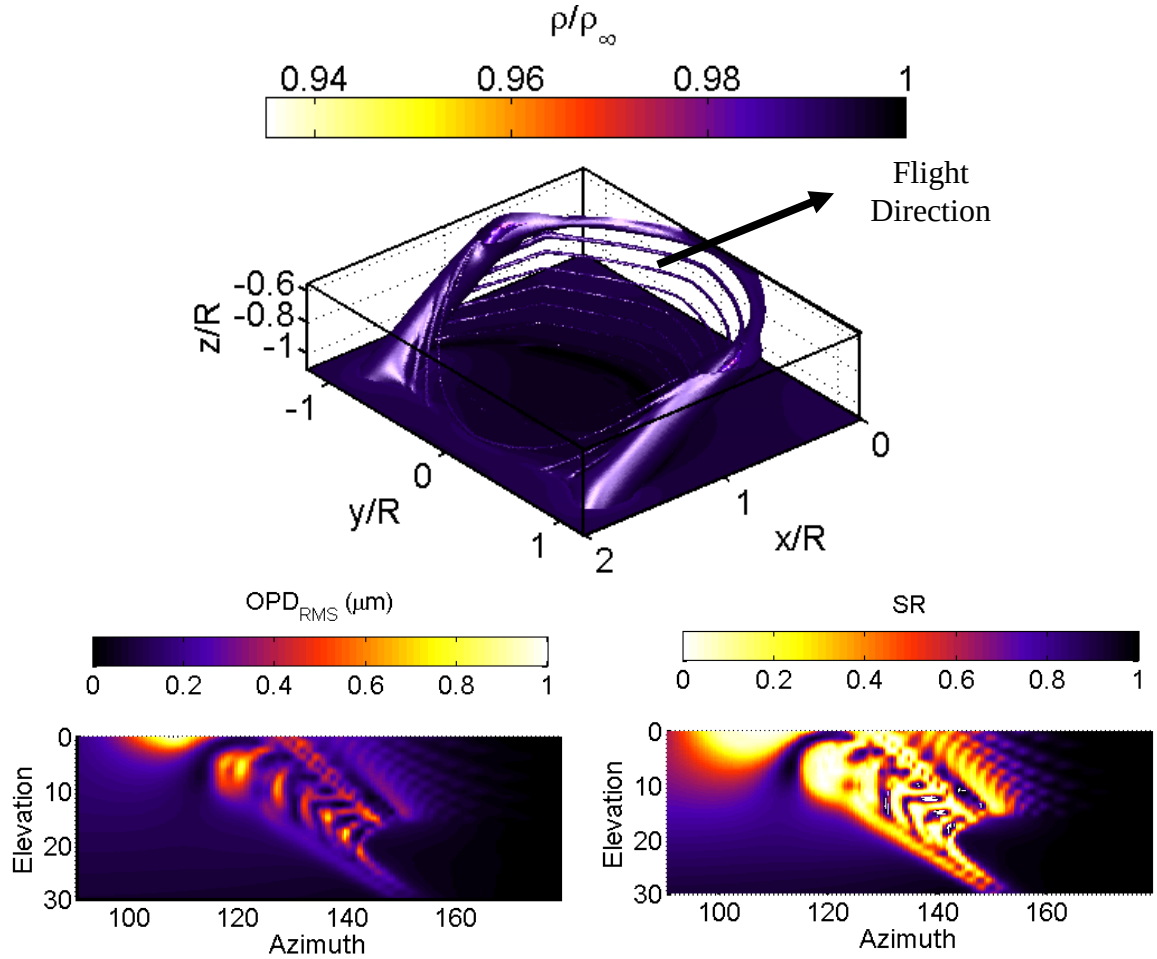

Figure 7.23: Instantaneous field-of-regard for a forward flight speed of 15 m/s and rotor angle of zero degrees: density field (top), OPD_{RMS} (left), and Strehl ratio (right).

7.9. Comparison of Isentropic and WCM Methods for Forward-Flight Case

The forward-flight optical results shown in the preceding section were computed using the WCM method. Figure 7.24 compares the OPD_{RMS} calculated using the isentropic and WCM methods over a range of azimuth and elevation angles. As shown in

the figure, the OPD_{RMS} calculated using the isentropic method is larger than the OPD_{RMS} calculated using the WCM throughout the field of regard; this is consistent with the findings of Chapters 4 and 5, and the hovering calculations shown above. Computed Strehl ratios for the two methods are compared in Figure 7.25, which shows that the minimum Strehl ratio in the field of regard computed using the isentropic method is around 0.2 lower than the minimum Strehl ratio determined using the WCM. In summary, the isentropic method generally predicts a stronger aberration and therefore lower Strehl ratio than the WCM; as such, if anything, the effect of the helicopter vortex wake on the farfield performance of an outgoing beam would probably be worse than the results computed using the WCM shown in this chapter.

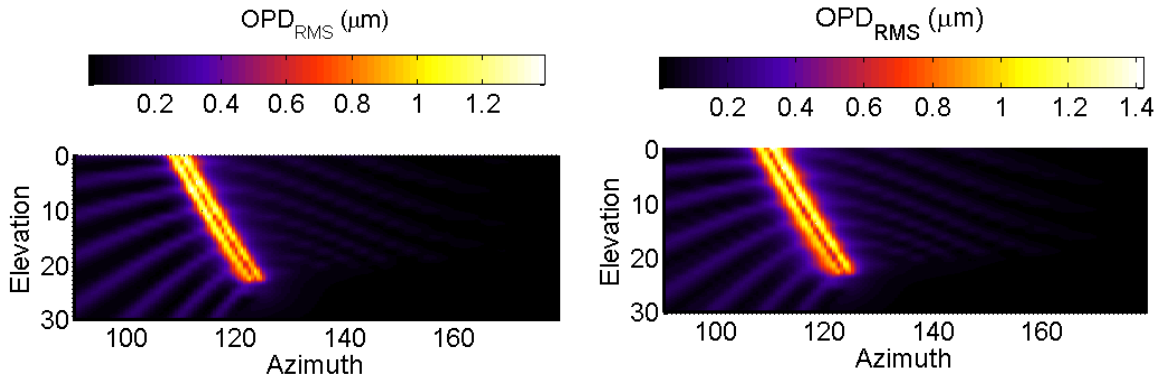

Figure 7.24: Calculated OPD_{RMS} over a range of azimuth and elevation angles using the WCM method (left) and isentropic method (right).

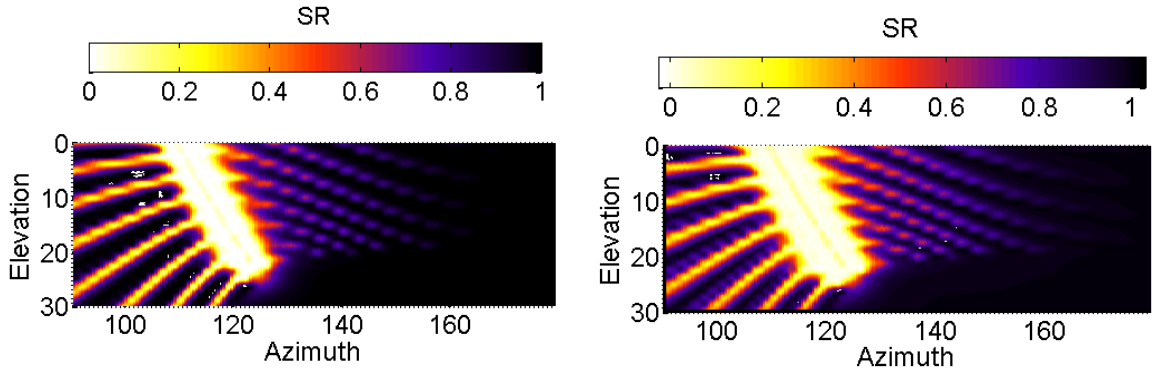

Figure 7.25: Calculated Strehl ratio over a range of azimuth and elevation angles using the WCM method (left) and isentropic method (right).

7.10. Forward Flight - Estimated Field-of-Regard

The field-of-regard calculations shown in the preceding section were limited by the size of the computational domain, which was made as large as possible based on the memory constraints of the computer hardware that was used for the investigation. However, it is possible to obtain a rough estimate of the field-of-regard based on the geometry of the helicopter wake, which can be predicted using Beddoes' model, in combination with the scaling relationship developed in Chapter 4. In this approximate method, the wake geometry is first determined using Beddoes' model, after which the azimuth and elevation angle from the optical turret to each vortex filament is calculated. At these azimuth and elevation angles, the corresponding OPD_{RMS} is calculated using the scaling relationship in Chapter 4. Note that this scaling relationship was developed for a single tip vortex under the assumption that the vortex is centered in and perpendicular to the outgoing beam. As such, the method is only an estimate since these assumptions are generally not fully met; on the other hand, as shown in Section 7.4, the scaling relationship developed in Chapter 4 can produce results that are reasonably close to the computations for the full wake.

Figure 7.26 shows field-of-regard results computed using this approximate approach for several rotor angles and a forward-flight speed of 10 m/s. Since the Large Aperture Approximation (LAA, Eq. (2.17)) does not provide an accurate estimate of the Strehl ratio for tip-vortex aberrations (Porter *et al*. 2011), the Gaussian basis function approximation (see Appendix B) was used to estimate the Strehl ratio. Comparing Figure 7.26 to Figures 7.20 - 7.22 shows that the approximate method captures with

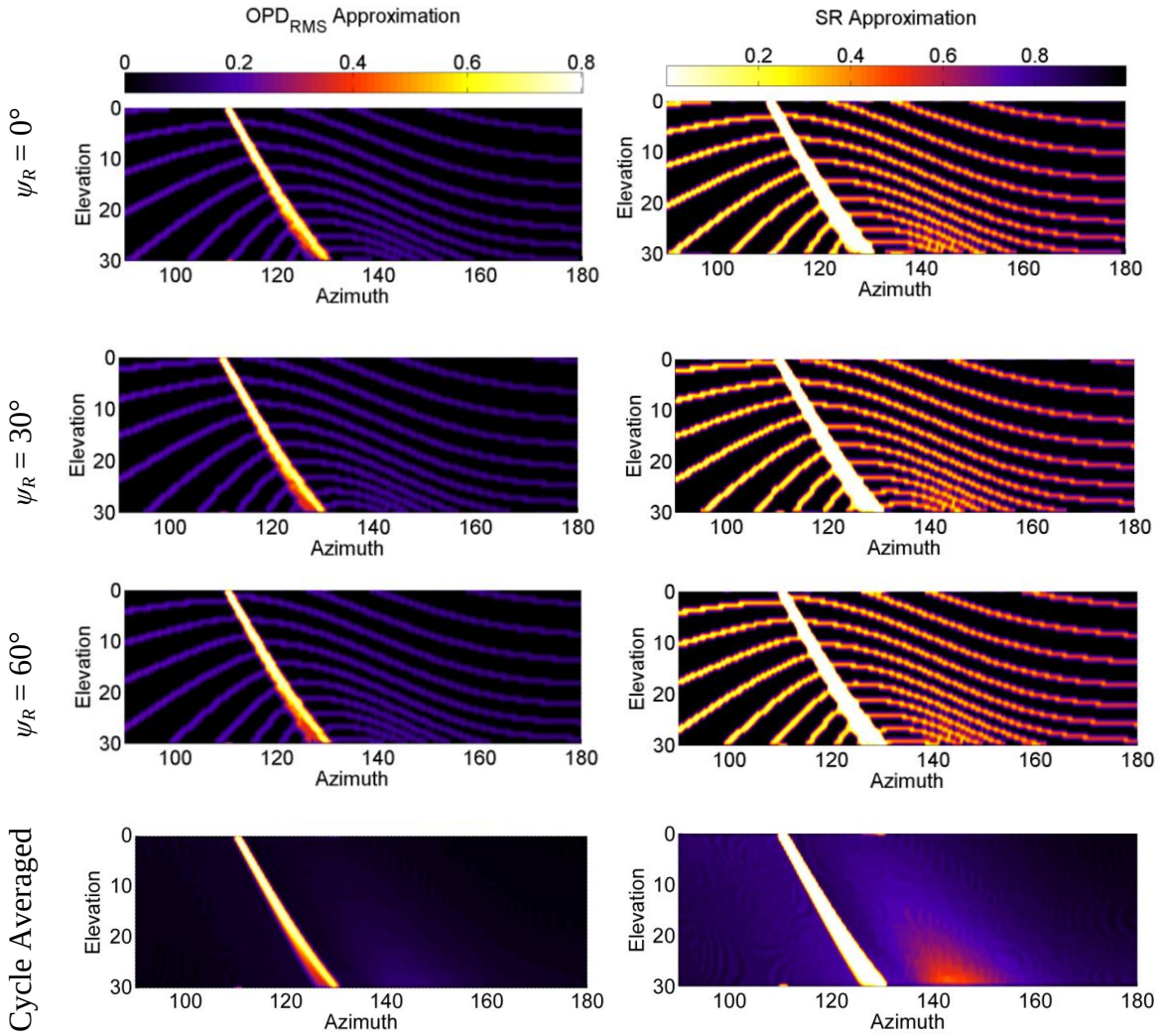

Figure 7.26: Estimated field-of-regard at a forward flight speed of 10 m/s at several rotor phase angles, computed using the scaling relationship for OPD_{RMS} developed in Chapter 4 and a Gaussian basis set to estimate the Strehl ratio (Appendix B). The left side of the figure shows the OPD_{RMS} while the right side shows the Strehl ratio.

reasonable accuracy the general trend of the field-of-regard predicted by the full weakly-compressible computational approach. The advantage of the approximate method is that it can produce an estimate of the field of regard over the full azimuth and elevation range of the turret, with a fraction of the computational effort required for the full approach shown in Section 7.9.

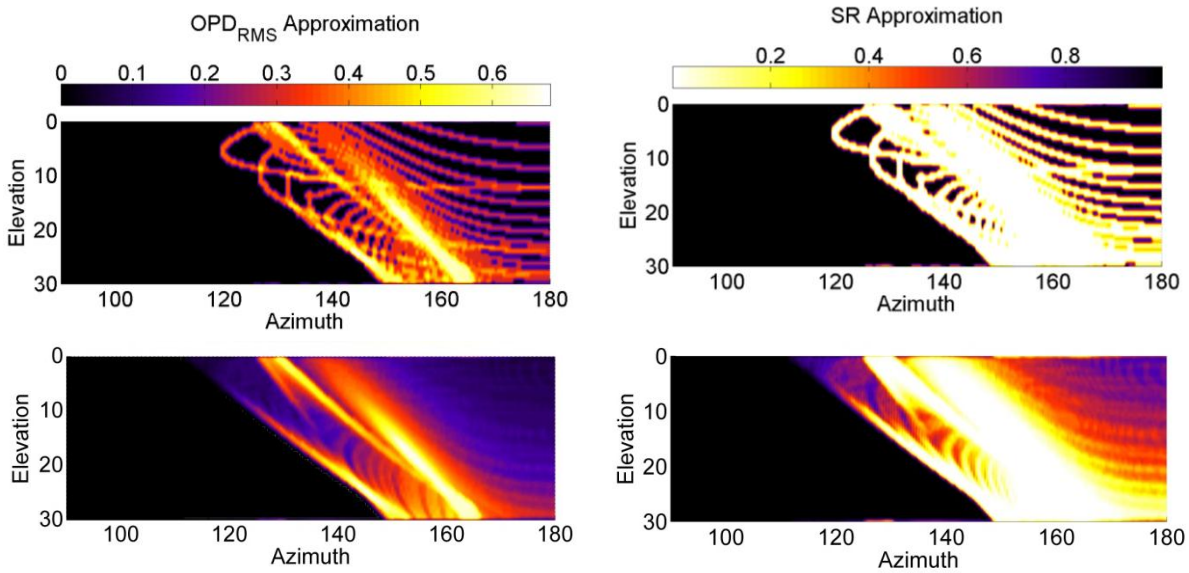

Figure 7.27: Estimated field-of-regard at a forward flight speed of 15 m/s based on the scaling relationship in Chapter 4 and a Gaussian basis set to estimate the Strehl ratio. On the top is a calculated instantaneous example with the time-averaged value on the bottom.

Figures 7.27 to 7.31 show the results for further applications of the approximate method for forward-flight speed of 15, 20, 30, 40, and 50 m/s. The same general pattern seen in Figure 7.23 is captured by this technique, illustrating its usefulness as a fast engineering approximation. Figures 7.27 to 7.31 show how the wake is swept more and more backwards as the flight speed increases, so that by 40 m/s, the field of regard is essentially unaffected by the rotor wake vortices.

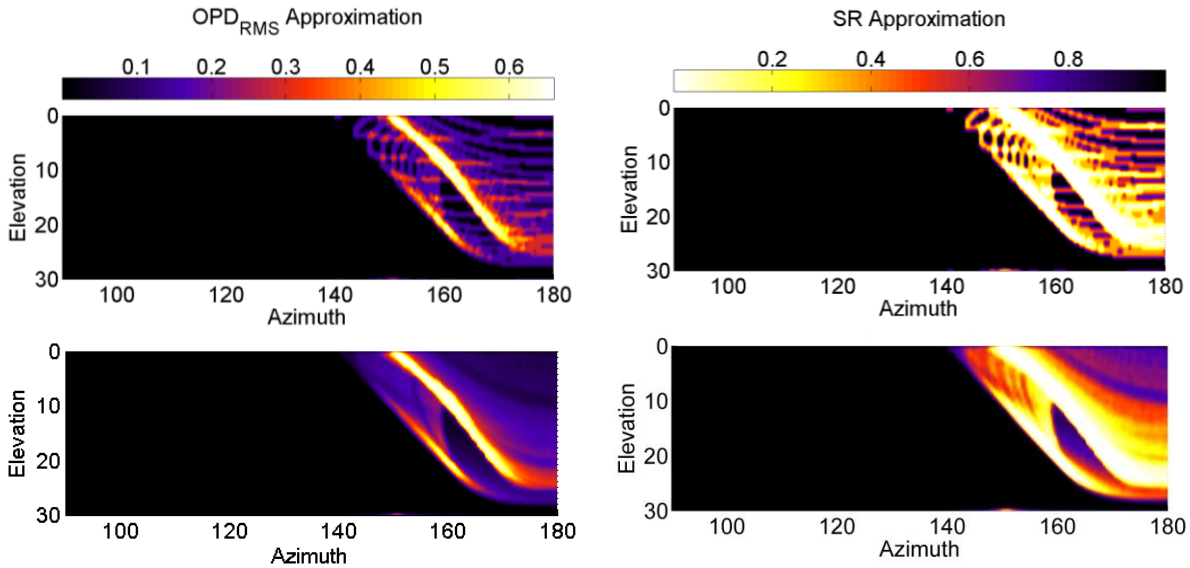

Figure 7.28: Estimated field-of-regard at a forward flight speed of 20 m/s based on the scaling relationship in Chapter 4 and a Gaussian basis set to estimate the Strehl ratio. On the top is a calculated instantaneous example with the time-averaged value on the bottom.

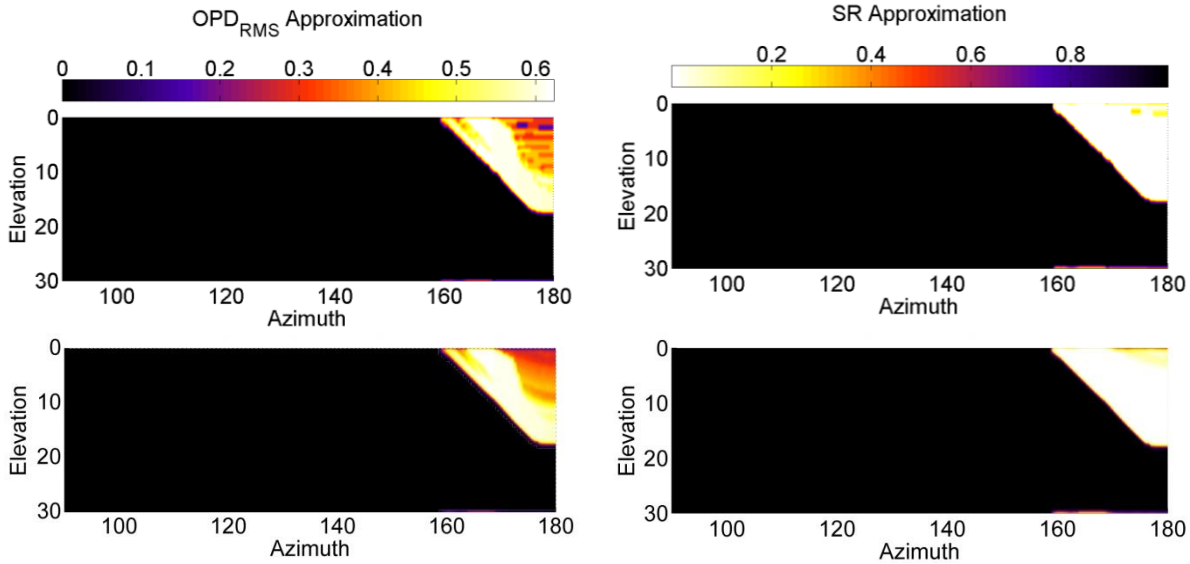

Figure 7.29: Estimated field-of-regard at a forward flight speed of 30 m/s based on the scaling relationship in Chapter 4 and a Gaussian basis set to estimate the Strehl ratio. On the top is a calculated instantaneous example with the time-averaged value on the bottom.

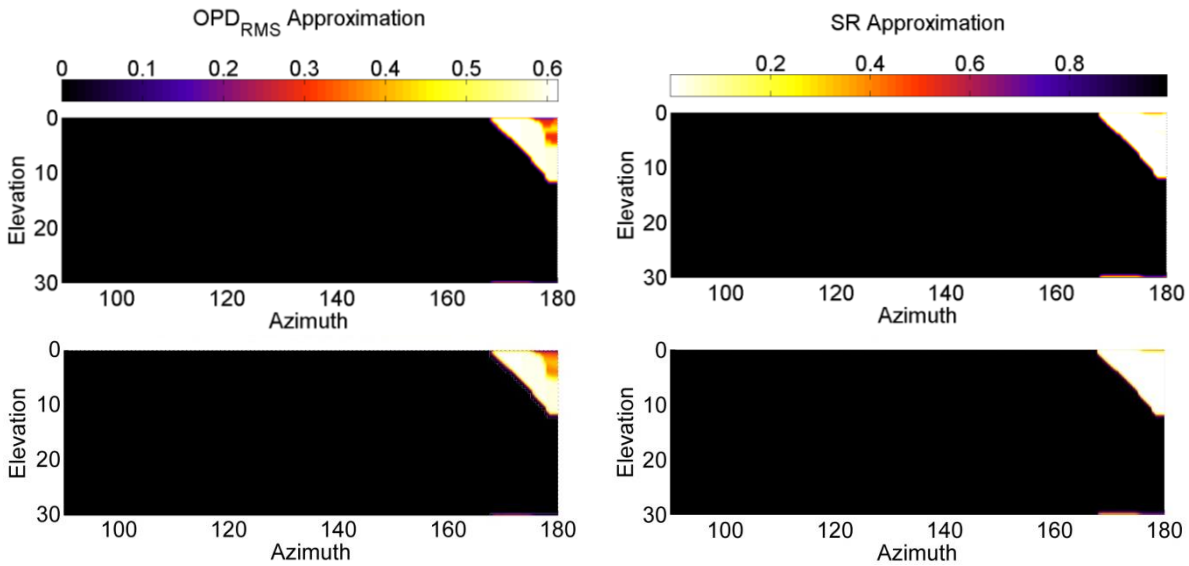

Figure 7.30: Estimated field-of-regard at a forward flight speed of 40 m/s based on the scaling relationship in Chapter 4 and a Gaussian basis set to estimate the Strehl ratio. On the top is a calculated instantaneous example with the time-averaged value on the bottom.

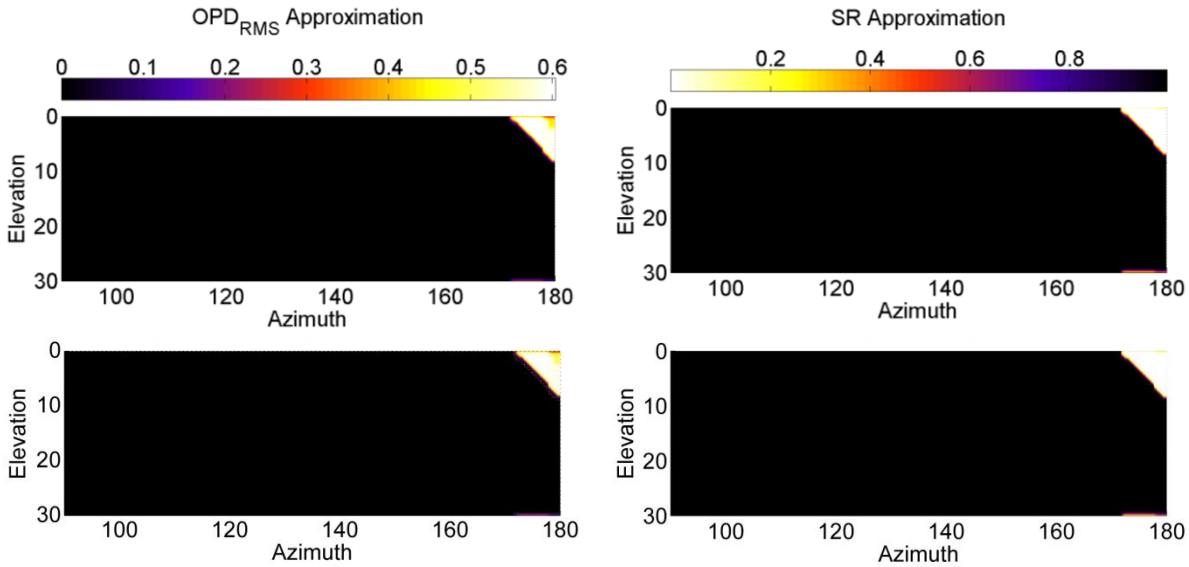

Figure 7.31: Estimated field-of-regard at a forward flight speed of 50 m/s based on the scaling relationship in Chapter 4 and a Gaussian basis set to estimate the Strehl ratio. On the top is a calculated instantaneous example with the time-averaged value on the bottom.

7.11. Summary

This chapter has presented numerical results for the optical aberrations caused by the wake vortex system of a helicopter in hover and in forward flight. The numerical data were generated using a weakly-compressible computational approach to determine density and hence optical aberrations from velocity fields that were computed using prescribed-wake methods.

For the case of hover, the computations showed that the largest optical effect of the helicopter wake occurs when the outgoing beam passes through a vortex in the wake, which happens at the blade rotation frequency. In this case, the Strehl ratio can be reduced to nearly zero depending on the flight conditions.

On the other hand, in forward flight, the greatest reduction in optical-system performance occurs when the beam passes through the lateral edge of the helicopter's wake where "super vortices" form. The location of these super vortices depends on the specific flight conditions, but primarily on the flight speed of the helicopter. Due to the size of the vortices collating and creating these "super vortices" along the lateral edge of the wake, the spatial scale of the optical aberration produced by these super vortices is about the same as a typical beam diameter; as such, the super vortices produce a large amount of optical tip/tilt and therefore bore-sight error. As the flight speed of the helicopter is increased, the wake is swept backwards, creating a larger unobstructed field-of-regard for the optical system so that, at a forward-flight speed of approximately 40 m/s, the field of regard for an optical system mounted below the helicopter is essentially unaffected by the helicopter wake system.

CHAPTER 8:

SUMMARY AND RECOMMENDATIONS

8.1. Findings and Contributions of This Research

The major findings and contributions of this dissertation research are summarized as follows:

8.1.1. Determination of Optical Effect of a Single Tip Vortex

Investigations into the optical effect of an isolated tip vortex in free space were conducted. These investigations consisted of an analysis of basic fluid-mechanic equations (i.e. the Euler equations) as well as a numerical effort based on the weakly-compressible approach, in which thermodynamic and optical properties of the tip-vortex flow were computed separately from the velocity field. The investigations showed that the optical aberration associated with a tip-vortex flow originates from the reduced pressure and density that exists at the center of the vortex. As such, this research further validates the findings of aero-optic investigations into other compressible turbulent flows, for example, compressible shear layers (Fitzgerald and Jumper 2004), where it was also shown that optical aberrations derive primarily from the reduced pressure and density within vortical structures in the flow.

Based on the preceding analysis, a scaling relationship was also developed to enable the scaling of the optical effect of a tip vortex to different flight conditions. This scaling relationship was "calibrated" using numerical data generated using the weakly-compressible approach, and shown to perform well when compared to experimental data.

8.1.2. Experimental Measurements of Optical Effect of Tip-Vortex Flow

Experimental measurements of the optical aberration in the tip vortex created by a delta wing and a vortex generator consisting of two rectangular-shaped wings were also performed as part of this investigation. The detailed wavefront data generated by these measurements constitute a significant contribution to the existing data on aero-optic flows.

The data generated by these measurements showed close agreement with the optical aberrations predicted by the weakly compressible approach, as well as the analytical result described in Section 8.1.1. As such, the experimental results showed that the weakly-compressible approach used by this investigation captures the essential physics governing the optical effect of tip-vortex flows. The data also indicated that the optical effect of the tip vortex is insensitive to the axial-flow component of the tip-vortex flow field.

It is worth reiterating at this point that this research has focused on the "fluid mechanic" origins of optical aberrations; in other words, optical effects that originate from pressure and density variations associated with the underlying flow. In this regard, the weakly-compressible approach developed as part of this research assumes a constant relationship ($C_{T\text{-}P}$) between temperature and pressure in the flow field and does not model

heat transfer, heat sources, or other effects that would produce optical aberrations caused by temperature variations alone. The close comparison, however, between the results of the weakly-compressible approach and the experimental measurements conducted in this investigation shows that the weakly-compressible approach is nonetheless a good model for actual flows.

8.1.3. Aero-Optic Environment of a Helicopter

Finally, using the numerical approach described above, this investigation has produced estimates for the optical effect of the vortex wake produced by a helicopter in hover and in forward flight. For the case of hover, the calculations showed that largest aberration on an optical system mounted on the helicopter occurred when the wake vortices passed through the line of sight of the optical system. For a medium-sized helicopter, the estimated average Strehl ratio over a blade-passing cycle was 0.75, with a minimum Strehl ratio of approximately 0.15, although the optical effect was also shown to vary significantly based on atmospheric and flight conditions.

For the case of forward flight, the research showed that the tip vortices are swept backwards and tend to coalesce to form “super vortices” along both sides of the wake. The super vortices along the lateral edges of the wake produce large optical aberrations that effectively eliminate this region from the effective field of regard. At low forward-flight speeds, smaller vortices also exist throughout the field of regard of the optical system; however, as the forward flight speed increases the vortex wake is swept back behind the helicopter, until the field of regard is effectively clear of aberrations at a flight speed of approximately 40 m/s.

8.2. Recommendations for Future Work

The following summarizes suggestions for additional work to validate the numerical models and aid in the understanding of the aero-optical environment surrounding a medium-sized helicopter.

8.2.1.Temperature Field Measurements

Chapters 4 and 5 showed that the main difference between the isentropic and WCM methods was in the predicted static and total temperatures. This discrepancy should be investigated via temperature measurements of a tip-vortex flow using, for example, a constant current anemometer and/or a thermocouple. These kinds of measurements would also contribute additional insight into the use of the WCM for compressible shear-layer flows; however, the tip vortex is an ideal flow for these kinds of measurements since it is relatively steady.

8.2.2. Unsteady Flow Effects

Note that one of the main assumptions within this dissertation has been the relatively steady nature of free-space tip-vortex flows. Due to the high frame rate of the wavefront sensor used in the dual-wing experiments (Chapter 5), temporal fluctuations in the optical data can be accessed. To gauge the fluctuations in the tip vortex aberrations, histograms of the 1,000 spatial OPD_{RMS} values normalized by the average OPD_{RMS} were calculated. Figure 8.1 shows three histograms from different data sets. To estimate the amount of fluctuation in the optical data, due to error in the measurements along with fluctuations in the size and strength of the vortex, the Cumulative Distribution Function (CDF) of the normalized OPD histograms was calculated. Figure 8.2 shows the three

CDF's corresponding to the histograms in Figure 8.1. As an arbitrary definition, the points where the CDF is 0.25 and the CDF is 0.75 were calculated to represent the spread in the data. For all the datasets, the normalized lower bound is 0.9413±0.0107 and the upper bound is 1.0597±0.0118.

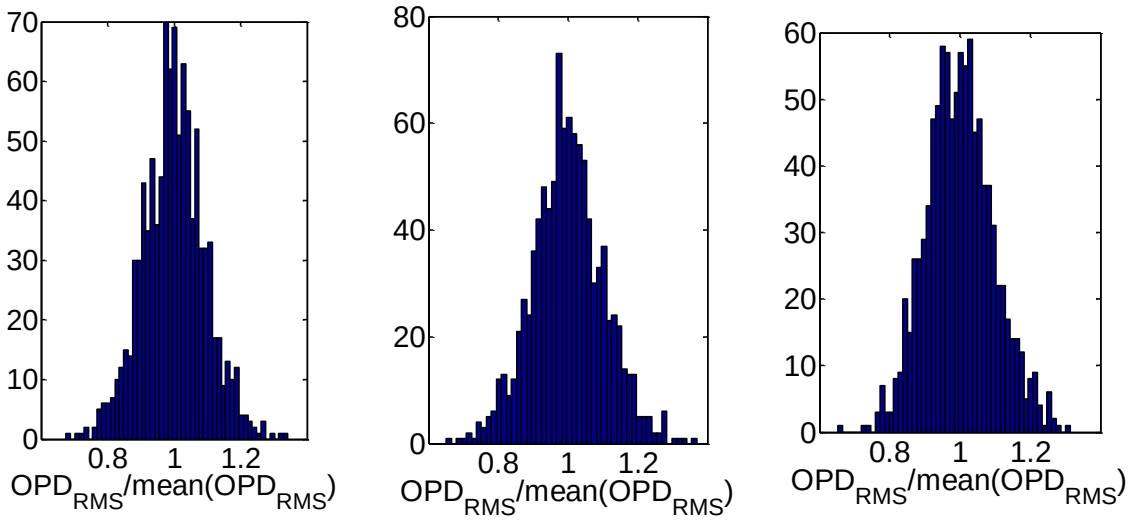

Figure 8.1: Histogram of measured wavefront statistics corresponding to Mach 0.38 at 14° (left), Mach 0.4392 at 12° (center), and Mach 0.55 at 6° (right).

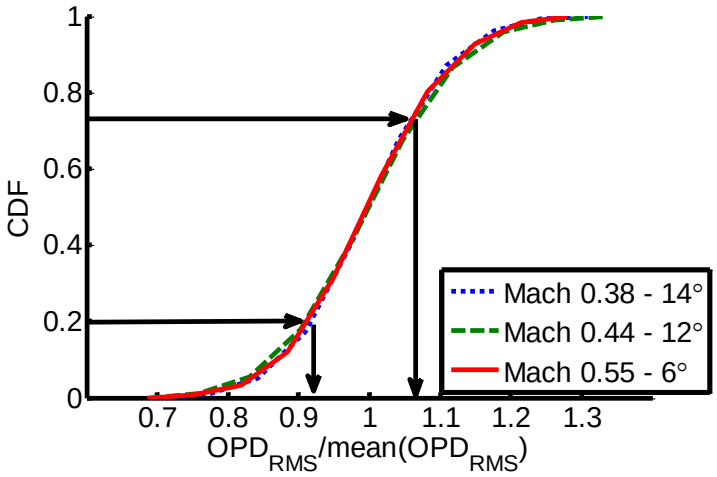

Figure 8.2: Computed Cumulative Distribution Functions (CDF) for the normalized OPD histograms in Figure 8.1.

While there is a wide span in the calculated $OPD_{RMS,}$ the increased frame rate of the new high-speed wavefront sensor is able to capture the unsteady fluctuations in the density field that were not resolved in the delta wing experiment. Figure 8.3 shows a series of calculated wavefronts. From Figure 8.3, the existence of unsteady structures propagating through the wavefronts are clearly evident. This could however be due to the merging of the two tip vortices or even potentially the vortex street from the cylindrical rod connecting the two wings. Figure 8.4 shows the corresponding OPD_{RMS} normalized by the mean OPD_{RMS} of all the wavefronts. For example, looking at the 17th to 27th instances in the series, the OPD_{RMS} starts at a local minimum, reaches a local maximum at the 22nd instance and then decreases again, corresponding to the propagation of a structure through the wavefront, highlighted by a circle around the structure in Figure 8.3. Increased insight into these unsteady effects will not only aid in a better estimation of the aero-optics of tip vortices but could also provide insight into the flow properties of tip vortices themselves.

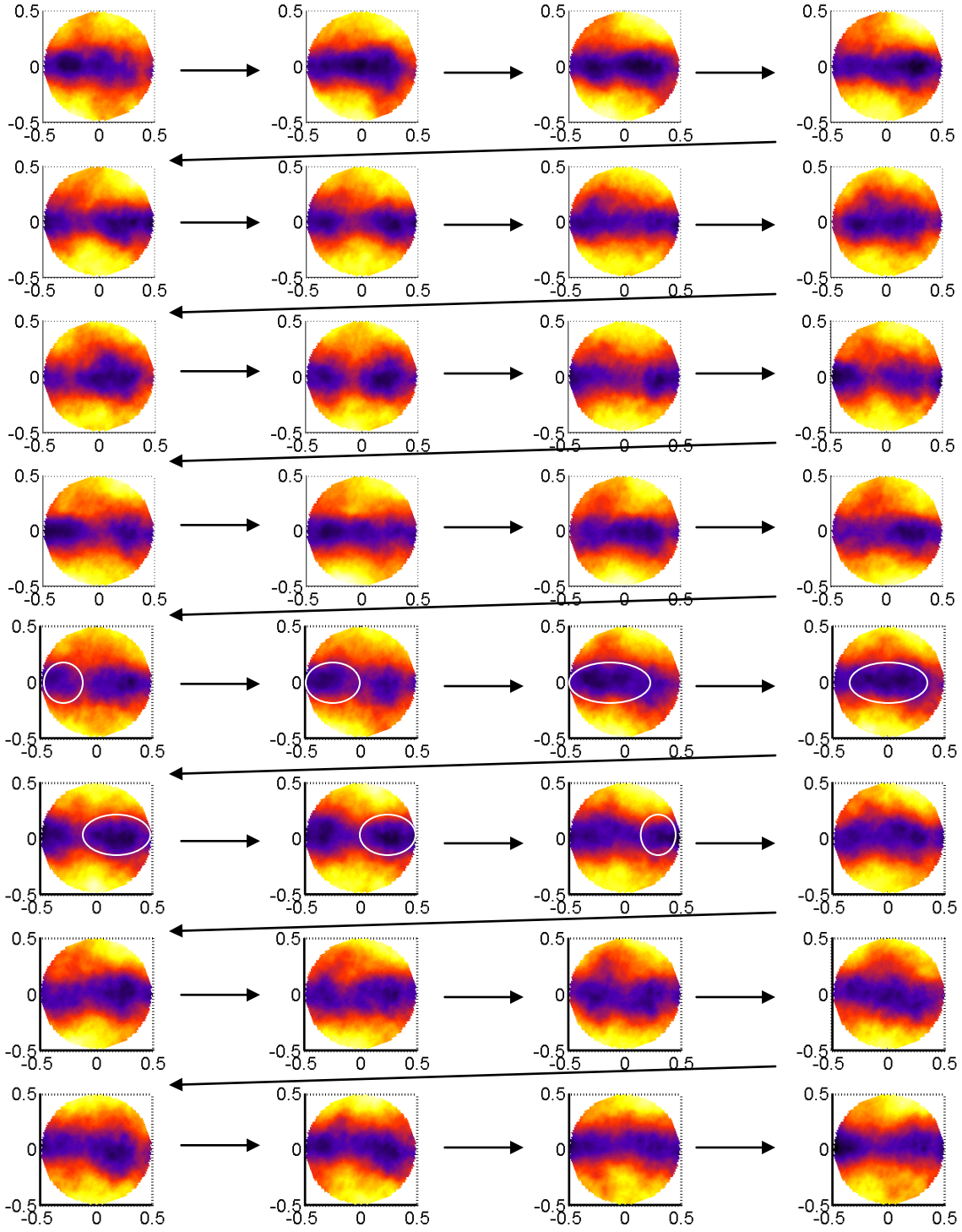

Figure 8.3: Time series of wavefronts illustrating the unsteady component of the wingtip optical measurements.

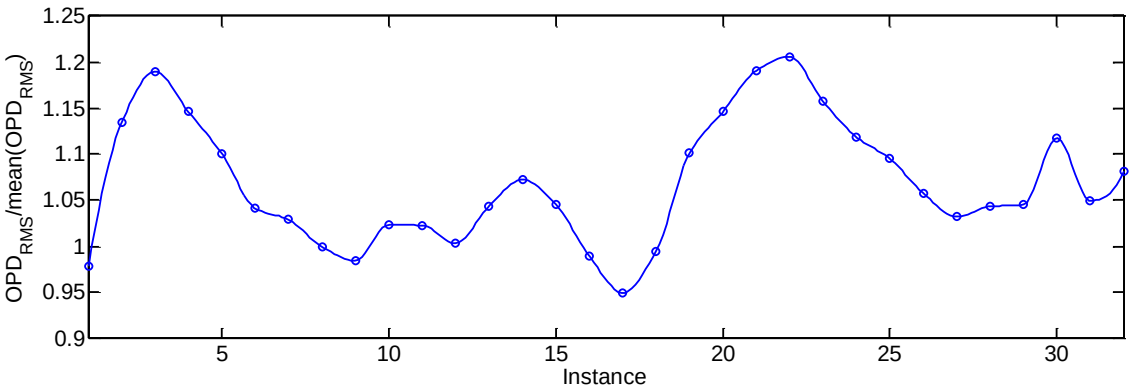

Figure 8.4: Calculated normalized OPD_{RMS} corresponding to the wavefronts shown in Figure 8.3.

8.2.3. Investigation of Small-Scale Turbulence in Tip Vortices

Figure 8.5 shows a comparison of several wavefronts obtained using the CLAS2D and the newer, high-speed, high-resolution wavefront sensors. The lower spatial resolution wavefronts are shown along the top row of Figure 8.5 with the higher resolution wavefronts shown along the bottom row. Although the statistics are similar, it is evident that the increased spatial resolution helps capture the fine scale structure within the vortex. These fine scale structures are probably associated with the small scale turbulence just outside the vortex core; investigation into these small scale structures would not only help refine aero-optic modeling of tip vortices, but also provide an additional avenue to investigate the flow physics of large vortex-Reynolds-number tip vortices (Kozlov *et al*. 2003; Ramasamy and Leishman 2007).

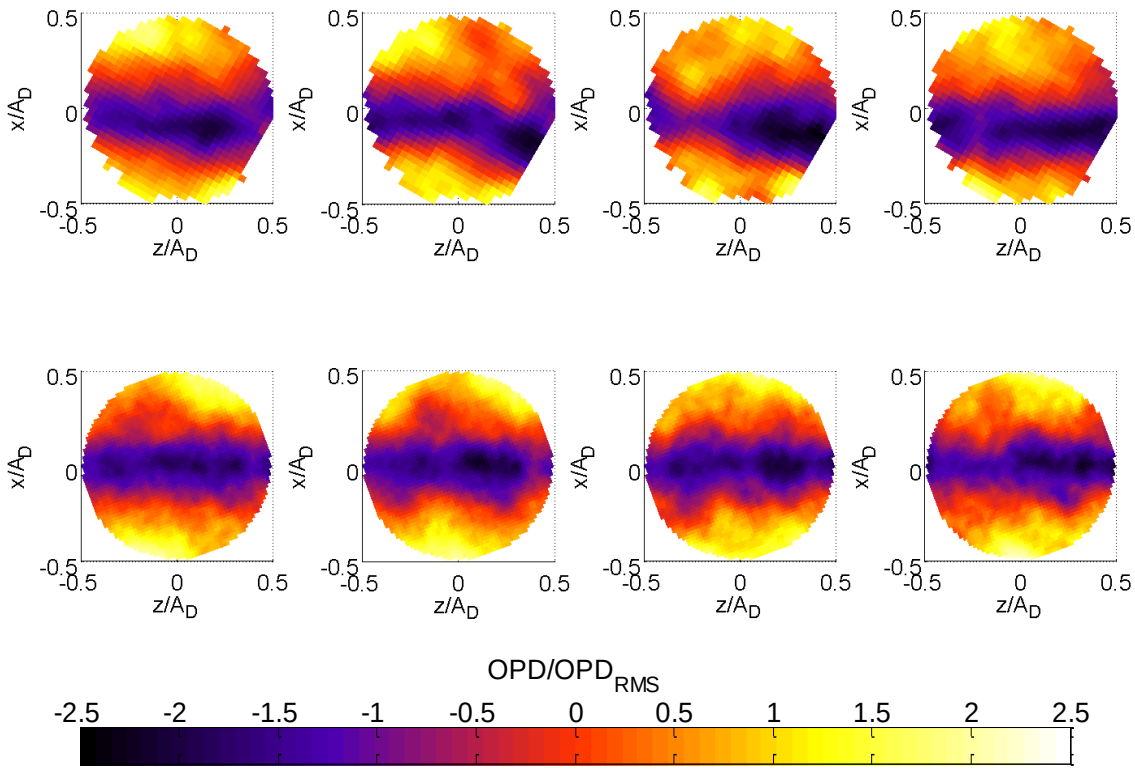

Figure 8.5: Comparison of wavefront sensors and the effects of increased spatial resolution.

8.2.4. Advanced Numerical Modeling of Helicopter Flows

The prescribed-wake/weakly-compressible approach used in this investigation has provided a good estimate of the optical effect of a helicopter vortex wake, where no such estimate was available before. The approach does not model, however, several important sources of optical aberrations, such as from temperature variations produced by the helicopter engine exhaust, Figure 8.6, or from the wake of the helicopter body itself. As such, future efforts should attempt to incorporate these effects, either into the numerical method used in this investigation, or into other, more advanced, numerical approaches such as free-vortex methods or full CFD simulations.

Figure 8.6: Thermal wake from the exhaust of a helicopter that could be another potential source of optical aberration to an optical system mounted on a helicopter. Pictures taken from guncopter.com and irishairpics.com.

8.2.5. Full-Scale Optical Tests

Full-scale tests of the aero-optical environment are essential to evaluate the accuracy of numerical predictions. A recommended test configuration is shown in Figure 8.6 with two possible beam paths illustrated. Note that each beam path is its own test, and the beam would be double passed from the return mirror on the test stand beneath the helicopter.

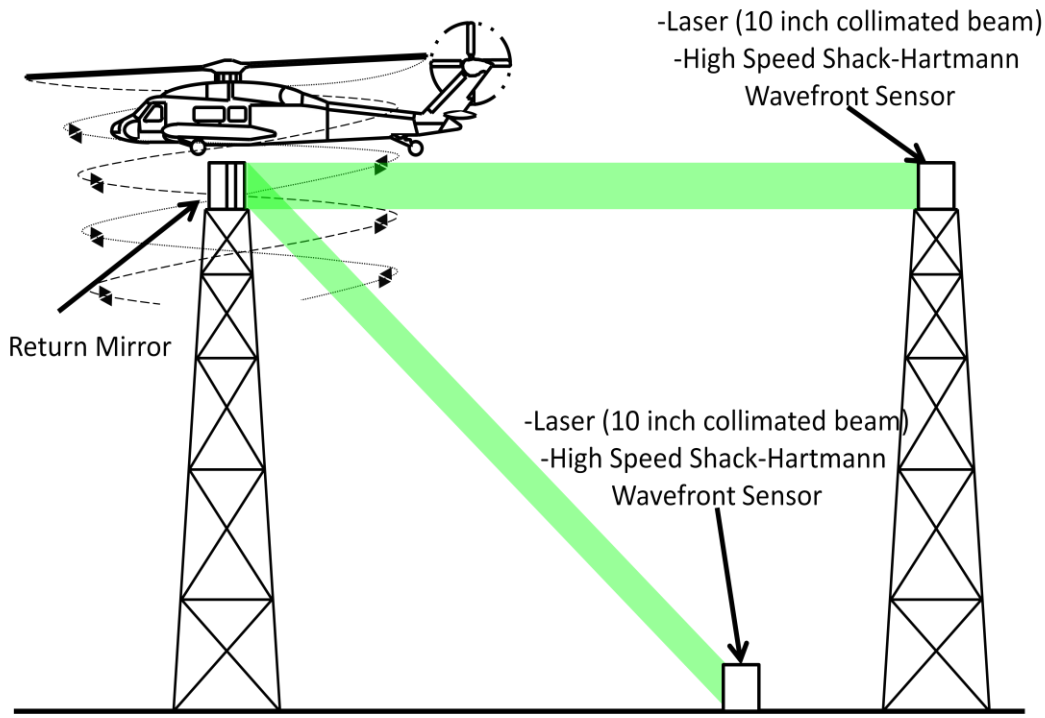

Figure 8.7: The proposed optical test to experimentally determine the aero-optic environment beneath a helicopter.

APPENDIX A:

SINGLE VORTEX OFFSET WITHIN THE APERTURE

Scaling relationships, presented in Chapter 4, were developed to predict the OPD_{RMS} of an optical system resulting from a planar wavefront propagating through a vortex centered within the optical aperture. These scaling relationships account for the strength of the tip vortex, the size of the vortex, and the associated momentum deficit. These three vortex properties allowed for the calculation of the thermodynamic properties of the vortex. Chapter 4 also demonstrated that the aperture ratio becomes very important in optical performance considerations. To account for the changes associated with the aperture, a gain function was developed.

As shown in Chapter 7, this scaling relationship is only valid for the instant when the vortex is centered in the aperture, which is a very small percentage of the vortex passage cycle. While the computations presented in Chapters 6 and 7 are parsimonious, they are still far beyond the realistic capabilities of a single desktop, requiring large computing centers to run efficiently. Computations of a single vortex on the other hand are easily accomplished on a personal computer. Therefore, the ability to model a single vortex propagating through the optical line-of-sight was investigated. Figure A.1

illustrates six different propagating instances ranging from the vortex centered within the aperture, to the vortex well outside the aperture.

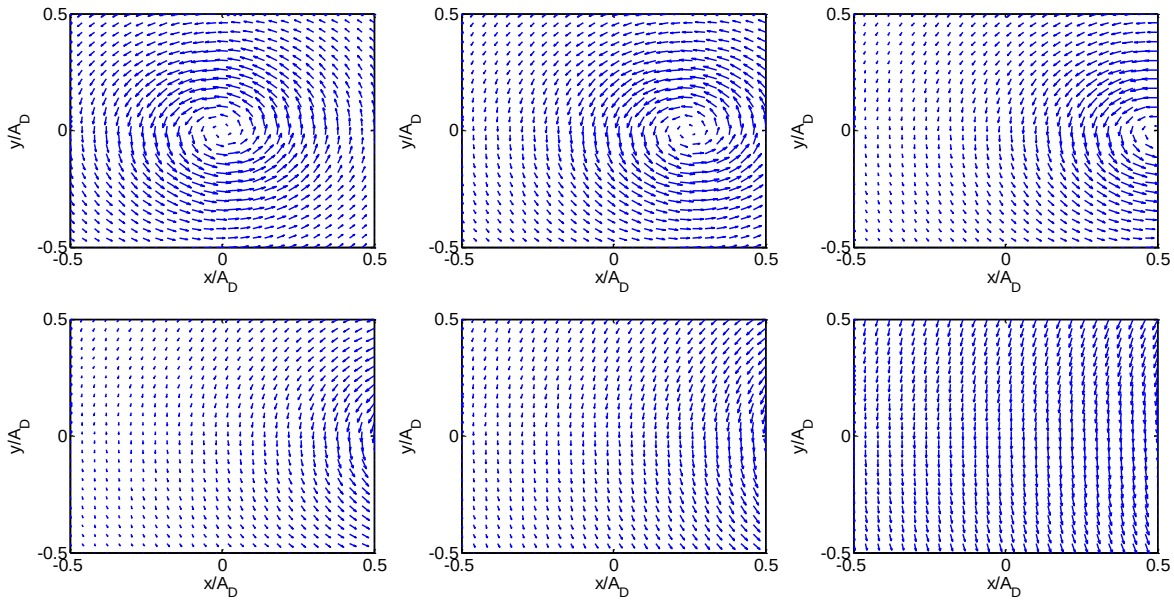

Figure A.1: Quiver plot of the velocity field within the viewing aperture. Top left to top right: $x_0/A_D = 0$, $x_0/A_D = 0.25$, and $x_0/A_D = 0.5$. Bottom left to bottom right: $x_0/A_D = 0.75$, $x_0/A_D = 1$, and $x_0/A_D = 2$.

For the cases shown, the center of the vortex (x_0,y_0) was only varied in one direction (x_0). For each x_0 offset, the scaling parameter $\left(\rho/\rho_{SL}\right)\Gamma^2/a^2 r_c$ was varied over a large range to obtain an accurate estimate of the slope relating the OPD_{RMS} across the aperture to this parameter. Figure A.2 shows how the OPD_{RMS} (tilt removed) changes with the scaling relationship developed previously.

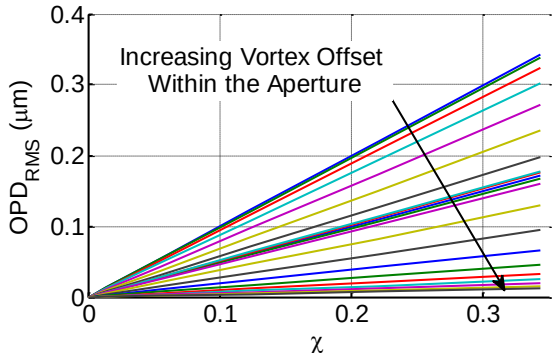

Figure A.2: Increasing the offset, x_0, of a vortex within an optical aperture generally decreases the resulting OPD_{RMS}.

Optically, the OPD_{RMS} is a function of the offset (x_0) and the aperture ratio (AP), but the two are not independent of one another. As the aperture ratio changes, the effect of the vortex offset in the aperture also changes. Figure A.3 shows how the calculated slope (calibration of the scaling relationship) changes for various aperture ratios over a range of offsets. For all the figures shown in Figure A.3, the slope has been normalized by the slope calculated when the vortex is centered in the aperture.

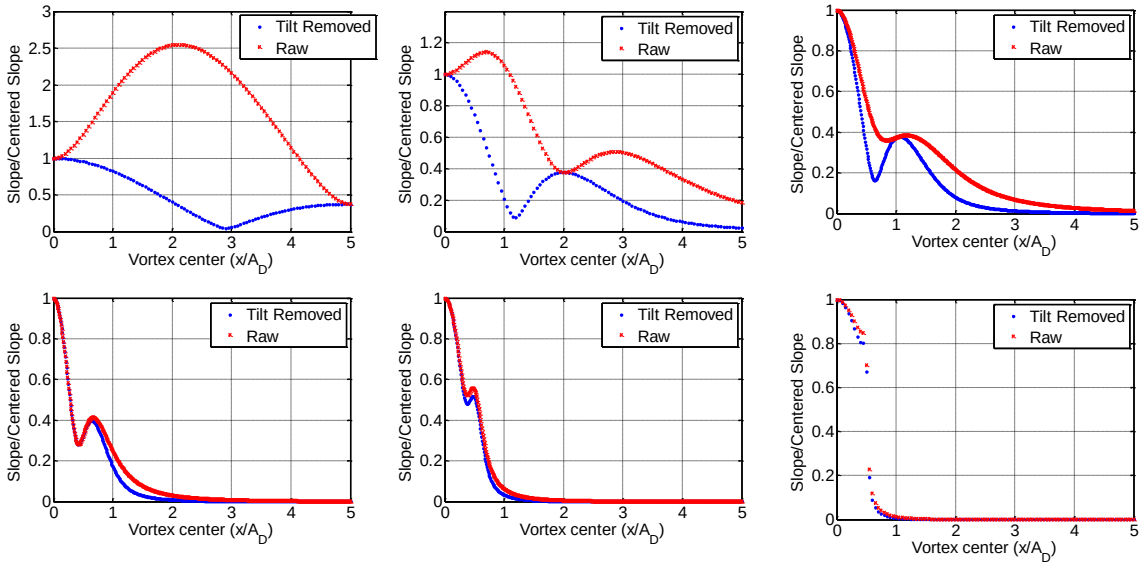

Figure A.3: Quiver plot of the velocity field within the viewing aperture. Top left to top right: AP = 0.1, AP = 0.25, and AP = 0.5. Bottom left to bottom right: AP = 1, AP = 2.5, and AP = 10.

Notice the exact same trend for the hovering OPD_{RMS} calculations, Figure 7.5, exists for the propagation of a single vortex across the aperture. At the lower aperture ratios, the OPD_{RMS} increases as the aperture becomes off-center due to a large increase in the optical tilt; this is indicated by the drastic reduction in slope by removing the tilt. Furthermore, the double hump seen in the hovering data is also present in the single vortex data. This is expected since the primary difference between the hovering data and this data is the existence of a slipstream and the interaction of other nearby vortices.

Therefore, a transfer function could be developed to quickly scale optical aberrations based on the vortex position and the aperture ratio. Figure A.4 shows two surface maps of such a transfer function: the first for raw OPD_{RMS} data, and the second for tilt removed OPD_{RMS} data. For consistency, the data was normalized by the data point $x_0 = 0$, AP = 10. As such, the line on the surface plot corresponding to $x_0 = 0$ is exactly the gain function presented in Chapter 4.

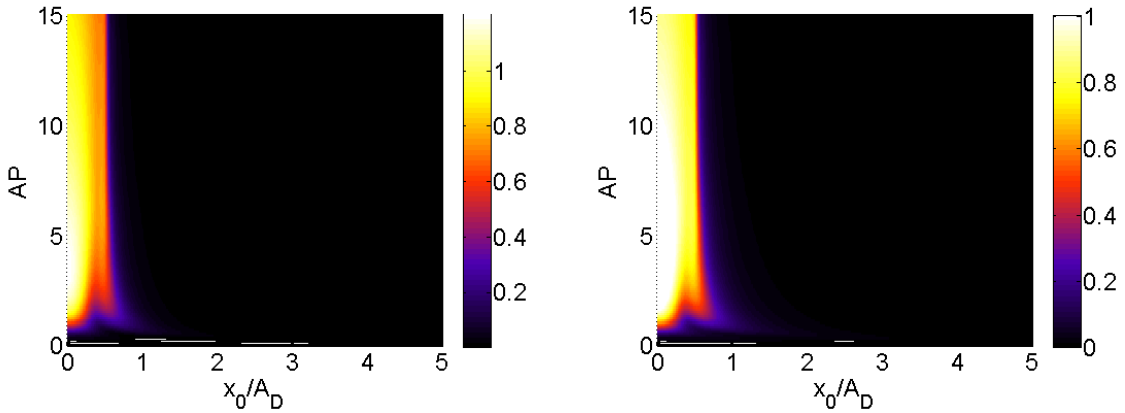

Figure A.4: Surface plot of the transfer function to scale optical aberrations from a single tip vortex as a function of offset (x_0) and aperture ratio (AP). Left) Raw OPD_{RMS}, Right) Tilt removed OPD_{RMS}.

APPENDIX B:

STREHL RATIO CONSIDERATIONS

Scaling relationships to determine the severity of optical aberrations are ideal since they allow for quick calculations of optical performance based on different flight conditions. However, from an application perspective, the OPD_{RMS} is not the quantity of concern, but rather the Strehl ratio (or some other metric for farfield optical performance). For most of the typical flow fields associated with aero-optics, the assumption of a Gaussian phase-error distribution has been made. The calculated OPD_{RMS} is used with the exponential form of the Maréchal approximation (large aperture approximation - LAA) to provide an estimate of the Strehl ratio. Therefore, being able to predict the OPD_{RMS} of a system directly allowed calculation of the Strehl ratio. However, recent investigations from flight test measurements on AAOL (Porter *et al.* 2011) have shown that in fact the phase error distribution around a flat-windowed turret is not Gaussian (at least at certain azimuth and elevation angles) and that the LAA equation under predicts the time-averaged Strehl ratio.

Histograms of the OPD, the skewness, and kurtosis from the dual-wing experiment are shown in Figure B.1. For reference, a Gaussian phase-error distribution would have a skewness of zero and kurtosis of three.

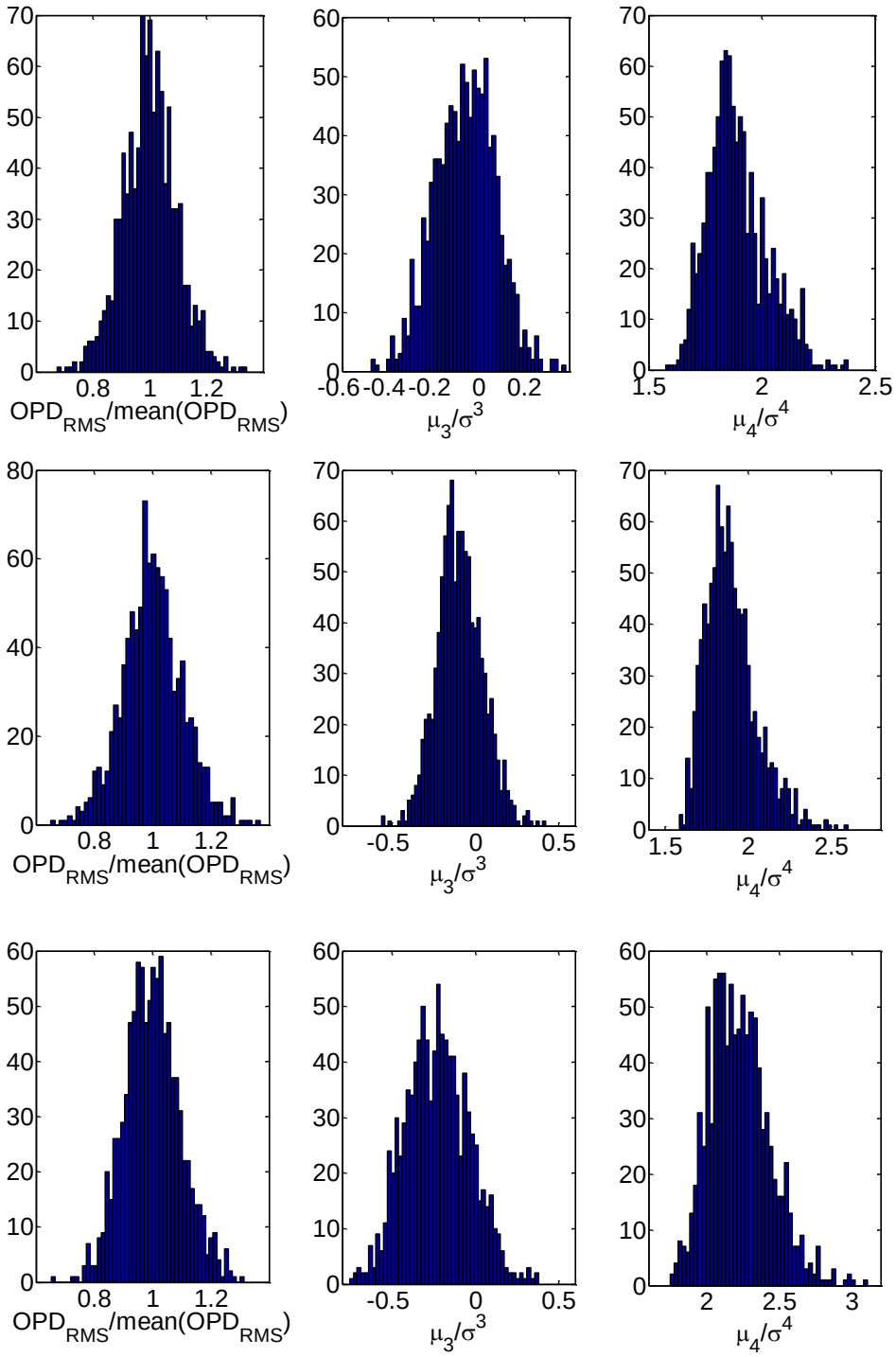

Figure B.1: Histogram of measured wavefront statistics corresponding to Mach 0.38 at 14° (top), Mach 0.4392 at 12° (middle), and Mach 0.55 at 6° (bottom).

The values in Figure B.1 indicate the calculated statistics from each of the 1,000 wavefronts taken for a given data set. As expected, the normalized OPD data is centered on one. However, the skewness is not centered on zero, but rather has a slightly negative value. This indicates that spatially there is a wider range of negative OPD values (regions of the wavefront leading the mean) with a larger majority of the wavefront having positive OPD values. The kurtosis distributions in Figure B.1 also did not equal the ideal Gaussian value of three. Instead, the average kurtosis value for the data set is approximately two, indicating a flatter distribution of OPD values with short narrow tails. An example histogram of the OPD from an instantaneous wavefront is shown in Figure B.2. For comparison, ideal phase error distributions for the Lamb-Oseen vortex, centered within the aperture, for different aperture ratios is shown in Figure B.3 along with the corresponding OPD across the aperture. For reference, a normal distribution is also shown, in which the LAA is valid.

Figure B.4 shows how the Strehl ratio changes as the OPD_{RMS} increases using the PDF's shown in Figure B.3; for reference, the LAA is shown in Figure B.4 also. For the data shown, the OPD across the aperture was altered by a simple gain; the distribution was identical for all RMS values, but the magnitude changed.

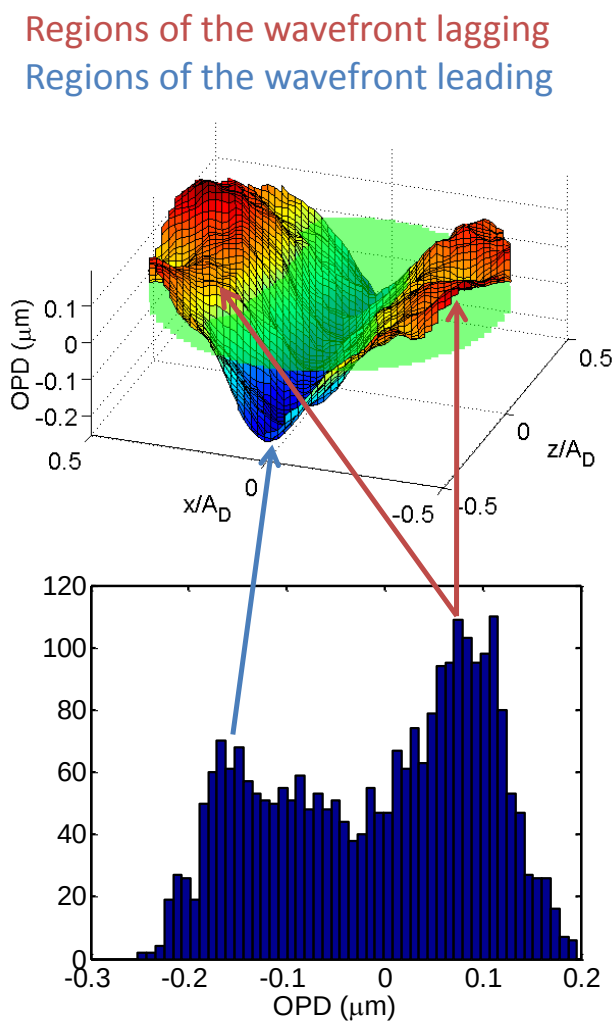

Figure B.2: Instantaneous wavefront at Mach 0.38 and a 14 degree angle of attack with the corresponding histogram of the OPD.

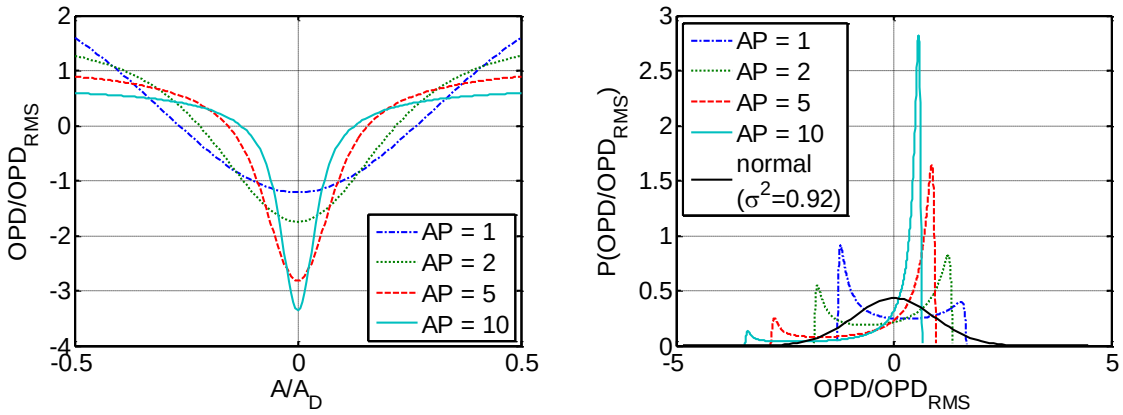

Figure B.3: Normalized OPD for various aperture ratios and the corresponding probability distribution function for each aperture ratio.

The LAA for all four aperture ratio does a good job up to some OPD_{RMS} value (~0.1). After that point, the LAA and the actual Strehl ratio (λ=1μm) deviate. For the smaller aperture ratios, the LAA provides a better estimate of the Strehl ratio at larger values of OPD_{RMS}, but it still deviates at some point. This is expected based on the probability distributions for the different aperture ratios, where the difference between the lower aperture ratios to a normal distribution is not as severe as the difference at large aperture ratios.

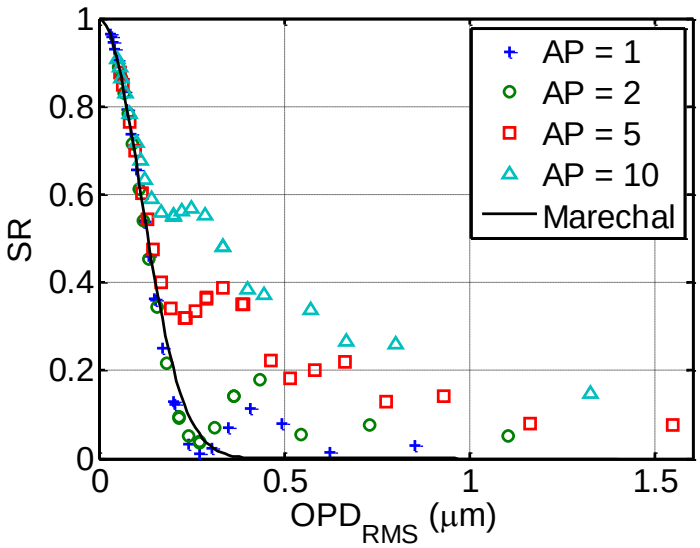

Figure B.4: Strehl ratio for various aperture ratio resulting from a tip vortex centered within the aperture (λ = 1.0 μm).

While scaling relationships therefore give insight into the underlying physics and the different mechanisms causing optical aberrations, they may not represent enough data to accurately predict the Strehl ratio on their own. The use of the LAA potentially leads to drastic error in Strehl ratio predictions and misinterpretations of the severity of an optical environment. For instance, based on the data shown in Figure B.4 (from free-

space vortex calculations), if an aperture ratio of 10 is used, at an OPD_{RMS} of 0.5 the LAA would predict a Strehl ratio of zero ($\lambda = 1.0\ \mu m$). However, in this case the Strehl ratio is actually only slightly below 0.4.

Analysis based on the LAA results in the belief that increasing the OPD_{RMS} necessarily correlates to a reduction in Strehl ratio. However, as shown, this is not necessarily the case, and in some instances, increasing the phase error increases the Strehl ratio. This can most easily be realized by the case of an optical system with only tilt as it aberration. The resulting Strehl ratio is predicted by a *sinc* function, $SR(OPD_{RMS}) \propto \mathrm{sinc}(OPD_{RMS})^2$. The interesting point here is that in terms of potential controls for AO systems, a local maximum might be more easily obtained by increasing the phase error variance or applying a completely different aberration (Mahajan 1982; Mahajan 1983).

B.1. Calculating the Strehl Ratio in Probability Space

By this point, it should be clear that the best approach to calculating the Strehl ratio is at a bare minimum to use the Fraunhofer approximation. However, for system design, the calculations needed to determine the wavefront of interest and then calculate the farfield pattern might become too cumbersome. The question then remains, "is there a means to provide a better solution than the LAA without the complexity of the Fraunhofer approximation?"

B.1.2. Expansion of the Fraunhofer Approximation - Moments or Cumulants

As shown in Ross (2009), the Strehl ratio (as calculated from the Fraunhofer approximation (Eq. B.1)) can be exactly written in terms of the wavefronts probability distribution function (Eq. B.2):

$$SR = \frac{\left|\iint_{-\infty}^{\infty} e^{\left(2\pi i W(x,y)/\lambda\right)} dxdy\right|^2}{\left|\iint_{-\infty}^{\infty} dxdy\right|^2}. \tag{B.1}$$

The difficulty in Eq. (B.1) comes from calculating numerator. Furthermore, this requires the knowledge of the actual wavefront to obtain a solution, something that is not available through scaling relations. Assuming that the wavefront phase error has a probability distribution function (PDF) associated with it, then the Strehl ratio can equivalently be calculated as:

$$SR = \left|\int_{-\infty}^{\infty} e^{\left(2\pi i W(X)/\lambda\right)} PDF(W) dW\right|^2. \tag{B.2}$$

The integral in Eq. (B.2) is the Fourier transform of the PDF and is the characteristic function, $\phi(2\pi/\lambda)$, of the wavefront, W. Therefore, the Strehl ratio is exactly defined as:

$$SR = |\phi(2\pi/\lambda)|^2. \tag{B.3}$$

In Eq. (B.3), the Strehl ratio is defined in terms of the wavefront's characteristic equation; therefore, it is based solely on the distribution of the phase error. In other words, two different wavefronts that yield identical PDFs will have identical Strehl ratios. For a normal distribution, the characteristic equation is given by (Abramowitz and Stegun 1972):

$$\phi(2\pi/\lambda) = e^{im(2\pi/\lambda) - \frac{\sigma^2 (2\pi/\lambda)^2}{2}}, \tag{B.4}$$

where the mean (m) is 0 and σ^2 is equal to the OPD_{RMS} squared; this is exactly the LAA. This not only holds true for Gaussian distributions but others as well. For example, a wavefront with only tilt yields a uniform distribution with a characteristic function equal to a *sinc* function such that

$$SR = sinc^2\left(\frac{\sqrt{12}\pi OPD_{RMS}}{\lambda}\right). \tag{B.5}$$

A plethora of PDFs and their corresponding characteristic function can be found in Abramowitz and Stegun (1972) yielding exact solutions to the Fraunhofer approximation. However, what happens when the characteristic function is not easily defined through mathematical function?

The use of characteristic functions is still appealing since they can be expanded in terms of their cumulants:

$$\ln\big(\phi(t)\big) = \sum_{n=0}^{\infty} \kappa_n \frac{(it)^n}{n!}, \tag{B.6}$$

where κ_n is the nth cumulant. Furthermore, cumulants are linearly related to central (mean removed) moments through a recursion relationship:

$$\kappa_n = \mu_n - \sum_{m=1}^{n-1} \binom{n-1}{m-1} \kappa_m \mu_{n-m}, \tag{B.7}$$

where μ_n is the nth moment. Combining Eq. (B.3) with (Eq. B.6) yields:

$$SR = \left| e^{\sum_{n=0}^{\infty} \kappa_n \frac{(it)^n}{n!}} \right|^2, \tag{B.8}$$

where $t = {}^{2\pi}/_{\lambda}$. Equation (B.8) is the exact solution provided $\phi(t)$ is not equal to zero, in which case this form of the solution becomes undefined. As a sanity check, for a

normal distribution, $\kappa_1 = 0$, $\kappa_2 = OPD_{RMS}^2$, and $\kappa_{3\text{ and up}} = 0$. Plugging these values into Eq. (B.8) yields the LAA once again. In terms of central moments, the Strehl ratio is defined as:

$$SR = \left| 1 + \sum_{n=1}^{\infty} \frac{(\mu_n it)^n}{n!} \right|^2, \tag{B.9}$$

although in this formulation no restriction is placed upon the value of the characteristic function.

B.1.3. Effects of Excess (Changes in Kurtosis)

To generate the phase error yielding the Strehl ratios shown in Figure B.5, the Pearson system for random number generation is used. This method is similar to typical random number generation, but allows for different distributions other than the normal distribution by specifying the skewness and kurtosis of the PDF. The corresponding PDF of the three distributions used to generate the phase error for Figure B.5 are shown in Figure B.6. The data in Figure B.5 and corresponding distribution in Figure B.6 have a skewness of zero (they are symmetric about the mean).

As shown in Figure B.5, a kurtosis less than three (normal distribution) results in an oscillation of the Strehl ratio. No matter how many terms are included in Eq. (B.8) the cumulant-method cannot predict this oscillation. However, the moment method is able to capture this oscillation, although a large number of terms are required. For reference, by 20 terms, the moment approximation was indistinguishable from the actual Strehl ratio up to $OPD_{RMS}/\lambda = 0.75$. Both methods (moments and cumulants), with only the use of

four terms provide a better approximation of the Strehl ratio compared to the LAA up to a value of $OPD_{RMS}/\lambda \cong 0.35$.

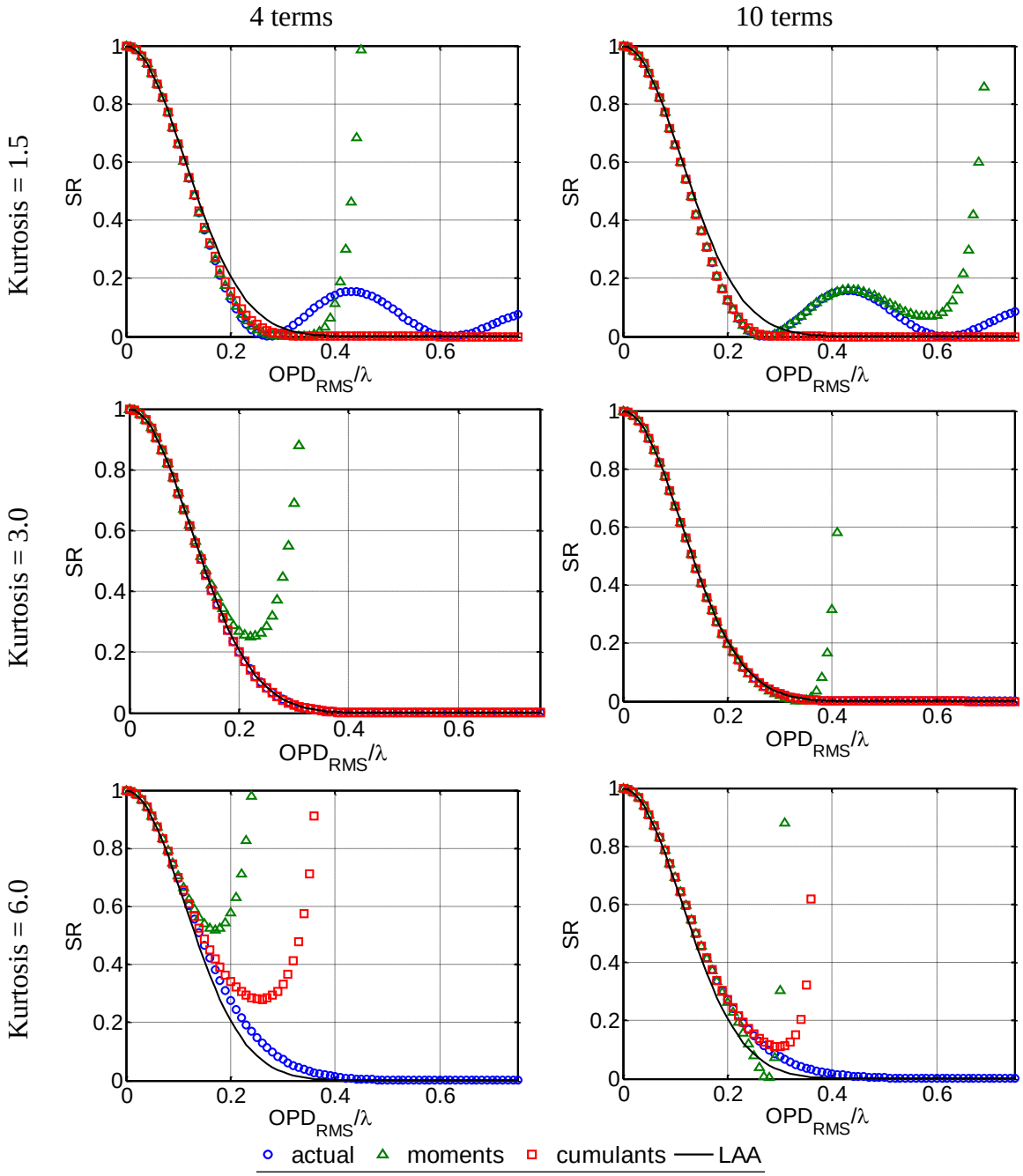

Figure B.5: Effect of excess kurtosis on the Strehl ratio and a comparison of approximate methods for estimating the Strehl ratio.

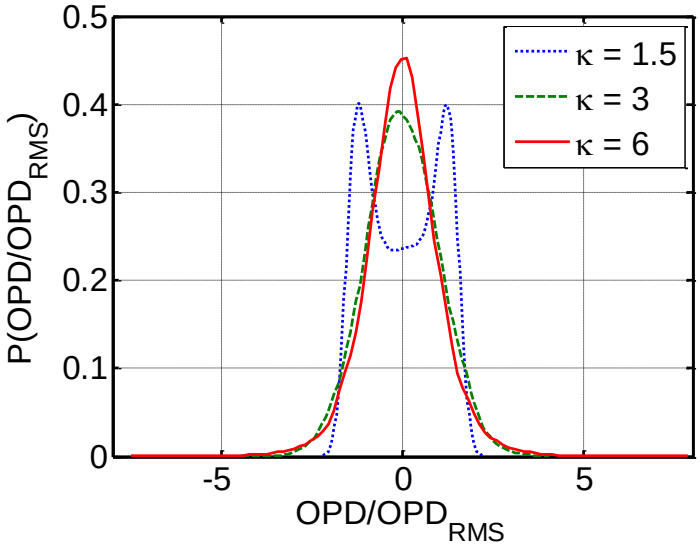

Figure B.6: Distributions of OPD/OPD_{RMS} for the different kurtosis values shown in Figure B.5.

As expected, for a normal distribution (kurtosis = 3), the cumulant method and the LAA accurately predict the Strehl ratio. The moment method can accurately predict the Strehl ratio also, although it requires a large number of terms. This is because the higher moments are not zero. When the excess is positive (kurtosis > 3), the LAA under predicts the Strehl ratio. The use of moments and cumulants both are able to accurately predict the Strehl ratio for these cases provided enough terms are used. Note that when using the method of cumulants, while four terms are used, that includes the first and third cumulants that are exactly zero. Therefore, a four-term expansion is actually only including one extra term above the LAA.

B.1.4. Effects of Skewness

For the data in Figure B.5 and corresponding distributions in Figure B.6, the skewness of the distributions was set to zero. However, for tip vortex data, the

corresponding skewness of the distributions is not zero (see Figure B.2 and Figure B.3). Figure B.7 shows how the Strehl ratio changes based on a distribution with a kurtosis of three, but changes in the skewness. As shown, skewness has a significant effect on the Strehl ratio. As the absolute value of the skewness of the distribution increases, the Strehl ratio increases for larger values of OPD_{RMS}/λ. This is because while the OPD_{RMS} values may be large, a significant portion of the wavefront is in phase with small regions out of phase. This is the case for large aperture ratio tip-vortex data. As before, the use of moments or cumulants can be used to approximate the solution to the desired accuracy needed, Figure B.8; the cumulant method is only able to able to predict the Strehl ratio up to the first minimum.

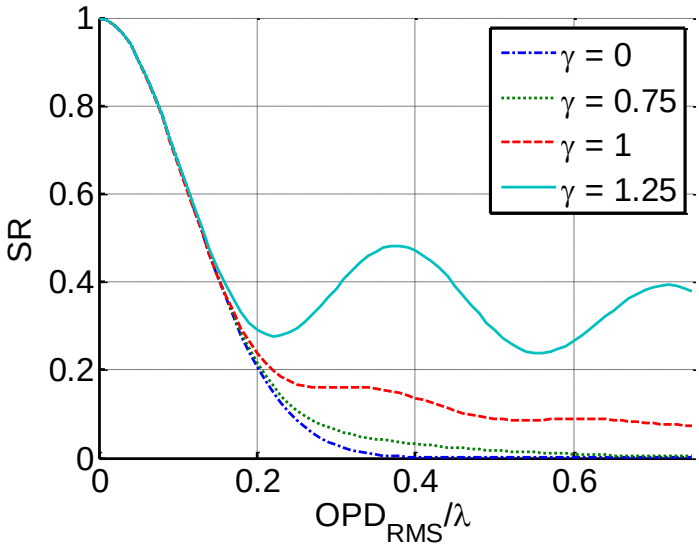

Figure B.7: Effect of skewness on the Strehl ratio.

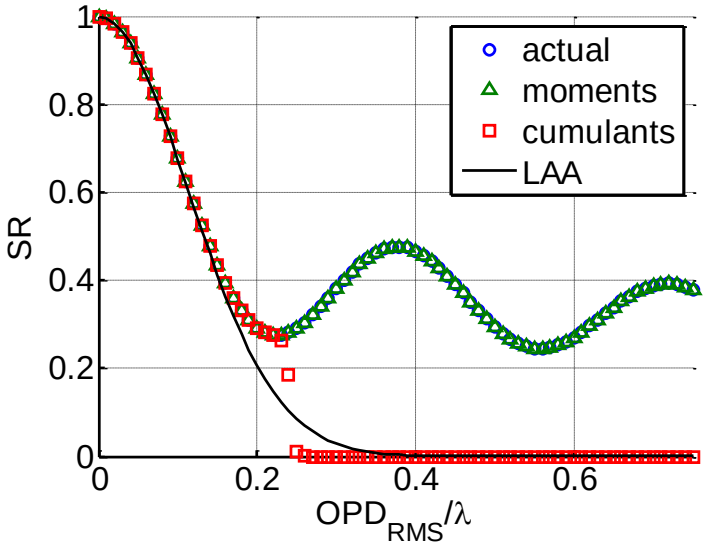

Figure B.8: Strehl approximation for skewness effects using 50 terms for both the moment and cumulant techniques.

B.1.5. Application to Wingtip Vortices

The data in Figure B.5 through Figure B.8 gives insight into how the Strehl ratio is effected based on the PDF of the phase error and shows how the LAA may be expanded to provide a more accurate prediction, although at the expense of an increase in complexity. Figure B.9 uses a 50 terms expansion (unrealistically large) of both Eqs. (B.8) and (B.9) to calculate the Strehl ratio for a single vortex in free-space at different aperture ratios. The moments and cumulants are calculated directly from the OPD (Figure B.3). With 50 terms, Eq. (B.9) is able to predict the Strehl ratio for very high phase error values even at the largest aperture ratio.

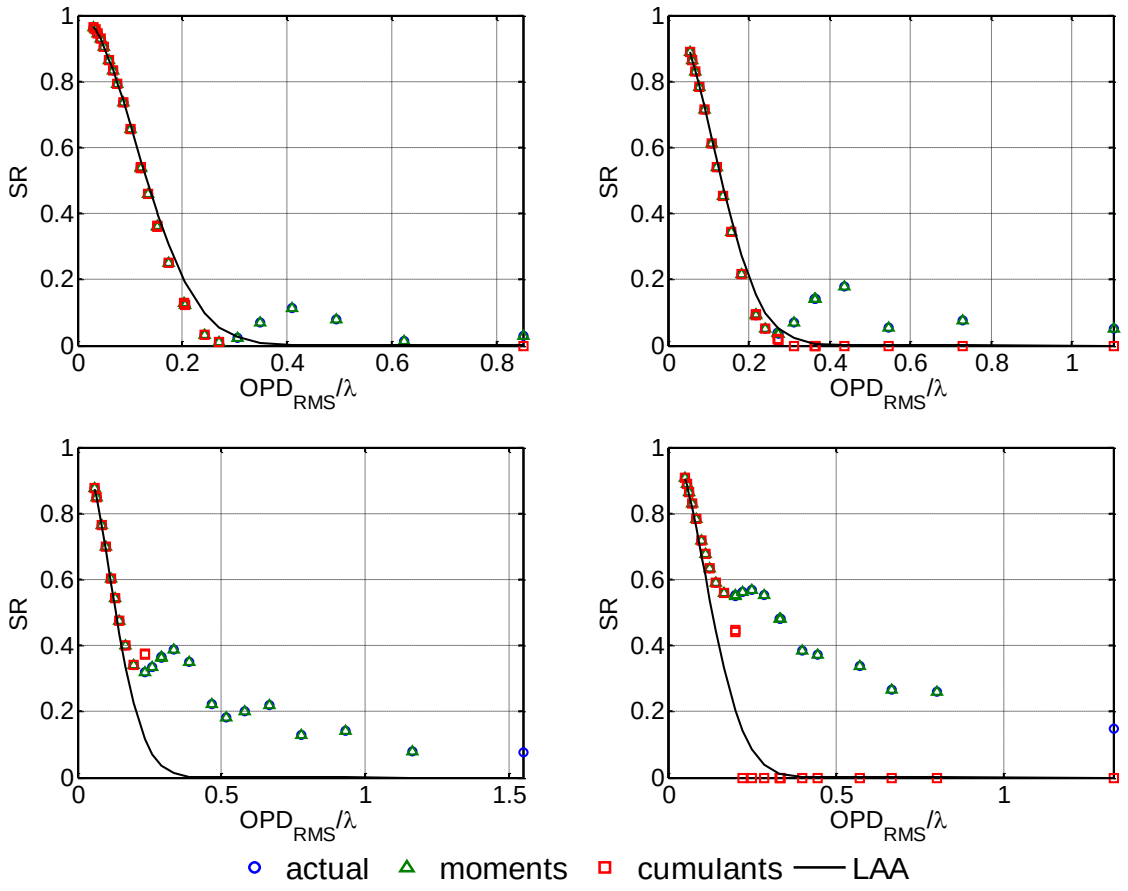

Figure B.9: Strehl ratio approximation of wingtip vortex data using the first 50 moments and cumulants.

Reproducing the higher aperture ratios requires a significant number of terms in the moment expansion. However, as shown in Chapter 6 and 7, the aperture ratio for realistic helicopter applications is around one or two. For these aperture ratios, not nearly as many terms are required to accurately predict the Strehl ratio. Figure B.10 show the Strehl ratio predictions using Eqs. (B.8) and (B.9) for a various number of terms (4, 6, and 10) in the approximation.

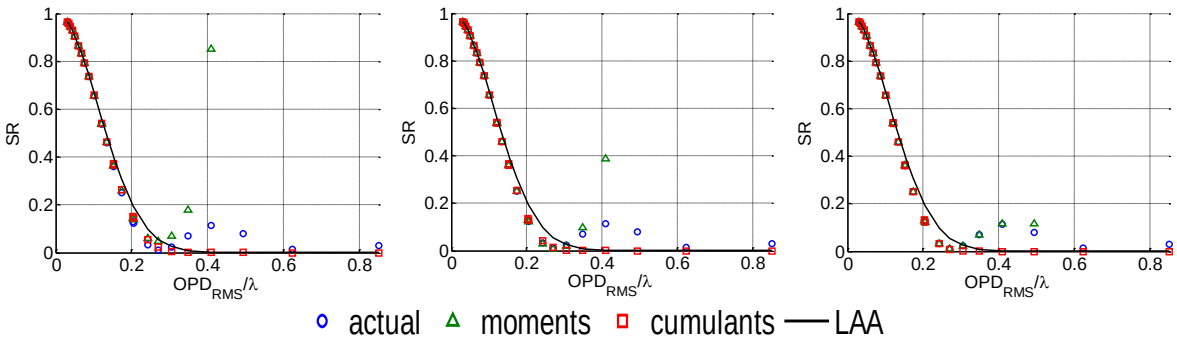

Figure B.10: Strehl ratio approximation using 4 (left), 6 (center), and 10 (right) term expansions of Eqs. (B.8) and (B.9) for an aperture ratio of 1.

The expansion of the Strehl ratio in terms of moments or cumulants appears to not provide a realistically feasible method to predict the Strehl ratio. In fact, solving the Fraunhofer equation may be simpler. However, it did provide insight into the behavior of the Strehl ratio for wing tip vortices with different aperture ratios illustrating the effect of the skewness and kurtosis of the distribution of OPD (something not expected from the LAA). It should be pointed out though that the expansion is realistically feasible for other aero-optic flow fields, such as flow around turrets where the distributions are *Gaussian-like*.

B.2. Strehl Ratio from a Gaussian-Basis Approximation

In the previous section, the Strehl ratio was found by solving the Fraunhofer approximation through a summation of moments or cumulants. While this method works well for phase-error distributions that are Gaussian-like, for the wingtip vortex data it requires a large number of terms. Another approach is to use basis-functions to approximate the Strehl ratio, similar to a Fourier-decomposition of a signal.

Several basis functions exist to decompose the calculated Strehl ratios. While several basis functions would work given enough terms, finding an optimum basis set will reduce the number of terms needed to minimize the error associated with the truncation of terms. The Gaussian basis functions are defined as:

$$G_n = e^{-x^2} H_n(x) \text{where } x = \frac{2\pi OPD_{RMS}}{\lambda}. \tag{B.10}$$

In Eq. (B.10), $H_n(x)$ are the standard Hermite polynomials:

$$\begin{gathered} H_1(x) = 1 \\ H_2(x) = 2x \\ H_3(x) = 4x^2 - 1 \\ H_n(x) = (-1)^n e^{x^2/2} \frac{d^n}{dx^n} e^{-x^2/2} \end{gathered} . \tag{B.11}$$

Using this basis set, the Strehl ratio is defined as:

$$SR = \sum_{n=1}^{\infty} a_n G_n. \tag{B.12}$$

The use of this basis set seems ideal since for exactly one term, with the first coefficient set equal to one, the LAA is obtained. Furthermore, every term goes to zero in the limit as *x* goes to infinity. Therefore, it does not explode like the moments and cumulants approximations did. The result of truncating the number of terms at larger OPD_{RMS}/λ values results in an approximation no worse than the LAA. In Eq. (B.12), the coefficients are solved for by minimizing the square of the error. Caution must be used as unrealistic results are possible, such as Strehl ratios larger than one. Figure B.11 shows the results of a six-term expansion to fit the Strehl ratio data for different aperture ratios. Notice by six terms, at the low aperture ratios, the approximation is good up to the second minima, something that would require approximately 20 terms using a moment

expansion. Furthermore, at the large aperture ratios, it is able to capture the first local minima fairly accurately, and all approximations tend to zero at large OPD_{RMS}/λ values making it no worse than the LAA. Table B.1 gives the coefficients to the Gaussian basis sets for the six-term expansion.

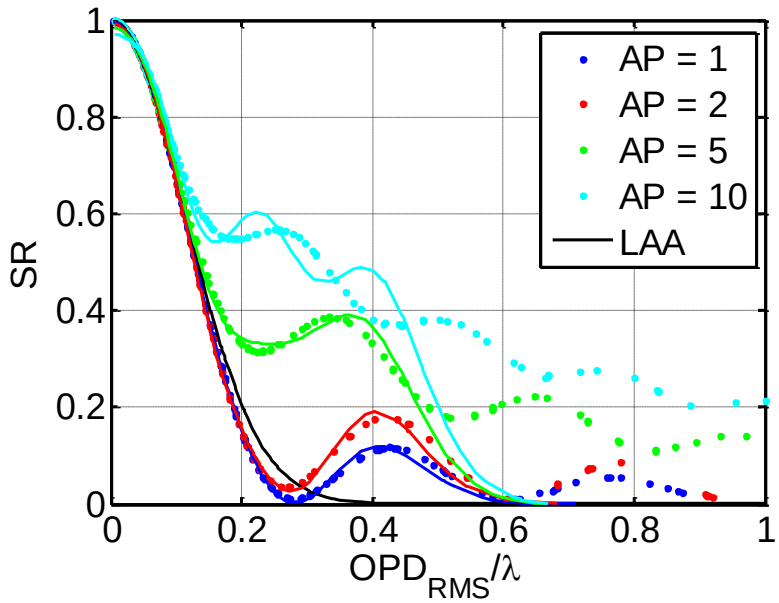

Figure B.11: Gaussian basis expansion using six-terms to calculate the Strehl ratio. Solid lines represent the Gaussian approximation.

TABLE B.1

GAUSSIAN BASIS SET COEFFICIENTS FOR STREHL RATIO APPROXIMATIONS FOR DIFFERENT APERTURE RATIOS FOR A SINGLE VORTEX IN FREE-SPACE

	a_1	a_2	a_3	a_4	a_5	a_6
AP = 1	0.6651	0.3634	-0.2242	0.0583	-0.0097	0.00075
AP = 2	0.4440	0.6346	-0.3709	0.1024	-0.0160	0.00118
AP = 5	0.2760	1.0215	-0.4801	0.1607	-0.0208	0.00157
AP = 10	-0.5593	2.3185	-1.0647	0.3625	-0.0499	0.00312

To emphasize the improvement of this technique to calculate the Strehl ratio for wingtip vortex data, the error associated with the Gaussian-basis approximation and the LAA is shown in Figure B.12 for an aperture ratio of one. The bottom graph in Figure B.12 is the same as the top graph except the axis limits have been changed; the figure is zoomed in on the primary region of interest. As shown in the bottom graph, using a six-term expansion instead of the LAA delays the point at which the error in approximating the Strehl ratio reaches 10%.

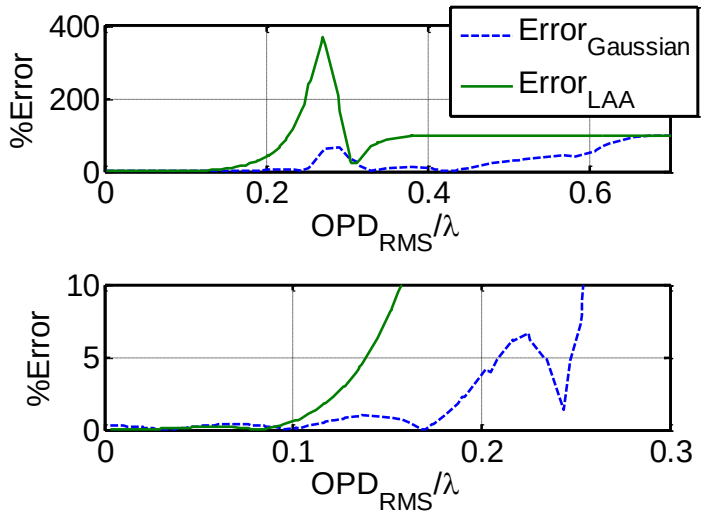

Figure B.12: Gaussian basis expansion using six terms to calculate the Strehl ratio.

B.3. Simulating Phase Error Data

The use of cumulants and moments have provided insight into the behavior of the Strehl ratio for wingtip vortex induced aberration, while using a Gaussian-basis has provided a engineering approximation to estimating the Strehl ratio. The approximation requires more terms then the LAA, but the author feels the additional terms and complexity is a good compromise between accuracy and feasibility. However, by providing the first four moments (mean, standard deviation, skewness, and kurtosis),

using the Pearson random number generator provides PDFs very similar to the measured PDFs. Therefore, the simplest way to obtain and guarantee accurate estimates based on only a few statistical measures is to solve the Fraunhofer equation using an appropriate PDF.

APPENDIX C:

NON-INTRUSIVE DETERMINATIN OF VORTEX PARAMETERS

To determine both the circulation and core radius of a vortex, velocity measurements have always been required; however, velocity measurements are inherently intrusive. For example, with tip-vortex flows the core of the vortex meanders, which results in an averaging effect. Hotwires tend to alter the path of the vortex, making it very hard to measure the core. Other methods which rely on seeding the flow, such as Laser Doppler Velocimetry (LDV), can lead to inaccurate results since getting the particles within the vortex core is very difficult; furthermore, LDV is a single point measurement, so that meander of the vortex core still results in a smoothing effect. Particle Image Velocimetry (PIV) acquires the whole flow field simultaneously, but still relies on seeding particles and so may not accurately measure the vortex core. Standard density-gradient methods, such as Schlieren, are non-intrusive but qualitative (Bagia and Leishman 1993).

The above examples illustrate the difficulty associated with experimental measurements of tip-vortex velocity fields. In this regard, wavefront measurements offer several advantages since they are both non-intrusive and quantitative (at least to a constant). A disadvantage of wavefront measurements is that they are integrated

measurements; that is, a three-dimensional density field yields a two-dimensional wavefront, resulting in a loss of information. However, multiple wavefronts obtained through different propagation paths of the same tip vortex would allow for the reconstruction of the three-dimensional index-of-refraction field using tomography and the Radon transformation.

Wavefront measurements of tip vortices can also yield other useful results; the wavefront information can be used to accurately determine the core radius of the vortex without the effects of wandering (assuming some thermodynamic model). For example, when light propagates through a vortex, a halo can be viewed through the use of shadowgraph techniques (Bagia and Leishman 1993). In a Schlieren system, an intensity profile similar to the vortex velocity profile can be obtained. Simplistically, Schlieren is related to the first spatial derivative of density, and shadowgraph is related to the second spatial derivative of density. Previous research indicated that the inner radius of the halo seen in shadowgraph corresponded to the core radius. However, Bagia and Leishman (1993) showed that this is not the case. They also showed that different vortex models, such as the Rankine, $n=1$, and $n = 2$, produce drastically different shadowgraphs.

If the core radius of the vortex can be determined from wavefront measurements, which are instantaneous, non-intrusive measurements, then from the scaling relationship derived in Chapter 4, the vortex circulation can be determined. The theoretical means to accomplish this is based on the uniqueness of the OPD for different aperture ratios (assuming that the vortex is centered in the aperture). If the aperture ratio can be determined, then the core radius can be calculated since the beam diameter is known. To determine the aperture ratio, a unique relationship must be found between the OPD and

the aperture ratio. One solution to this problem is to normalize the OPD by the maximum OPD (which would ideally occur at the edge of the aperture – Figure C.1). In Figure C.1, the circles represent the location of the core radius. In this way, a unique relationship is obtained by calculating the radius at which the OPD is zero.

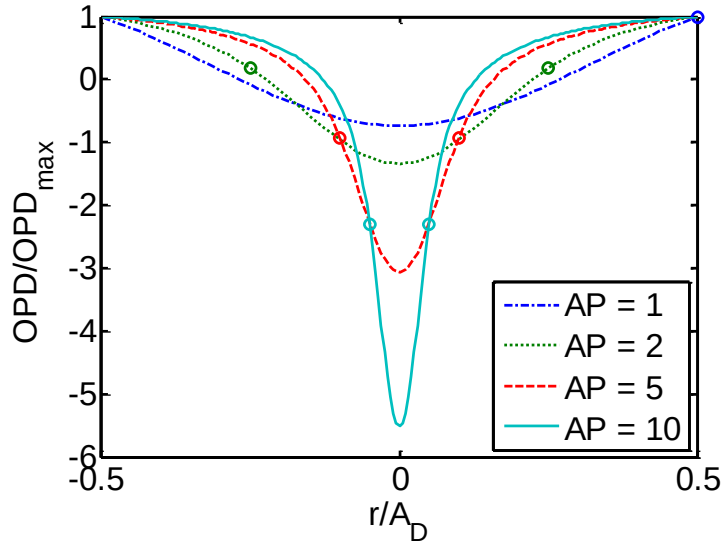

A

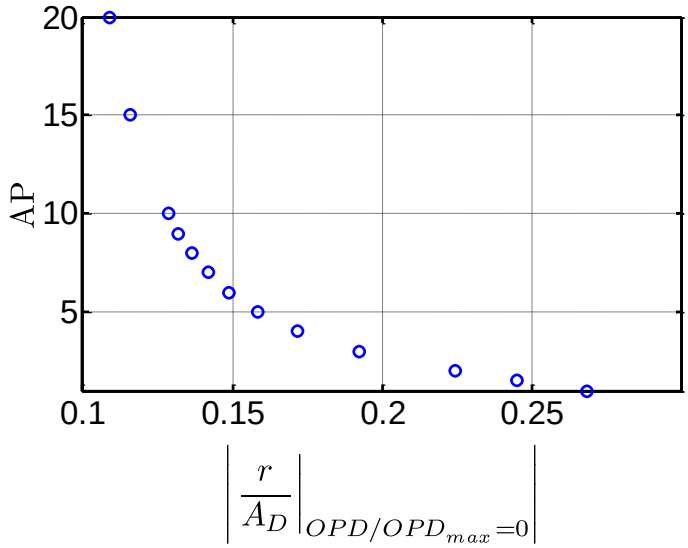

B

Figure C.1: Determination of the zero-crossing of the OPD for different aperture ratios.

With the zero-crossing known, the aperture ratio may be determined from Figure C.1B. From the aperture ratio, the core radius is calculated, and the use of the scaling relationship in Chapter 4 may be used to back out the circulation strength. As an example of the potential to measure vortical properties optically, Figure C.2 shows the first 100 instances of the optical wavefronts from the White Field tunnel data at a Mach number of 0.38 and an angle of attack of 14 degrees. Figure C.3 shows the calculated aperture ratio and vortex core radius from the optical method presented above compared to the calculated values from the SHP.

At this point, the only unknown is the circulation strength. This can be solved for by using the scaling relationships developed in Chapter 4. Note that the relationships in Figure C.1 were developed based on the thermodynamic overlays and calibrated coefficients. Therefore, any error in those calculations will propagate through all of these calculation, and are therefore only as accurate as the developed scaling relationship. However, the optical measurements compare favorably to the values obtained from the SHP.

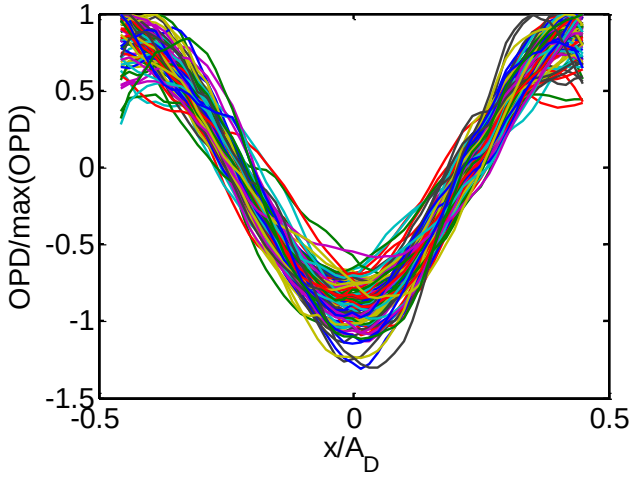

Figure C.2: Instantaneous realizations of the OPD/max(OPD) from wind tunnel tests.

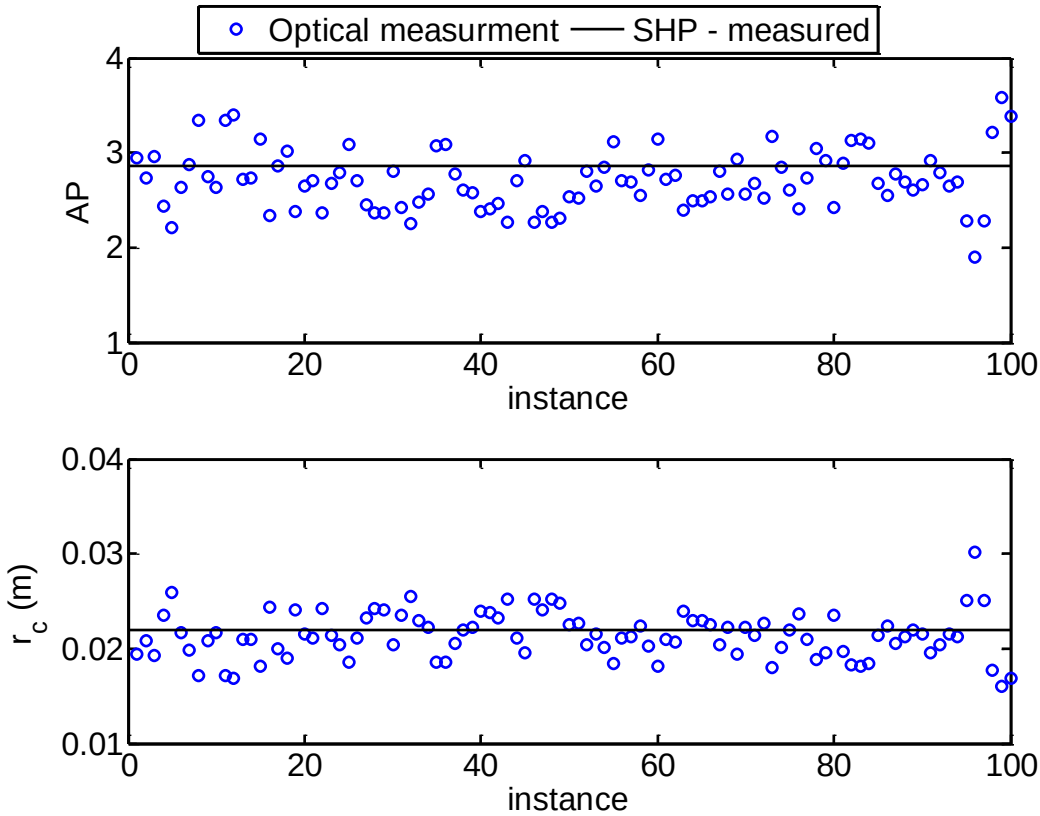

Figure C.3: Calculated aperture ratio and core radius using the wavefront technique compared to the seven hole probe.

APPENDIX D:

MEDIUM-SIZED HELICOPTER DEFINITIONS

For the example tip-vortex calculations presented throughout this dissertation, a standardized set of values have been used. These values were obtained using the equations in Chapter 3 with the following helicopter parameters (see below). The following values were used throughout this dissertation unless otherwise noted:

Parameter	Value
k	2.4
Blade chord (c)	0.5307 m
Blade radius (R)	8.18 m
Velocity of the blade tip (V_{TIP})	Mach 0.8
Number of blades	4
Hub rotation (Ω)	33.3 (1/s)
Solidity (σ)	0.0826
Thrust Coefficient (C_T)	0.0051
Location of Turret relative to TPP	Z = -4.8 m, directly beneath the Hub
Beam diameter (A_D)	0.3 m

APPENDIX E:

OPTICAL EFFECT OF THE VORTEX SHEET IN HOVER

In Chapter 7, the aero-optical effect of the helicopter wake was computed using only the tip-vortices. However, only approximately one third of the total rotor bound vorticity rolls up into the tip vortices, with the rest of the rotor vorticity being shed into a vortex sheet and root vortex. To verify that the vortex sheet and root vortex have a negligible effect on the predicted optical performance, the optical effect of a helicopter in hover was also calculated using Landgrebe's model including the root vortex and vortex sheet. For this calculation, the root vortex and vortex sheet were modeled using 18 individual filaments per rotor blade, each with its own circulation strength and core radius. Furthermore, for this check calculation, the computational requirements were reduced by only modeling 20 revolutions of the wake and by reducing the computational domain in the vertical direction to twice the aperture diameter; however, the same spacing of grid points used in Chapter 7 was used in this computation.

The resulting velocity field was used with the WCM method to calculate the thermodynamic properties. Figure E.1 shows the calculated density field using only the tip-vortex system (top) and the complete wake (bottom). To help clarify the effect of the vortex sheet, the percent difference between the two density fields is shown in Figure

E.2. As expected from the arguments made in Chapter 6, the density variations occur primarily around the tip vortices. Furthermore, the close comparison of the density fields computed with and without the rotor vortex sheet shown in Figure E.2 indicates that the density variation around the tip vortex is not influenced by the vortex sheet.

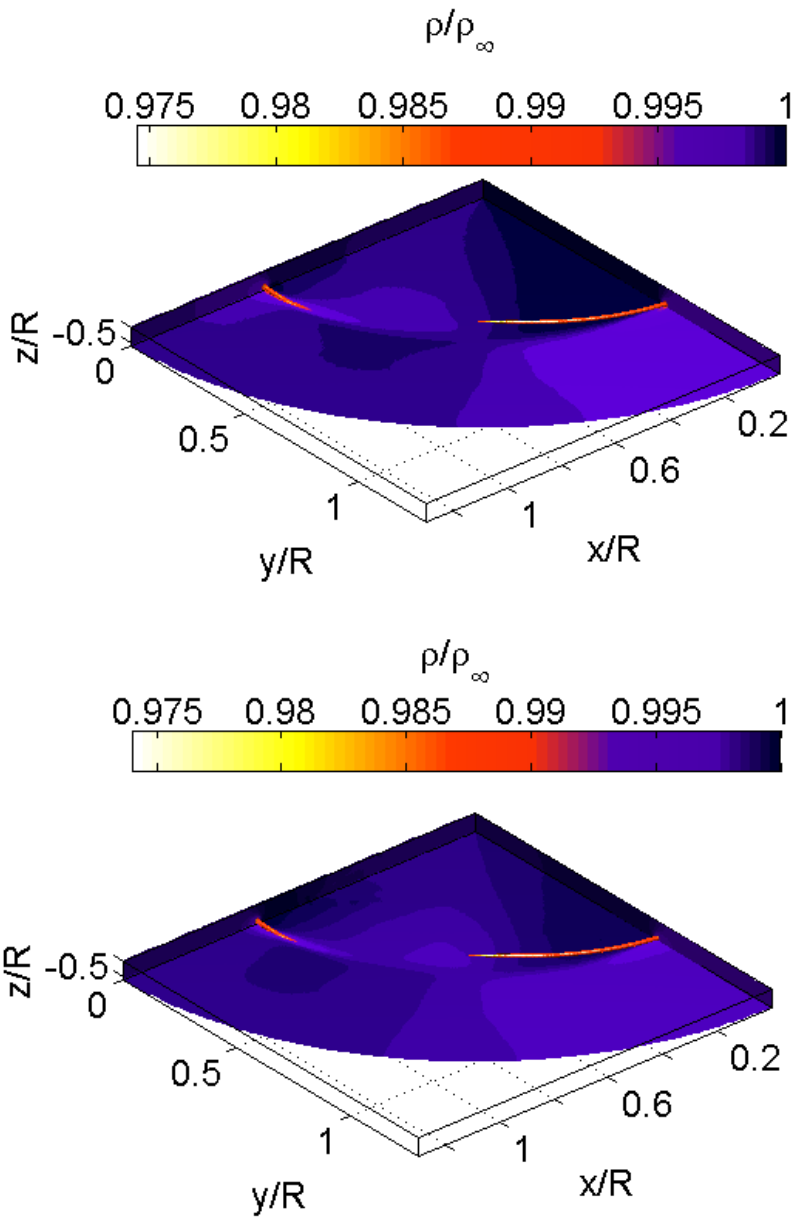

Figure E.1: Comparison of the density field using only the tip-vortex system (top) and including the vortex sheet and root vortex (bottom).

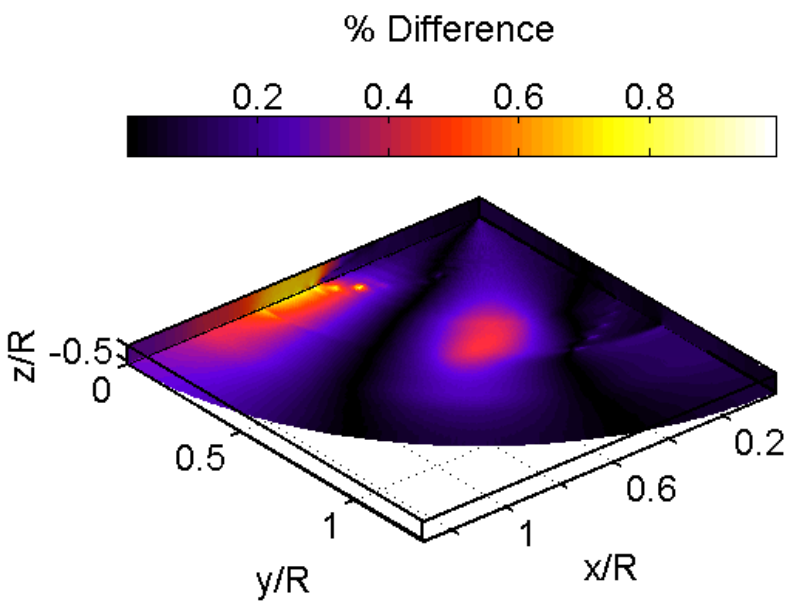

Figure E.2: Percent difference of the density fields using only the tip-vortex system and including the vortex sheet.

To see the optical effect that these small density variations have, a beam was propagated through each density field, and the OPD_{RMS} and resulting Strehl ratio were calculated. Figure E.3 shows the comparison of the resulting OPD_{RMS} as a function of the relative beam angle, ζ. In this case, the main effect of the vortex sheet occurs at a relative beam angle of 40-50 degrees, which results in a small, but negligible, increase in the OPD_{RMS}. Finally, the corresponding Strehl ratio was also calculated, shown in Figure E.4. As shown, no discernible difference is evident in the calculated Strehl ratio.

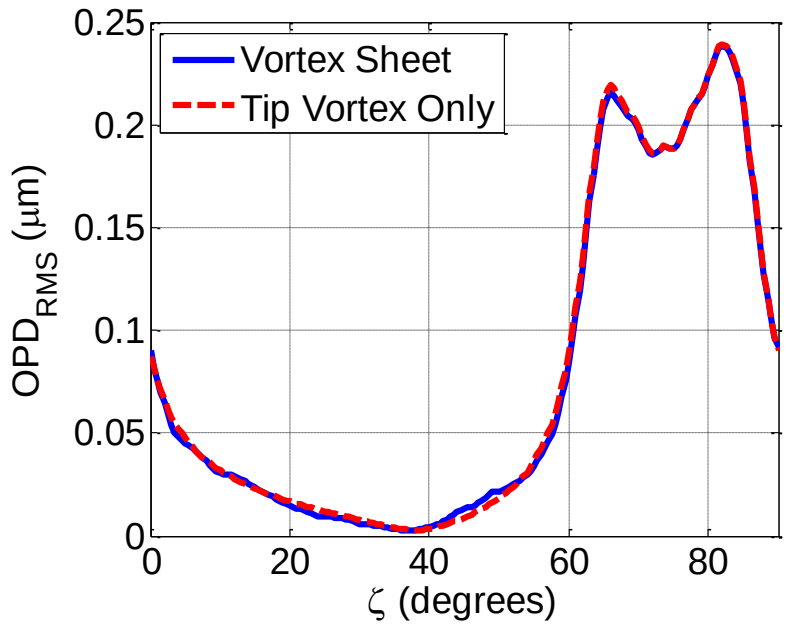

Figure E.3: Comparison of the OPD_{RMS} for a beam propagating through the wake of a helicopter modeled using on the tip vortices or modeled including the vortex sheet and root vortex.

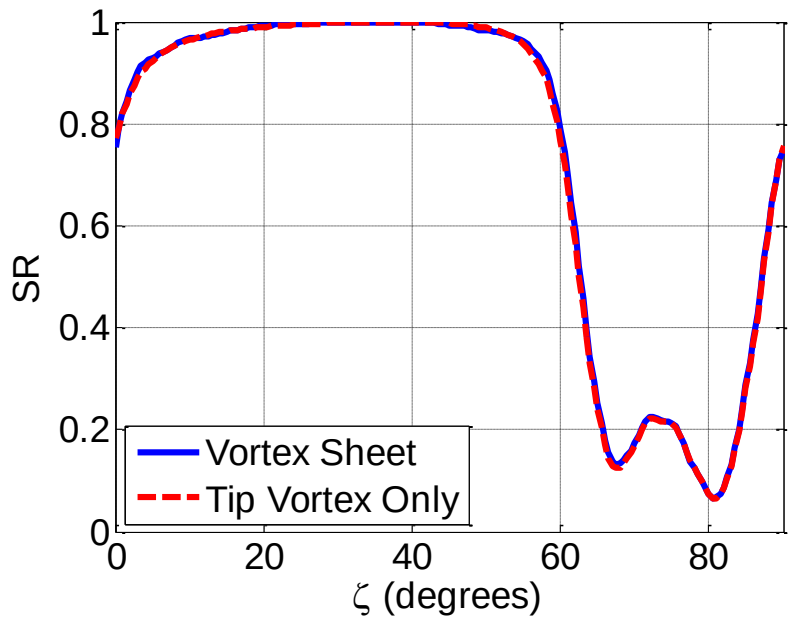

Figure E.4: Comparison of the Strehl ratio for a beam propagating through the wake of a helicopter modeled using on the tip vortices or modeled including the vortex sheet and root vortex.

REFERENCES

Aboelkassem, Y., and Vatistas, G.H., (2007) On the refracted patterns produced by liquid vortices, *Acta Mech Sin,* 23, 11-15.

Aboelkassem, Y., and Vatistas, G.H., (2007b) New Model for Compressible Vortices, *Journal of Fluids Engineering,* Vol. 129 (1073), August 2007.

Abramowitz, M., and Stegun, I.A., (1972) Handbook of Mathematical Functions with Formulas, Graphs, and Mathematical Tables, 10th printing, National Bureau of Standards – Applied Mathematics Series – 55.

Ananthan, S. and Leishman, J. G., "Role of Filament Strain in the Free-Vortex Modeling of Rotor Wakes," *Journal of the American Helicopter Society,* Vol. 49, No. 2, pp. 176-191, 2004.

Babie, B.M., (2008). An experimental and analytical study of the stability of counter-rotating vortex pairs with applications for aircraft wake turbulence control. *PhD thesis,* University of Notre Dame.

Bagai, A., and Leishman, G.J., (1993). Flow visualization of compressible vortex structures using density gradient techniques, *Exp Fluids,* 15, 431-442.

Bhagwat, M. J., and Leishman J. G., (2002). Generalized Viscous Vortex Model for Applications to Free-Vortex Wake and Aeroacoustic Calculations. 58th Annual Helicopter Society International, Montreal, Canada, June 11-13.

Beddoes, T.J., (1985). A wake model for high resolution air loads. *International Conference on Helicopter Basic Research.* Research Triangle Park, N.C.

Berry, M.V., and Hajnal, J.V., (1983), The shadows of floating objects and dissipating vortices, *Optica Acta,* 30(1), 23-40.

Born, M. and Wolf, E., *Principles of Optics*, 6th ed. (Pergamon 1997), Chap 9.1.3, Eq. (24), p. 464.

Butts, R., and Weaver, L. D., (1994). Airborne laser experiment (ABLEX): theory and simulations, *SPIE – Laser beam propagation and control*, 2120(10).

Cengel, Y. A., and Boles, M. A., Thermodynamics: An Engineering Approach, 4th Edition, McGraw Hill, 2002.

Cheung, K., "A simple criterion for vortex breakdown", Master's thesis, University of Notre Dame, May, 1993.

Cole, M., and Washburn, D., Closed-Loop AO Assessment Code, MZA Associates, private communications.

Coleman, H. W. and Steele, W. G., Experimentation and Uncertainty Analysis for Engineers, 2nd Edition, Wiley-Interscience Publication, 1999.

Colonius, T., Keke, S.K., and Moin, P., The free compressible viscous vortex, *J. Fluid Mech*. (1991), vol. 230, pp. 45-73/

Conlisk, A.T., (2001). Modern helicopter rotor aerodynamics. *Progress in Aerospace Sciences*, 37, 419-476.

Cotel, A.J., and Breidenthal, R.E., Turbulence inside a vortex, *Physics of Fluids*, 11(10), 3026-3029.

Cress, J.A., Gordeyev, S., Post, M.L., and Jumper, E.J., (2008). Aero-optical measurements in a turbulent, subsonic boundary layer at different elevation angles, *AIAA paper 2008-4214*.

Cress, J.A., Optical Aberrations Caused by Coherent Structures in a Subsonic, Compressible, Turbulent Boundary Layer, *Dissertation* – University of Notre Dame, June 2010.

Devenport, W., Rife, M., Stergios, L., and Gordon, F., (1996). The structure and development of a wing-tip vortex, *Journal of Fluid Mechanics*. 326, 67-106.

Duffin, D.A., (2009). Feed-forwards adaptive-optic correction of a weakly compressible high-subsonic shear layer. *PhD thesis*, University of Notre Dame.

Duffner, R., (2009). The Adaptive Optics Revolution: A History, *University of New Mexico Press*, 202-235.

Ellenrieder, K. V. and Cantwell B. J., Self-similar, slightly compressible, free vortices. *J. Fluid Mech*. (200), Vol. 423, pp. 293-315.

Fitzgerald, E.J., and Jumper, E.J., (2004). The optical distortion mechanism in a nearly incompressible free shear layer. *Journal of Fluid Mechanics*, 512, 153-189.

Gallington, R.W., 1980, Measurement of very large flow angles with non-nulling seven-hole probe, Aeronautics Digest, USAFA-TR-80-17, 60-88.

Gilbert, K.G., and Otten, L.J., (1982). Aero-Optical Phenomena. *Progress in Astronautics and Aeronautics*, Volume 80.

Goodman, J.W., (2005). Introduction to Fourier optics. *Roberts and Company*, 3rd Edition.

Gordeyev, S., and Jumper, E.J., Fluid dynamics and aero-optical environment around turrets, *AIAA Paper 2009-4224*.

Gordeyev, S., and Jumper, E. J., (2010). Fluid dynamics and aero-optics of turrets. *Prog. Aerospace Sci.* (2010), 46, 388-400.

Gordeyev, S., Jumper, E.J., Ng, T.T., and Cain, A.B., (2003). Aero-optical characteristics of compressible, subsonic turbulent boundary layers, *AIAA Paper 2003-3606*.

Green, S. I. and Acosta, A. J., (1991). Unsteady flow in trailing vortices, *Journal of Fluid Mechanics*, 227, 107-134.

Huu Nho, E.L., and Béguier, C., (1995) Velocity measurements in 3D turbulent flows by means of a rotating x-wire probe. *Meas. Sci. Technol.*, 6, 843-850.

Iungo, G., Skinner, P., and Buresti, G., (2009). Correction of wandering smoothing effects on static measurements of a wing-tip vortex. *Experiment of Fluids*, 46, 435-452.

Jumper, E.J., and Fitzgerald, E.J. (2001). Recent advances in aero-optics. *Progress in Aerospace Sciences*, 37, 299-339.

Kist, R.A., and Garry, K.P., (1993) Hazards due to helicopter wakes, *COA report No. 9311*, Cranfield University-College of Aeronautics.

Kini, S., and Conlisk, A. T., (2002) Nature of Locally Steady Rotor wakes, *Journal of Aircraft*, Vol. 39 (6), pp. 750-758.

Klein, M.V., (1970). Optics. *John Wiley and Sons, Inc*. New York, 1st Edition.

Kozlov, V.E., Lebedev, A.B., Lyubimov, D.A., and Sekundov, A.N., (2003) Distinctive Features of the Turbulent Flow in a Trailing Vortex, *Fluid Dynamics*, Vol. 39 (1), pp 69-75.

Kuethe, A.M., and Chow, C.Y., (1998) Foundations of aerodynamics: bases of aerodynamic design, *John Wiley & Sons, Inc.*, 5th Edition.

Ladd, J., Mani, M., and Bower, W., (2009). Validation of aerodynamic and optical computations for the flow about a cylindrical/hemispherical turret, *AIAA Paper 2009-4118*.

Leishman, J.G., (2000). Principles of helicopter aerodynamics. *Cambridge Aerospace Series*, 1st Edition.

Leishman, J.G., Bhagwat, M.J., and Bagai, A., (2002). Free-Vortex filament methods for the analysis of helicopter rotor wakes, *Journal of Aircraft*, 39(5), 759-775.

Liepmann, H. W., (1952). Deflection and Diffusion of a Light Ray Passing Through a Boundary Layer. *Douglas Aircraft Company - Report No. SM-14397*, Santa Monica Division.

Mahajan, M.V., (1982). Strehl ratio for primary aberrations: some analytical results for circular and annular pupils. *Journal of Optical Society of America*. 72(9), 1258-1266.

Mahajan, M.V., (1983). Strehl ratio for primary aberrations in terms of their aberration variance. *Journal of Optical Society of America.* 73(6), 860-861.

Nightingale, A.M, et al, "Regularizing Shear Layer for Adaptive Optics Control Applications, AIAA-2005-4774, June, 2005.

Nightingale, A.M., Mitchell, B., Goodwine, B. and Jumper, E.J., (2008). "Feed-forward" adaptive-optic mitigation of aero-optic disturbances, *AIAA Paper 2008-4211*.

Orangi, S., Foster, M. R., and Bodonyi, R.J., On the structure of a three-dimensional compressible vortex, *Computers and Fluids* (2001), Vol. 30, pp 115-135.

Payne, F.M., (1987). The structure of leading edge vortex flows including vortex breakdown, *PhD thesis*, University of Notre Dame.

Ponder, Z. B., Rennie, M. R., Abado, S., and Jumper, E. J., Span-wise Wavefront Measurements Through a Two-Dimensional Weakly-Compressible Shear Layer, AIAA 2010-4495, 41st Plasmadynamics and Lasers Conference, 28 June-1 July, Chicago IL.

Ponder, Z., Gordeyev, S., Jumper, E., Griffin, S., and McGaha, C., Passive Mitigation of Aero-Induced Mechanical Jitter of Flat-Window Turrets, In Press, 42nd AIAA Plasmadynamics and Lasers Conference, 27-30 Jun 2011, Honolulu, HI.

Porter, C. O., Gordeyev, S., Zenk, M., and Jumper, E., Flight Measurements of Aero-Optical Distortions from a Flat Windowed Turret on the Airborne Aero-Optics Laboratory (AAOL), In Press, 42nd AIAA Plasmadynamics and Lasers Conference, 27-30 Jun 2011, Honolulu, HI.

Ramasamy, M., and Leishman, J. G., " A Reynolds Number-Based Blade Tip Vortex Model," *Journal of the American Helicopter Society*, Vol. 52, No. 3, pp. 214-223, 2007.

Ramasamy, M., and Leishman, J. G., "Interdependence of Diffusion and Straining of Helicopter Blade Tip Vortices," *Journal of Aircraft*, Vol. 41, No. 5, pp. 1014-1024, 2004.

Rennie, R.M., Crahan, G., and Jumper, E.J., (2010a). Aerodynamic design of an aircraft-mounted pod for improved aero-optic performance, *AIAA Paper 2010-437*.

Rennie, R.M., Cross, G., Goorskey, D., Whiteley, M.R., Cavalieri, D., and Jumper, E.J., (2010b). Optical measurement of a compressible shear layer using a laser-induced air breakdown beacon, *AIAA Paper 2010-1158*.

Rennie, R.M., Duffin, D.A., and Jumper, E.J., (2008). Characterization and aero-optic correction of a forced two-dimensional weakly compressible shear layer, *AIAA Journal*, 46(11), 2787-2795.

Rennie, R.M., Ponder, Z., Gordeyev, S., Nightingale, A., and Jumper, E., (2008b). Numerical Investigation of Two-Dimensional Compressible Shear Layer and Comparison to Weakly Compressible Model, *DEPS*.

Ross, T. S. (2009). Limitations and applicability of the Maréchal approximation, *Applied Optics*, 48(10), 1812-1818.

Rossow, V. J., (1999). Lift-generated vortex wakes of subsonic transport air, *Progress in Aerospace Sciences*, 35, 507-660.

Rossow, V.J., (2006). Origin of exponential solution for laminar decay of isolated vortex, *Journal of Aircraft*, 43(3), 709-712.

Rott, N., On the viscous core of a line vortex II, *ZAMP*, Vol. X, 1959, pp. 73-81.

Schlichting, H., Boundary-Layer Theory, 8th Edition, 2000.

Schonberger, J.R., Fuhs, A.E., and Mandigo, A.M., (1982). Flow control for an airborne laser turret, *Journal of Aircraft*, 19(7), 531-537.

Siegenthaler, J.P., (2008). Guidelines for adaptive-optic correction based on aperture filtration. *PhD thesis*, University of Notre Dame.

Sonntag, R., Borgnakke, C., and Van Wylen, G., Fundamentals of Thermodynamics, 6th Edition, Wiley and Sons, 2003.

Stallings, R.L., (1992) Low Aspect Ratio Wings at High Angles of Attack. *Tactical Missile Aerodynamics: General Topics*, AIAA Progress in Astronautics and Aeronautics, 141, 251-286.

Stathopoulos, F., Constantinou, P., and Panagopoulos, A.D., Impact of various flow-fields on laser beam propagation. *IEEE* 978-1-4244-3559-3.

Sterling, M.H., Gorman, M., Widmann, P.J., Coffman, C., Strozier, J., and Kiehn, R.M., (1987) Why are these disks dark? The optics of Rankine vortices, *Physics of Fluids: Brief Communications*, 30(11), 3624-3626.

Stine, H. A., and Winovich, W. (May 1954). Light diffusion through high-speed turbulent boundary layers. Research Memorandum A56B21, NACA, Washington.

Stock, M. J., Gharakhani, A., and Stone, C. P., Modeling Rotor Wakes with a Hybrid OVERFLOW-Vortex Method on a GPU Cluster, AIAA 2010-5099, AIAA Conference, 28 June-1 July, Chicago IL.

Sutton, G. W., (1985). Aero-optical Foundations and Applications, *AIAA Journal*, 23(10), 1525-1537.

Tangler, J. L., Wohlfeld, R. M., and Miley, S. J., An Experimental Investigation of Vortex Stability, Tip Shapes, Compressibility, and Noise for Hovering Rotor Models, NASA CR-2305, September 1973.

Tatarskii, V. I., and Zavorotnyi, V. U., (1985). Wave propagation in random media with fluctuating turbulent parameters. *J. Opt Soc Am A*, 2(12), 2069-2076.

Teager, S.A., Biehl, K.J., Garodz, L.J., Tymczyszym, J.T., and Burnham, D.C., (1996) Flight test investigation of helicopter wake vortices in forward flight, *Final Report*, DOT/FAA/CT-94/117.

Tyson, R.K., *Principles of Adaptive Optics*, Academic Press, Inc., San Diego, 1991.

Visbal, M.R. and Rizzetta, D.P., (2008). Effect of Flow Excitation on Aero-Optical Aberration, *AIAA paper* 2008-1074.

Vatistas, G.H., (2006). The optics of the compressible N = 2 vortex, *Transactions of the CSME/de la SCGM*, 30(1), 143-166.

Vatistas, G. H., Kozel, V., and Mih, W. C., (1991). A Simpler Model for Concentrated Vortices, *Experiments in Fluids*, Vol. 11, 73-76.

Vatistas, G. H., (1998). New Model for Intense Self-Similar Vortices, *Journal of Propulsion and Power*, 14(4), 462-469.

Visser, K.D., (1991). An experimental analysis of critical factors involved in the breakdown process of leading edge vortex flows, *PhD thesis*, University of Notre Dame.

Wallace, R.D., Shea, P.R., Glauser, M.N., Vaithianathan, T., and Carlson, H.A., (2010). Feedback flow control for a pitching turret (Part II), *AIAA Paper2010-361*.

Weaver, L. D., and Butts, R., (1994). ABLEX: High altitude laser propagation experiment, *SPIE – Laser Beam Propagation and Control*, 2120(30).

Wie, S. Y., Lee, S., and Lee, D.J, "Potential Panel and Time-Marching Free-Wake Coupling Analysis for Helicopter Rotor," *Journal of Aircraft*, Vol. 46 (3), 2009, 1030-1041.

Wittich, D.J., (2009). Subsonic flow over open and partially-covered, rectangular cavities. *PhD thesis*, University of Notre Dame.

Xiaoliang, M., Guowei, Y., and Yiqing, S., (2007). Laser beam propagation in compressible vortical field, *Chinese Journal of Computational Physics*, 25(5), 602-606.[1]

Zang, H.J., Zhou, Y., Whitelaw, J.H., (2006). Nearfield Wing-Tip Vortices and Exponential Vortex Solution, *Journal of Aircraft*, 43(2), 445-449.

[1] Paper is written in Chinese with an English abstract and figure captions. Inferences are made from math and figures alone as the author cannot read Chinese.